

**NASA TECHNICAL
MEMORANDUM**

NASA TM X-71814

NASA TM X-71814

(NASA-TM-X-71814) CENTAUR STANDARD SHROUD
(CCS) HEATED ALTITUDE JETTISON TESTS (NASA)
238 p HC \$8.00

CSCL 22D

N76-17179

Unclass

G3/15 14157

**CENTAUR STANDARD SHROUD (CSS)
HEATED ALTITUDE JETTISON TESTS**

Lewis Research Center
Cleveland, Ohio 44135
August 1975



1 Report No NASA TM X-71814	2 Government Accession No	3 Recipient's Catalog No	
4 Title and Subtitle CENTAUR STANDARD SHROUD (CSS) HEATED ALTITUDE JETTISON TESTS		5 Report Date	
		6 Performing Organization Code	
7 Author(s) Lewis Research Center Staff		8 Performing Organization Report No E-8508	
		10 Work Unit No	
9 Performing Organization Name and Address Lewis Research Center National Aeronautics and Space Administration Cleveland, Ohio 44135		11 Contract or Grant No	
		13 Type of Report and Period Covered Technical Memorandum	
12 Sponsoring Agency Name and Address National Aeronautics and Space Administration Washington, D.C. 20546		14 Sponsoring Agency Code	
15 Supplementary Notes			
16 Abstract Three altitude jettison tests, at a pressure of 20 torr (0.39 psia), were performed on the Centaur Standard Shroud (CSS) in a 100-foot diameter vacuum chamber. The test chamber is a part of the Space Power Facility at the Plum Brook Station of Lewis Research Center. These jettison tests were part of a series of flight qualification tests which were performed on the new CSS system in preparation for the Helios and Viking missions. The first two tests subjected the CSS to a thermal cycle which simulated aerodynamic heating during ascent flight and the third test was performed at altitude pressure and in ambient temperature conditions. The purpose of the ambient temperature test was to provide base line data by which the separate mechanical and thermal factors that influence jettison performance could be evaluated individually. The CSS was successfully jettisoned in each of the three tests. Also, thermal, stress, and structural deflection data were obtained which verified the CSS contractor's (Lockheed Missiles and Space Co., Inc.) analytical predictions of CSS response to flight environmental conditions and performance during jettison. In addition, much important information was obtained on critical CSS-to-payload clearance losses due to shell motions prior to and during jettison. The effectiveness of the Super*Zip separation system was successfully demonstrated at maximum flight temperatures.			
17 Key Words (Suggested by Author(s))		18 Distribution Statement Unclassified - unlimited	
19 Security Classif (of this report) Unclassified	20 Security Classif (of this page) Unclassified	21 No of Pages	22 Price*

TABLE OF CONTENTS

SECTION NO.		PAGE
	TABLE OF CONTENTS	ii
	ABBREVIATIONS	1
I	SUMMARY	2
II	INTRODUCTION	3
III	APPARATUS	10
IV	PROCEDURE	46
V	TEST RESULTS AND DISCUSSION	48
VI	CONCLUDING REMARKS	188
	APPENDIX A: Calculations of CSS Edge Motions	189
	APPENDIX B: Comparison of Test Results to Thermal Model Calculations	207
	APPENDIX C: Differences in Configuration between the Proof Flight and Test CSS	224
	APPENDIX D: Calculations of CSS edge Motions from Accelerometer Data	226

ABBREVIATIONS

C.G.	- Center of Gravity
CSS	- Centaur Standard Shroud
E/M	- Equipment Module
FBR	- Forward Bearing Reactor
FSR	- Forward Seal Release
GDC	- General Dynamics Convair Division
HJT	- Heated Altitude Jettison Test
IST	- Intermediate Scale Tests
LH ₂	- Liquid Hydrogen
LMSC	- Lockheed Missiles and Space Company, Inc.
MMC	- Martin Marietta Corporation
MTL	- Maximum Thermal Line
PYC	- Pyrotechnic Control Unit
SFC	- Squib Fire Circuit
SMDC	- Shielded Mild Detonating Cord
SPF	- Space Power Facility, Plum Brook
SRM	- Solid Rocket Motor
TC-2	- Titan/Centaur, Flight No. 2
TVC	- Thrust Vector Control
VDC	- Volts, Direct Current

1. SUMMARY

by Thomas F. Niezgoda

Three altitude jettison tests, at a pressure of 20 torr (0.39 psia), were performed on the Centaur Standard Shroud (CSS), in a 100-foot diameter vacuum chamber. The test chamber is a part of the Space Power Facility at the Plum Brook Station of Lewis Research Center. These jettison tests were part of a series of flight qualification tests which were performed on the new CSS system in preparation for the Helios and Viking missions. The first two tests subjected the CSS to a thermal cycle which simulated aerodynamic heating during ascent flight and the third test was performed at altitude pressure and in ambient temperature conditions. The purpose of the ambient temperature test was to provide base line data by which the separate mechanical and thermal factors that influence jettison performance could be evaluated individually.

The CSS was successfully jettisoned in each of the three tests. Also, thermal, stress, and structural deflection data were obtained which verified the CSS contractor's (Lockheed Missiles and Space Co., Inc.) analytical predictions of CSS response to flight environmental conditions and performance during jettison. In addition, much important information was obtained on critical CSS-to-payload clearance losses due to shell motions prior to and during jettison. The effectiveness of the Super*Zip separation system was successfully demonstrated at maximum flight temperatures.

II. INTRODUCTION

All spacecraft require some form of protection from weather and a thermally controlled environment during prelaunch operations. In addition, protection is required from aerodynamic and thermal environments during launch and ascent. These requirements are usually satisfied by a shroud or fairing attached to the forward end of the launch vehicle and enclosing the spacecraft. The shroud is jettisoned after the most adverse conditions are passed in the launch and ascent phase of flight.

In addition to spacecraft protection, launch vehicles utilizing cryogenic propellants require thermal insulation during prelaunch operations to prevent excessive propellant boiloff. Insulation is also required during ascent for protection from aerodynamic heating.

The Centaur upper stage vehicle, mated with the Titan IIID booster, shown in figure II-1, was chosen to be the launch vehicle for the Viking spacecraft which is to orbit and soft land on the planet Mars in 1976. This Centaur vehicle shown in figure II-2 is called the Centaur D-1T (ref. 1).

The Centaur was the United States' first upper stage vehicle to use liquid hydrogen and liquid oxygen as propellants. As the upper stage for the Atlas booster, this combination has been the launch vehicle for Surveyor, Mariner, Pioneer, OAO, and a series of communication satellites.

The D-1A Centaur upper stage vehicle, using the Atlas as the booster stage, utilizes several shroud designs for spacecraft protection dictated by spacecraft size and mission requirements. Thermal protection for the Centaur vehicle during prelaunch and ascent is provided by jettisonable insulation panels.

The Viking spacecraft requires a large diameter aeroshield. This meant an increased diameter shroud would be required for spacecraft enclosure. The larger diameter shroud would also be heavier than existing shrouds and aerodynamic loading during ascent would tax the strength of the Centaur. One possibility to enhance structural capability would be to make the Centaur tank heavier and redesign the present insulation panels to be capable of carrying structural loading. This, however, meant increased complexities and many modifications to existing designs. Instead, a large shroud that would cover both the spacecraft and Centaur, and act as a structural member as well as incorporating insulation for Centaur's cryogenic propellant tanks, was conceived and studied. This was the design concept chosen and Lockheed Missiles and Space Company, Inc. (LMSC) was awarded the contract to design and build the shroud. This shroud has been designated the Centaur Standard Shroud (CSS).

In addition to many development and qualification tests on subsystems conducted by the manufacturers (e.g., separation joint test described in ref. 1a) the CSS has undergone flight qualification testing at the NASA Lewis Research Center's Plum Brook Station. The Plum Brook test program consisted of the following series of tests:

1. Hinge Loading Tests (ref. 2), in which strength and deflection characteristics of the jettison hinges, boattail section, and Centaur Interstage Adapter were determined.
2. Cryogenic Unlatch Tests (refs. 3 and 4), which demonstrated that the CSS will thermally protect the Centaur tanked with cryogenic propellants during launch operations, and that the CSS will begin to jettison ("unlatch") from the Centaur under cryogenic conditions.
3. Static Limit Load Structural Tests (ref. 5), which demonstrated that the CSS can safely withstand aerodynamic and initial loads up to limit (design) loads.
4. Altitude Jettison Tests, reported herein, which provided data for future mission analyses and demonstrated that the CSS will jettison successfully after being subjected to heating which simulates aerodynamic heating during ascent flight.

Test Objectives

The test objectives for the Altitude Jettison Tests were as follows:

1. Provide data to verify analytical tools used to predict CSS dynamic motions, trajectories, and thermal stress distributions during flight conditions of ascent, both prior to jettison and during jettison.
2. Determine CSS-to-payload envelope clearance at test conditions.
3. Determine CSS hinge loads, and load distribution in the Centaur Interstage Adapter and interface ring.
4. Determine loads developed in the CSS structure by CSS heating.
5. Verify the functional and structural capability of the CSS to separate during jettison.
6. Determine the trajectory of the CSS halves during these jettison tests.
7. Determine the CSS shell motions during these jettison tests.

8. Obtain jettison "signature" data for flight instrumentation.
9. Determine the effectiveness of the Super-Zip separation system after having been subjected to temperatures equivalent to aerodynamic heating, for both primary and secondary firing modes.

For the Altitude Jettison Tests, the CSS was assembled in the Space Power Facility on the Centaur Interstage Adapter as shown in figure 11-3. Inside the CSS were assembled a Truss Adapter, Stub Adapter, Equipment Module, all important hardware which interfaces with the CSS, and structures to simulate the Centaur tank and the payload dynamic envelope. A large electrically powered heating fixture which radiated energy to the CSS, was placed around the CSS as shown in figure 11-4. After evacuating the test chamber, the CSS was heated to simulate aerodynamic heating during a thermally severe flight at the end of the heating period. The heating fixture was retracted and the CSS was jettisoned into catching nets by activating the Super-Zip separation system.

Two heated tests, plus one unheated test to obtain data to separate the mechanical and thermal factors affecting jettison performance, were performed. The heated tests differed in that the Maximum Thermal Line (MTL) was located at 328° and at 0° azimuths because the initial CSS dynamic shell motions were expected to be a worst case for these conditions.

This report presents data and test results to show that all objectives were attained successfully. In addition, the report presents a comparison of test results with analytical predictions made by Lockheed Missiles and Space Company, Inc. (LMSC), the CSS contractor.

The Altitude Jettison Tests were performed for the Titan/Centaur Project Office by the Space Power Facility Division of Lewis Research Center's Plum Brook Station during the period from November 1973 to February 1974. The tests were supported by LMSC and General Dynamics Convair Division (GDC), the Centaur contractor.

Details on instrumentation for these altitude jettison tests may be found in reference 10. This document describes the total test requirements and includes all instrumentation designation numbers, locations on the CSS, instrument type, etc.

TITAN III E/CENTAUR D-IT

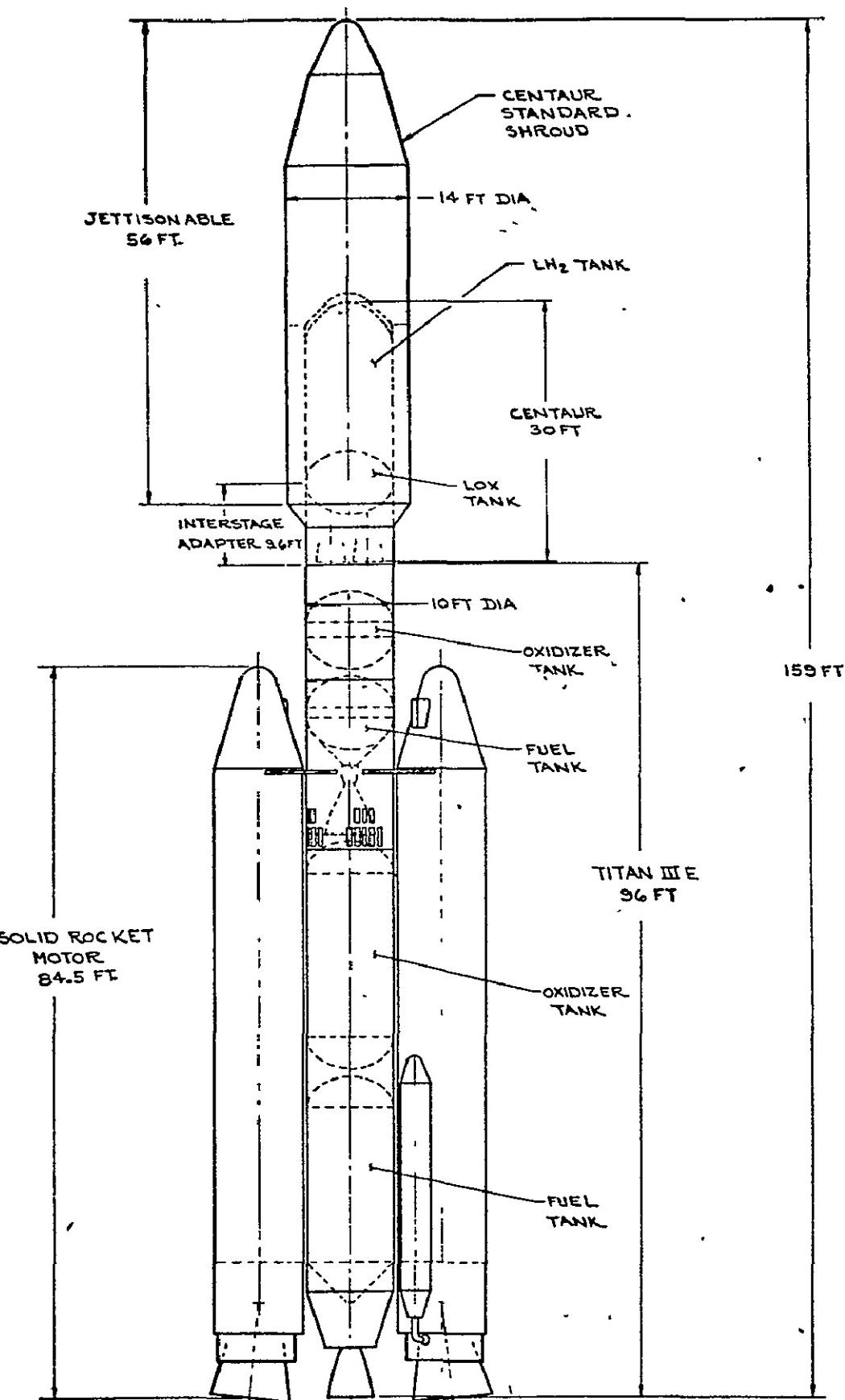


FIGURE II-1 TITAN/CENTAUR LAUNCH VEHICLE

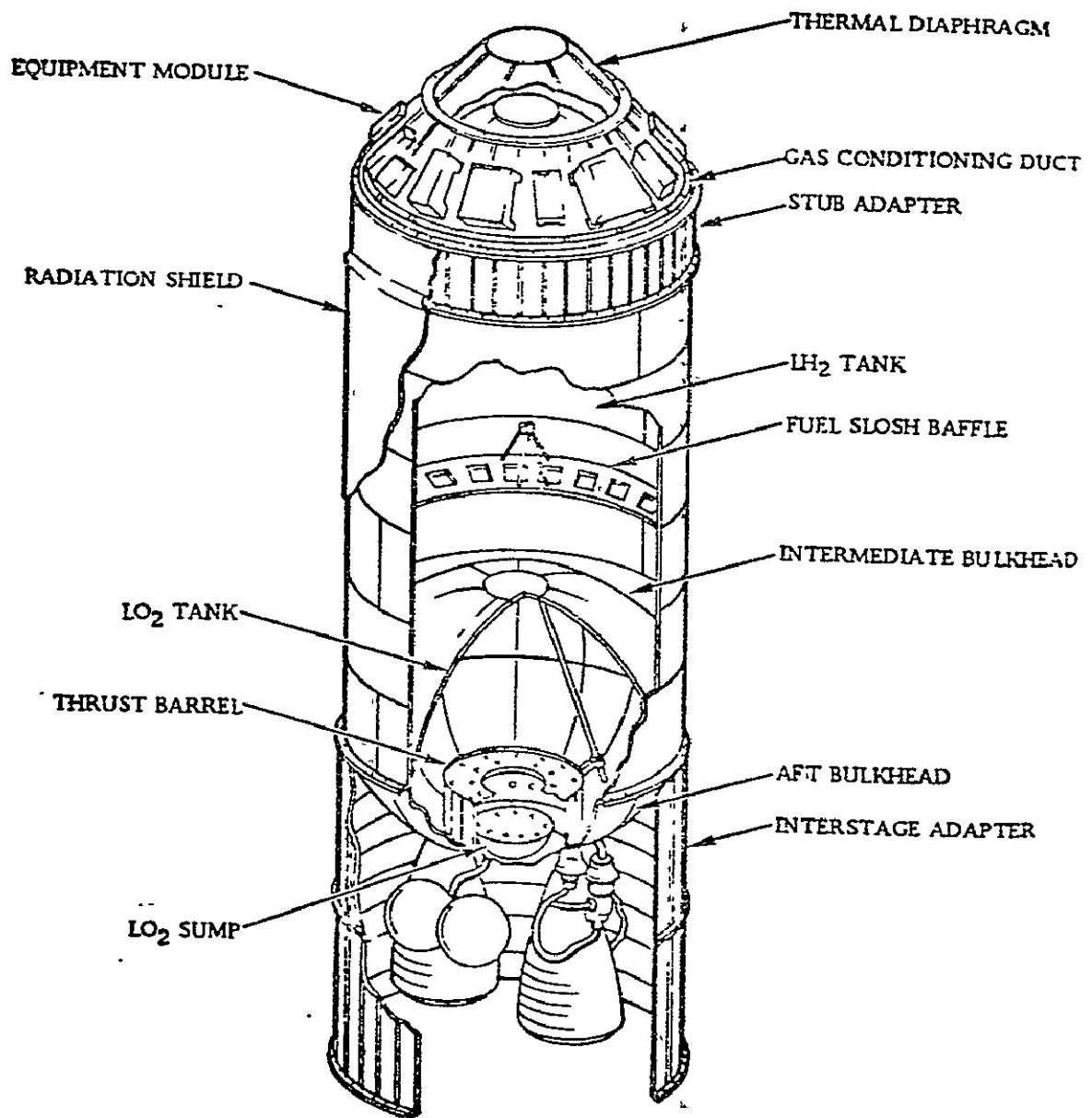


FIGURE II-2 IMPROVED CENTAUR UPPER STAGE

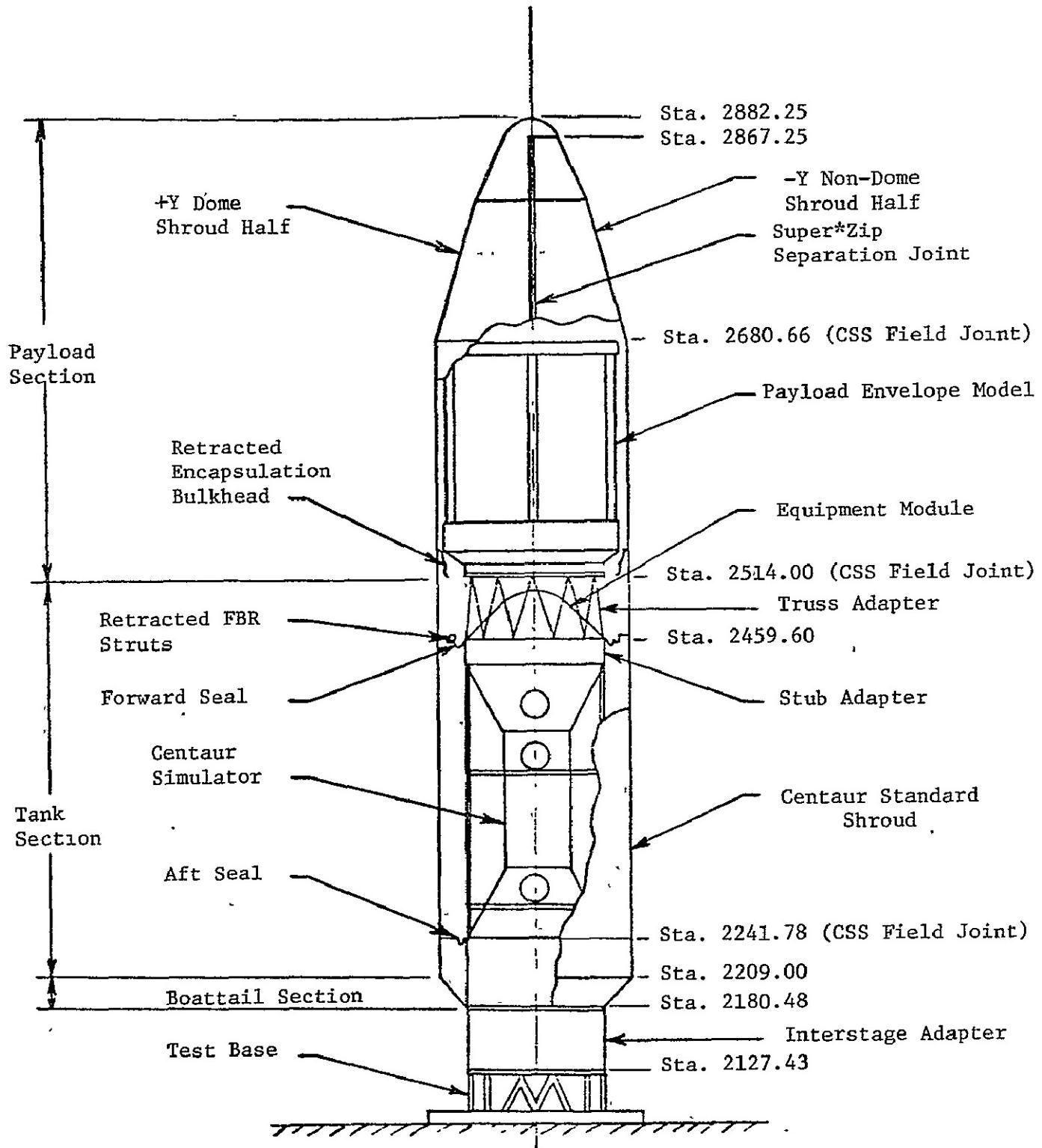


FIGURE II-3 TEST HARDWARE STACK-UP FOR ALTITUDE JETTISON TESTS

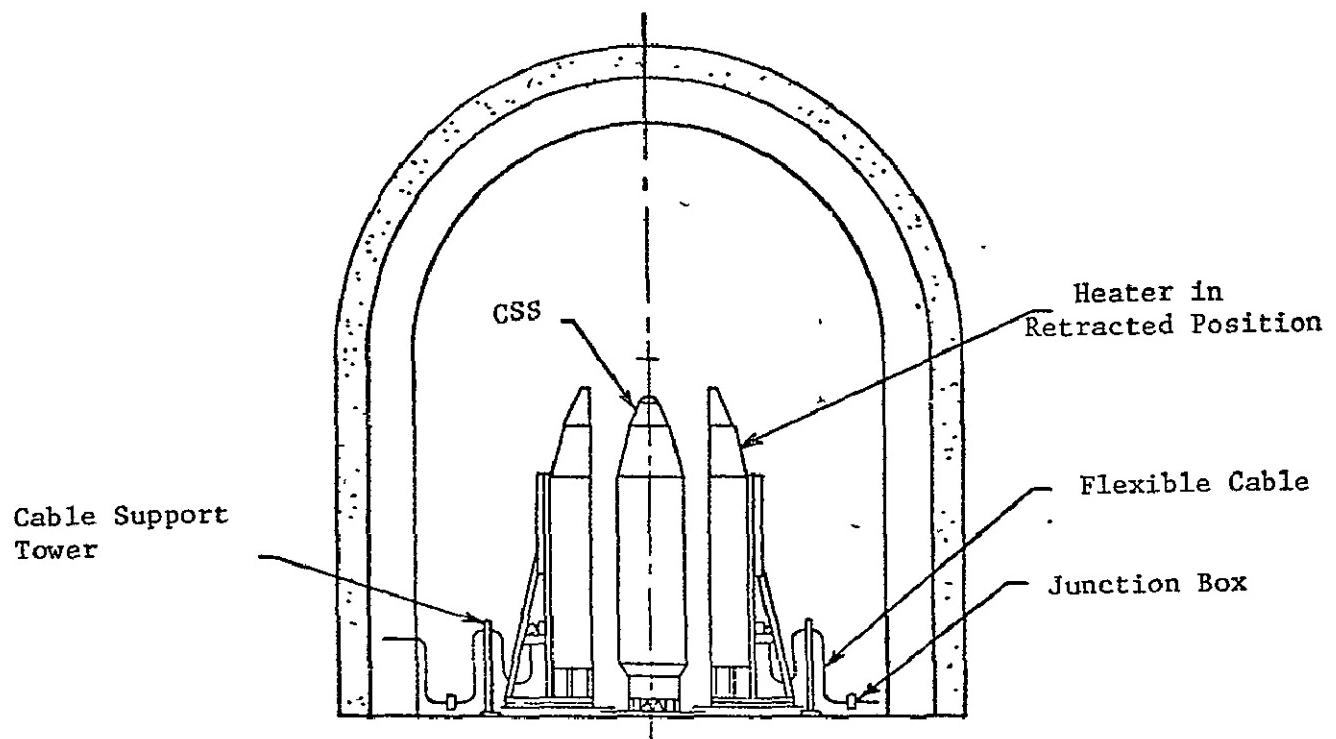
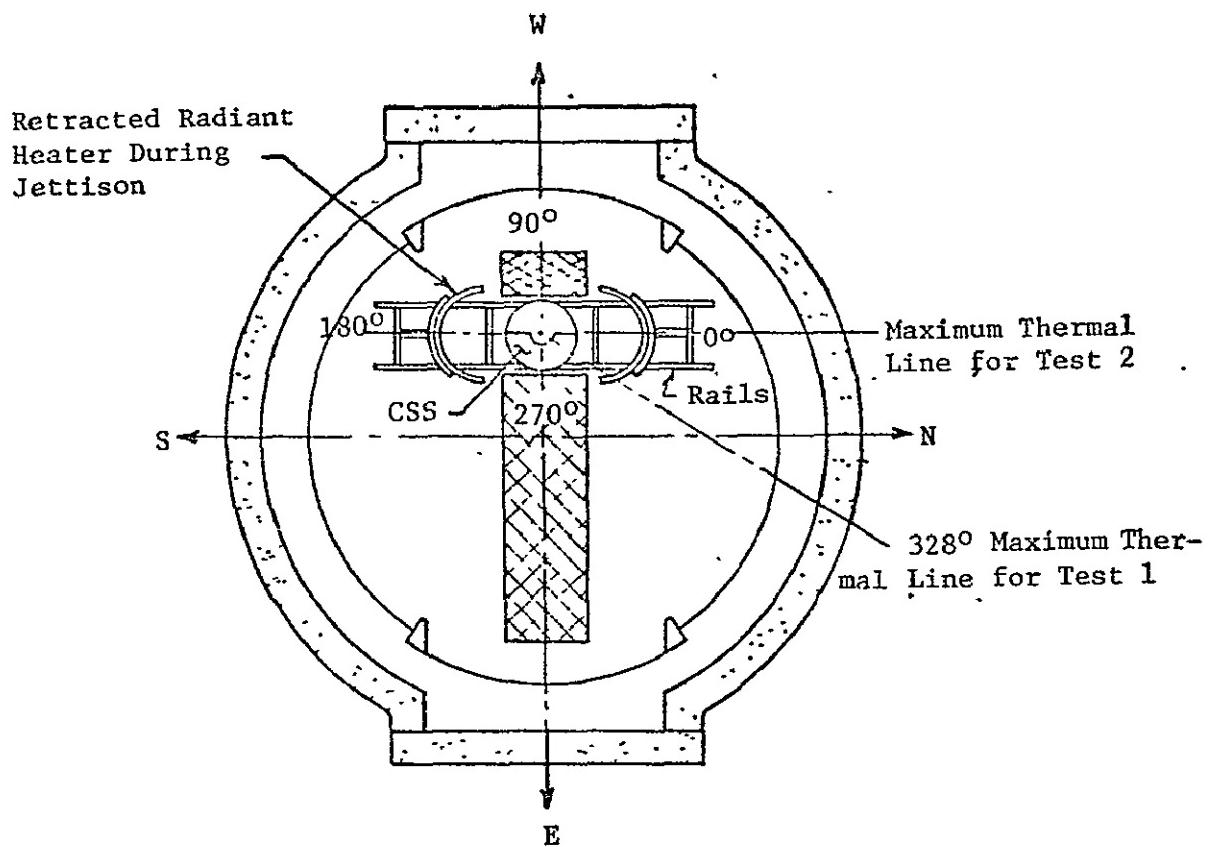


FIGURE II-4 VIEW OF TEST HARDWARE AND HEATER SYSTEM IN
SPACE POWER FACILITY .

III. APPARATUS

Eugene J. Cieslewicz, Richard W. Heath, and Roy L. Pickrell

Test Facility

The heated jettison tests were conducted in the high vacuum test chamber at the Space Power Facility, Plum Brook. The test chamber consists of an inner aluminum shell made up of a 100-foot diameter by 70-foot high cylindrical portion, topped by a 50-foot radius hemispherical dome. The center height to the top of the dome is 120 feet. The aluminum shell is enclosed by a concentric concrete shell with inside dimensions of 130-foot diameter by 150-foot height to the dome top (fig. III-1). Access to the chamber is by means of two 50- by 50-foot doors on opposite sides of the chamber and a smaller 8- by 8-foot personnel access door. The test CSS was displaced from the center of the chamber to provide space for fully jettisoning one CSS half. A view of the test article through the east facility door is shown in figure III-2.

Instrumentation and Data System

Instrumentation sensors were installed on the CSS to define the temperatures, structural stresses, shock vibration, and CSS movement during the heating and part of the jettison trajectory. All sensors are hard-wired to the facility. The majority of these circuits were carried through a total of 18 instrumentation disconnects which were disconnected on command before the jettison command was generated. The remaining were either located on the internal structure or were connected to the facility through umbilicals which traveled with the shell half during jettison.

All data recorders and displays are located outside the test chamber. A system of instrument cabling and patch panels was used to connect the test instrumentation channels to the facility recorders. The low change rate parameters, such as temperatures and most strain gages and deflectometers were recorded on the XDS 930 computer, through the MUX channels assigned to the XDS. The XDS scans the MUX inputs once each second. Parameters requiring a higher frequency response but less than 1000 Hz are recorded on the FM MUX equipment. Two Ampex 14 wide-band channel recorders are used with a 200-channel FM MUX system. High frequency parameters such as accelerometers were recorded on the two 14 wide-band channel Sangamo recorders.

Use of the data recording systems is shared by the test article and the test support equipment. In general, the test article is instrumented

for the research requirements. The test support equipment and the test article are instrumented to establish that the test support equipment functioned properly.

The types of instrumentation sensors used, quantities, and estimated accuracies are as follows:

250 Copper Constantan temperature-thermocouples	$\pm 5^{\circ}\text{F}$
150 Resistance Bridge type sensors (strain gages)	$\pm 10\%$
50 Potentiometer type sensors (deflectometers, etc.)	$\pm 10\%$

A total of 31 cameras were used to record the dynamic motion of the CSS and to define the trajectory.

CSS Heater

A clamshell-type CSS heater was built to surround and heat the CSS and be withdrawn prior to jettison to provide jettison clearance (fig. III-3). Some 6000 one-kilowatt quartz lamps were installed in anodized aluminum reflector shell halves mounted on a retractable support. This support moved back on rails to provide jettison clearance after the heating cycle. An elevation view of the heater is shown in figure III-4 and an internal view of the heater showing the lamp arrangement is shown in figure III-5. The reflector shell was dimensioned to provide a one-foot reflector clearance around the CSS while heating. The lamps were mounted inside the heater approximately four inches from the reflectors and eight inches from the CSS. The anodized surface of the heater reflector gave a reflectivity of 0.84 for the energy spectrum of the heater lamps when operated at full load.

The heater lamps were connected to 18 independent circuits each controlling two half zones for control zone purposes. Twenty-two of these half zones were in the cylindrical portion of the heater and 14 in the biconic portion (fig. III-6). The zones were arranged circumferentially around the CSS and the heat gradient required to establish the circumferential temperature gradient (fig. III-7) was provided by controlling each control zone by a unique temperature versus time-control profile. Variation in temperature vertically was achieved by varying the lamp density to achieve the relative heating levels indicated in figure III-8. The heater design was simplified by making the lamp density configuration of each zone within the cylindrical portion the same and within the conical zones the same. Although the resultant heating pattern differs from actual flight conditions to some extent in the vertical plane, the analytical treatment of the test results can make allowance for this difference without impacting the validity of the test.

As shown in figure III-7, the heating pattern is symmetrical about the MTL in the circumferential direction. This symmetry permits the individual control zone to be divided into half zones and located symmetrically to either side of the MTL. Both half zones are controlled by the same power controller, thus assuring identical heating patterns for each half zone and true symmetry about the MTL.

Heater Power Supply and Temperature Control System

The heater control system consists of 18 separate power controllers, one for each of the heater zones. The controllers are three-phase SCR phase-angle control type. Power is supplied from 480-volt, three-phase substation transformers set to deliver approximately 440-volt/line voltage under load. Each controller can supply up to 360-kilowatt power to the zone being controlled.

The CSS skin temperature is the control parameter in the control system. The electrical analog signal equivalent of the command temperature is generated by a device (control tracker) which tracks a temperature-time chart (temperature control program) equivalent to the CSS temperature during flight and converts the temperature points to equivalent thermocouple millivolt outputs. The value of the command output is continuously compared to the output of a control thermocouple mounted on the inside skin position of the CSS and the difference signal is used by the control system to modulate the power applied to the heater circuits to cause the CSS temperatures to follow the command profile. The block diagram of the control system is shown in figure III-9 and an example of the temperature control programs is shown in figure III-10.

These control programs are installed in the control tracker and all analog trackers are started simultaneously on signal from the combined test control system. A correction for the thermal time lag of the CSS temperatures behind the actual command temperatures due to the inertia of the thermal masses is made by offsetting the command curves so that the command temperatures actually are generated approximately two seconds earlier than their flight equivalent. Thus, when the monitoring systems check the temperature performance against the requirements based on a common reference point, which is flight lift-off, the correct correlation exists. The monitoring provisions are discussed in more detail in the combined test control system section.

Test Support Equipment

The test article (CSS, internal stackup) and CSS heater were centered along the East-West centerline of the test chamber and offset 15 feet

toward the West of the North-South centerline to allow for fully jettisoning the -Y CSS half (see fig. III-11). The CSS heater halves were retracted 10 feet along the North-South rails after the heating cycle, to provide for jettison clearance. Heater lamp power for the heater movable halves was supplied through a total of 178 electrical cables connecting the heater circuits with the power controllers located outside the test chamber walls. The cables attached to the heater were special design, highly flexible 300 MCM welding type cables with low outgassing insulation characteristics.

Cameras and camera lighting were installed in the test chamber to record the CSS jettison and details of their location are described later. Control of the cameras and lights was accomplished through cabling run through hermetically sealed connectors to the controls outside the chamber. In a like manner, instrumentation cabling was routed to the outside control and monitoring circuits.

The CSS test base was a rigid structure fabricated to simulate the Titan skirt interface with a Centaur vehicle. It was constructed of structural steel as required to support all static loads and transmit dynamic loads due to jettison tests to the test chamber floor. The CSS test base, together with the catch net towers, and the CSS heater were supported by a massive beam structure base support which rested on the chamber floor. During the prerun checkouts, tests were conducted to establish the interaction between the support structure and the elements being supported.

Camera System Layout

The high speed motion picture cameras and targets used to obtain data on trajectory and breathing motions of the CSS through the three tests were installed as shown in figure III-12. Cameras 1 thru 6 and 19 thru 32 locations are not shown because they do not support data presented in this section. Cameras 1 thru 6 were used by LMSC to obtain trajectory data. NASA/LeRC instead used cameras 9 and 10 to determine trajectories. Cameras 19 thru 32 were used to monitor overall jettison performance and internal motions of the CSS.

Data reduction film reading combined with the proper data reduction program yielded plots of breathing motions and the CSS trajectory. The breathing motions are those radial and tangential motions of the CSS edges along the Super-Zip split lines. Plots of radial motion versus time and tangential motion versus time were produced for all target stations shown on figure III-12.

Pyrotechnic Electrical Systems

Included in this system are the forward seal, the instrumentation disconnects, and the CSS Super-Zip subsystems. Operation of any of these subsystems initiate irreversible events and special provisions are required to assure against inadvertent or spurious commands. The design of the controls provide that at least two positive actions must be taken to bring about the intended event. In the control systems these are called an arming (enabling) command and a firing (trigger) command. Arming is accomplished by energizing a relay which excites the electrical bus from which the firing or trigger signal voltage originates. Firing is accomplished by connecting this bus to an electrical conductor to ignite the explosive or other secondary device. In addition, for safety requirements, removable electrical links are provided in the circuits to give additional assurance that the circuits cannot be energized while personnel are handling the pyrotechnics. This system is part of the Test Operations Control installation which is discussed in the following section.

Combined Test Control System

The combined test control system (CTCS) is made up of the control and abort system (TECAS), the test operations system (TOCS), the XDS 930 data and alarm system, and the real time cathode ray tube (CRT) display readout system. A DEC minicomputer is used in combination with a logic interface and MUX channel analog to digital converters to form the TECAS which outputs command signals at preprogrammed times relative to a program start signal. The TECAS verifies that all prerequisites for each timed signal have been met prior to issuing that command. For certain critical commands, such as ordnance firing, the prerequisites include verification that the previous command has been accomplished, or an abort command will be issued. A listing of the output commands, verifications, and aborts are shown in figure III-13. The block diagram of the TECAS system is shown in figure III-14.

As shown in figure III-13, the test was divided into three phases of discrete command functions. Phase one was initiated by the test conductor starting the TECAS and terminated at T+190 seconds (or Super-Zip sensitization). Phase two began at T+190 seconds and ended with the end of the heating cycle or T+250 seconds. Phase three began at T+250 seconds and continued to the end of the test. The differences in the phases were primarily the out-of-limit conditions which caused aborts, and the action taken in the event of an abort. An abort during phase one shut down all heater controllers and brought all test support equipment to their safe or nonarmed condition. Aborts during the other two phases, additionally, retracted the heater system to aid in cooldown of the test article.

The jettisoned CSS halves were caught in nets constructed of "Nomex" nylon straps. These nets and their associated braking mechanisms caught, restrained, and brought to rest both the partially jettisoned domed half and the fully jettisoned nondomed half of the CSS.

The braking mechanisms decelerated the CSS halves at a low, uniform rate to prevent crushing of the corrugated skin and to limit longitudinal bending moments. At no time during the tests were the allowable crushing loads of 100 pounds per inch or the allowable bending moment of 1 million inch-pounds exceeded.

The partially jettisoned CSS half contacted the net at an angle of 16° to the vertical axis. The CSS continued rotation to an angle of 21° before rotational motion was fully arrested. At rest, this half was supported on the hinges at the base and by the net near the biconic section. The -Y nondomed CSS half fell free of the hinge restraints and contacted the net after approximately 84° of rotation. The CSS was brought to rest after approximately 6° added rotation. See figure III-15 for net configurations.

Test Hardware

The CSS general configuration is shown in figure II-3. The CSS encloses the entire Centaur vehicle and the payload. The aft end of the CSS is mounted on the Interstage Adapter (ISA) at station 2180.48. From there, the CSS extends forward for a distance of 702 inches to station 2882.25. The cylindrical part of the CSS is 14 feet in diameter. The forward section of the CSS is a biconic configuration terminating in a dome at the tip.

The cylindrical parts of the CSS are of ring stiffened aluminum skin and corrugation construction. A cross-section view of the cylinder shell wall is shown in figure III-16. The skin and corrugations are joined by a spot-welding process through an epoxy adhesive bond in each of the corrugation valleys. The shell is internally stiffened by three-inch deep "Z" configuration rings spaced 15 inches apart. The rings are riveted to the skin in each of the corrugation valleys.

The 168-inch diameter cylinder tapers to the 120-inch diameter ISA through the boattail section. The boattail construction is a riveted ring and hat-section stringer aluminum shell, as shown in figure III-17.

The nose cone of the CSS is made of magnesium thorium sheet reinforced by internal rings, as shown in figure III-18. The nose cone is made up of a 15° and a 25° half angle conical segment. A 24-inch radius stainless steel dome mounts on the forward ring.

The Super-Zip jettison separation joints are illustrated in figure 11-4. Cross sections of the joints are shown in figure 11-19.

During jettison, the CSS halves pivot away from the vehicle on four hinges, two on each half shell. The hinges are located at the cylinder-to-boattail interface. Hinge details are shown in figure 11-20. The forward half of the hinge jettisons with the CSS and the aft half remains on the boattail.

The jettison force is provided by eight longitudinal thruster springs, two lateral thruster springs mounted across the separation joint at station 2459, and two lateral thrust springs in the nose cone dome. The longitudinal springs are located at the aft end of the cylinder. A typical view of a longitudinal spring is shown in figure 11-21. All springs are cocked shortly before flight and their force is stored until the separation joints are cut.

In addition to the insulation for the Centaur LH₂ tank in the tank section, the inside of the payload and conical section of the CSS is lined with insulating material to prevent heating of the payload during ascent flight.

The CSS, as tested, differed from the flight configuration in several respects, as described in Appendix C. None of the differences affected the test results. An obvious change from the flight configuration is the removal of the hydrogen vent fin, which was taken off to relieve interference with the facility catching system, and was replaced by a cover plate. The CSS external skin was painted flat black to improve heat absorption from the heating fixture and thus reduce heater power requirements.

Interstage Adapter (ISA) and Centaur Simulator

The ISA is a structural spacer between the forward end of the Titan skirt and the aft end of the Centaur tank. It is 120 inches in diameter and 113 inches long. It is an aluminum ring stiffened, sheet-and-stringer structure. Longeron fittings which are part of the aft end of the ISA mate with the Titan skirt longerons. The ISA supports the CSS boattail by a flange at station 2180.48, approximately half way along its length.

The ISA was mounted on a facility base structure which replaced the Titan skirt. The interface with the base was shimmed under each longeron in order to level the top of the boattail. Following that, the space between the shim packs was filled with steel filled epoxy to provide a continuous bearing surface.

The Centaur simulator, figure 11-3, is a steel assembly which was fitted between the top of the ISA and the bottom of the Stub Adapter.

The simulator replaced the Centaur tank in order to simplify the test setup. It also provided a mounting base for instrumentation and photo equipment and provided internal access, cable-way routes, and work platforms.

The simulator consisted of a cylindrical mid-body 60 inches in diameter and a conical transition piece at each end expanding to a 120-inch diameter. The conical transitions terminated in flanges which interfaced with appropriate ISA and Stub Adapter rings. The overall length of this structure was 194 inches.

Centaur Equipment and Payload Simulator

The following items of Centaur equipment were assembled in flight configuration for these tests:

- * 1. Aft Purge Gas Seal
- 2. Stub Adapter
- 3. Forward Purge Gas Seal
- 4. Equipment Module
- 5. Truss Adapter
- 6. Forward Bearing Reaction System
- 7. Hydrogen Vent Disconnects
- 8. Helios Electrical Disconnect
- 9. CSS Electrical and Antenna Disconnects

The Aft Purge Gas Seal, shown in figure III-22, isolates the tank-shroud annulus from the boattail. It consists of a rigid aft seal plate and a flexible seal attached to the CSS aft purge seal bulkhead. The seal is held to the plate by interlocking fingers. During jettison, the interlock is pulled apart by cables attached to the CSS.

The Stub Adapter is mounted on the Centaur at station 2435.84. It is a cylindrical structure 25 inches high and 120 inches in diameter. It consists of a ring stiffened titanium skin-and-stringer structure.

The Forward Purge Gas Seal, shown in figure III-23, isolates the tank-shroud annulus from the electronic equipment section. It consists of a silicon rubberized fabric section which is mounted at the forward end of the Stub Adapter.

The Equipment Module mounts on the forward end of the Stub Adapter at station 2459.6. It is a truncated cone made of aluminum skin and stringers with reinforcing rings. The Module is 30 inches high and tapers from a 120-inch diameter at the aft end to a 60-inch diameter at the forward end. Steel blocks were positioned and weighted to replace flight electrical packages on the Module; this caused the structure to dynamically simulate the flight structure.

The Truss Adapter is also mounted on the forward end of the Stub Adapter and supports the payload. It is 120 inches in diameter and 49 inches high. It consists of 24 aluminum struts spaced around the circumference. They are attached to 12 fittings on the Stub Adapter and 12 fittings attached, in this case, to the aft ring of the Payload Model. The struts themselves are three inches in diameter in the middle and taper to a fitting eye at each end.

The Forward Bearing Reaction System, shown in figure III-24, consists of six struts located at station 2460 which tie the CSS to the Stub Adapter. The system provides load sharing between the CSS and the Centaur. In flight, the struts are cut after maximum loading, and before significant aerodynamic heating occurs, by firing a pyrotechnic bolt in each strut. After bolt firing, the strut halves are retracted against the CSS and the Stub Adapter by springs. For the jettison tests, the struts were installed in the retracted position.

The Hydrogen Vent Disconnects, shown in figure III-25, provide a flexible duct between the CSS and the Centaur LH₂ tank vent system. During CSS jettison, the disconnects detach themselves from the coast flight vent nozzles mounted on the Stub Adapter. They are located at azimuths 112° - 30 minutes and 292° - 30 minutes, and approximately station 2440.

The Helios Electrical Disconnect, located on 270° azimuth at approximately station 2567, consists of three electrical connectors which disconnect at CSS jettison. A flight-type connector suspension arm and cable harness is mounted on the CSS opposite the Helios connector. The Helios mounted half of the assembly was attached to the Payload Model.

CSS Electrical and Antenna Disconnects are installed at the forward end of the Stub Adapter at approximately 66° and 252°. An additional antenna disconnect is installed at the aft end of the CSS in the boat-tail area near 280°.

A Payload Model mounts on the forward end of the Truss Adapter in the space normally occupied by the spacecraft. The Payload Model carried small thin wooden rods which projected radially outward. The rods were mounted in a styrofoam base so they could deflect permanently in the base if they were impacted by the CSS during jettison. The outer ends of some of the rods were carefully placed at the boundary of the payload envelope, some two inches inboard, and some two inches outboard, of the envelope boundary. In addition, the Payload Model was equipped with a shelf which

represented the bottom of the Helios spacecraft. A motion picture camera viewed this area to determine if the Helios Electrical Disconnect connector suspension arm contacted the shelf during CSS jettison. The Model further provided mounting capability for motion picture cameras, deflectometers, and instrumentation and pyrotechnic cabling.

A view of the assembled ISA, boattail, Centaur simulator, Stub Adapter, Truss Adapter, and Payload Model is shown in figure III-26. Figure III-15 illustrates the operation of the catch net system.

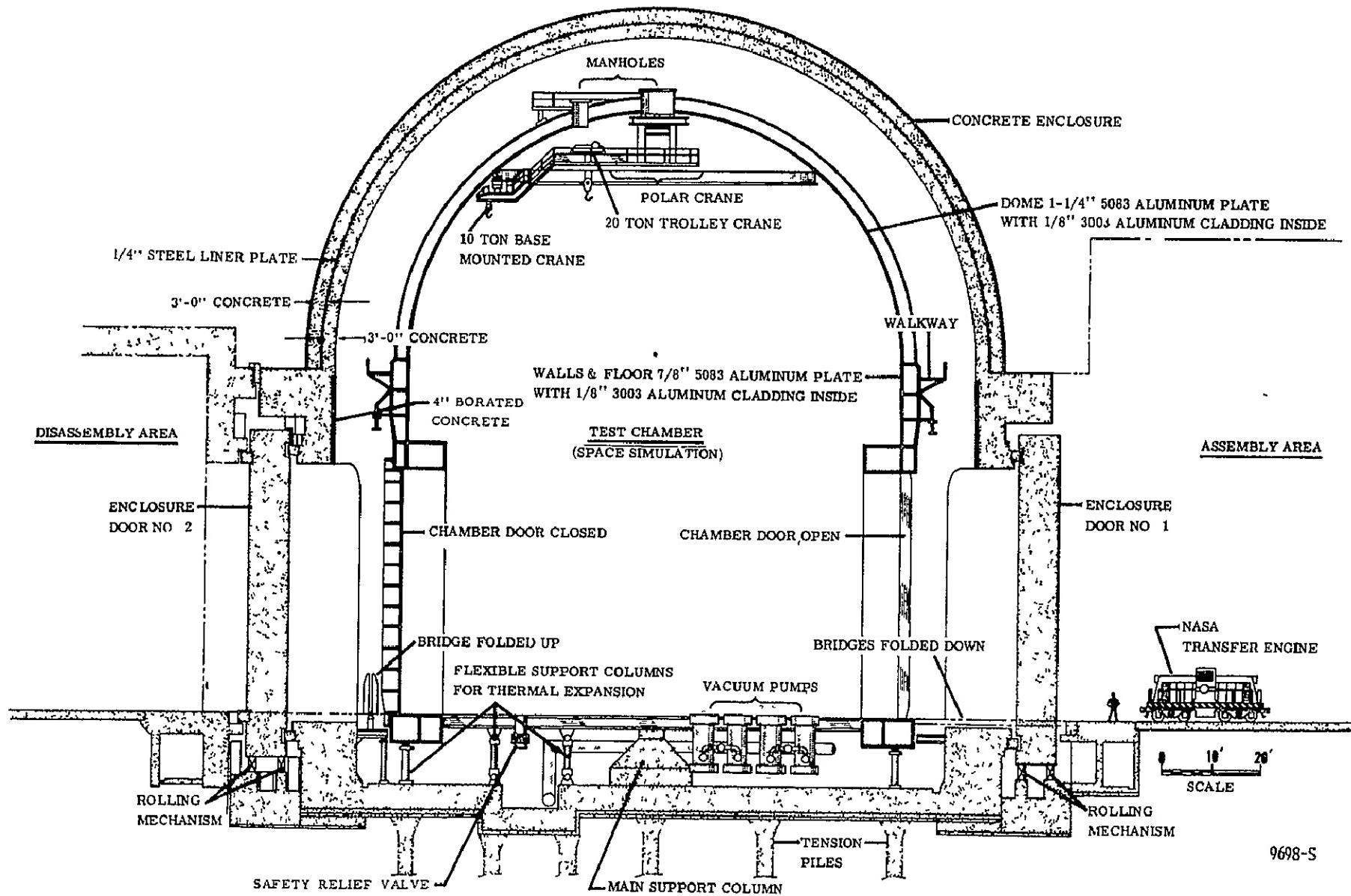
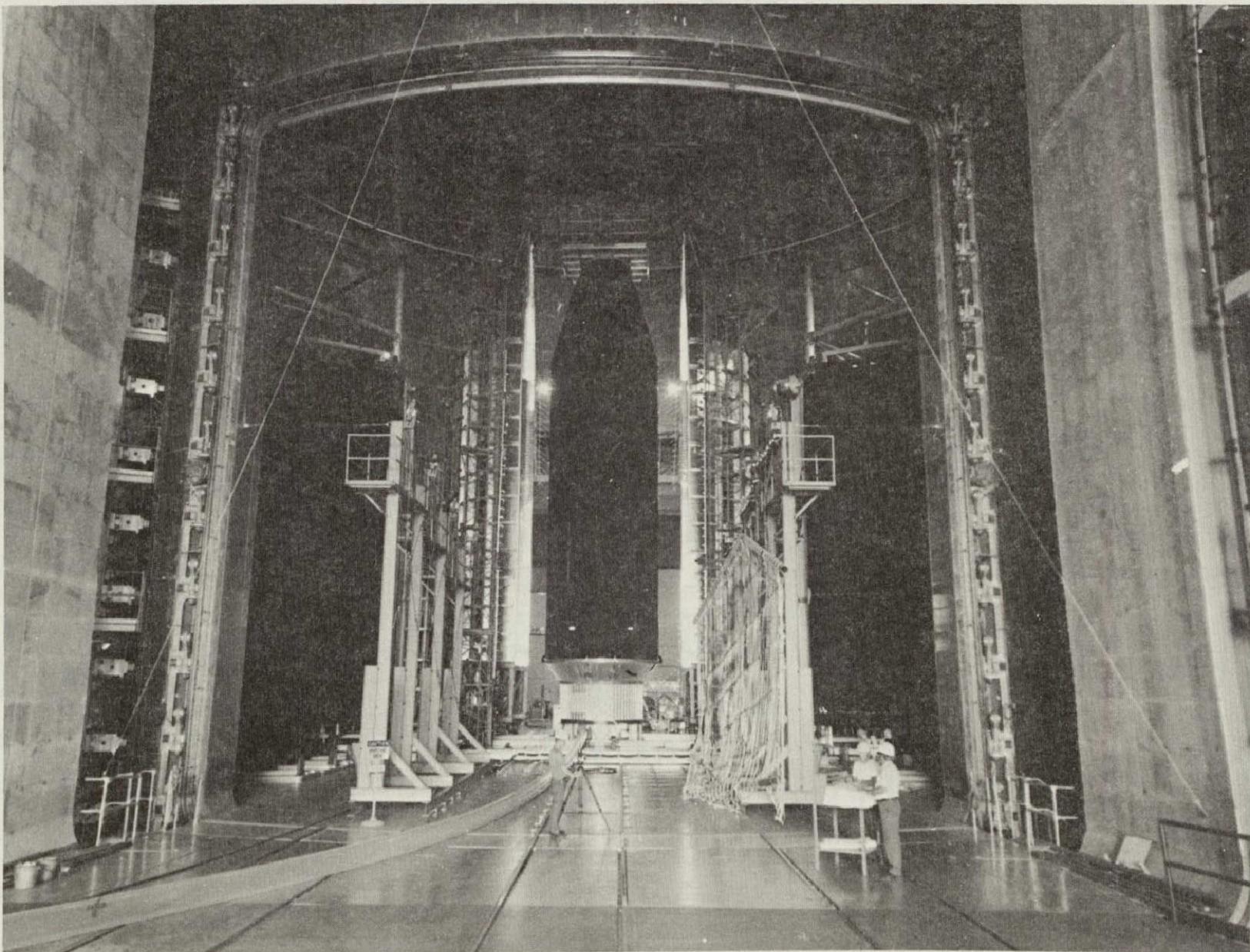


FIGURE III-1 Space Power Facility
Elevation Cross-Section



21

REPRODUCIBILITY OF THE
ORIGINAL PAGE IS POOR

FIGURE III-2 CSS AND TEST SUPPORT EQUIPMENT IN VIEW SEEN THRU EAST DOOR

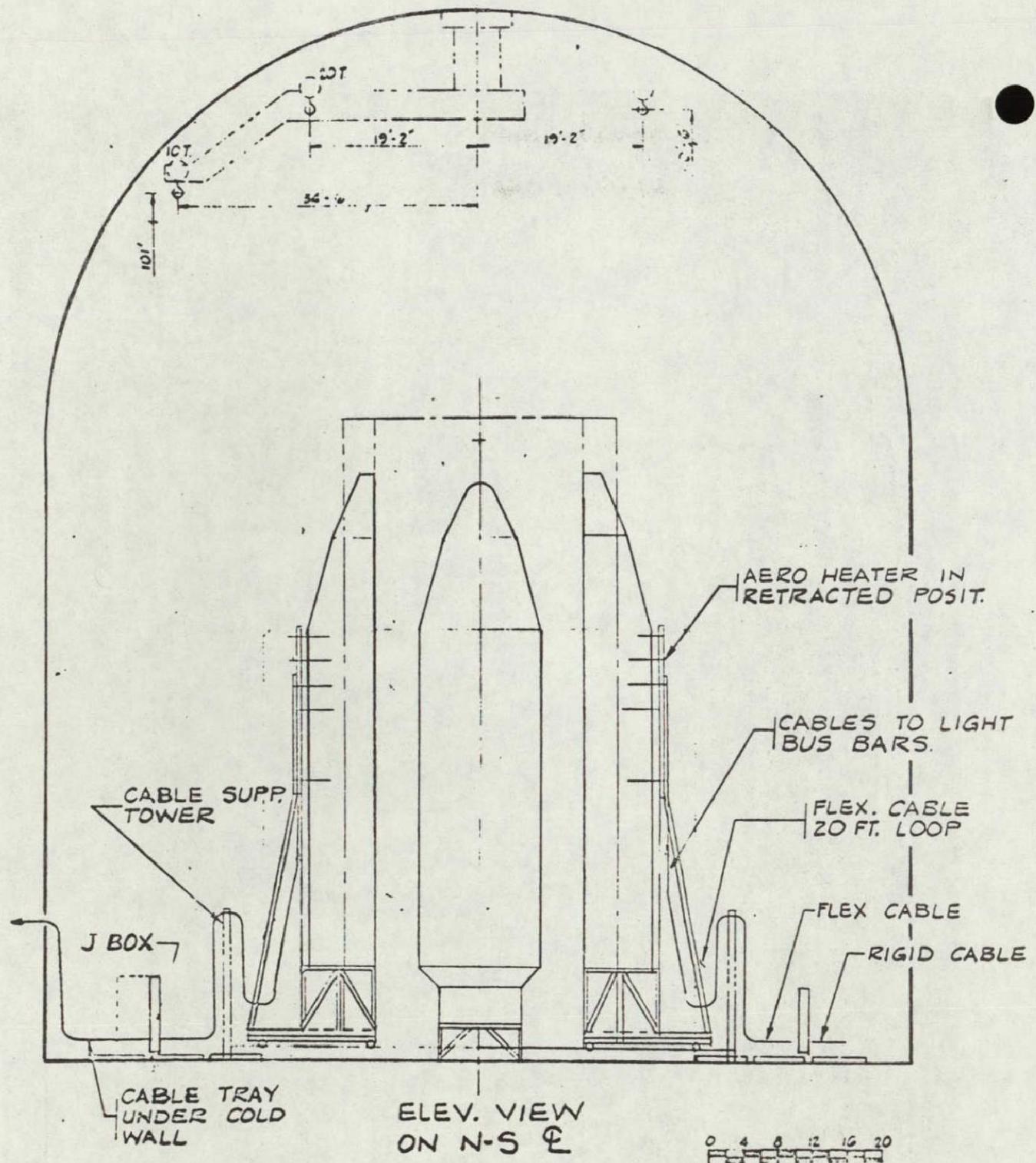


FIGURE III-3 HEATER INSTALLATION ELEVATION

REPRODUCIBILITY OF THE
ORIGINAL PAGE IS POOR

NASA
C-73-2149

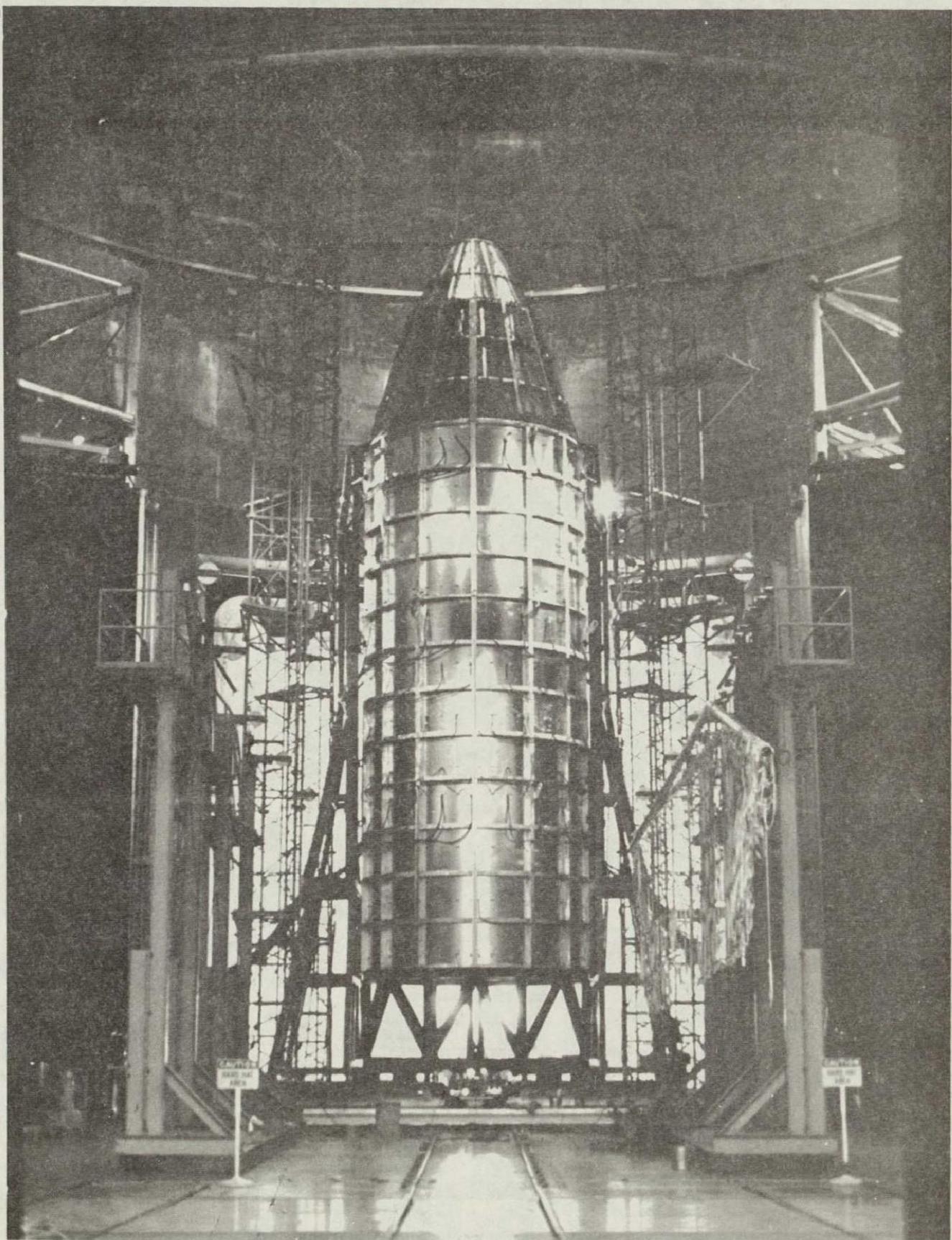


FIGURE III-4 HEATER INSTALLED IN TEST CHAMBER VIEW FROM EAST DOOR

E-8508

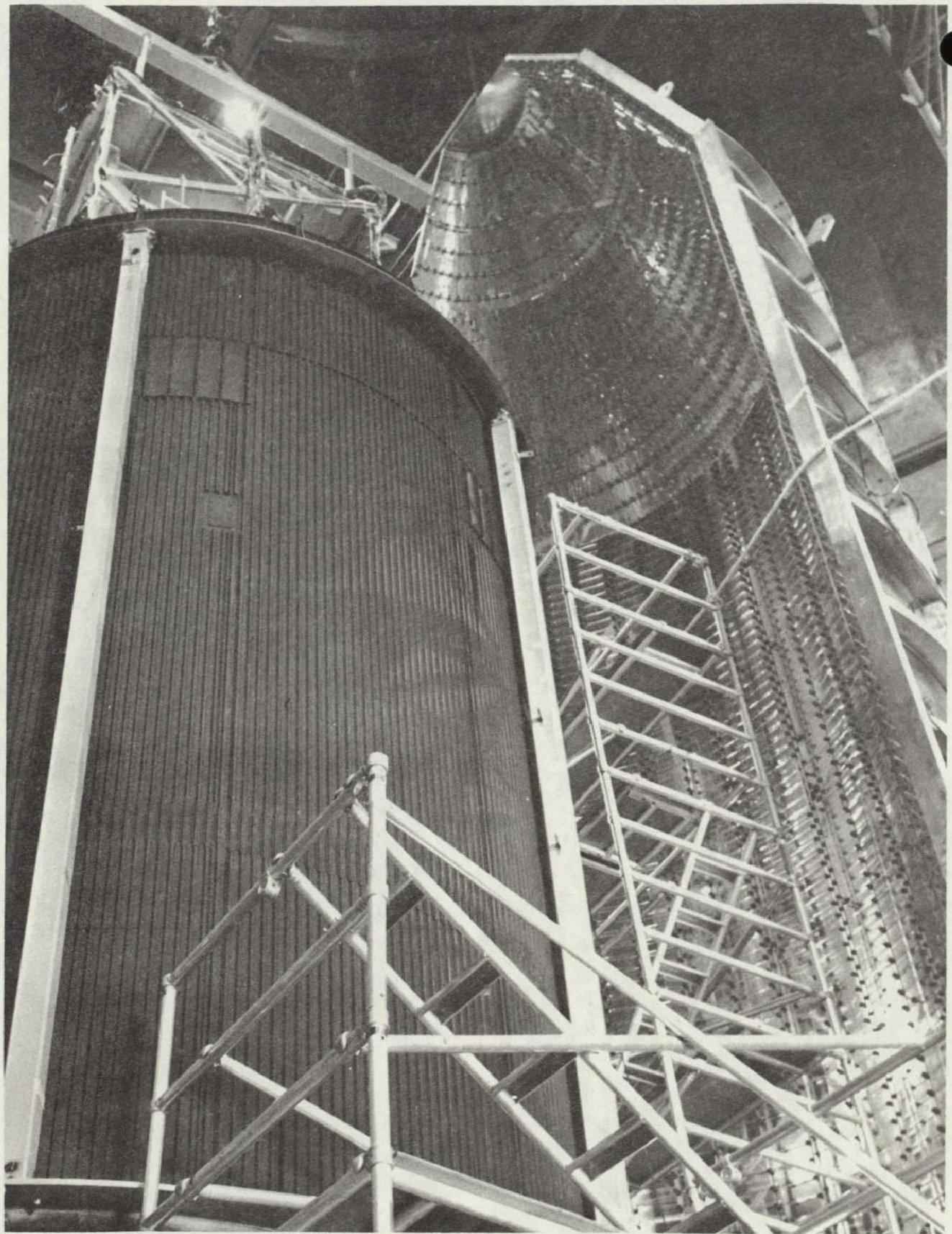


FIGURE III-5 HEATER SHELL - INTERNAL VIEW SHOWING LAMP ARRANGEMENTS

24

REPRODUCIBILITY OF THE
ORIGINAL PAGE IS POOR

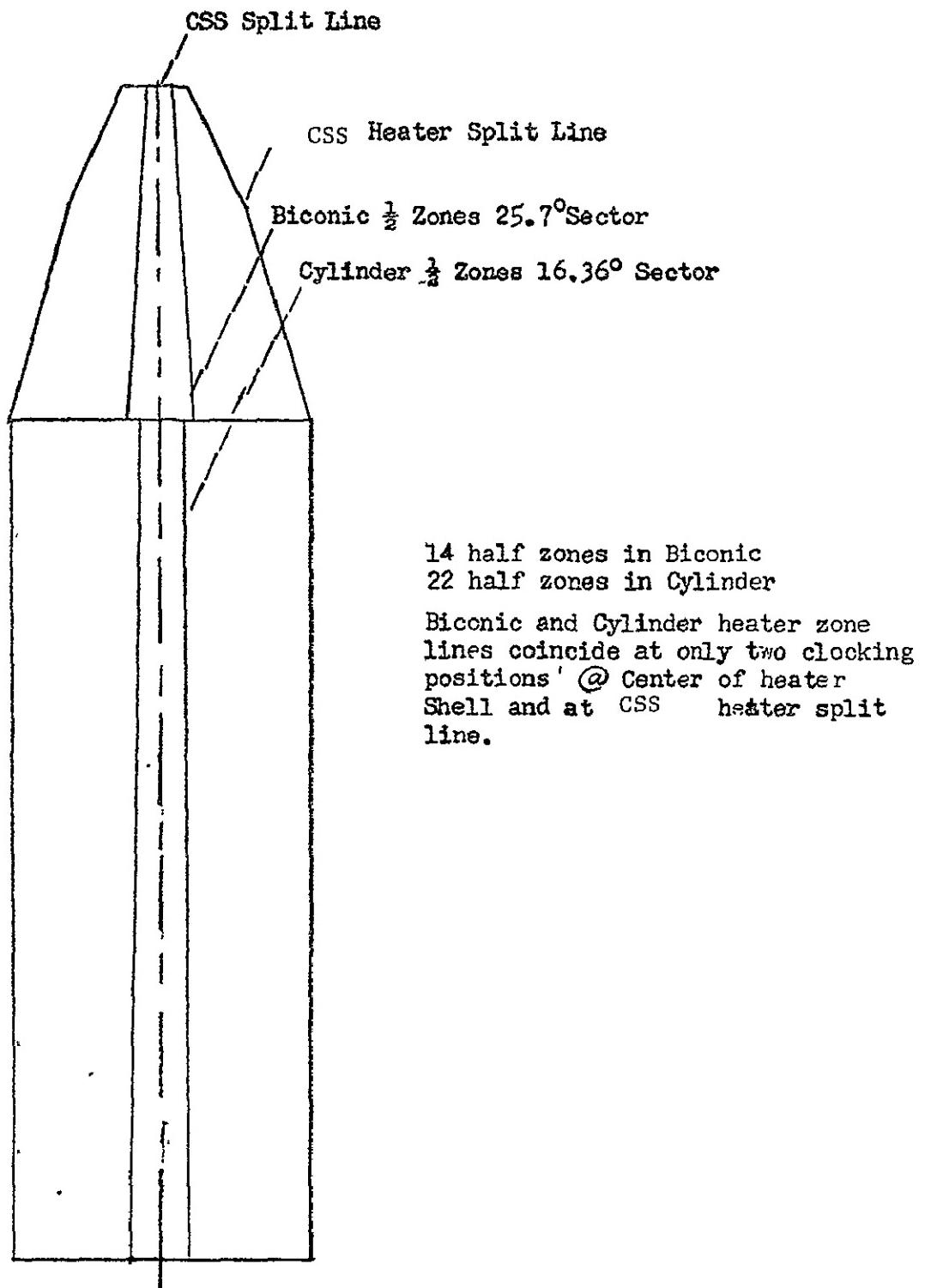


FIGURE III-6 CSS HEATER HALF SHELL SHOWING AREA ALONG HEATER BACKBONE

SKEWED TEMPERATURE DISTRIBUTION

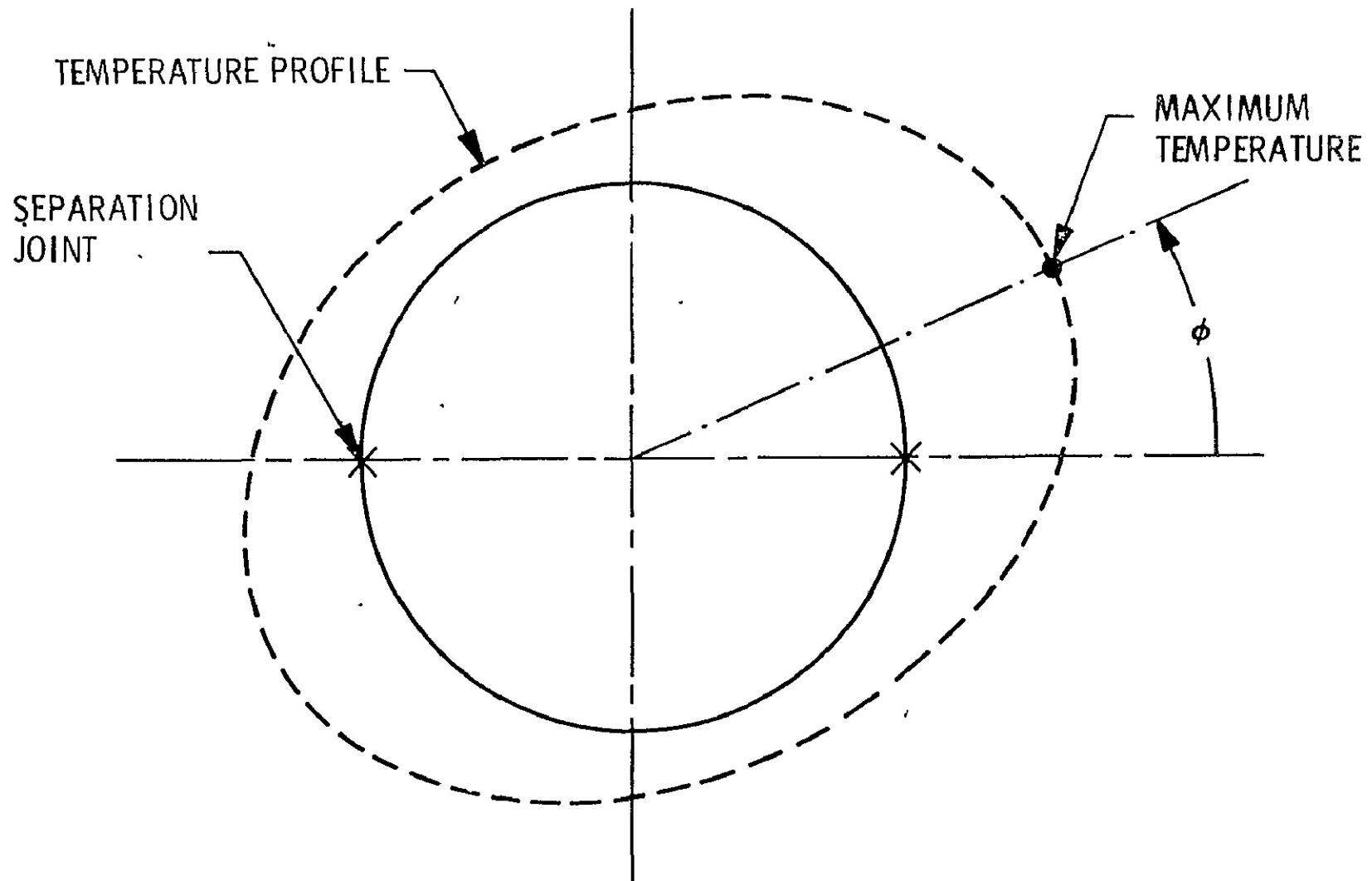


FIGURE III-7 CIRCUMFERENTIAL HEAT PATTERN ON CSS

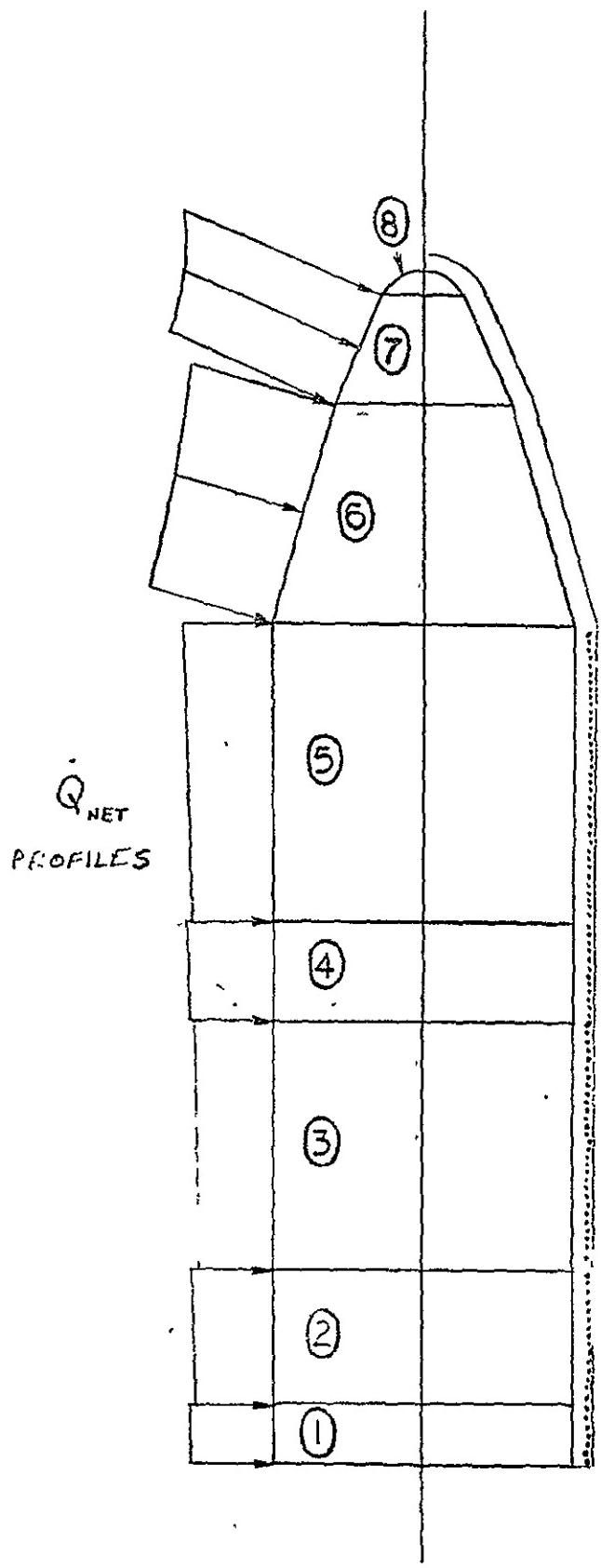


FIGURE III-8 VERTICAL HEAT PATTERN ON CSS

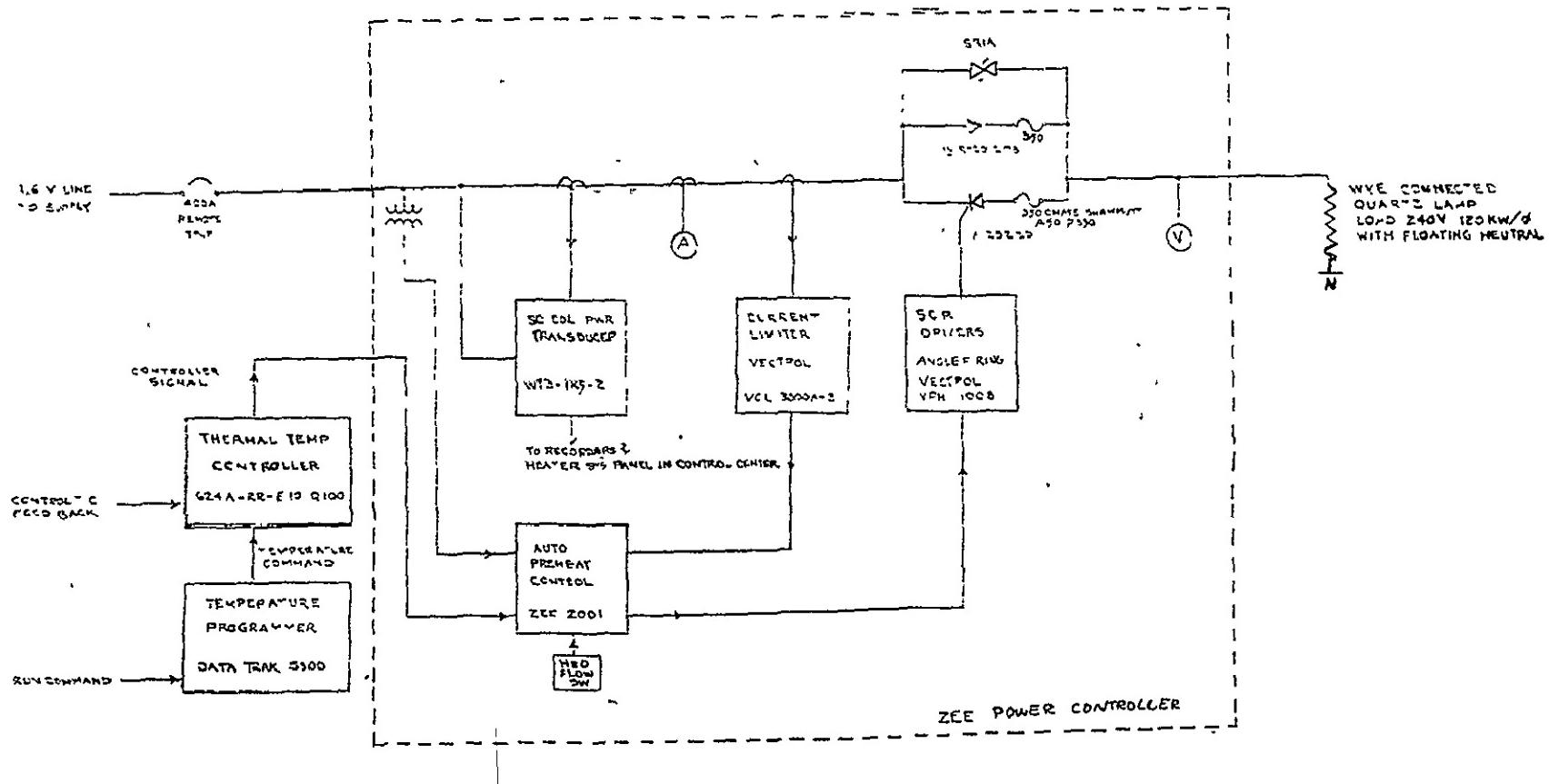
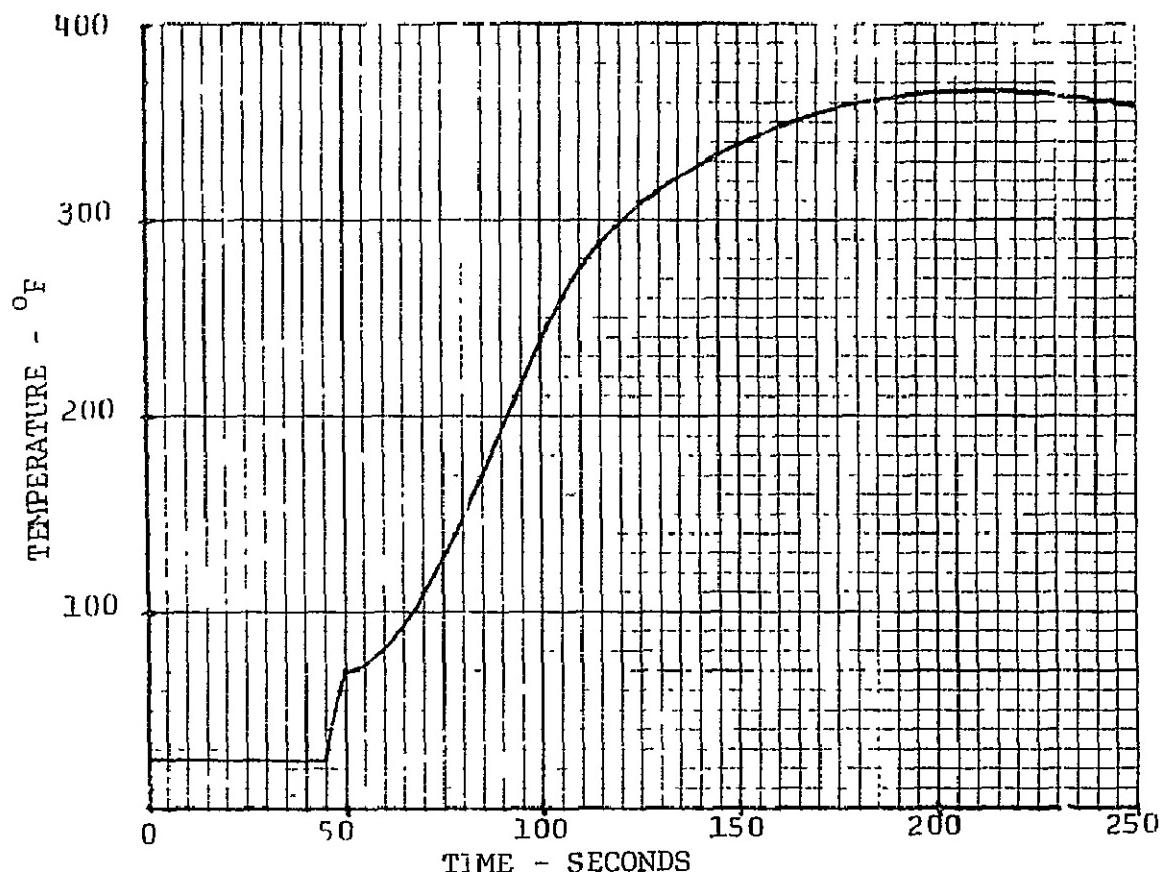
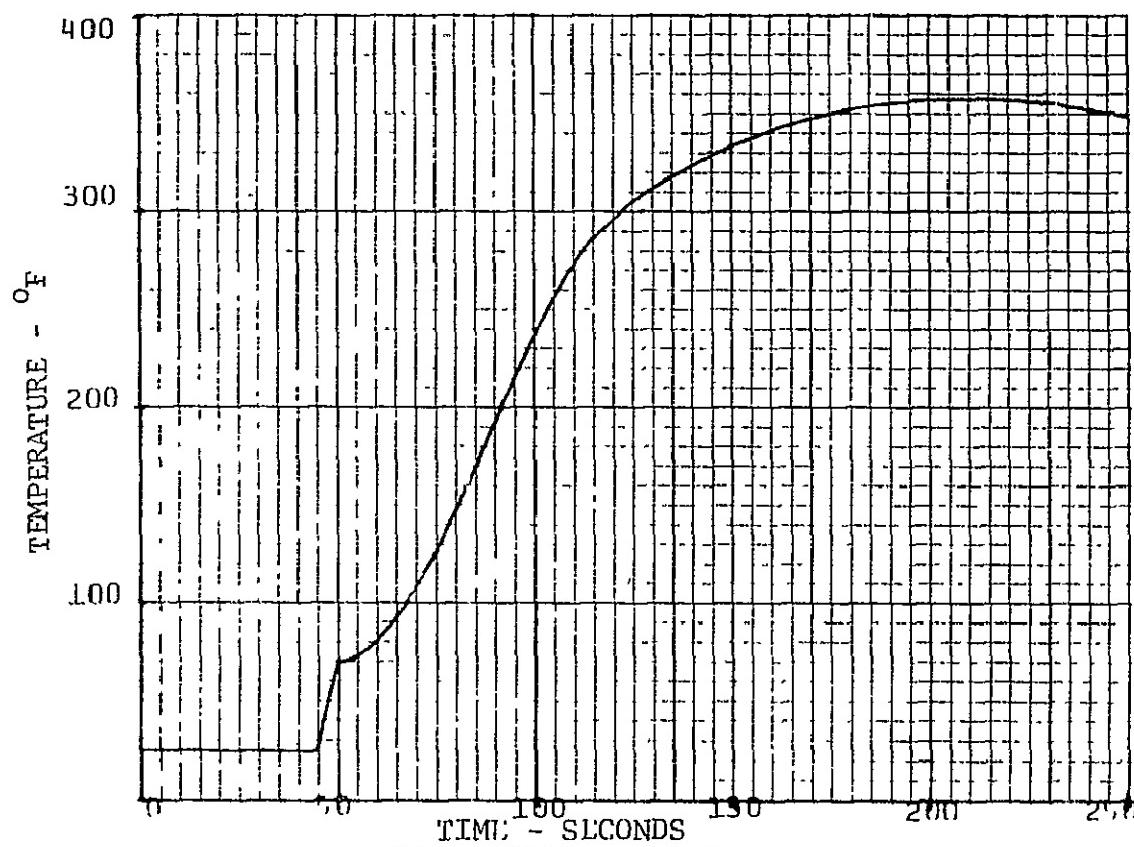


FIGURE III-9 BLOCK DIAGRAM OF CONTROL SYSTEM FOR A TYPICAL HEATER CONTROL ZONE



(a) CONTROL ZONE 1



(b) CONTROL ZONE 2

FIGURE III-10 CONTROL ZONE TEMPERATURE VERSUS TIME VARIATIONS FOR CSS HEATED ALTITUDE JETTISON TESTS IN PLUM BROOK SPF RH758B LEADING EDGE FROM LMSC TSS-13503-17B

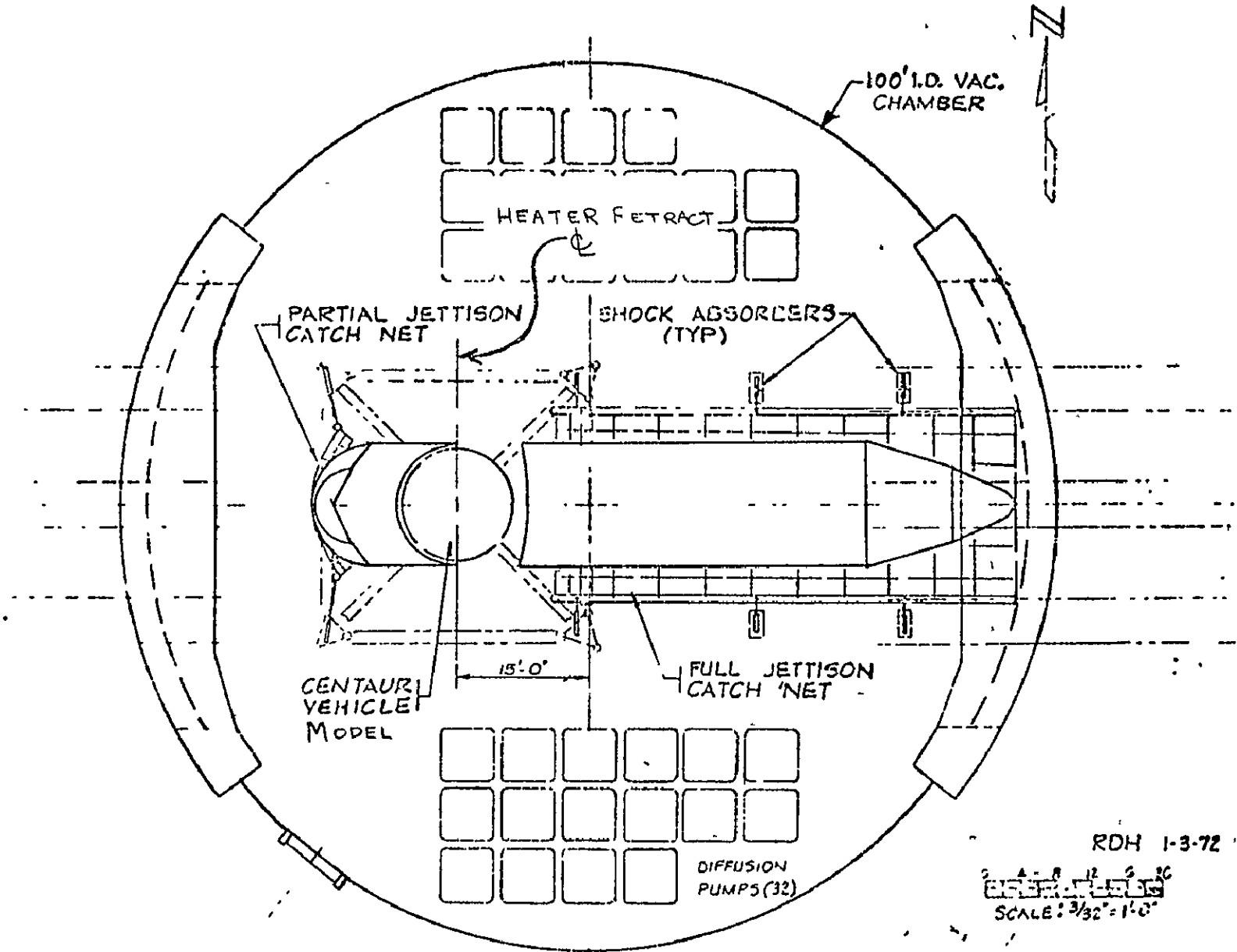


FIGURE III-11 JETTISONED CSS IN CATCHNETS

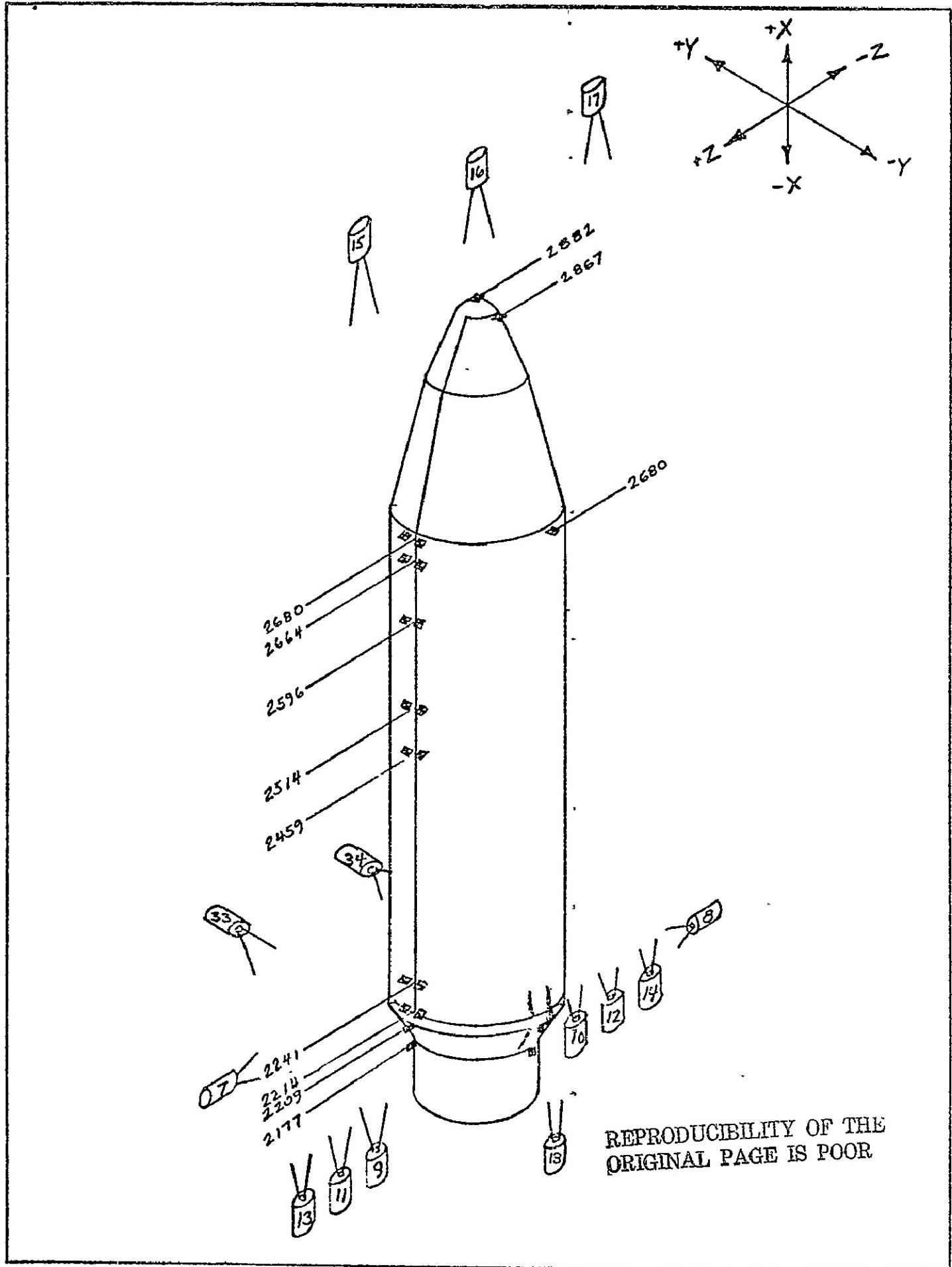


FIGURE III-12 CAMERA LOCATIONS FOR TESTS 1, 2 AND 3

32

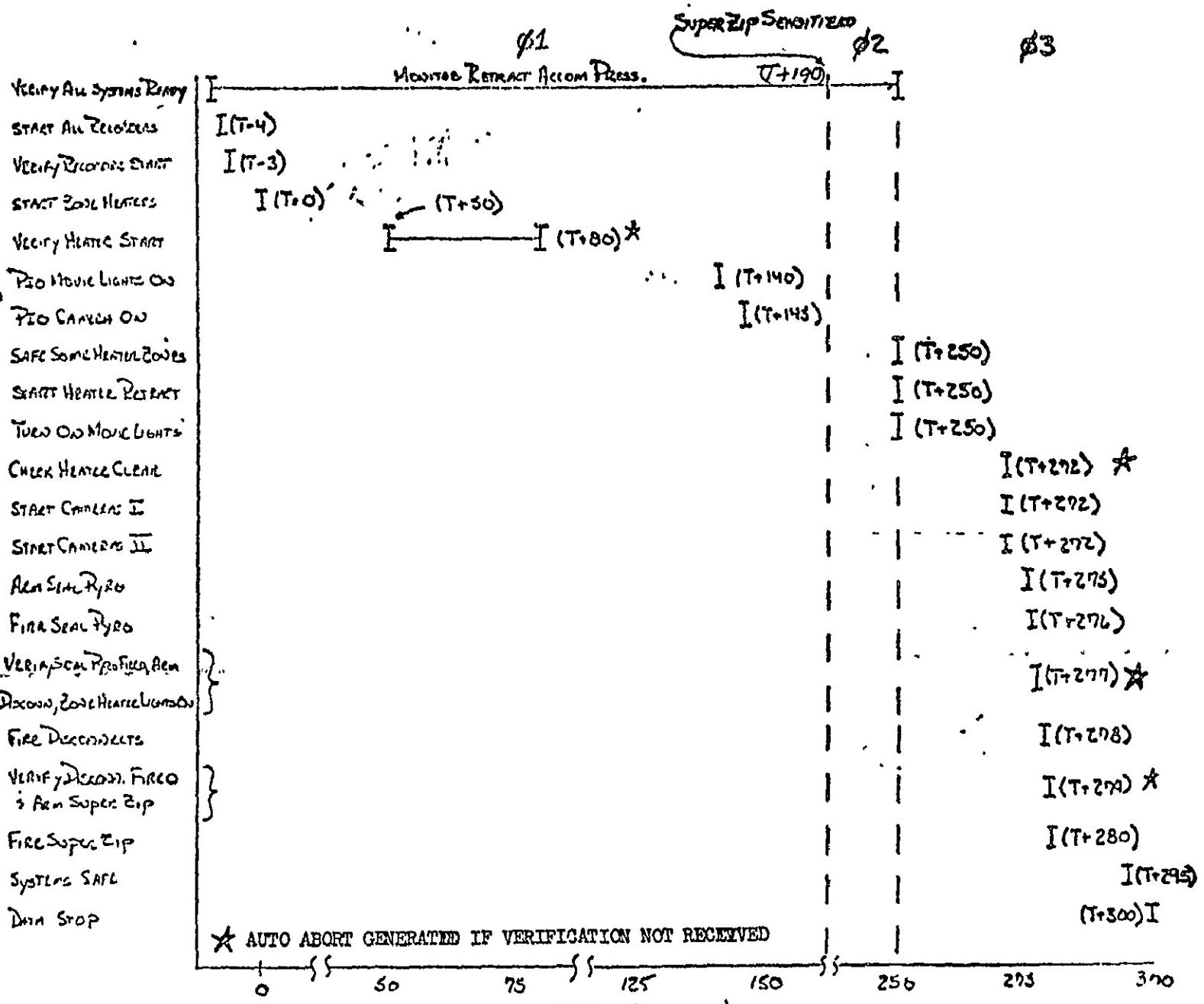


FIGURE III-13 HEATED JETTISON TEST SEQUENCE

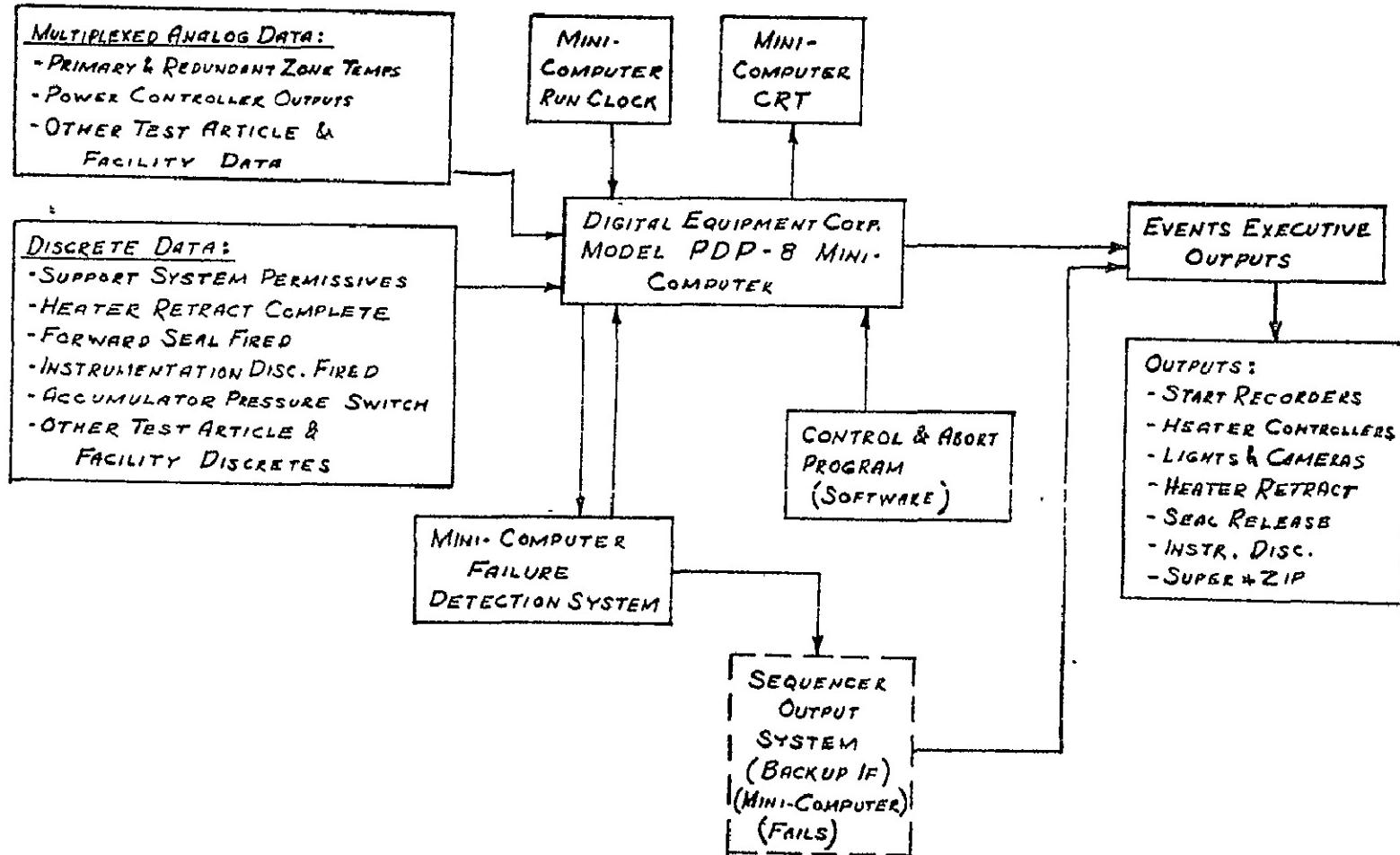


FIGURE III-14 BLOCK DIAGRAM OF TEST CONTROL AND ABORT SYSTEM (TECAS) FOR.
SPF HEATED ALTITUDE JETTISON TESTS

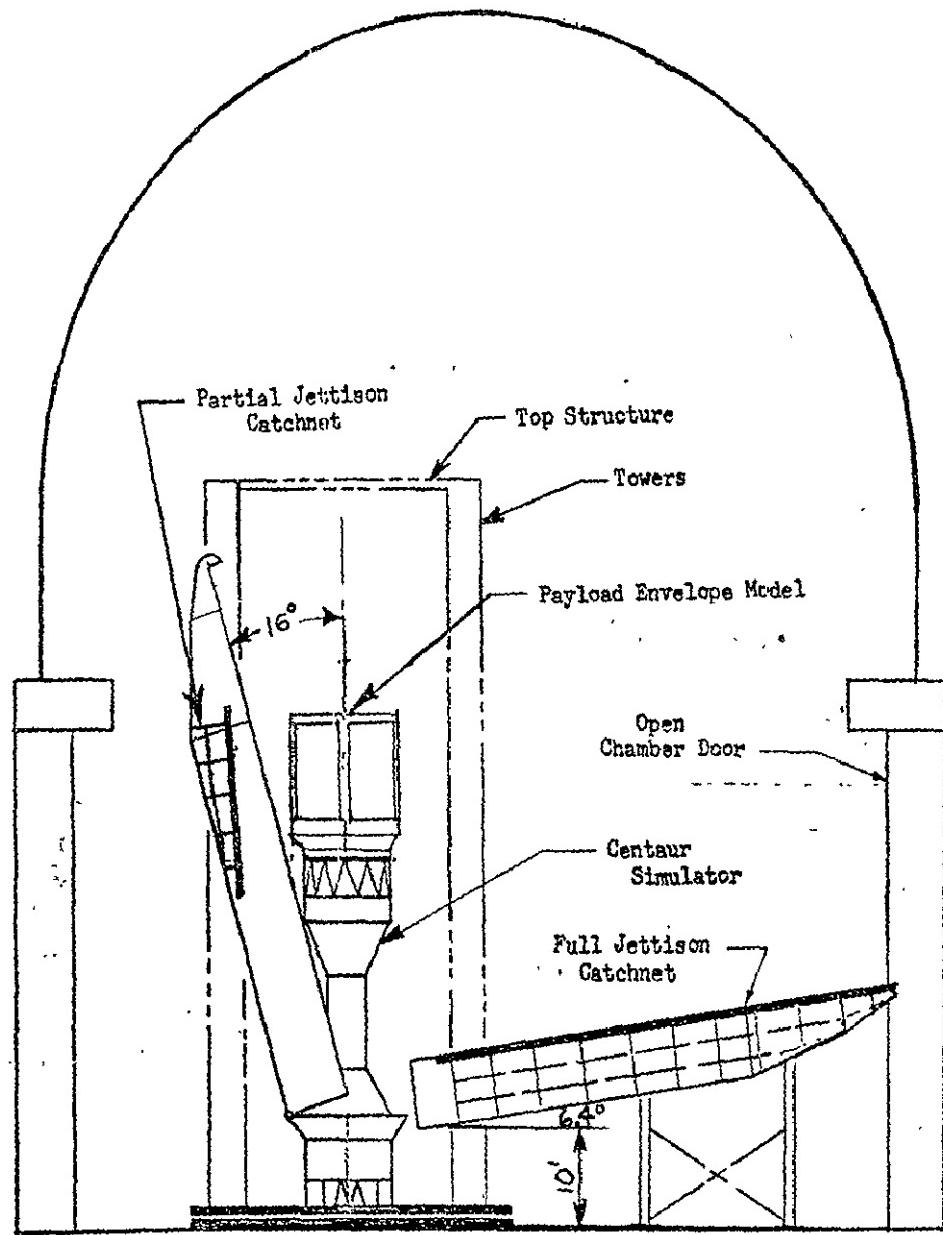


FIGURE III-15 OPERATION OF CATCHNET SYSTEM

LOCATION (STA)	SKIN	CORRUGATION
2680.66 - 2514.00	0.032	0.020
2514.00 - 2458.10	0.010	0.025
2458.10 - 2316.78	0.032	0.020
2316.78 - 2241.78	0.010	0.025
2241.78 - 2209.00	0.050	0.032
2209.00 - 2180.48	0.080	0.040

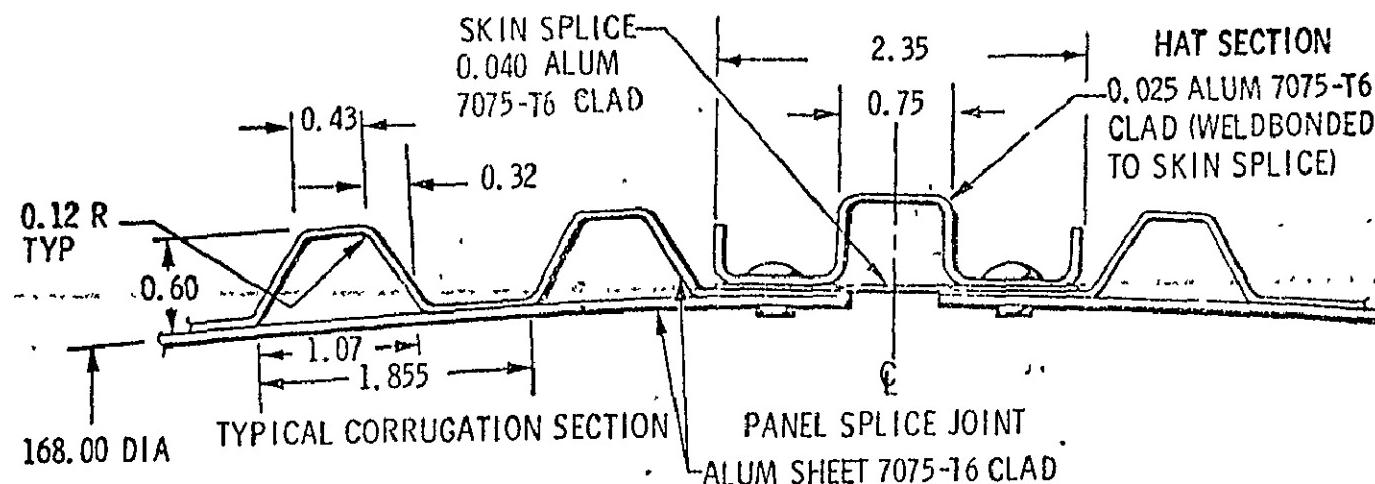


FIGURE III-16 CSS CYLINDRICAL SHELL WALL

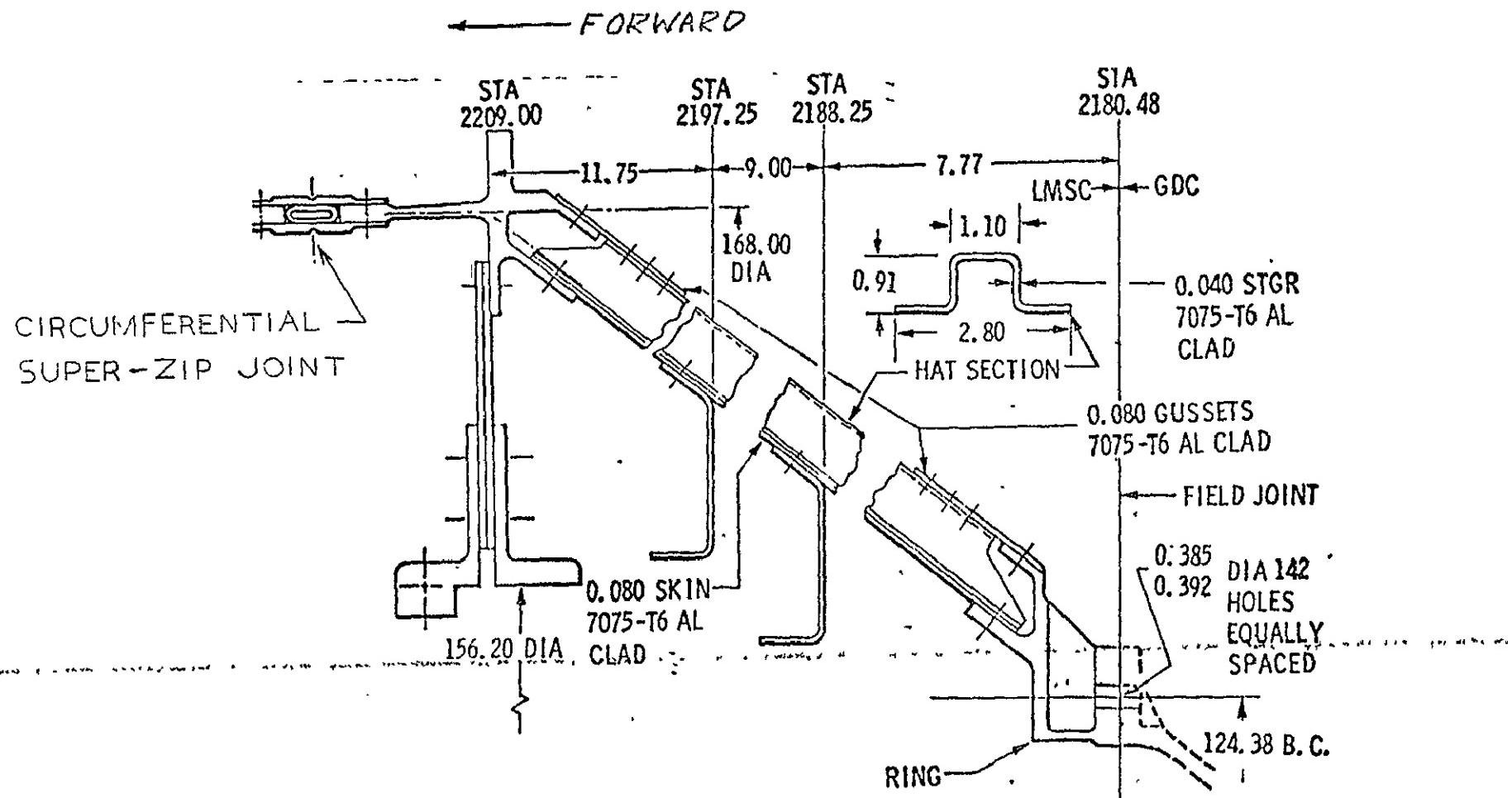


FIGURE III-17 CSS BOATTAIL SECTION

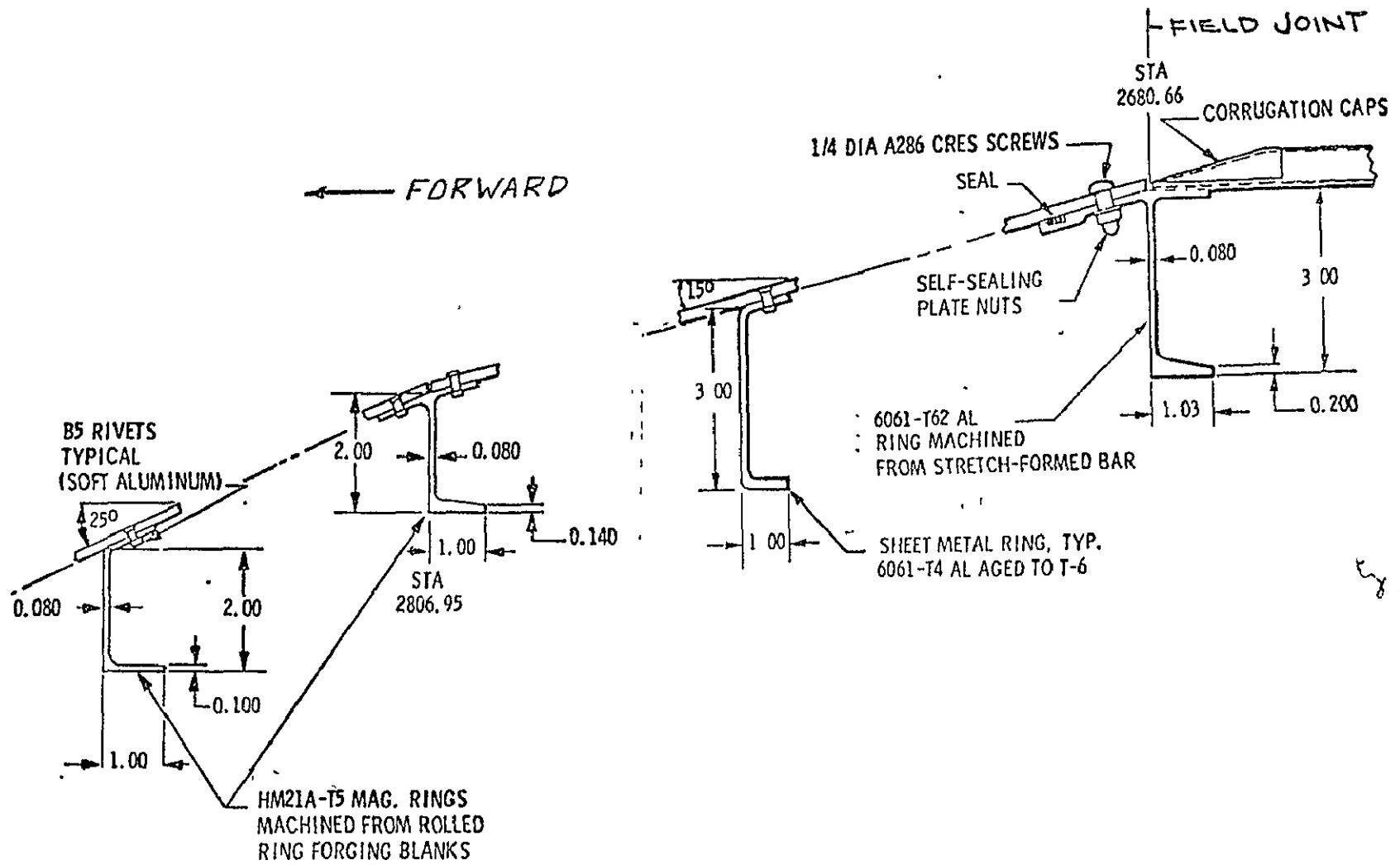
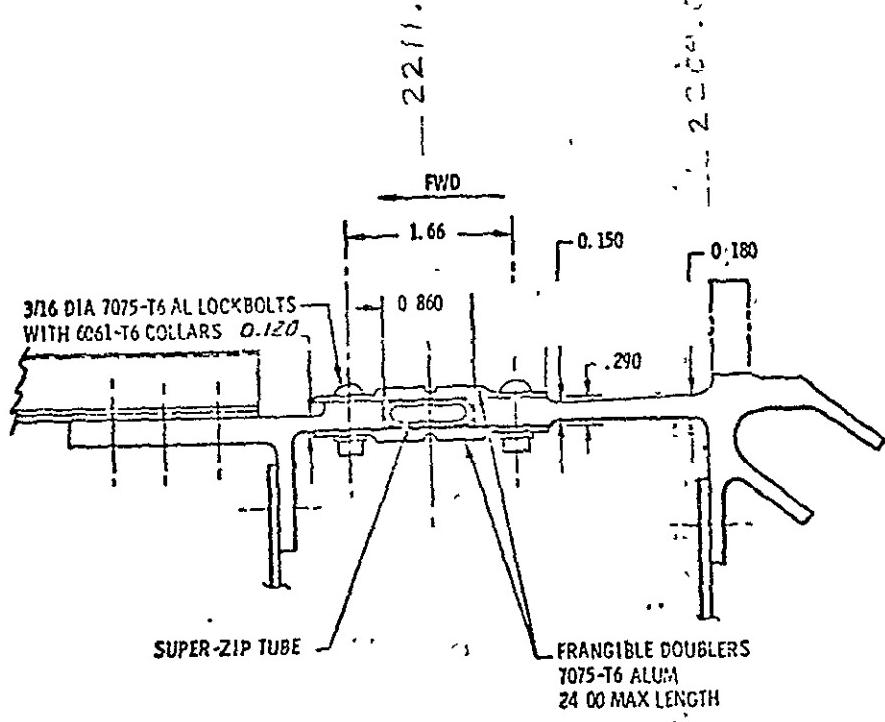
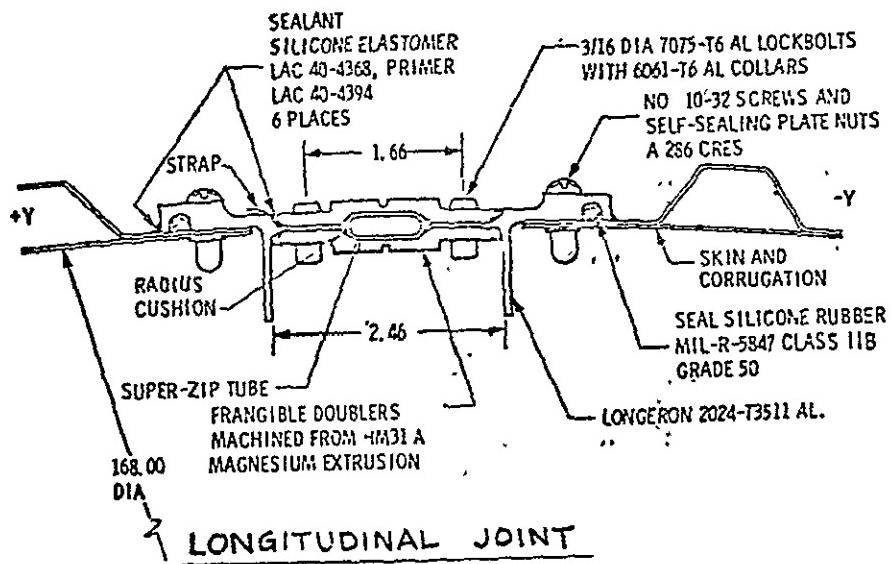


FIGURE III-18 CSS NOSE CONE SECTION



CIRCUMFERENTIAL JOINT



REPRODUCIBILITY OF THE
ORIGINAL PAGE IS POOR

FIGURE III-19 CSS SEPARATION JOINTS

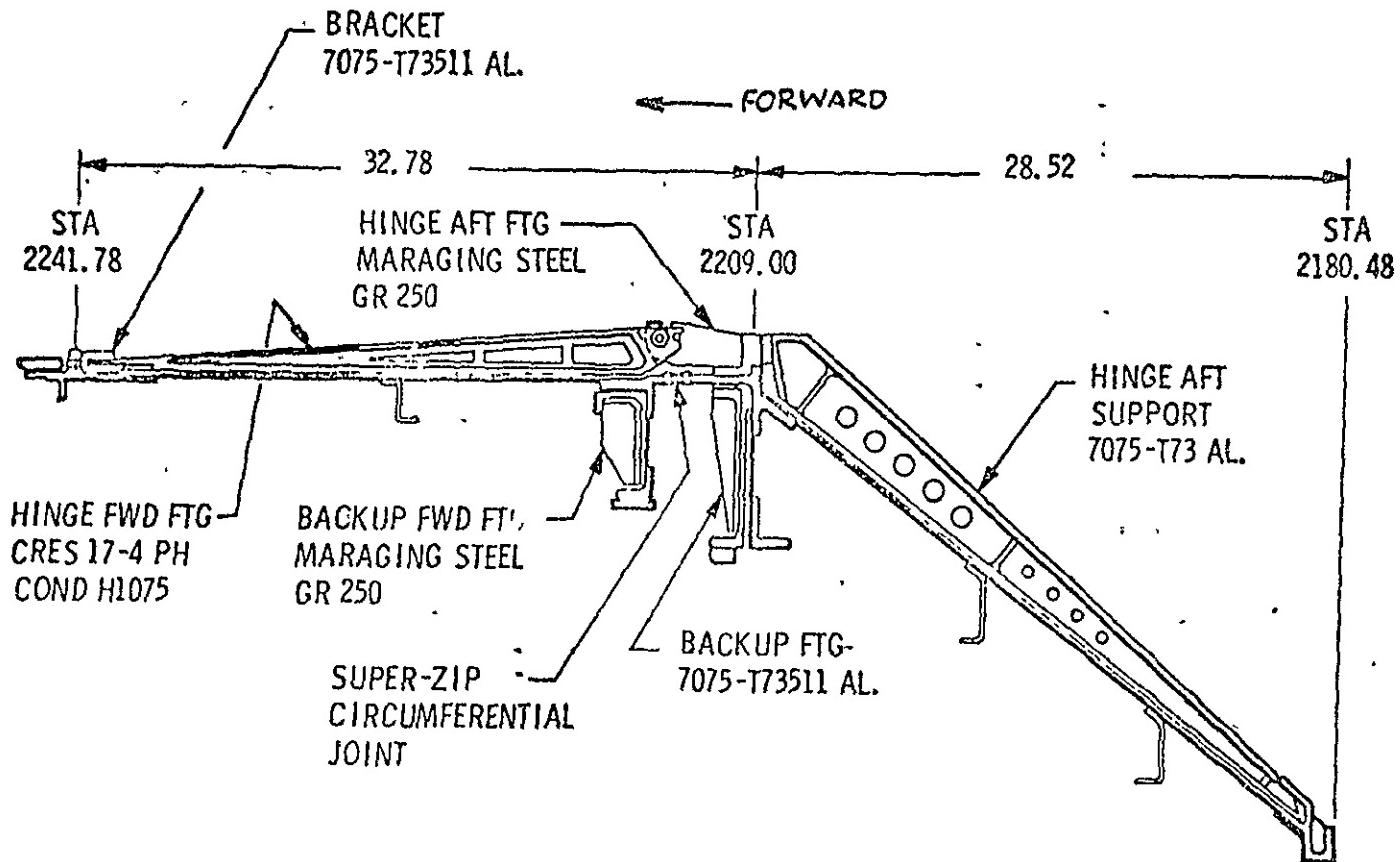


FIGURE III-20 CSS JETTISON HINGE

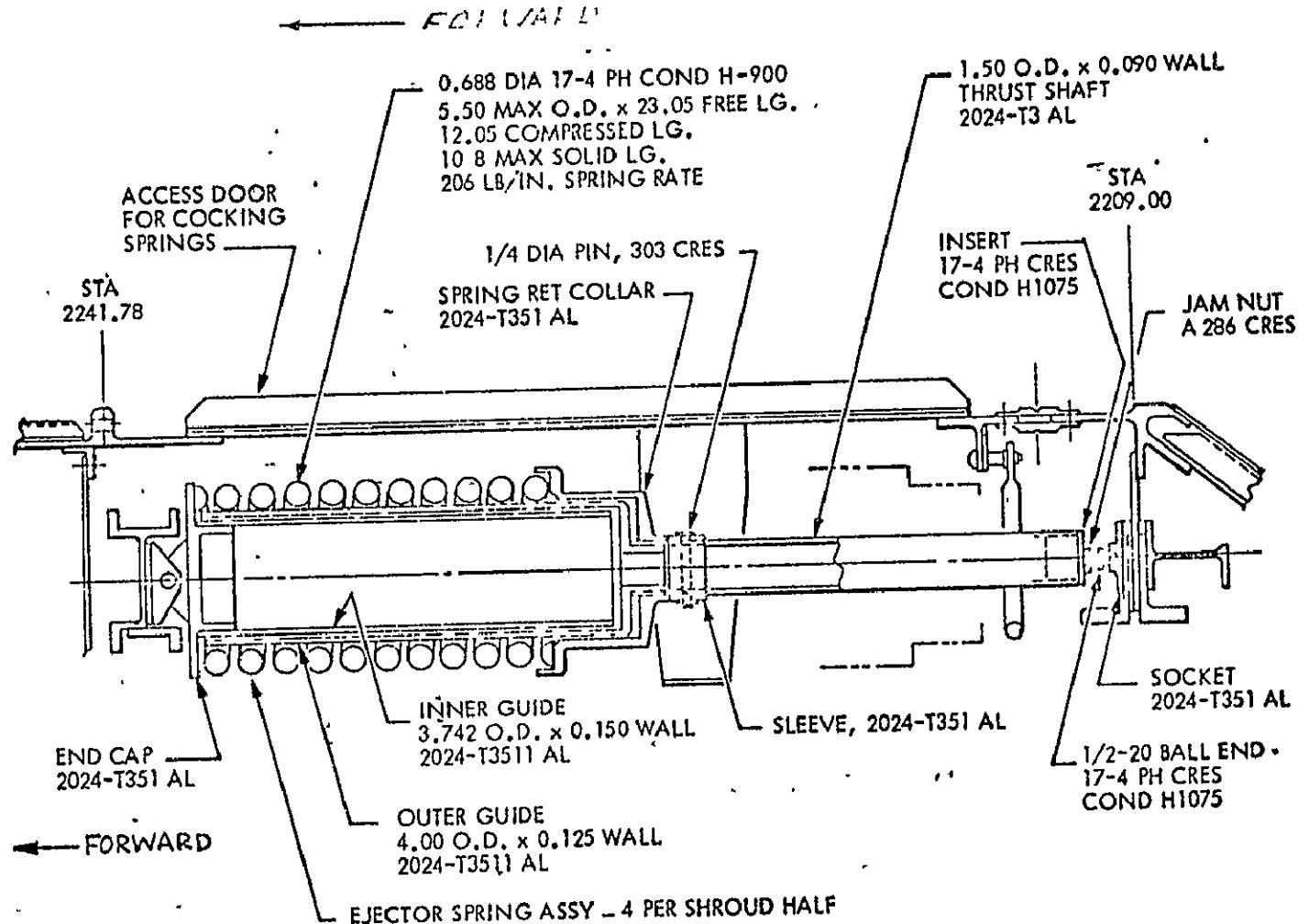


FIGURE III-21 CSS JETTISON SPRING

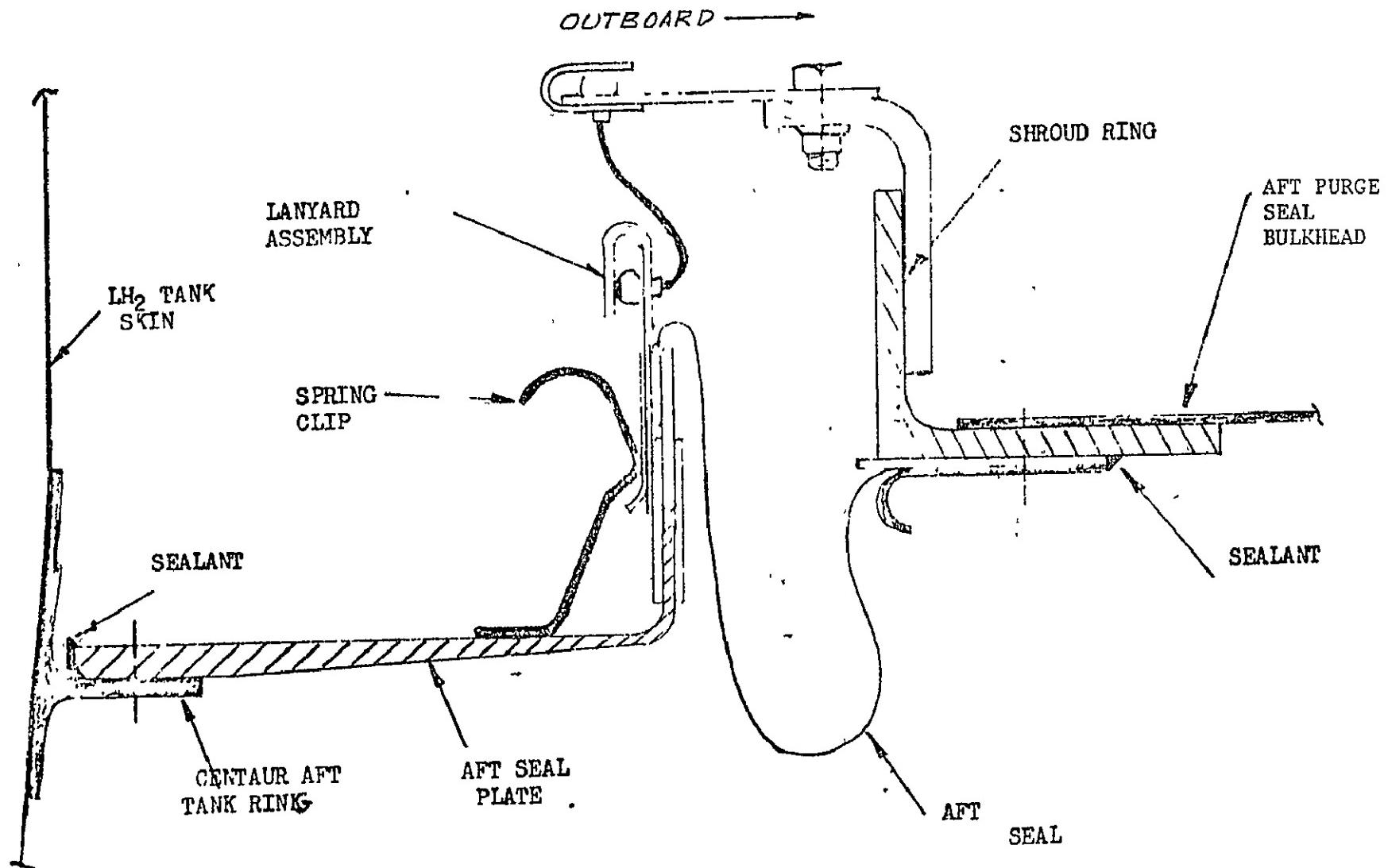


FIGURE III-22 SECTION VIEW OF CSS/CENTAUR AFT GAS PURGE SEAL ASSEMBLY

REPRODUCIBILITY OF THE
ORIGINAL PAGE IS POOR

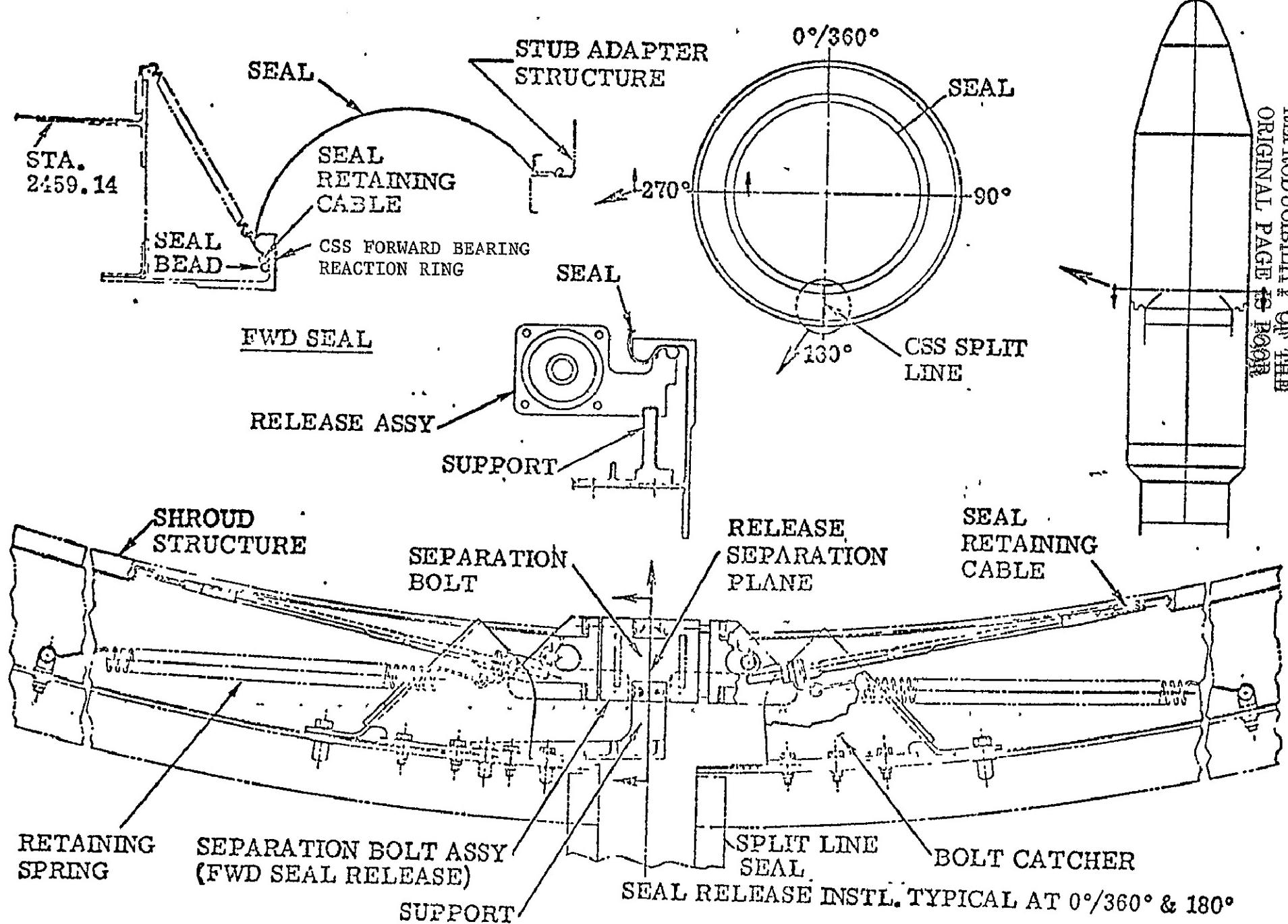


FIGURE III-23 CSS/CENTAUR FORWARD PURGE GAS SEAL

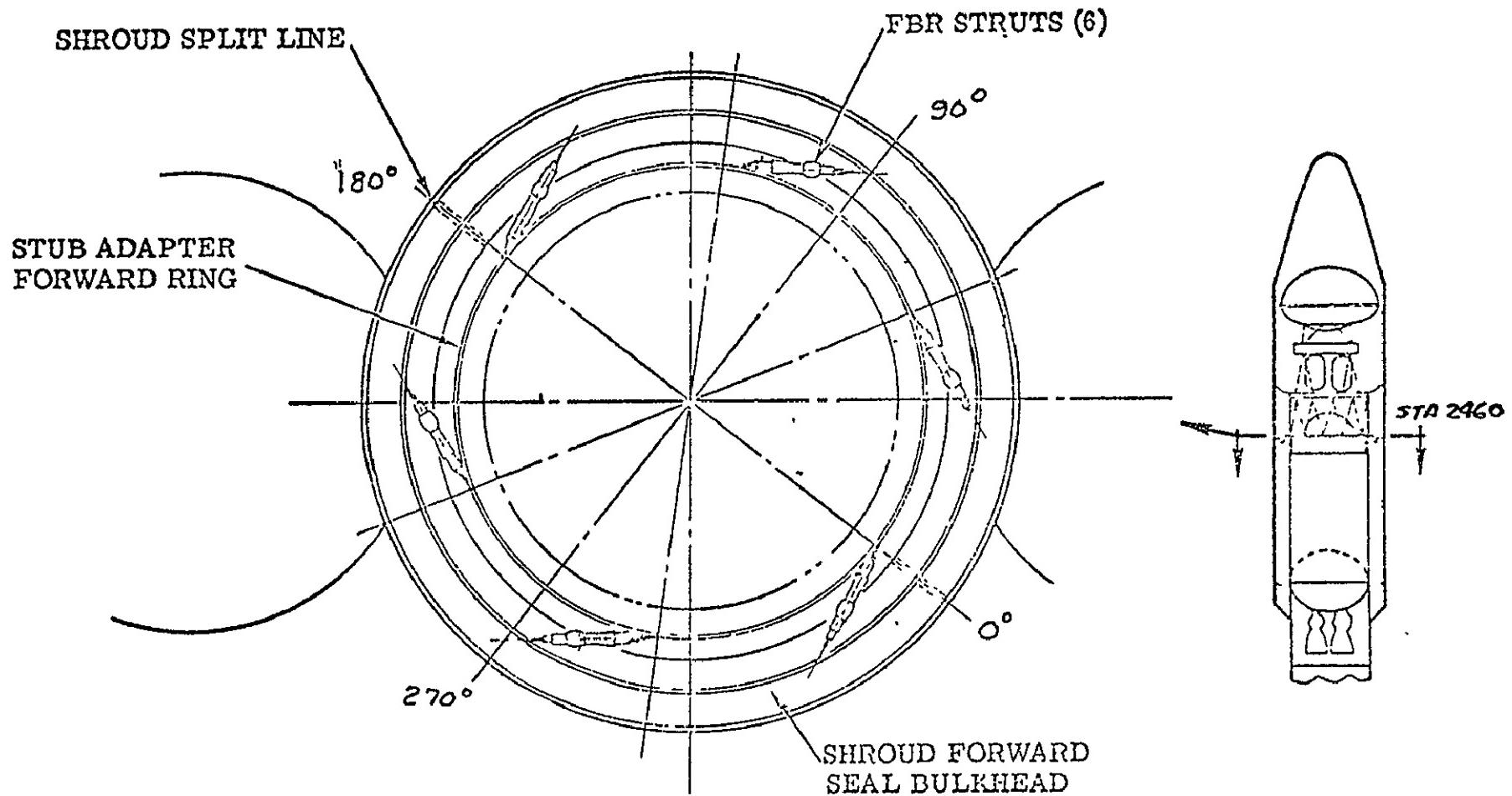


FIGURE III-24 CSS/CENTAUR FORWARD BEARING REACTION SYSTEM

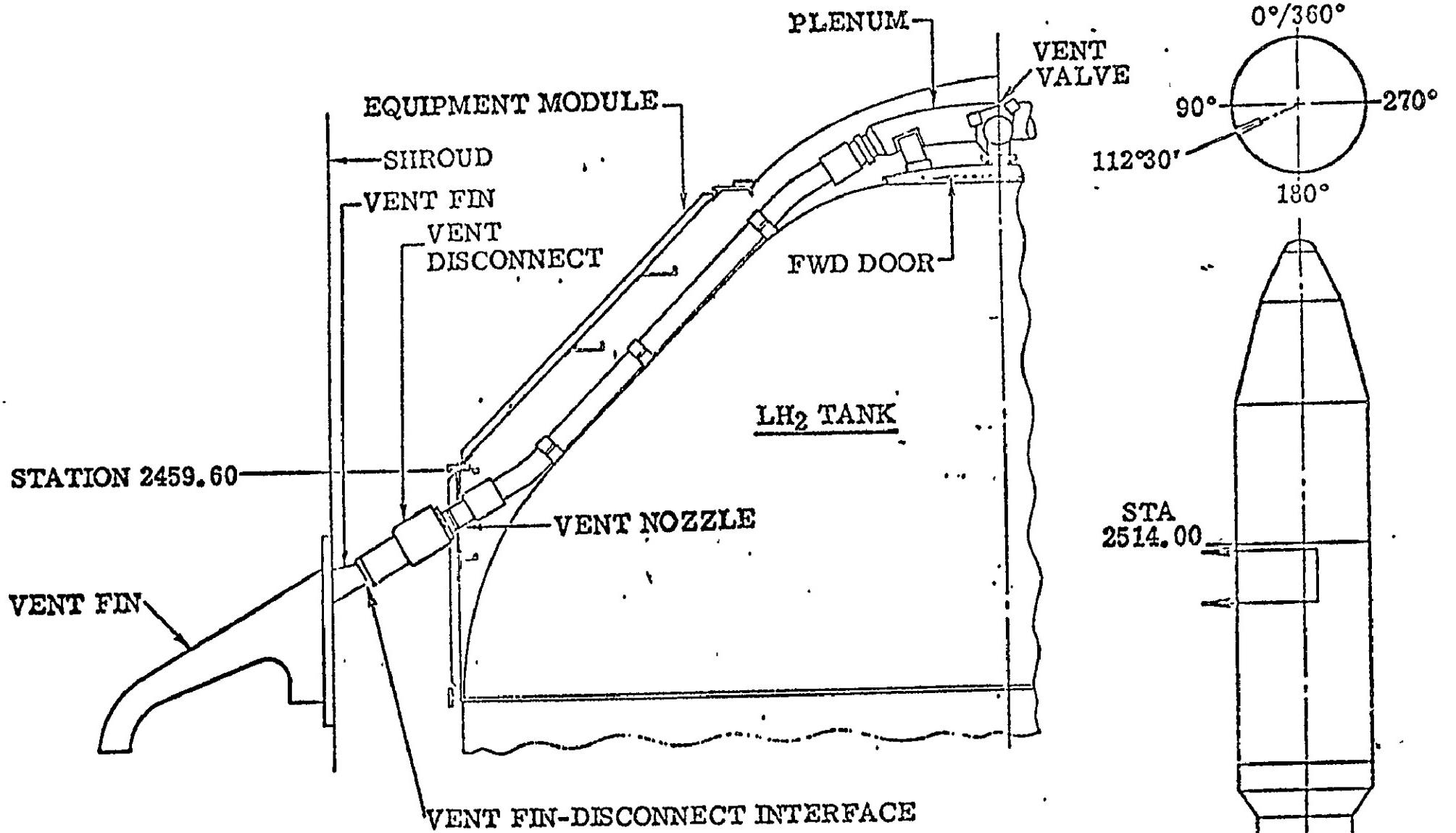


FIGURE III-25 CSS/CENTAUR HYDROGEN VENT DISCONNECT SYSTEM

REPRODUCIBILITY OF THE
ORIGINAL PAGE IS POOR

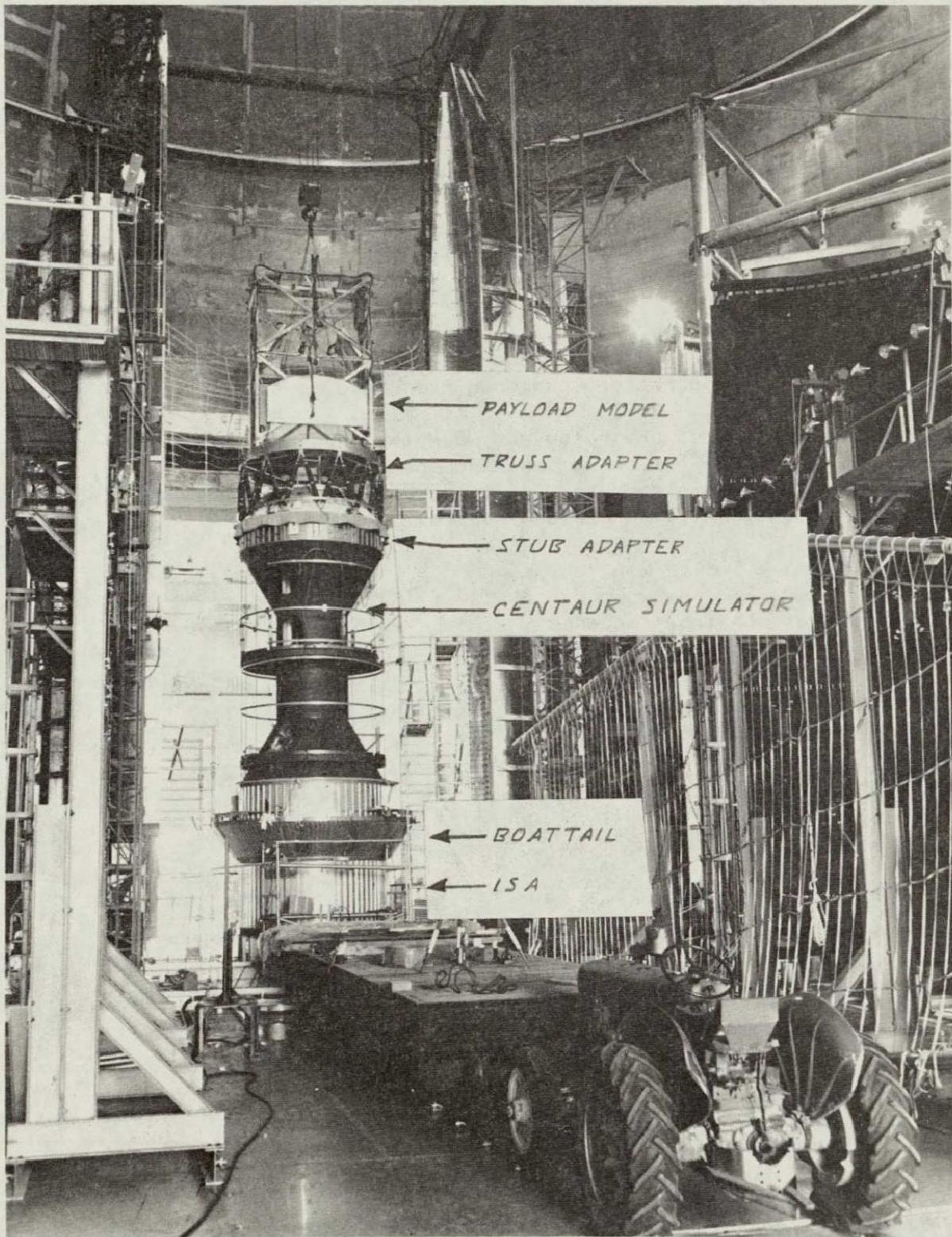


FIGURE III-26 ASSEMBLED STACK OF TEST HARDWARE
INTERNAL TO THE CSS

IV. PROCEDURE

B. Holmes Neal

The CSS and associated test hardware were assembled in the test chamber with all CSS jettison springs cocked. After a final visual inspection of the CSS and facility equipment, the Super-Zip and Forward Seal Releaser pyrotechnics were loaded. The test chamber was then closed. The test control systems were checked out and set up by operators in the control room according to the Master Countdown Procedure.

When all systems were ready and when the pressure in the test chamber was 20 ± 2 torr, the following test sequence was performed automatically under control of a minicomputer. (At the beginning of the sequence, the CSS was at a uniform temperature of approximately 55°F .)

Event*	Time, seconds
Start control sequence	T-10
Start all data recorders	T-10
Verify FM data system running	T-8
Start zone heaters**	T-0
Verify digital data system running	T+2
Verify heater start***	T+80
Turn on overall-view movie camera lights	T+160
Turn on overall-view movie camera	T+165
Start heater retract	T+250
Safe some heater zones**	T+250
Start camera timing lamps	T+250

*Events listed for heated tests. For unheated tests, delete events related to heater (except for providing additional lights for movie cameras), Forward Seal Releaser, and instrumentation disconnects.

**Indicates control system requirements only. Heat was applied to the CSS from T+50 until T+250 seconds.

***Indicates abort items.

Turn on movie camera lights	T+250
Verify heater retracted***	T+272
Start movie camera group 1	T+272
Start movie camera group 2	T+272
Arm Forward Seal Releaser pyrotechnics	T+275
Fire Forward Seal Releaser pyrotechnics	T+276
Verify Forward Seal Releaser separated***	T+277
Turn on some heater lamps for additional lights for movie cameras	T+277
Arm instrumentation disconnect pyrotechnics	T+277
Fire instrumentation disconnect pyrotechnics	T+278
Verify instrumentation disconnects separated***	T+280
Arm Super-Zip pyrotechnics	T+280
Fire Super-Zip pyrotechnics	T+281
Safe all pyrotechnic firing systems	T+295
Stop all data recorders	T+300

After the test, the test chamber pressure was raised to atmospheric pressure and opened. The CSS and facility equipment were inspected visually, and photographs were taken as deemed necessary. The CSS was then removed from the test chamber, refurbished, and assembled for the next test.

The following tests were performed:

Test	Date
Heated Altitude Jettison Test 1, MTL at 328° azimuth	November 19, 1973
Heated Altitude Jettison Test 2, MTL at 0° azimuth	January 16, 1974
Unheated Altitude Jettison Test 3	February 14, 1974

***Indicates abort items.

V. TEST RESULTS AND DISCUSSION

V.A. Thermal Simulation

Anthony Fortini

In order to simulate the "worst case" of aerodynamic heating acting on the CSS, skin temperatures were calculated using wind tunnel data (ref. 6) and GDC trajectory RH758B. These temperatures were used to control the thermal simulation during tests 1 and 2 (See "Apparatus" section) and as preliminary inputs to the thermal models. A discussion of the models, their predictions, and comparison with experimental data are presented in Appendix B.

As described in the "Apparatus" section, the heat applied to the CSS was controlled by thermocouples on the free skin near the cone-cylinder junction. (The term "free skin" in this report refers to the CSS shell in areas where the temperature is not influenced significantly by heat sink effects of structural rings, doublers, or other thermal masses.) These thermocouples followed the desired (programmed) temperatures within $\pm 15^{\circ}\text{F}$. The data in figure VA-1 are typical of results for both tests 1 and 2.

Other free-skin temperatures (not shown herein) were calculated accurately using radiation heat transfer equations, shell properties, heater lamp spacing, and the temperature at the control thermocouple. Whenever a large deviation from the expected free-skin temperature occurred, investigation determined that the effect was caused by large nearby thermal masses. Typical data are depicted in figure VA-2. This deviation is due to a large door and reinforcing brackets which acted as heat sinks.

Circumferential Temperature Gradients

The circumferential temperature gradient for test 1 is presented in figure VA-3. The desired and actual temperatures are shown for the control thermocouple station on the cone and on the cylinder, and for station 2221, which is near the aft end of the cylinder. Data are shown for test 1 at ($T+276$ sec), the time of jettison. Similar data were obtained for other times during the test 1 heating cycle and for test 2. At the control thermocouples, the desired temperatures were successfully attained. At station 2221, the shape of the gradient curve is correct, but the temperatures attained were low because of nearby structural thermal masses.

The data show that the maximum temperatures occur at the MTL, and that the heating was symmetrical about the MTL. On the cone, the minimum temperature occurred 180° in azimuth away from the MTL. On the cylinder, minimum

temperatures occur at approximately 80° and 220° azimuth, which are 110° in azimuth away from the MTL. All of these results were expected.

Longitudinal Temperature Gradients

The desired and actual temperatures for the hot and cold sides are displayed in figure VA-4 for test 1. Similar data were obtained for test 2. The gradients are caused by axial variation in the heat applied to the CSS, plus differences in shell material and material thicknesses. The data show that the desired temperatures were achieved except in the aft portion of the CSS. This deviation is expected for reasons mentioned previously.

Radial Temperature Gradients in Rings

A major contribution to the CSS pinch and loss of payload clearance is the radial temperature gradient in the structural rings. Several rings were instrumented so that the actual temperature gradients may be compared to gradients calculated (predicted) by the LMSC thermal models (See Appendix B). Some typical data are shown in figures VA-5 through VA-8. The data are represented by unconnected symbols, and the calculations (which are always based on a nearby actual free-skin temperature) are shown by curves. For all rings, the shapes of the temperature history curves are as expected. The gradient, as well as the temperature level, is greater near the MTL (compare data in figs. VA-6 and VA-7). Near the MTL, the ring gradient is 65°F at the time of CSS jettison. These results, plus other results presented in Appendix B, indicate that the outboard and inboard flange temperatures each are calculated within $\pm 15^{\circ}\text{F}$ at the time of jettison for this type of trajectory. The temperature difference between the outboard and inboard flanges is calculated within $\pm 10^{\circ}\text{F}$.

Overall Thermal Simulation

The temperature data show that trajectory RH758B heating was successfully simulated on the CSS in both tests 1 and 2. Control thermocouple temperatures were within $\pm 15^{\circ}\text{F}$ of the desired (programmed) temperatures. Circumferential, longitudinal, and ring thermal gradients were generally as expected in both magnitude and direction. Repeatability of the temperature data was good.

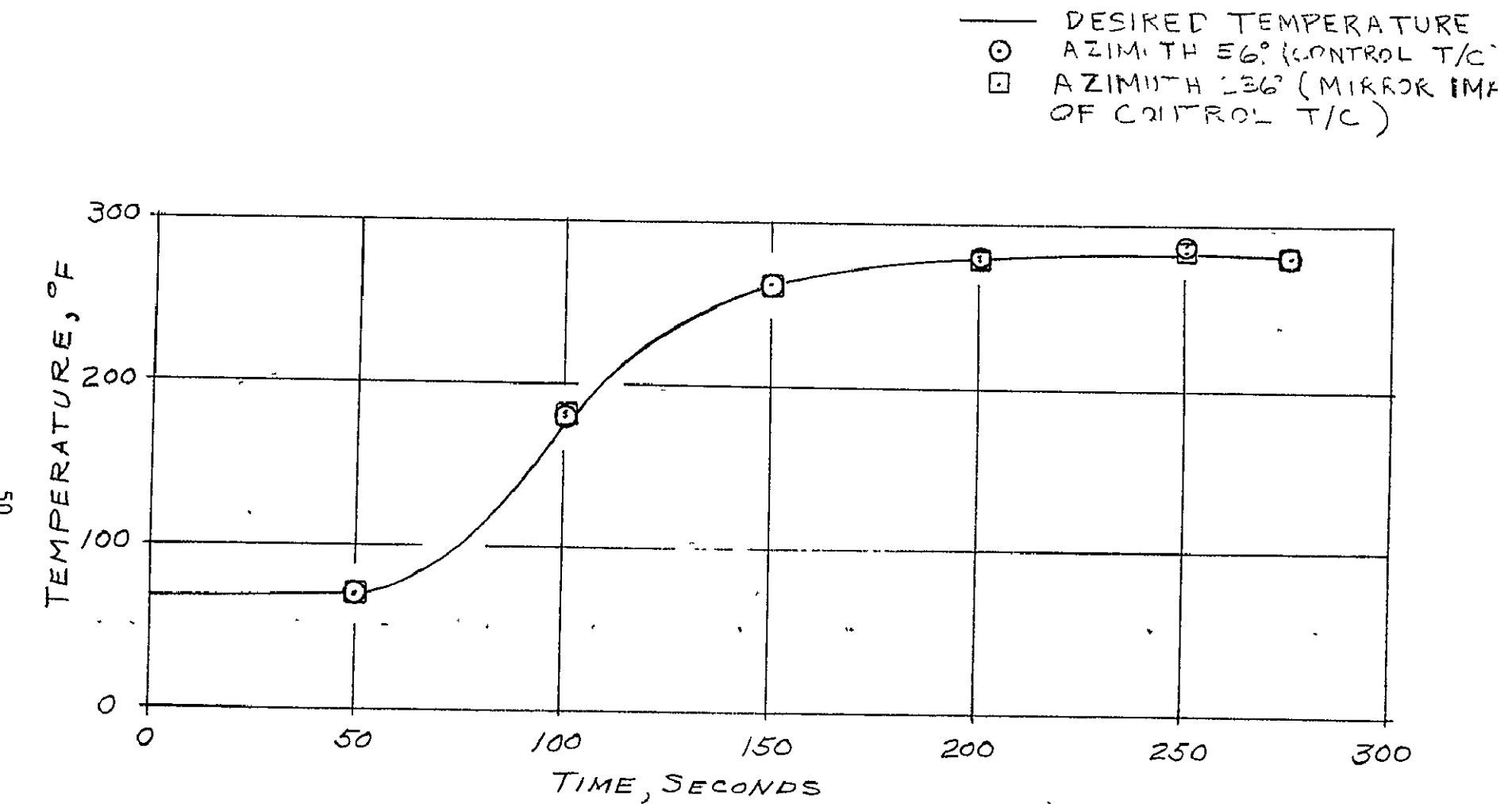


FIGURE V A-1 CONTROL THERMOCOUPLE TEMPERATURE AND FREE-SKIN TEMPERATURE HISTORIES, STATION 2724

○ ACTUAL SKIN TEMPERATURE
— CALCULATED FREE-SKIN TEMPERATURE

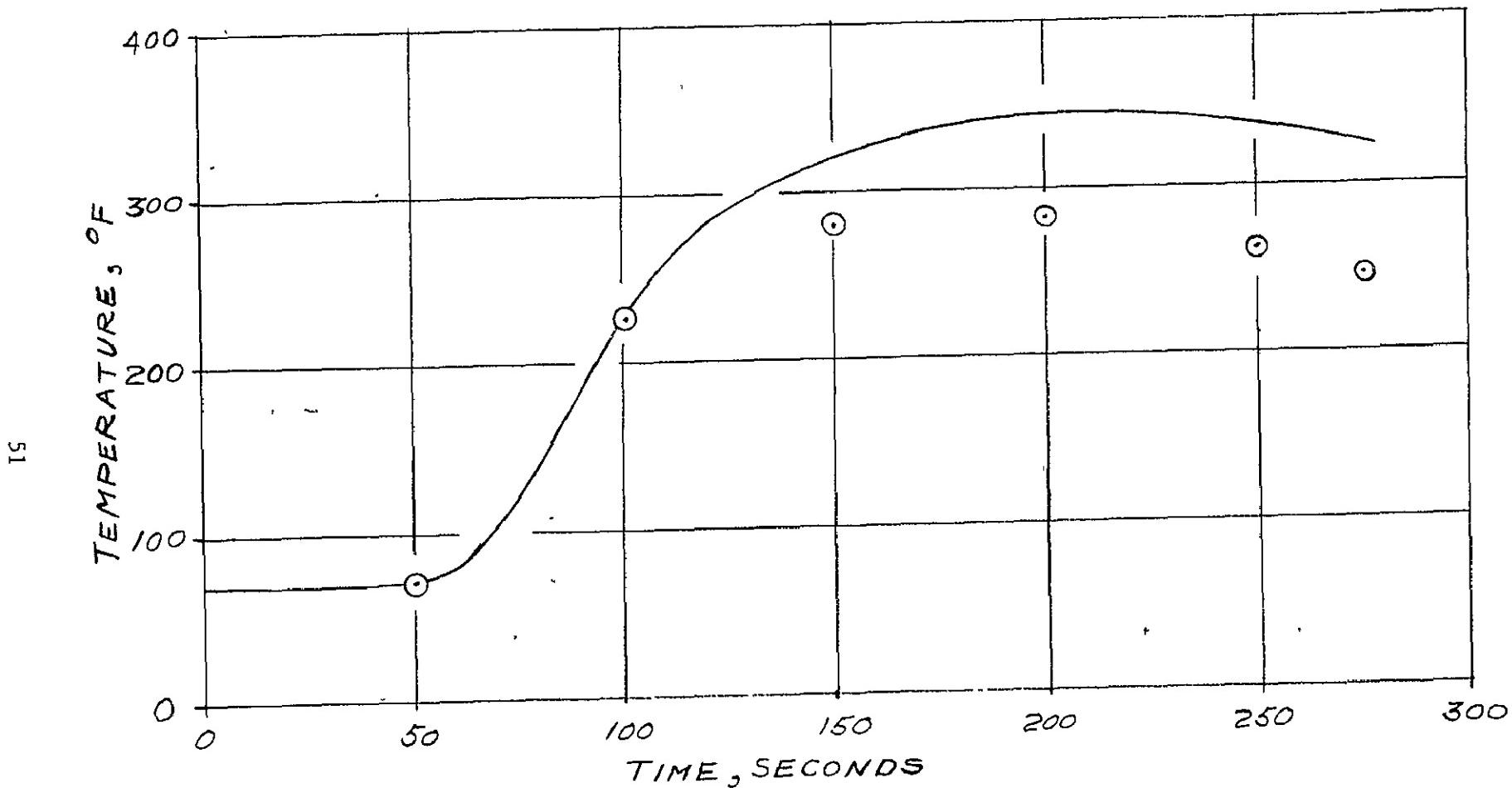


FIGURE IV-A-2 CALCULATED AND ACTUAL FREE-SKIN TEMPERATURE
HISTORIES AT STATION 2454, AZIMUTH 351°, TEST 1

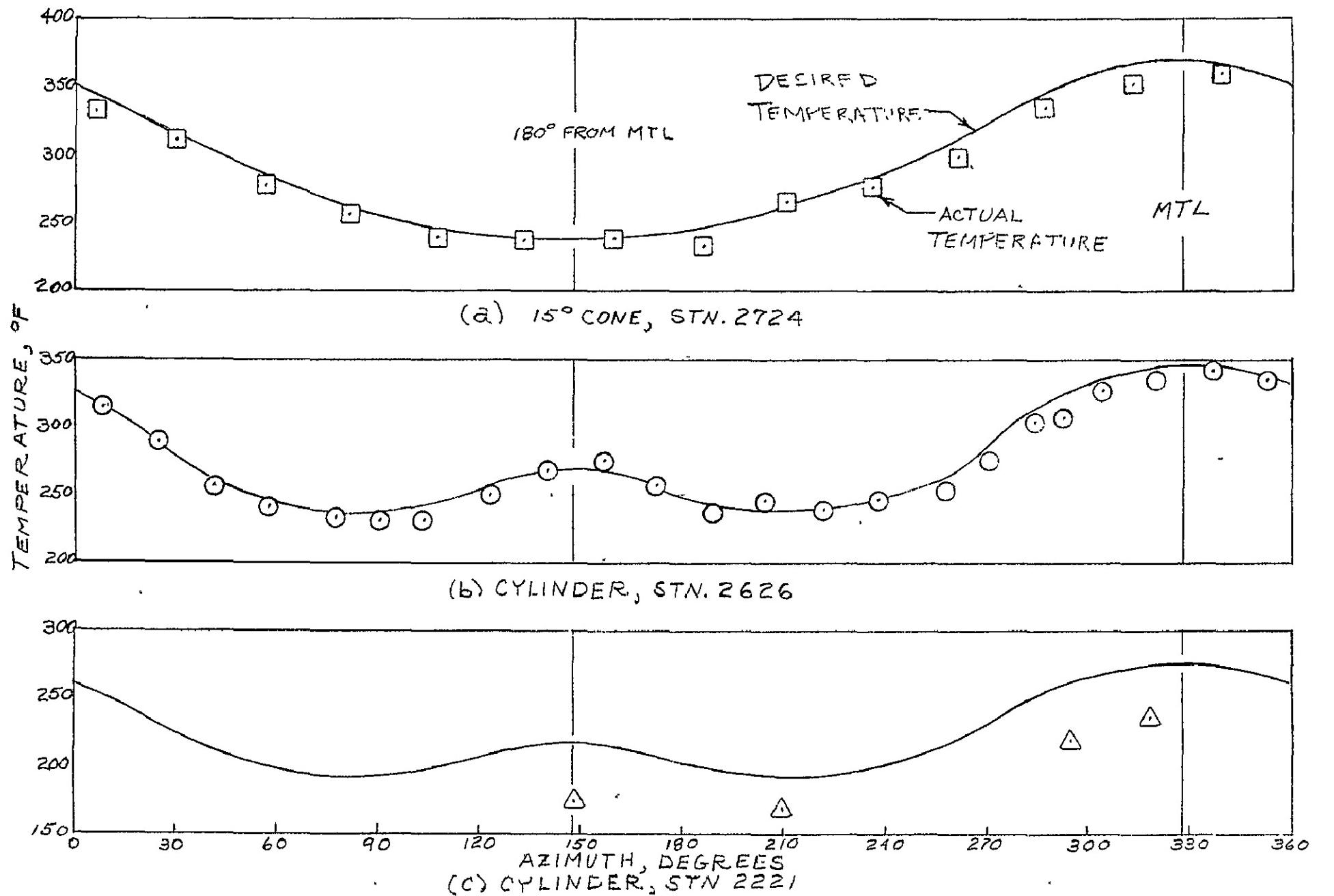


FIGURE VI-A-3 DESIRED AND ACTUAL CSS CIRCUMFERENTIAL TEMPERATURE GRADIENTS AT THREE STN. FOR 328° SKEW HEATING ($T_f = 76$ SEC.) TEST 1

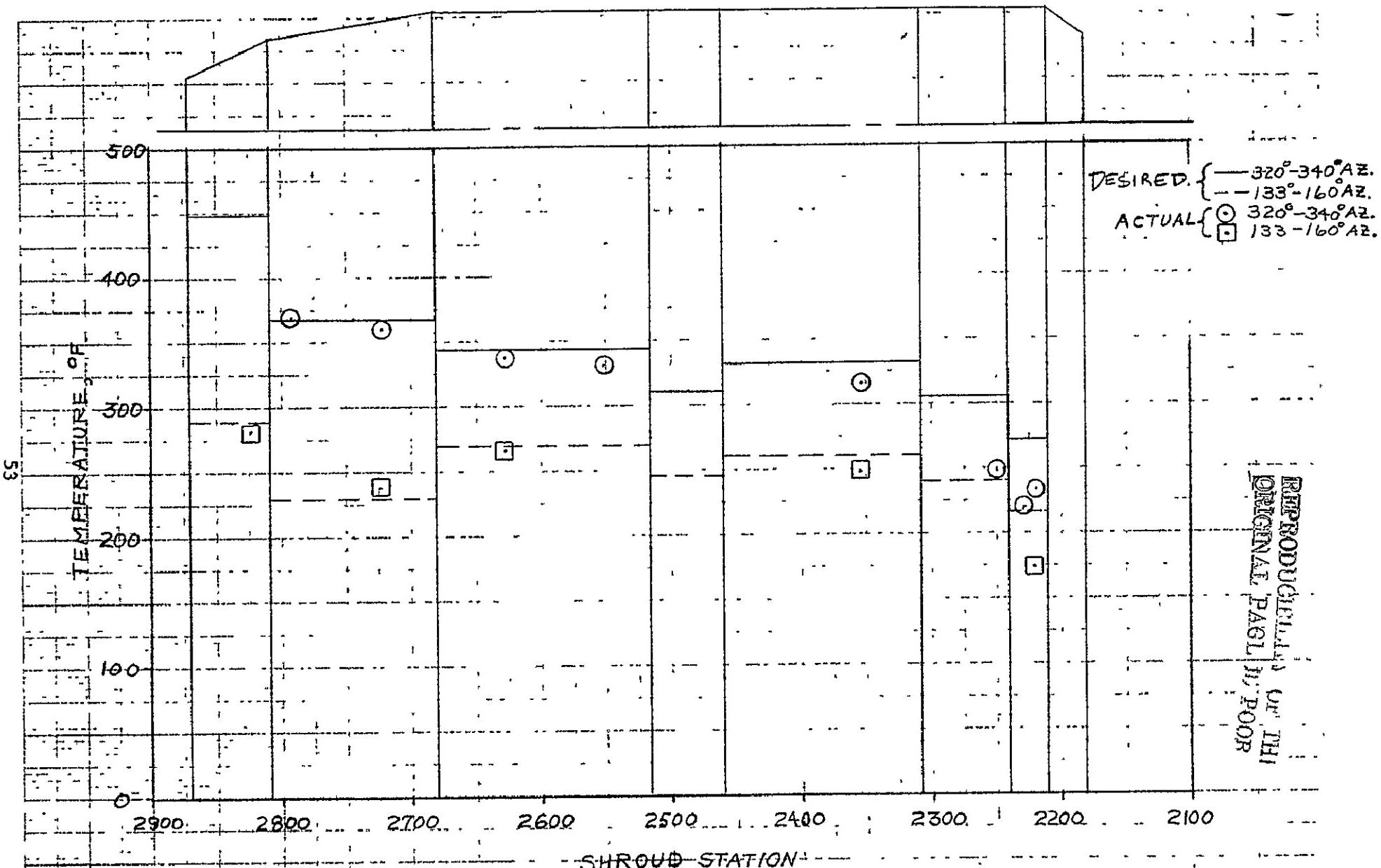


FIGURE VII-4 DESIRED AND ACTUAL LONGITUDINAL TEMPERATURE GRADIENTS, ($T + 276$ SEC.), TEST 1

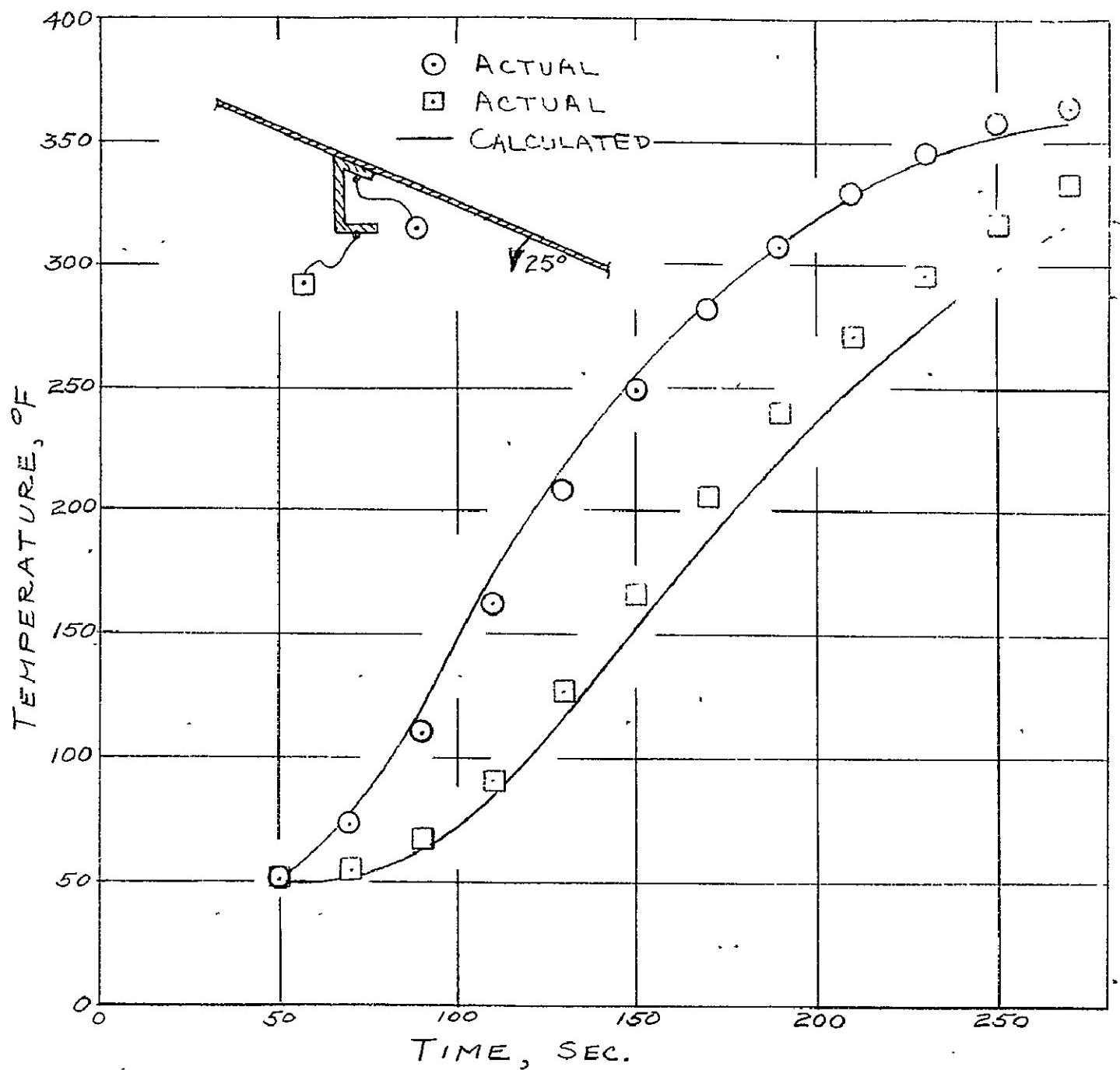


FIGURE IV-A-5 CALCULATED AND ACTUAL TEMPERATURE HISTORIES FOR 25° CONE RING (MODEL NO. 1) AT STATION 2827, AZIMUTH 339° , TEST 2

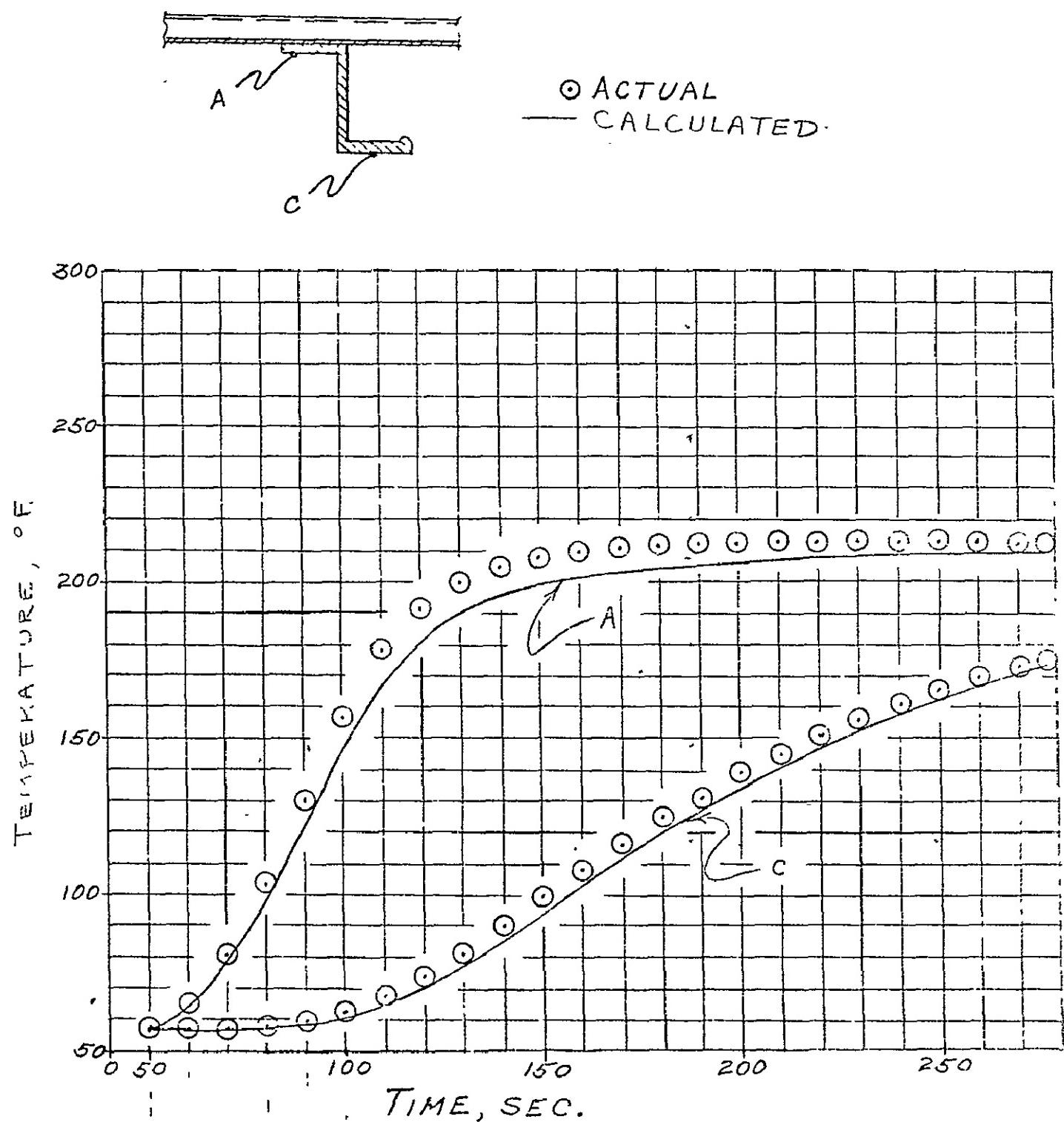


FIGURE VIIA-6: CALCULATED AND ACTUAL TEMPERATURE HISTORIES FOR CYLINDER ZEE RING, (MODEL NO. 4) STATION 2634, AZIMUTH 206°, TEST 1

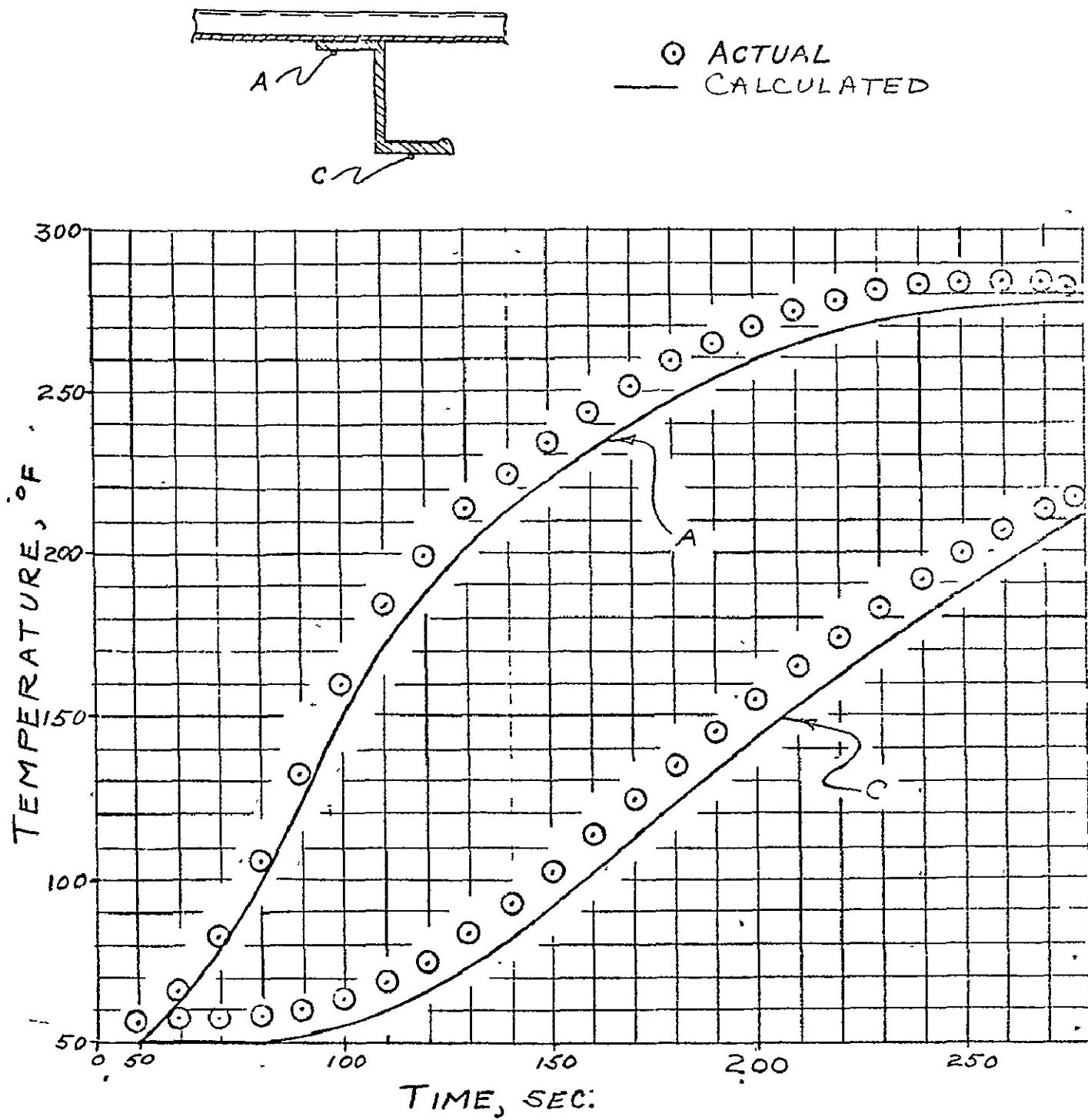


FIGURE IV A--" CALCULATED AND ACTUAL TEMPERATURE HISTORIES FOR CYLINDER ZEE RING,
(MODEL No. 4), STATION 2634, AZIMUTH 335°
TEST 1

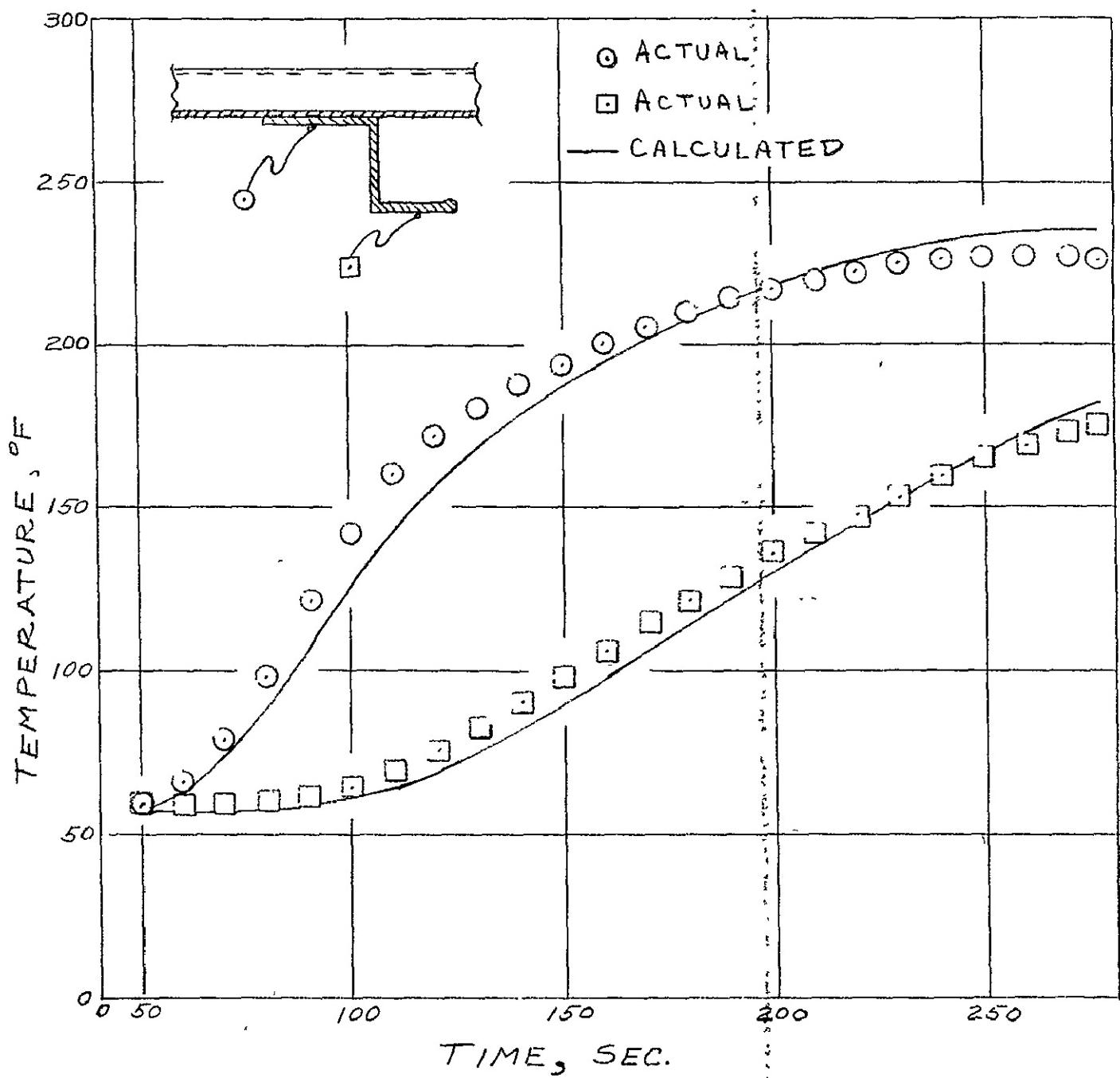


FIGURE VIIA-8 CALCULATED AND ACTUAL TEMPERATURE HISTORY FOR CYLINDER ZEE-RING, (MODEL NO. 5), STATION 2478, AZIMUTH 351° , TEST 1

REPRODUCIBILITY OF THE
ORIGINAL PAGE IS POOR

V.B. Distortions Due to Heating

John C. Estes

The test simulation of asymmetric flight heating caused three types of thermal gradients in the CSS: axial, circumferential, and radial.

The primary effect of the axial temperature gradient was to cause axial elongation. Figures VB-1 and VB-2 show final pre-separated (277-sec) axial growth versus station for tests 1 and 2. All deflection in these plots is relative to the CSS base ring at station 2214. Both test measurements and LMSC analytic predictions are shown in the figures.

Figures VB-1 and VB-2 also show effects of the circumferential temperature gradients. The hotter (windward) side of the CSS elongated more than the cooler (leeward) side. As a result, the asymmetrically heated CSS assumed a thermally distorted position, bent away from the MTL. This deflection has been referred to as "hot-dogging." Radial deflections versus station at 0° and 180° are shown for tests 1 and 2 in Figures VB-3 and VB-4. A maximum pre-separated radial deflection of about 0.6 inches away from the MTL was observed at station 2664 at 0° . Figures VB-3 and VB-4 also show LMSC analytic predictions superimposed on the test observations.

An additional type of radial deflection was superimposed on the "hot-dogging" distortions by the radial temperature gradients. Figures VB-3 and VB-4 show that the radial deflections at 0° moved farther from the MTL than did the deflections at 180° . This was caused by the radial temperature gradients from the CSS skin across the Zee-rings. These radial gradients caused bending in the rings. Such bending was not circumferentially uniform because of circumferential variation in the radial gradient. In addition, the Zee-rings had bending discontinuities at each split line, since the Super-Zip joints were unable to resist appreciable bending moments. These moment discontinuities caused the rings to tend to pinch from their original circular shapes into figure eight patterns. The tendency of the 180° split line to pinch toward the MTL explains the lack of symmetry in the radial plots of Figures VB-3 and VB-4. The final pre-separated (277-sec) deflections of the Zee-rings at stations 2377, 2459, and 2664 are shown in Figures VB-5 to VB-10. The test points on these plots represent measurements from "string pot" deflectometers. The deflectometer measurements were not corrected for the generally minimal axial or tangential motions except at the split lines. Tangential distortions at the split lines were determined by averaging data from adjacent camera targets immediately prior to separation. Figures VB-5 to VB-10 show generally excellent comparison between test results and LMSC analytic predictions.

The thermal distortions of the joined shell halves differ from the distortions assumed by the separated shell halves after the Super-Zip joints are fired. Section VF discusses the test observations of the dynamic motions of the shell halves enroute to reaching new post-separated equilibrium positions.

FIGURE IVB-1
CSS AXIAL THERMAL GROWTH
HJT-1, 328° SKEW, 277 SEC.

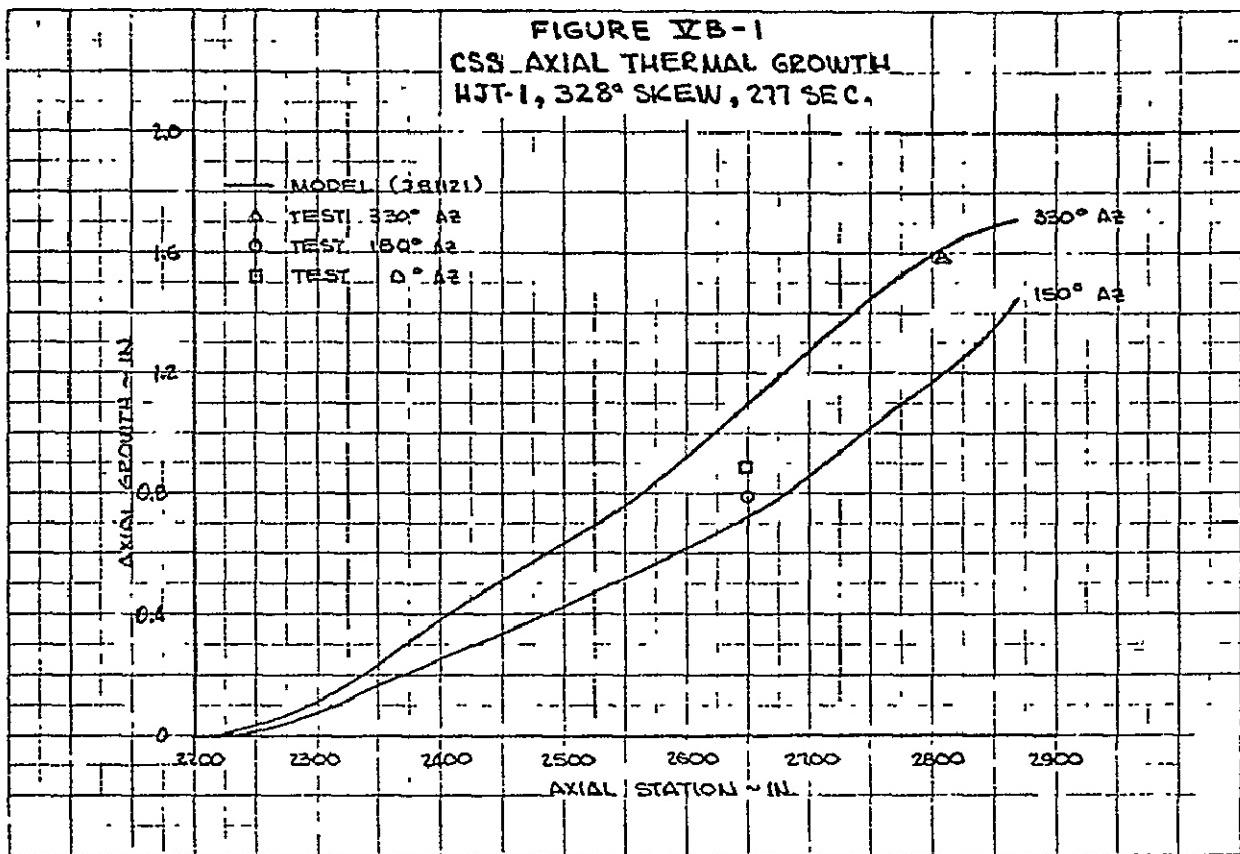


FIGURE VIB-2

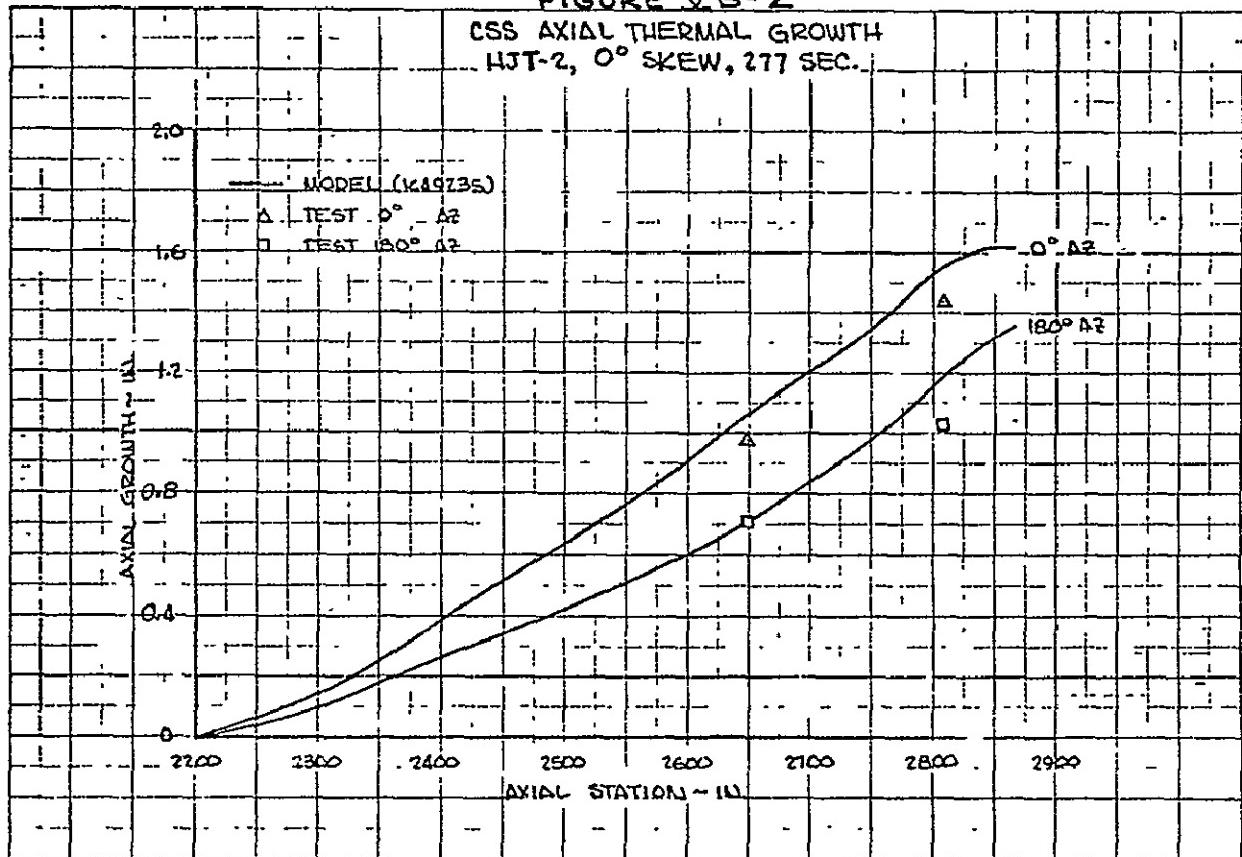


FIGURE IVB-3
CSS HJT-1 RADIAL DEFLECTION
VS. STATION, 277 SECONDS

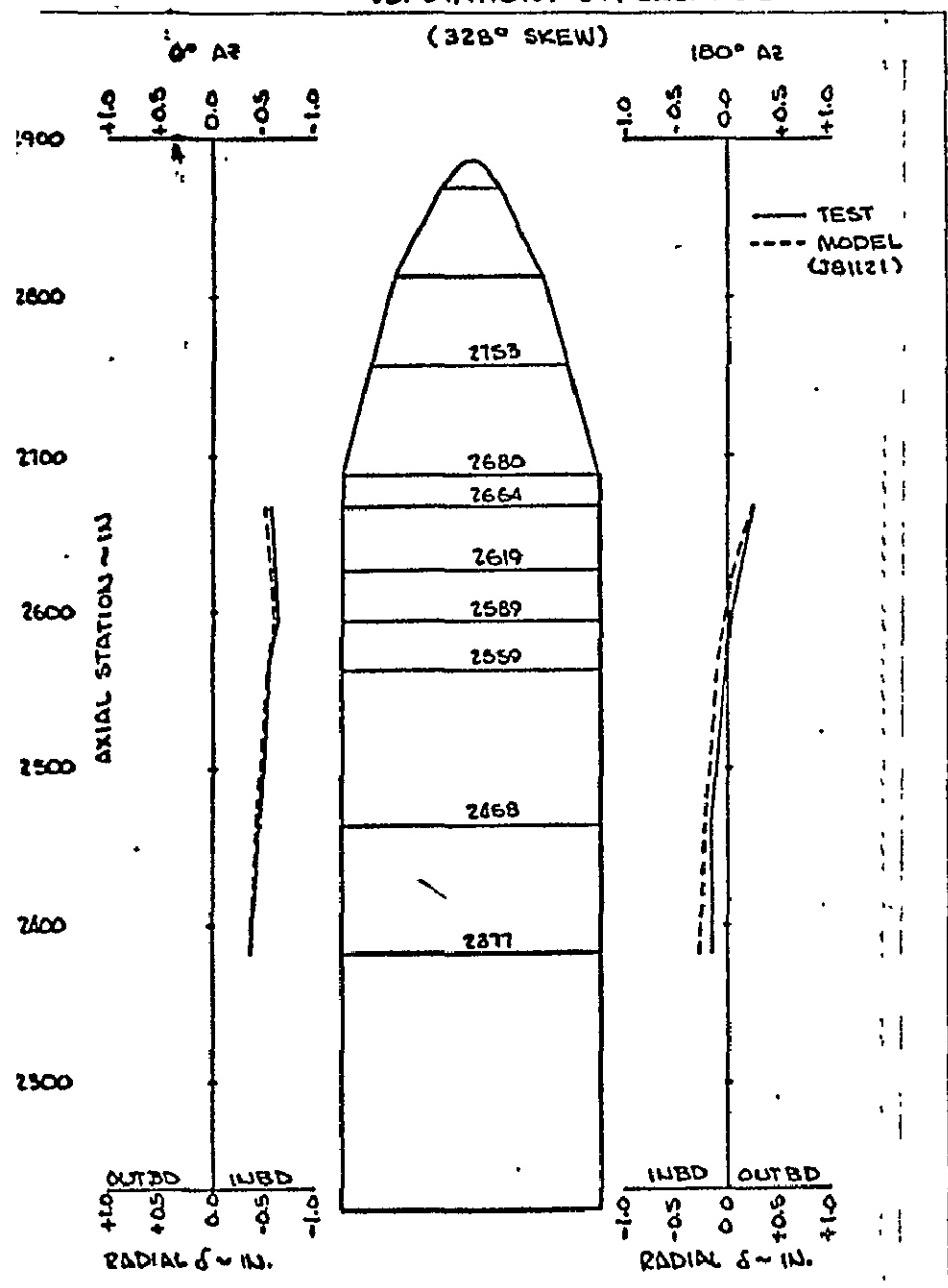


FIGURE IVB-4
CSS HJT-2 RADIAL DEFLECTION
VS. STATION, 277 SEC.

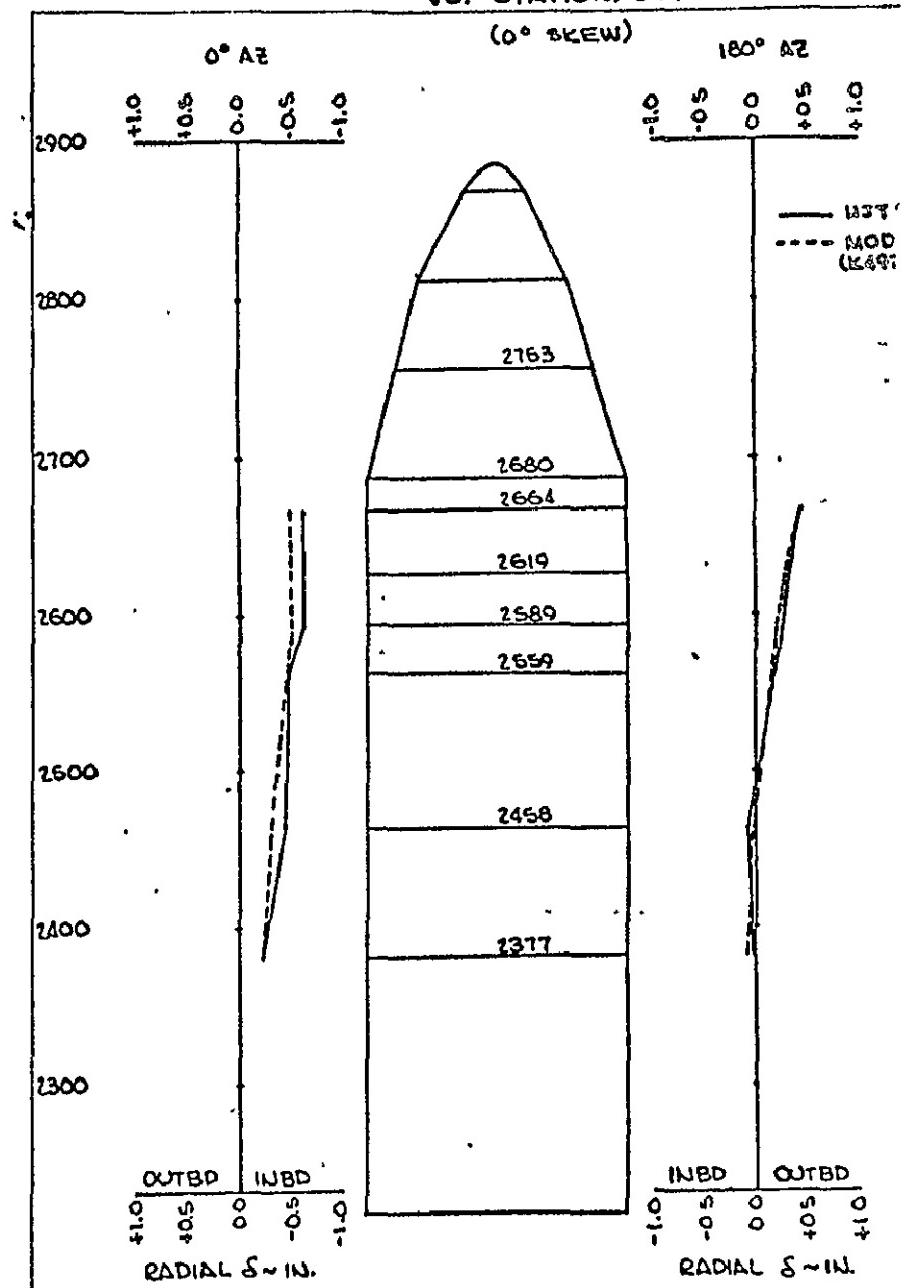
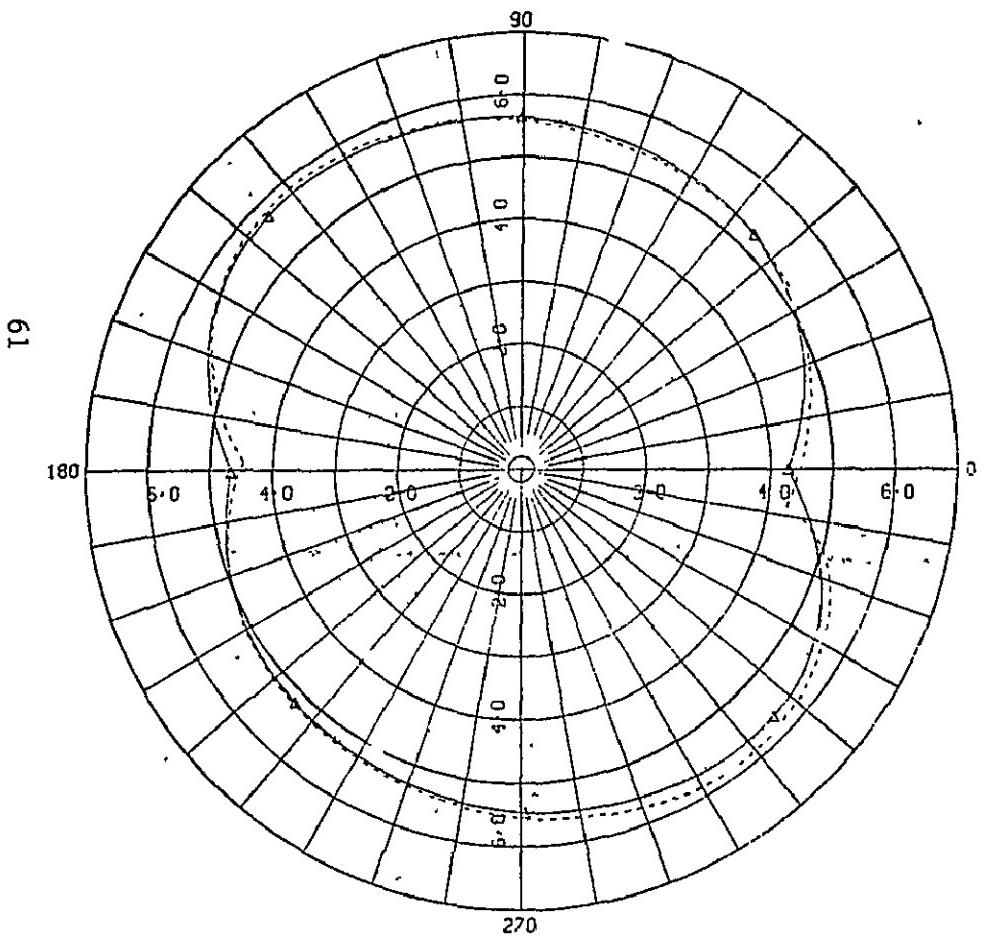


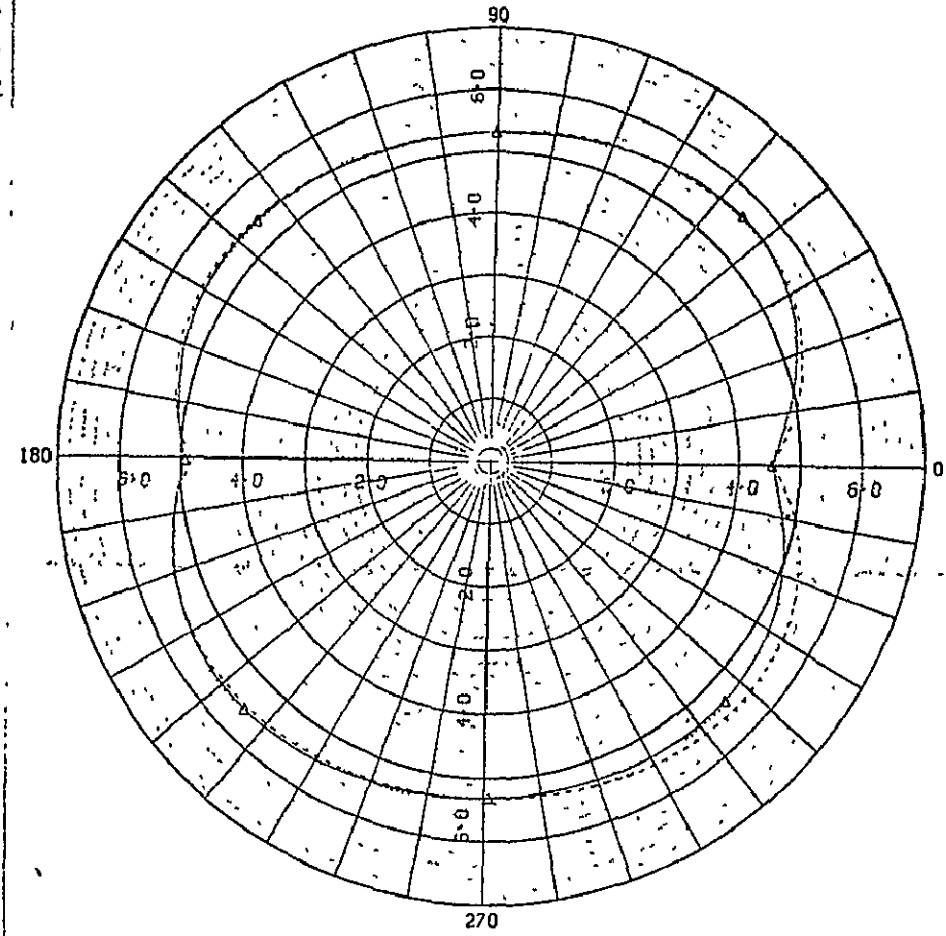
FIGURE IVB-5
CSS PRESEPARATED RING DEFLECTION
HJT 1 STATION 2377 277 SEC.
MODEL - TEST COMPARISON



HJT 1 —
MODEL - - -
(JB1121)

SCALE: 1 UNIT = 0.5 IN.

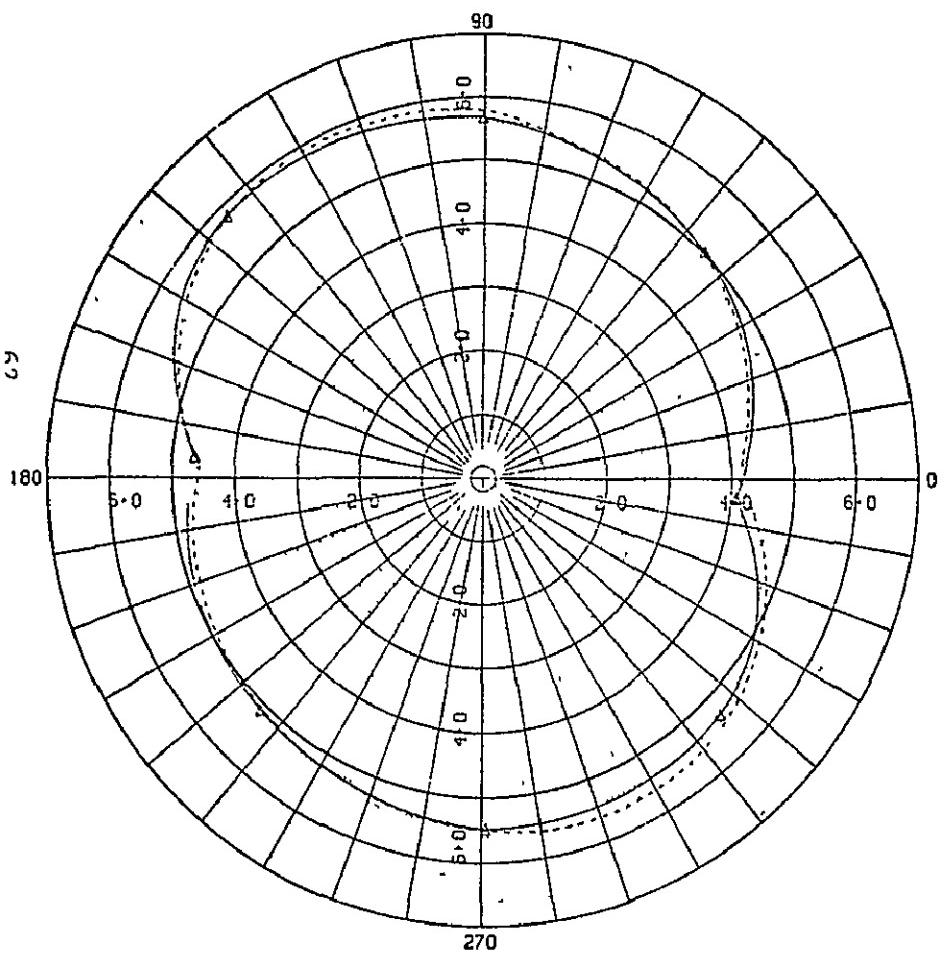
FIGURE IVB-6
CSS PRESEPARATED RING DEFLECTION
HJT 2 STATION 2377 277 SEC.
MODEL - TEST COMPARISON



HJT 2 —
MODEL - - -
(K49235)

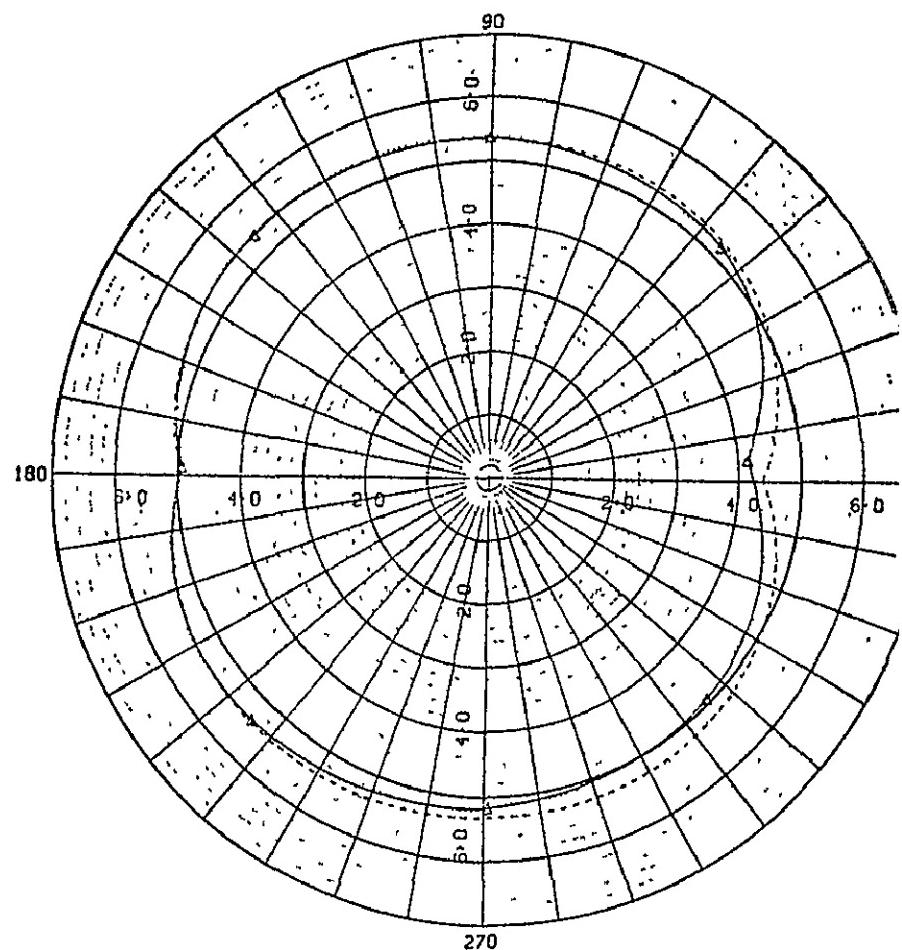
SCALE: 1 UNIT = 0.5 IN.

FIGURE IVB-7
CSS PRESEPARATED RING DEFLECTION
HJT 1 STATION 2459 277 SEC.
MODEL - TEST COMPARISON



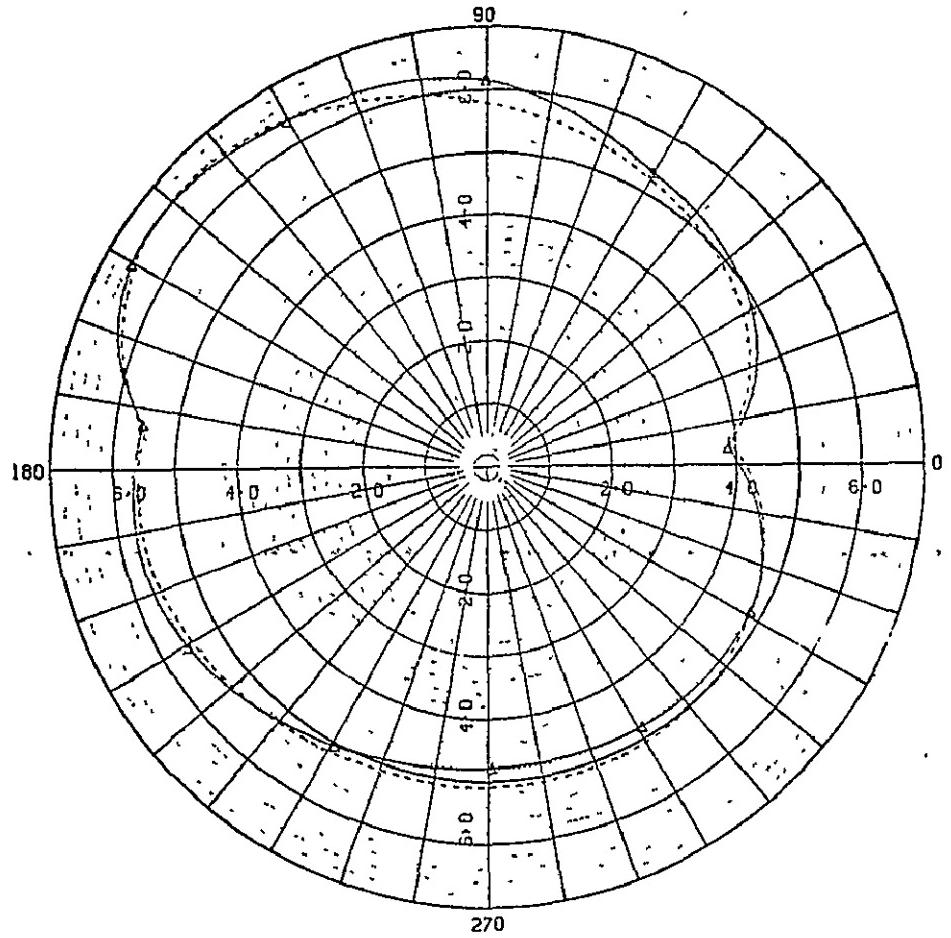
HJT 1 —
MODEL -----
(J81121)
SCALE: 1 UNIT = 0.5 IN.

FIGURE IVB-8
CSS PRESEPARATED RING DEFLECTION
HJT 2 STATION 2459 277 SEC.
MODEL - TEST COMPARISON



HJT 2 —
MODEL -----
(K49235)
SCALE: 1 UNIT = 0.5 IN.

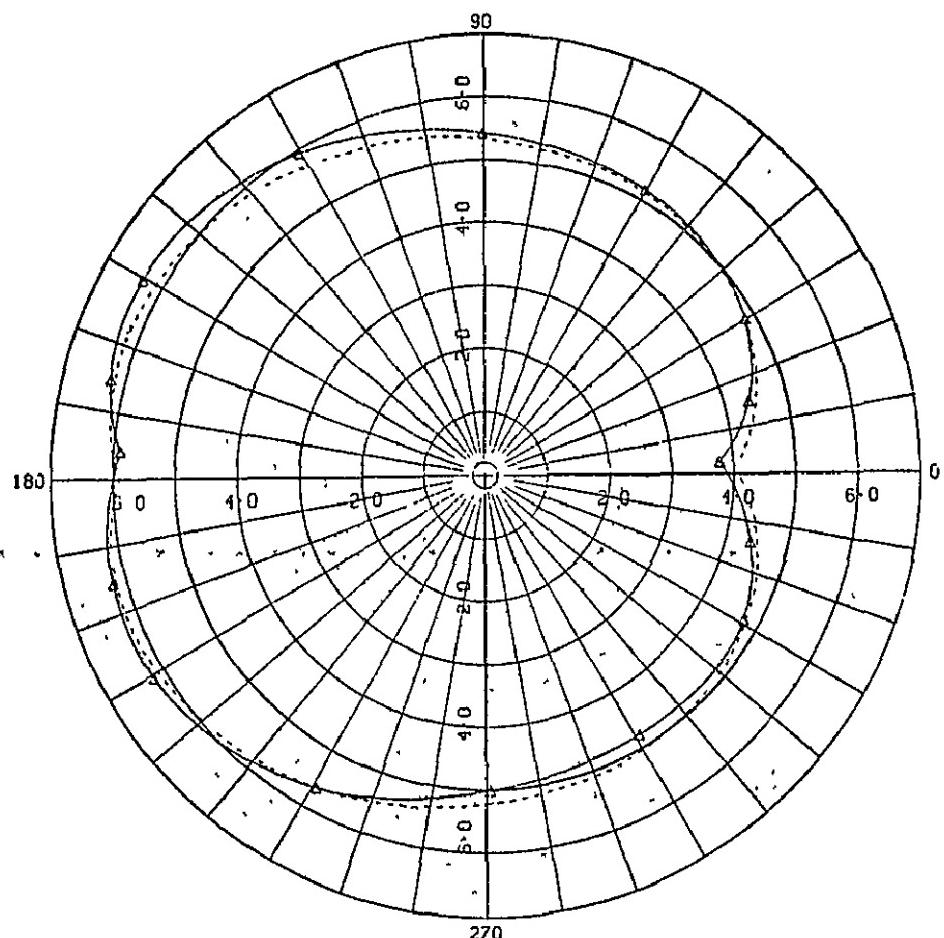
FIGURE VB-9
CSS PRESEPARATED RING DEFLECTION
HJT 1 STATION 2664 277 SEC.
MODEL - TEST COMPARISON



HJT 1 —
MODEL -----
(JB1121)

SCALE: 1 UNIT = 0.5 IN.

FIGURE VB-10
CSS PRESEPARATED RING DEFLECTION
HJT 2 STATION 2664 277 SEC.
MODEL - TEST COMPARISON



HJT 2 —
MODEL -----
(K492351)

SCALE: 1 UNIT = 0.5 IN.

V.C. CSS Thermal Stresses

George S. Sarvay

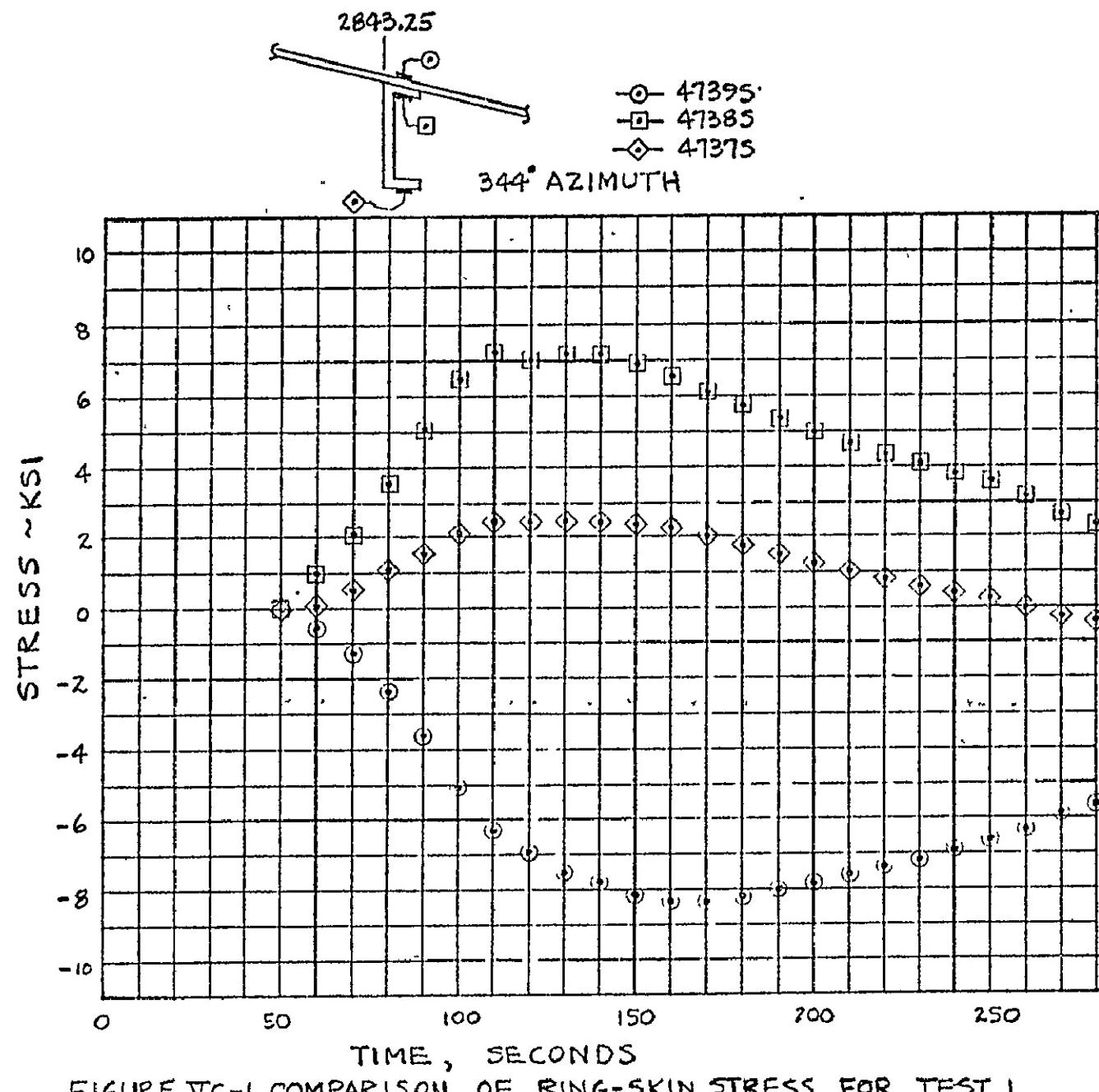
The CSS structure was subjected to temperatures during tests 1 and 2, which are equivalent to that sustained during flight ascent aerodynamic heating. Strain gages were installed on the cylindrical and nose cone shells and the nose cone rings in order to measure the thermal stress levels during heating.

Nose Cone Stresses

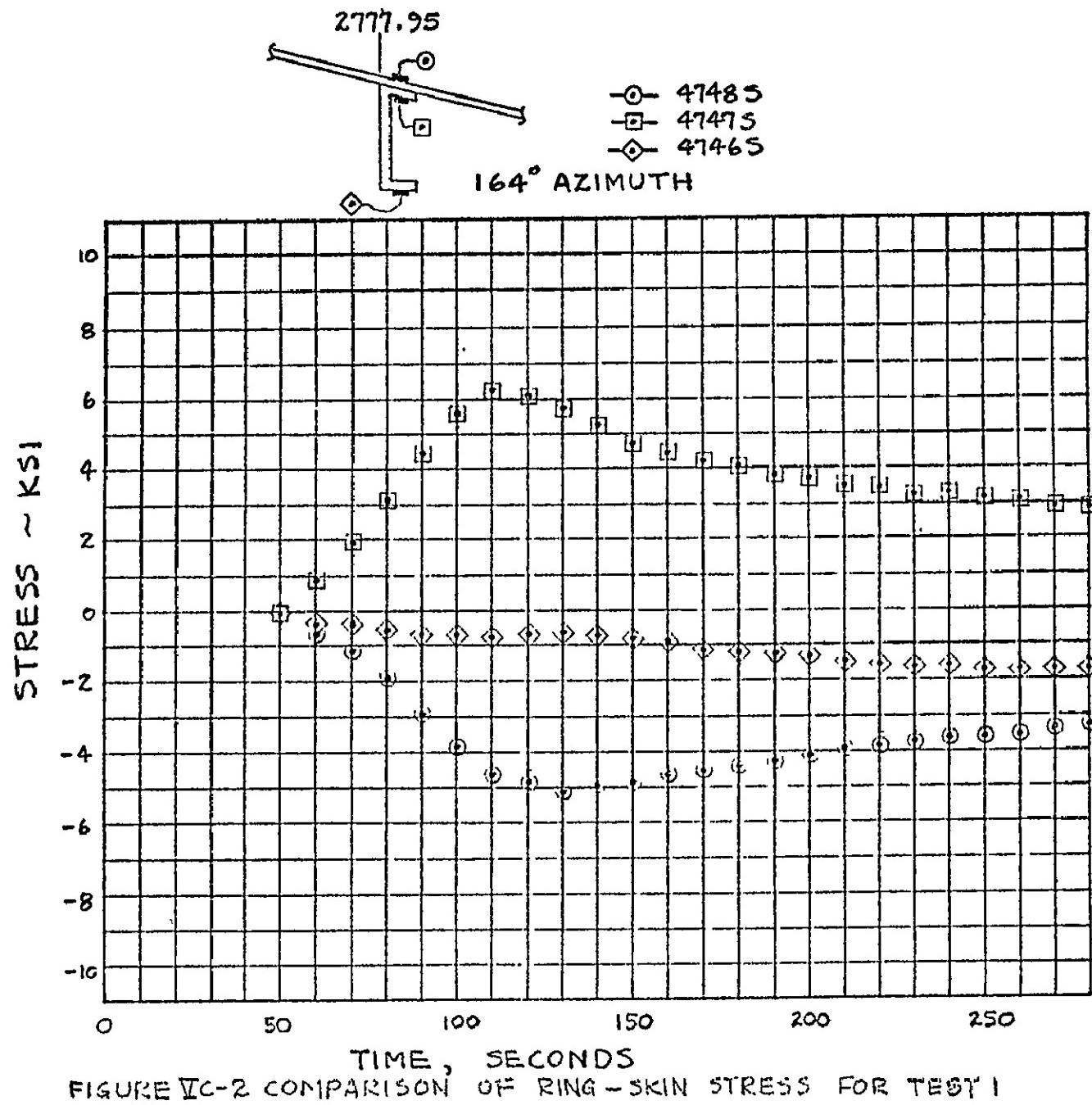
During external heating of the CSS, the shell becomes hotter than the support rings because of the radial temperature gradient in the structural rings. Figures VC-1 through VC-8 illustrate the results of the conical shell and ring stress levels versus time at two CSS stations and azimuths during the heating phase of tests 1 and 2. During the initial phase of heating (110 to 150 sec), the difference in radial expansion, due to thermal gradients at the shell and ring junction, results in high local bending meridional stresses in the shell as well as circumferential stresses on the inboard and outboard caps of the support rings. At the termination of the heating cycle, the stresses in the shells and rings are reduced because of the decreased thermal gradient between the rings and shells. The data show that the maximum stresses occur at the MTL (328° and 0°) and are reduced away from the maximum heated zone. The maximum measured stresses of 7600 psi tension and 8500 psi compressions are well below the yield or crippling allowables for the shell skin and support rings (See ref. 9).

Cylindrical Section Skin Stresses

The cylindrical section meridional stress levels for tests 1 and 2 are presented in figures VC-9 through VC-28. The data show that the maximum stresses were obtained at station 2536 during test 2. The maximum tensile stress of 10 617 psi occurred at approximately 74° azimuth and is well below the yield allowable for the aluminum material. The maximum compressive stress of 7562 psi located at the 164° azimuth is well within the compressive allowable of 19 778 psi (See ref. 9).



REPRODUCIBILITY OF THE
ORIGINAL PAGE IS POOR



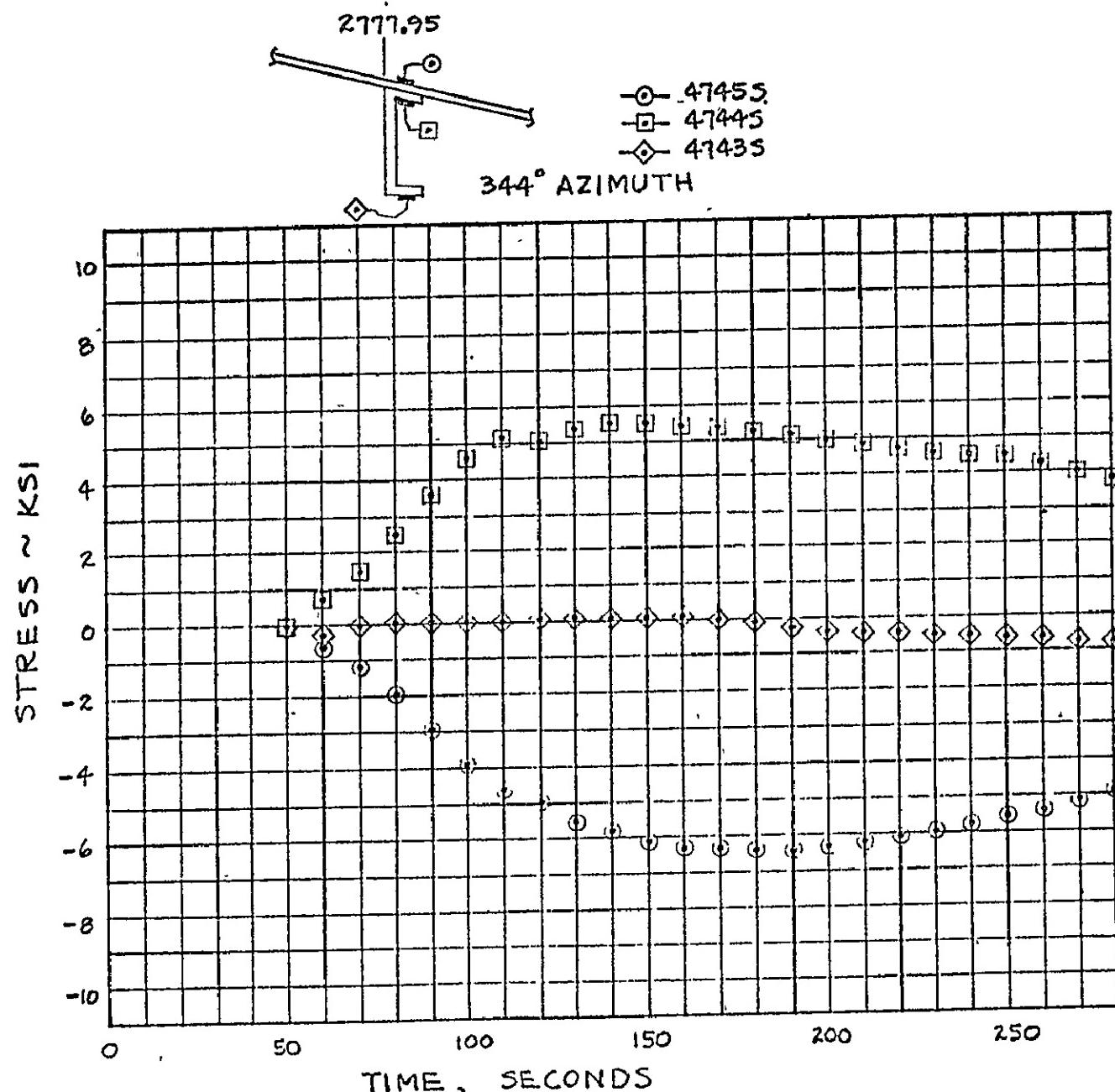


FIGURE IV-C-3 COMPARISON OF RING-SKIN STRESS FOR TEST 1

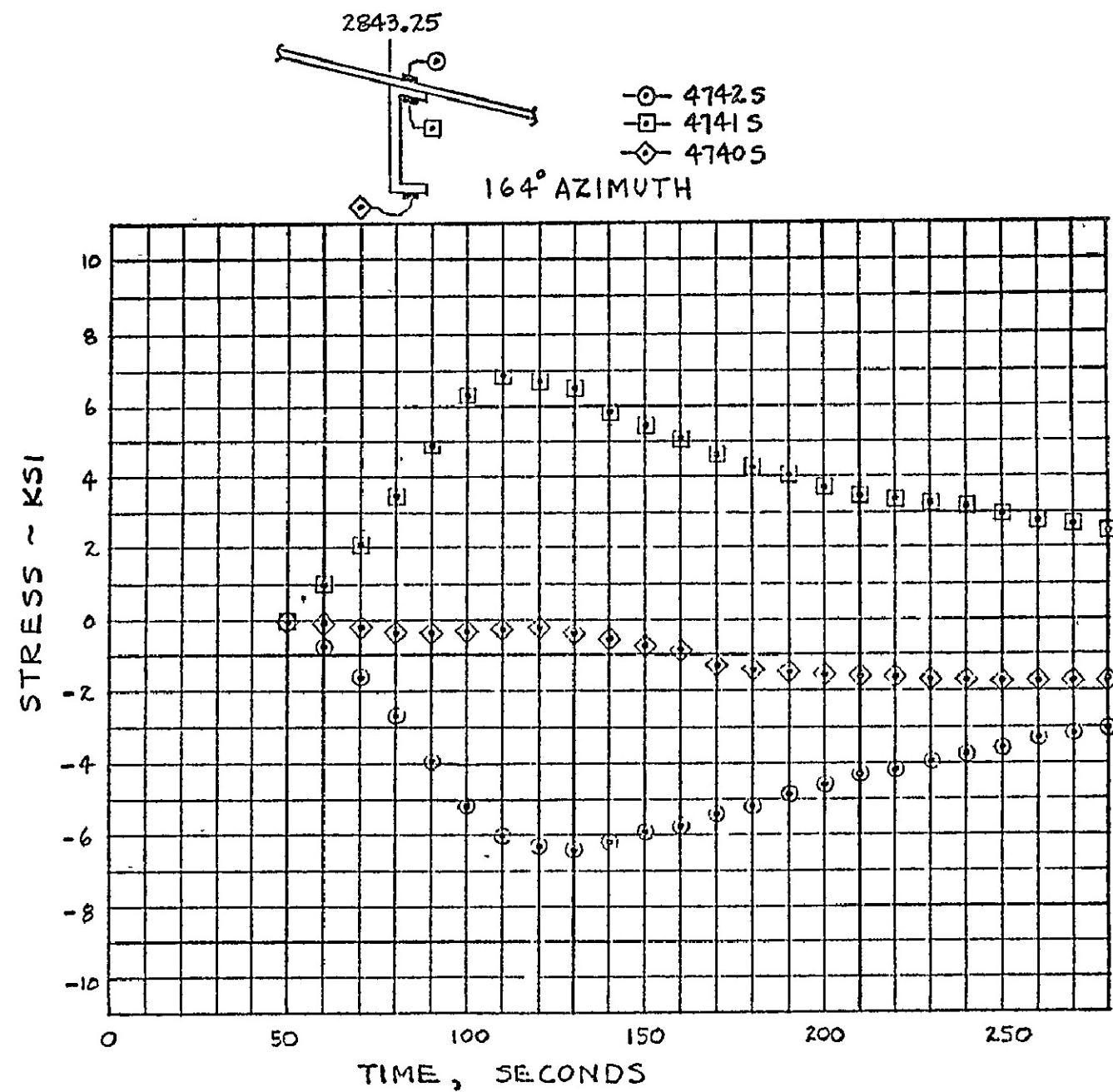


FIGURE II-C-4 COMPARISON OF RING-SKIN STAGES FOR TEST I

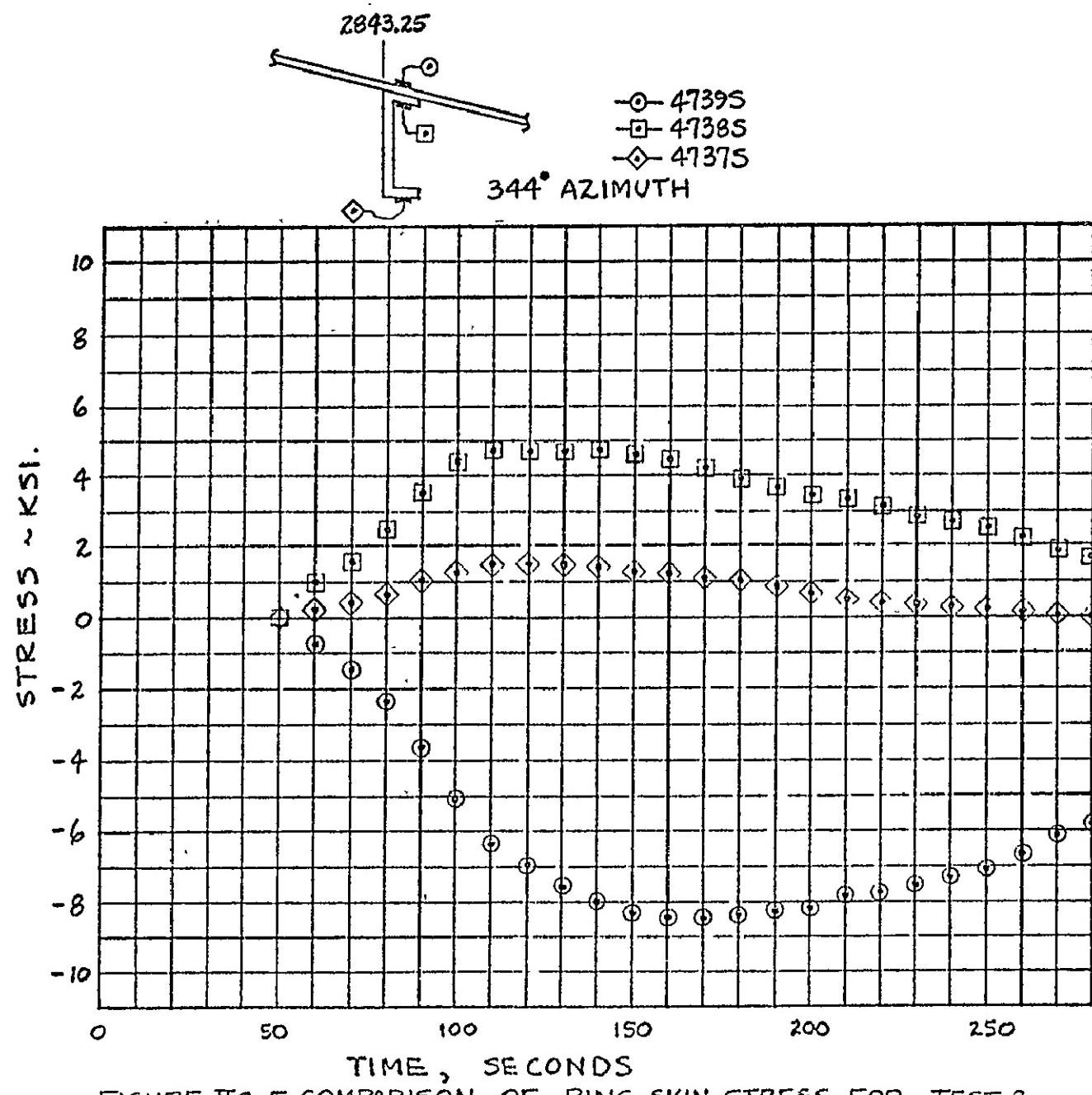


FIGURE IC-5 COMPARISON OF RING-SKIN STRESS FOR TEST 2

REPRODUCIBILITY OF THE
ORIGINAL PAGE IS POOR

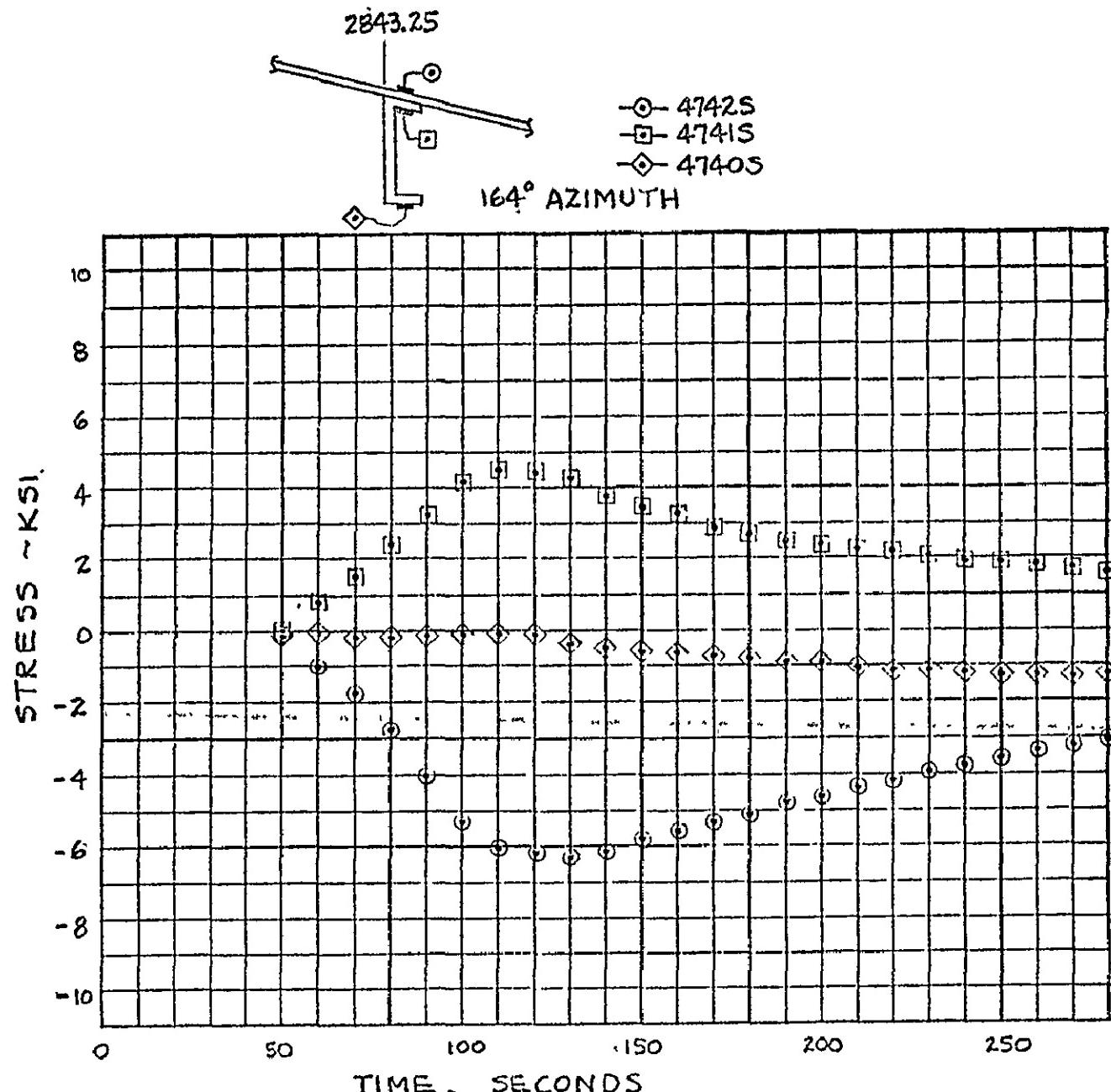


FIGURE VI-C-6 COMPARISON OF RING-SKIN STRESS FOR TEST Z

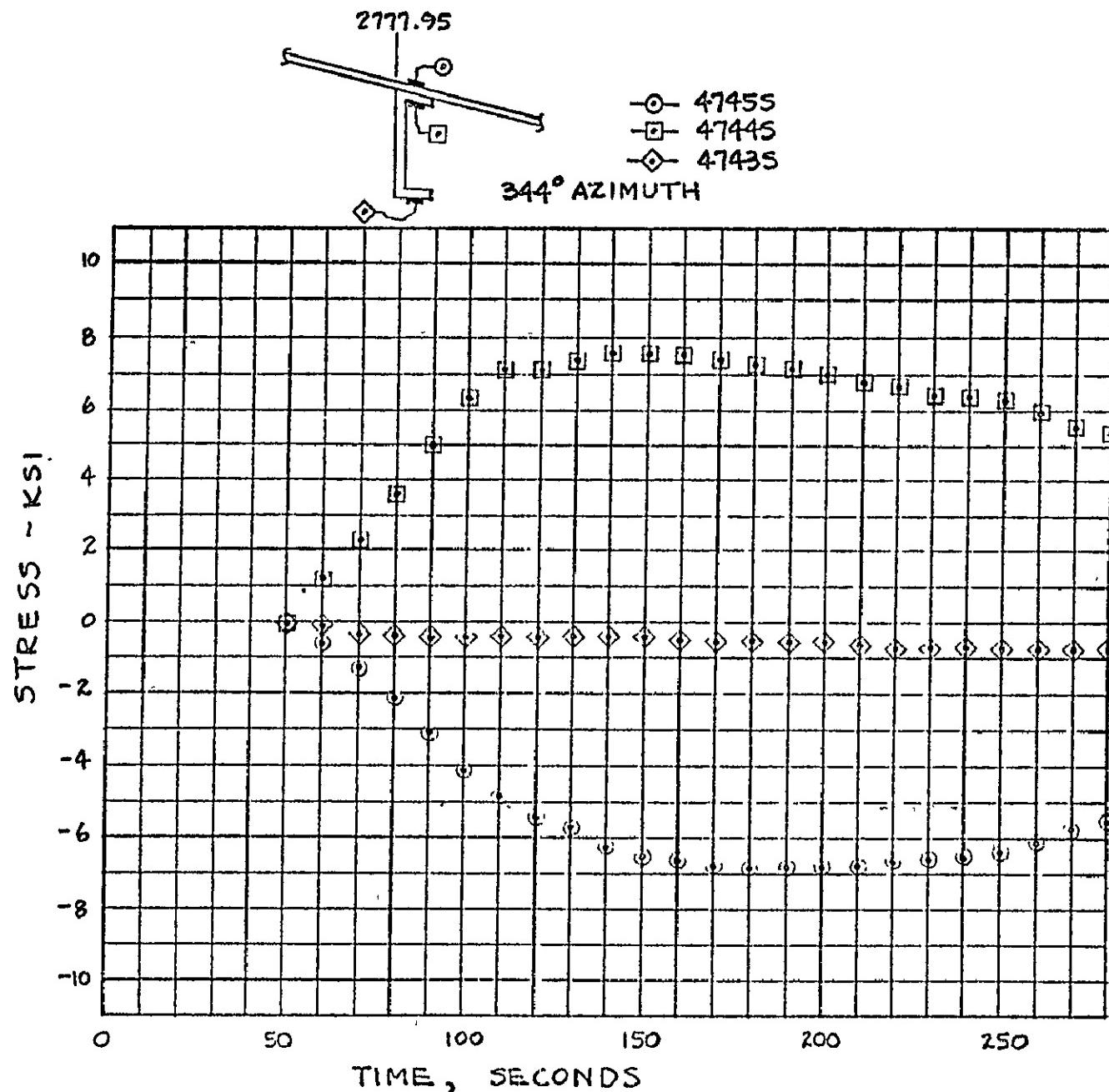


FIGURE VJC-7 COMPARISON OF RING-SKIN STRESS FOR TEST 2

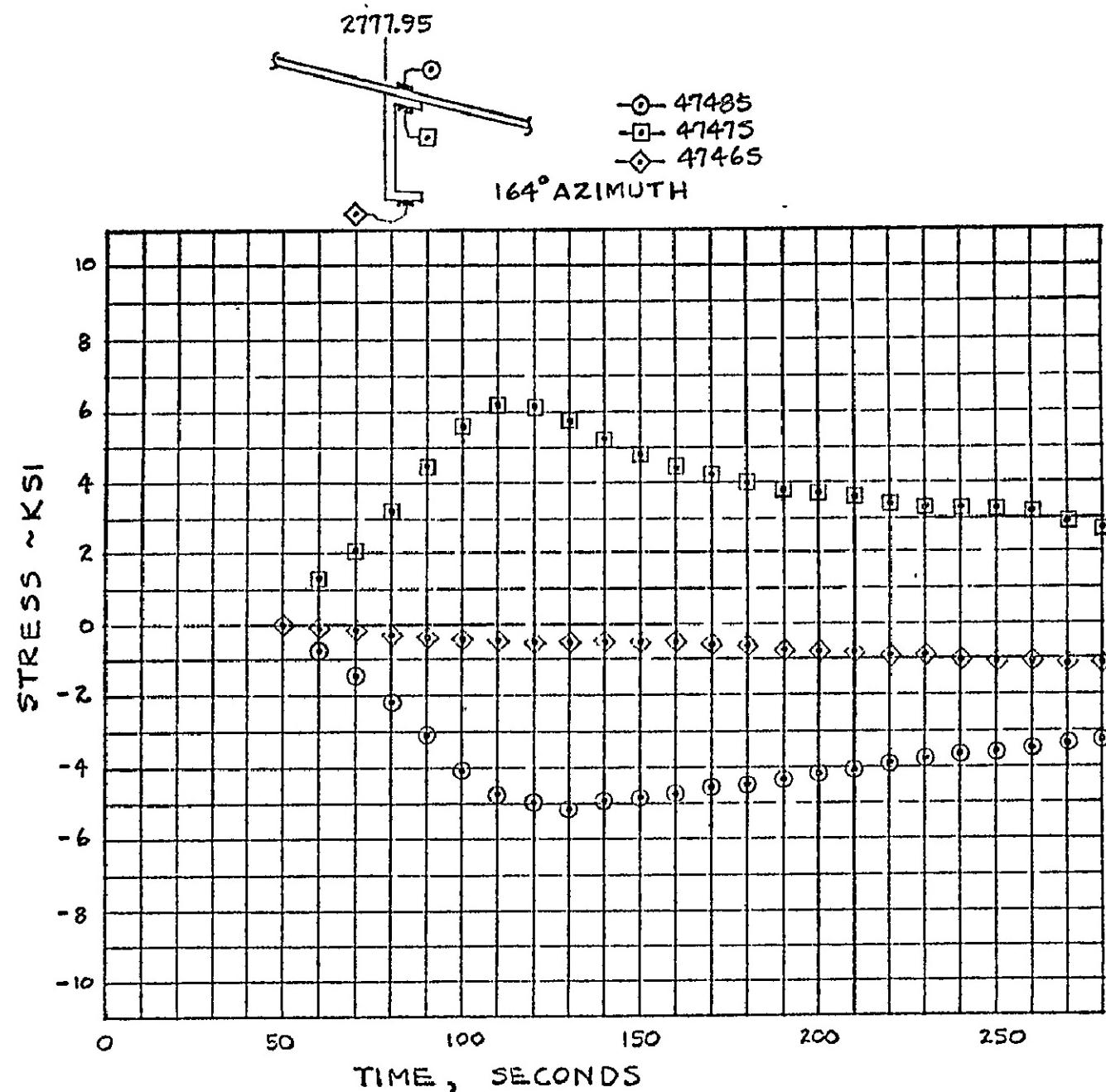


FIGURE IC-8 COMPARISON OF RING-SKIN STRESS FOR TEST 2

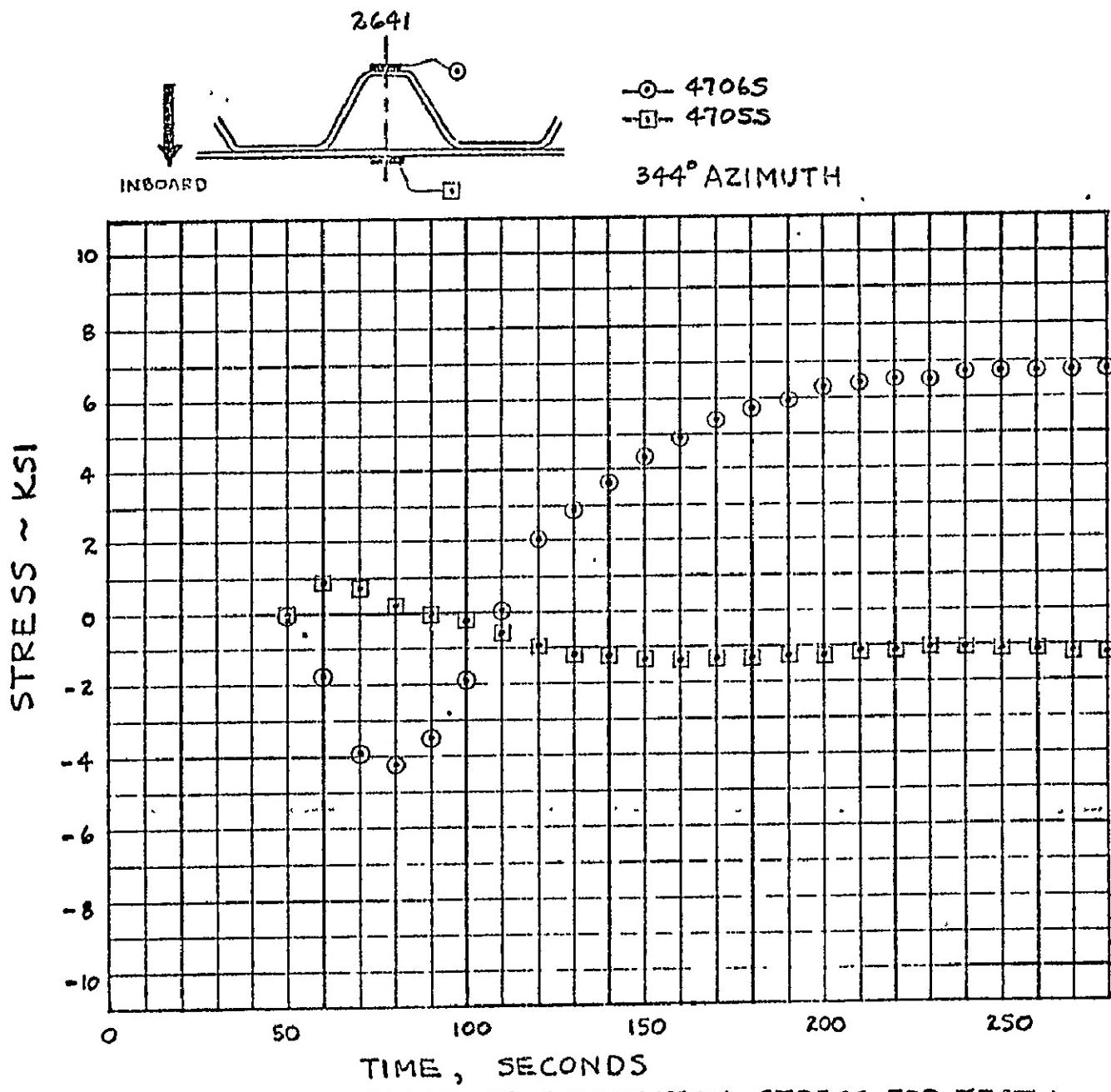


FIGURE VII-C-9 COMPARISON OF CORRUGATION STRESS FOR TEST I

7L

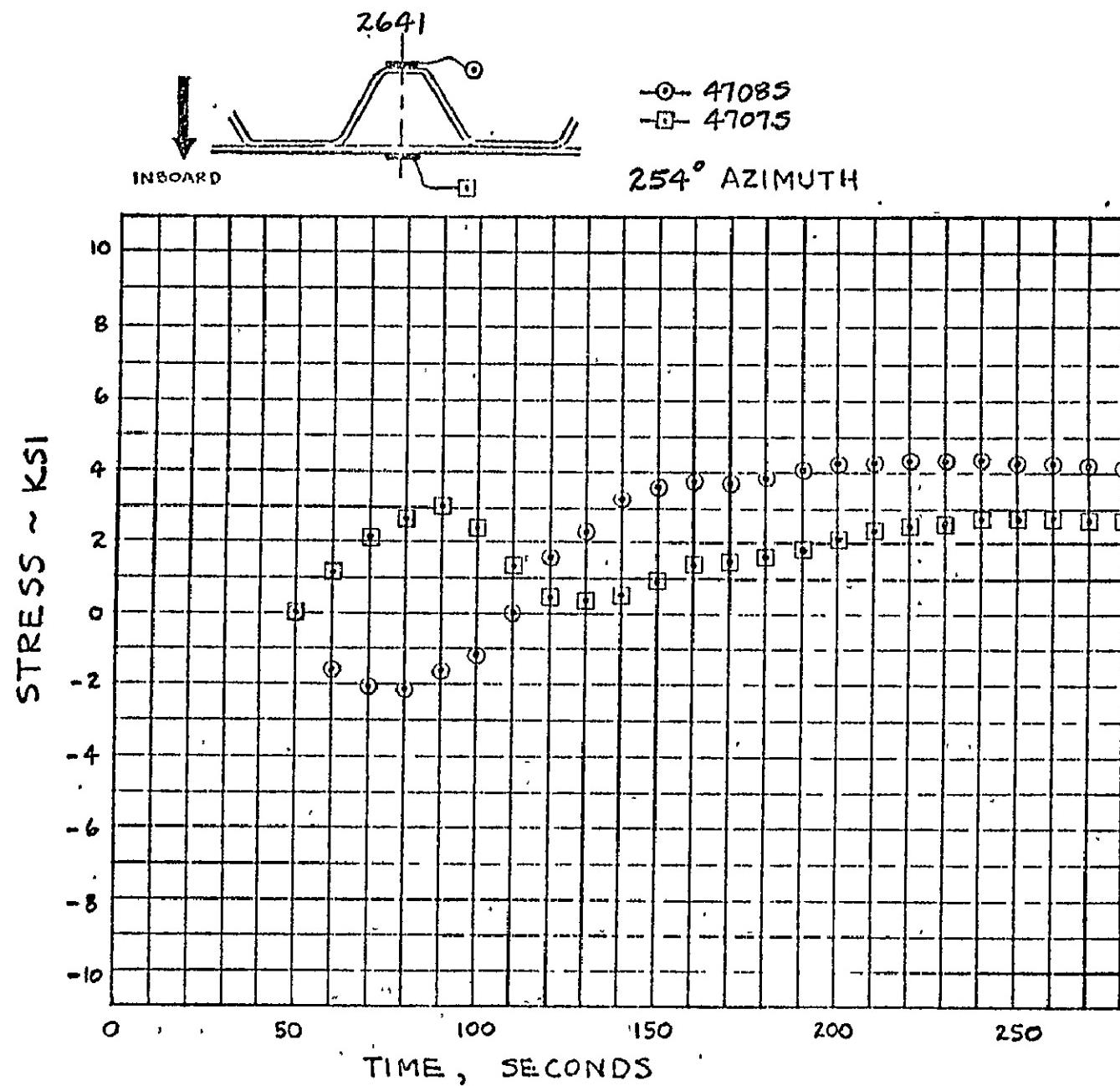


FIGURE IC-10 COMPARISON OF CORRUGATION STRESS FOR TEST I

57

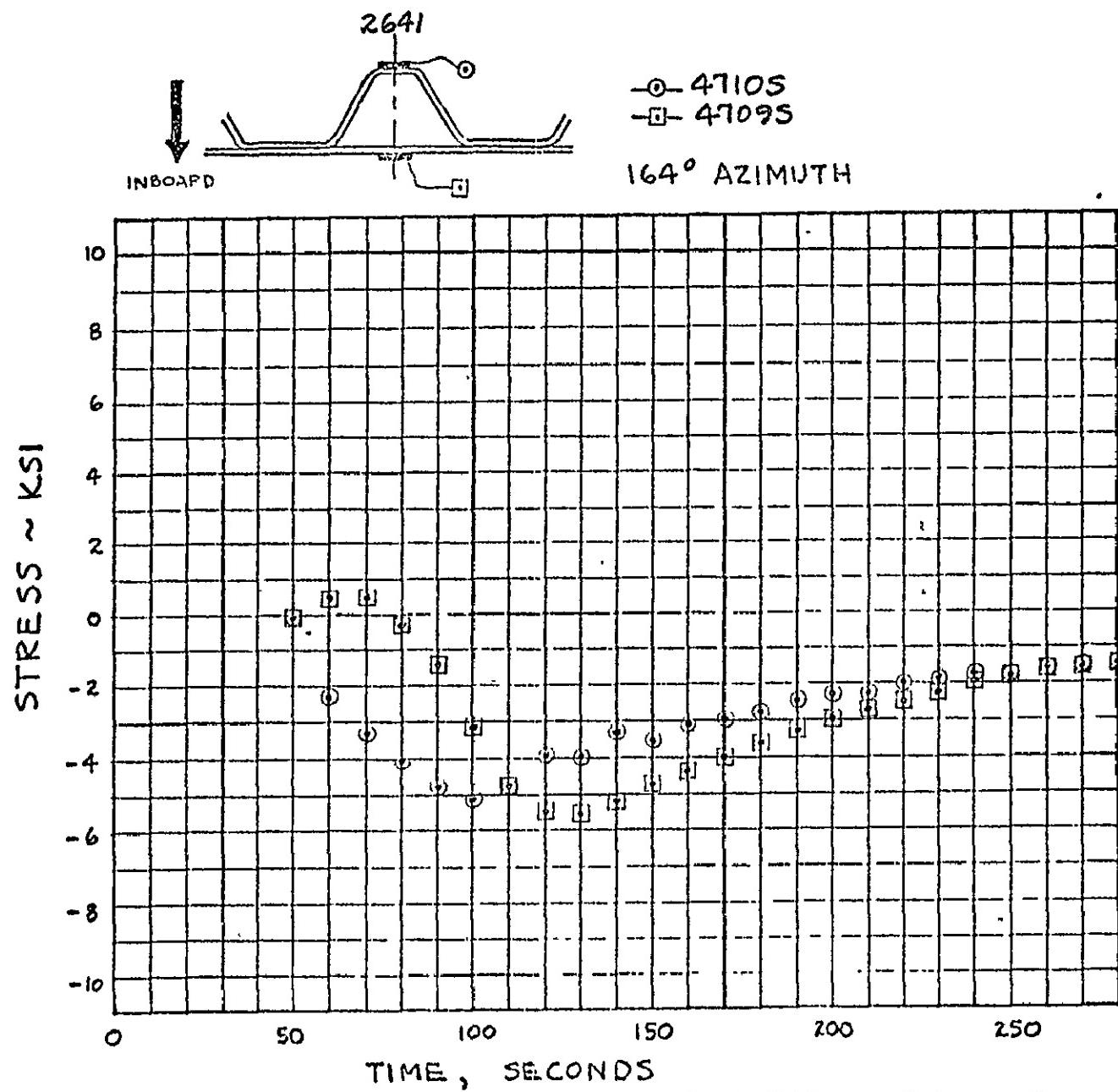


FIGURE IV-C-11 COMPARISON OF CORRUGATION STRESS FOR TEST I

REPRODUCIBILITY OF THE
ORIGINAL PAGE IS POOR

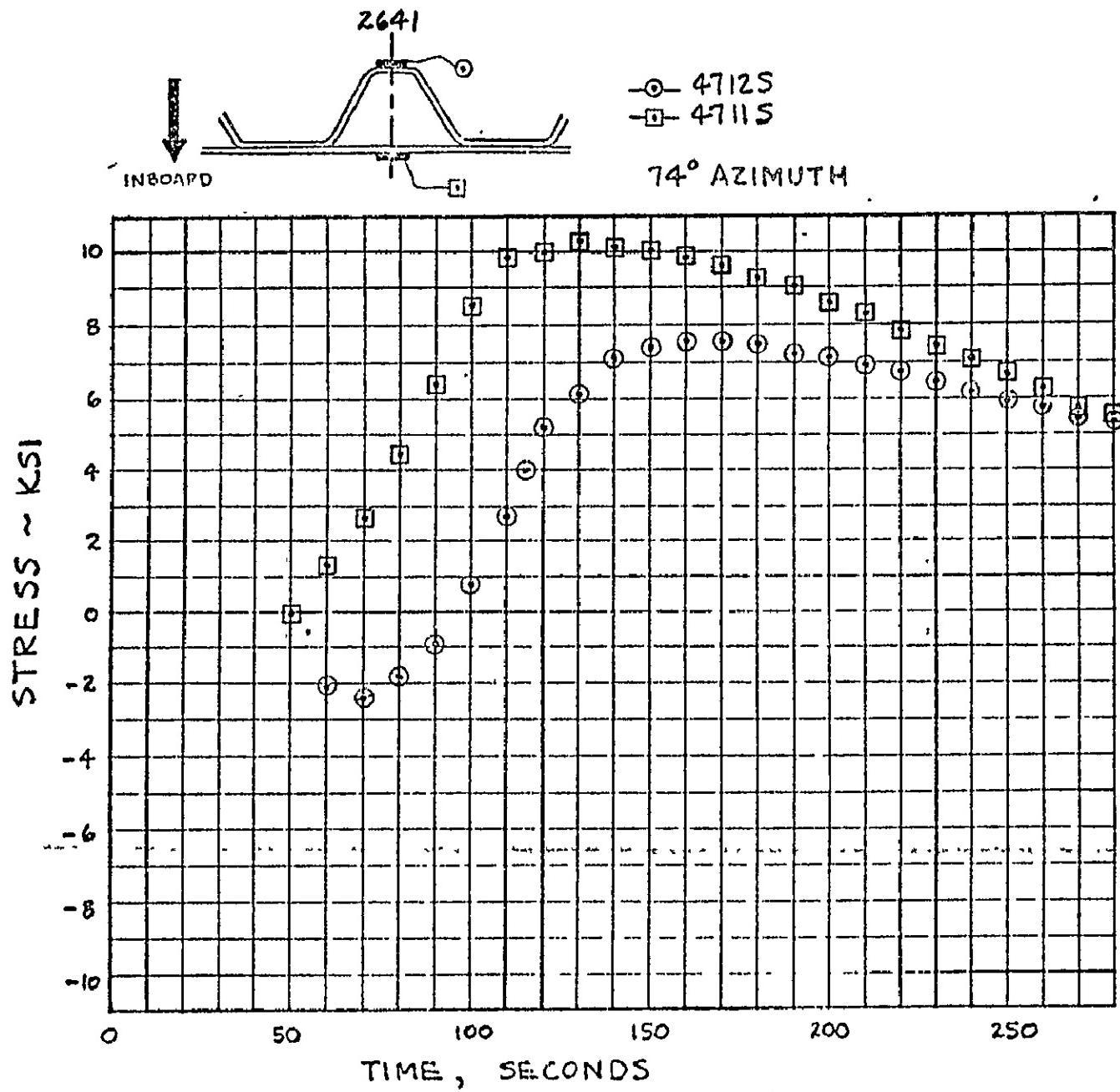


FIGURE IC-12 COMPARISON OF CORRUGATION STRESS FOR TEST 1

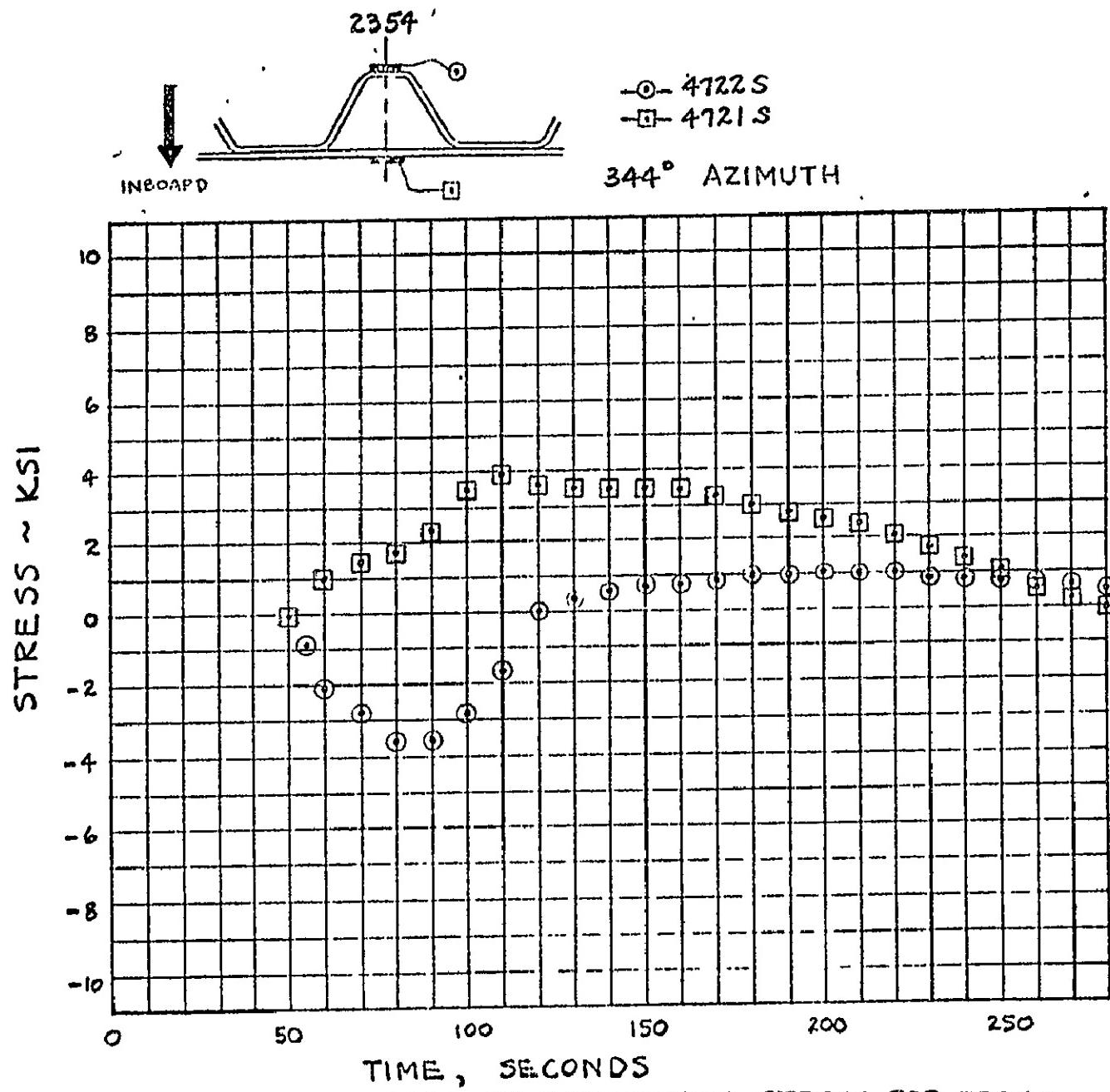


FIGURE IC-13 COMPARISON OF CORRUGATION STRESS FOR TEST I

8L

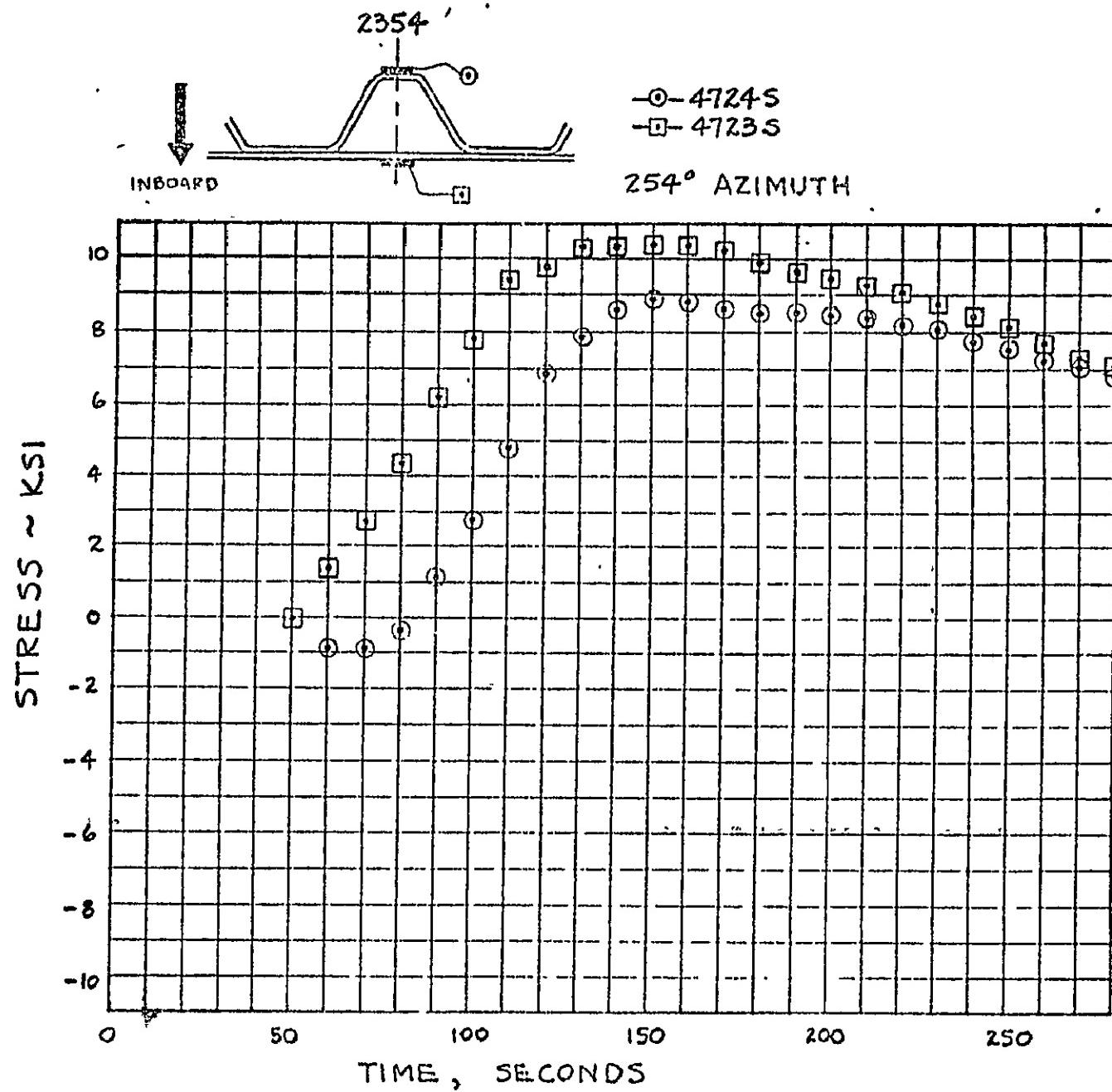


FIGURE VI-C-14 COMPARISON OF CORRUGATION STRESS FOR TEST 1

6L

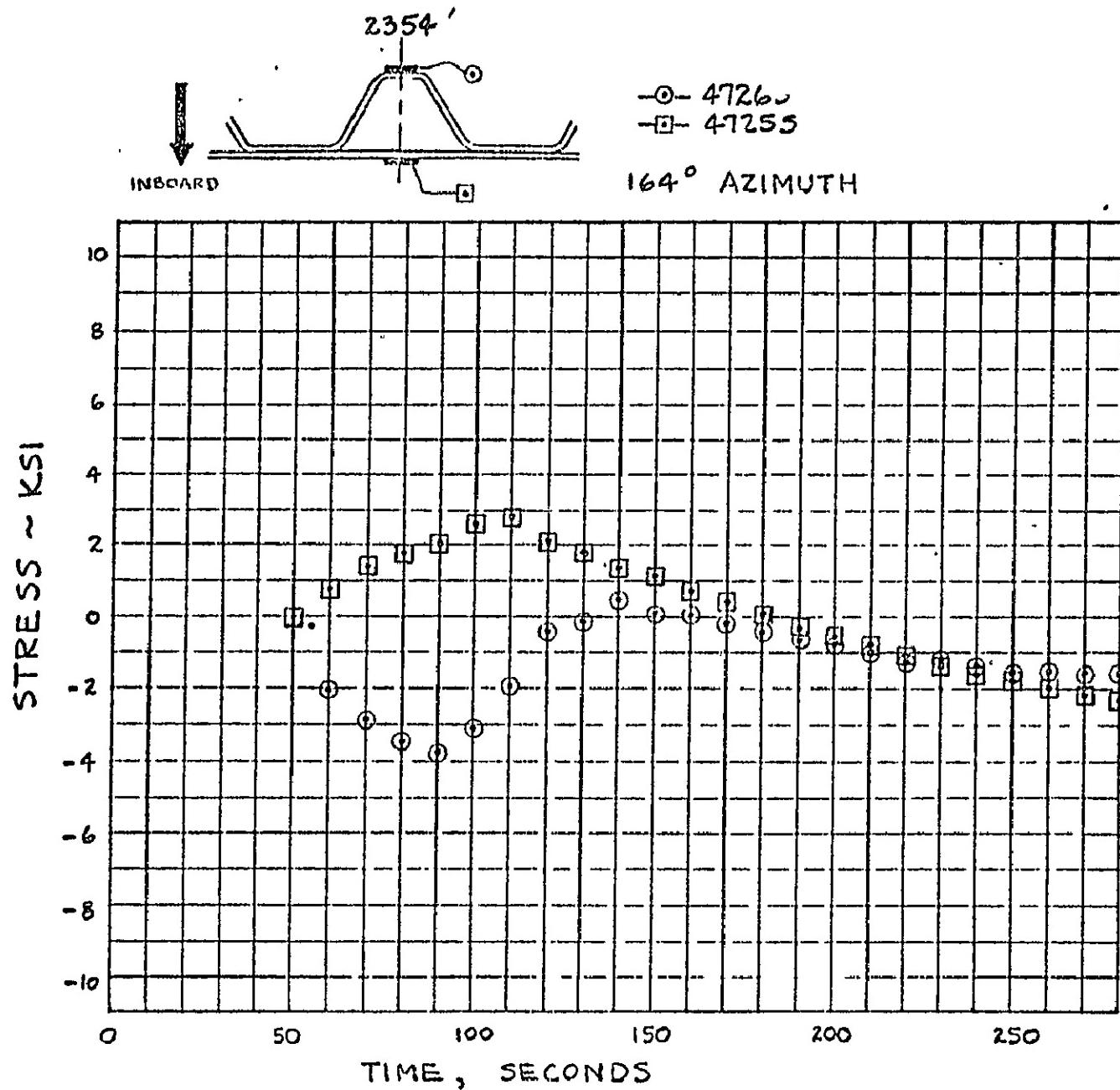


FIGURE VC-15 COMPARISON OF CORRUGATION STRESS FOR TEST 1

08

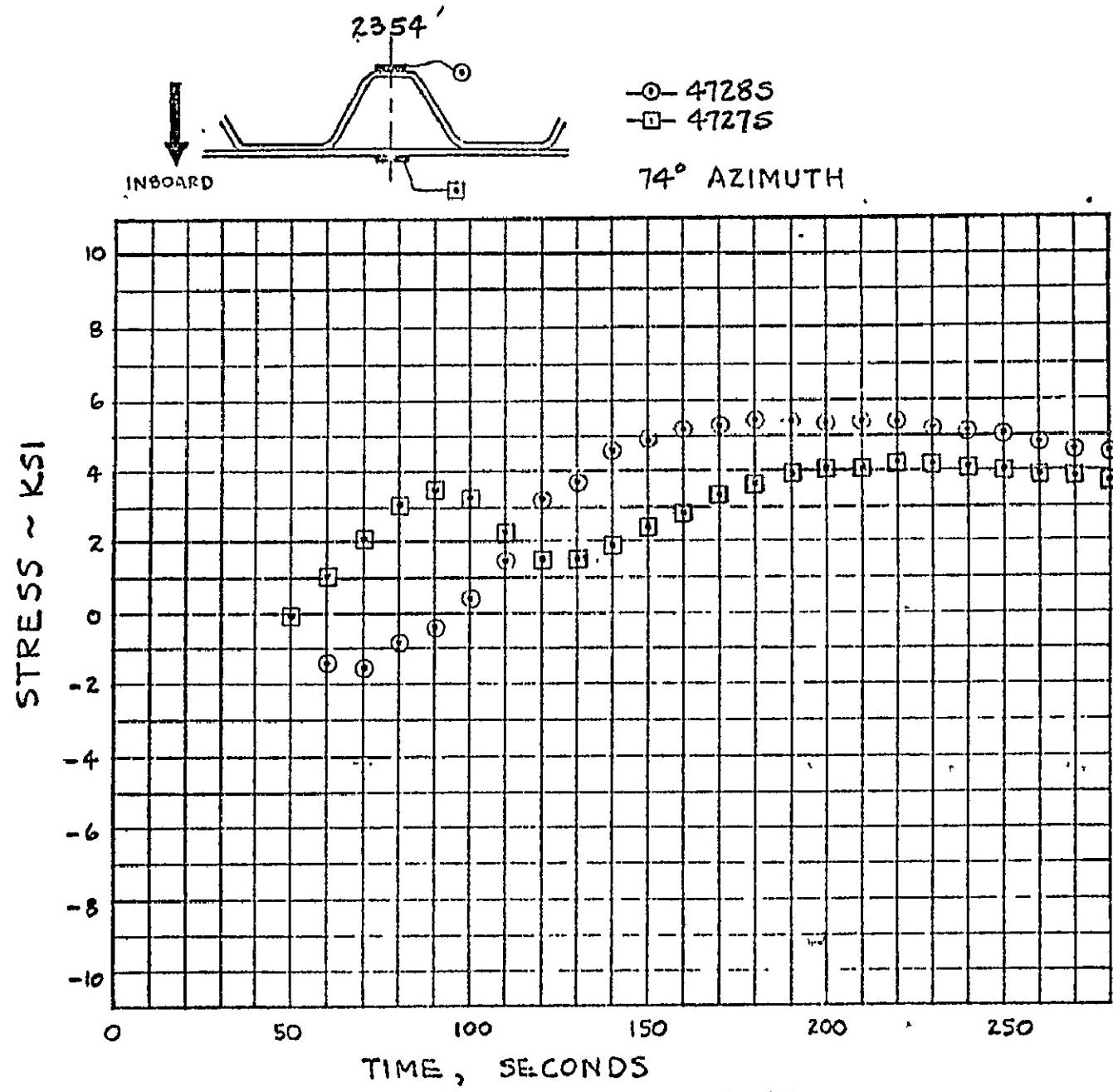


FIGURE IC-16 COMPARISON OF CORRUGATION STRESS FOR TEST 1

18

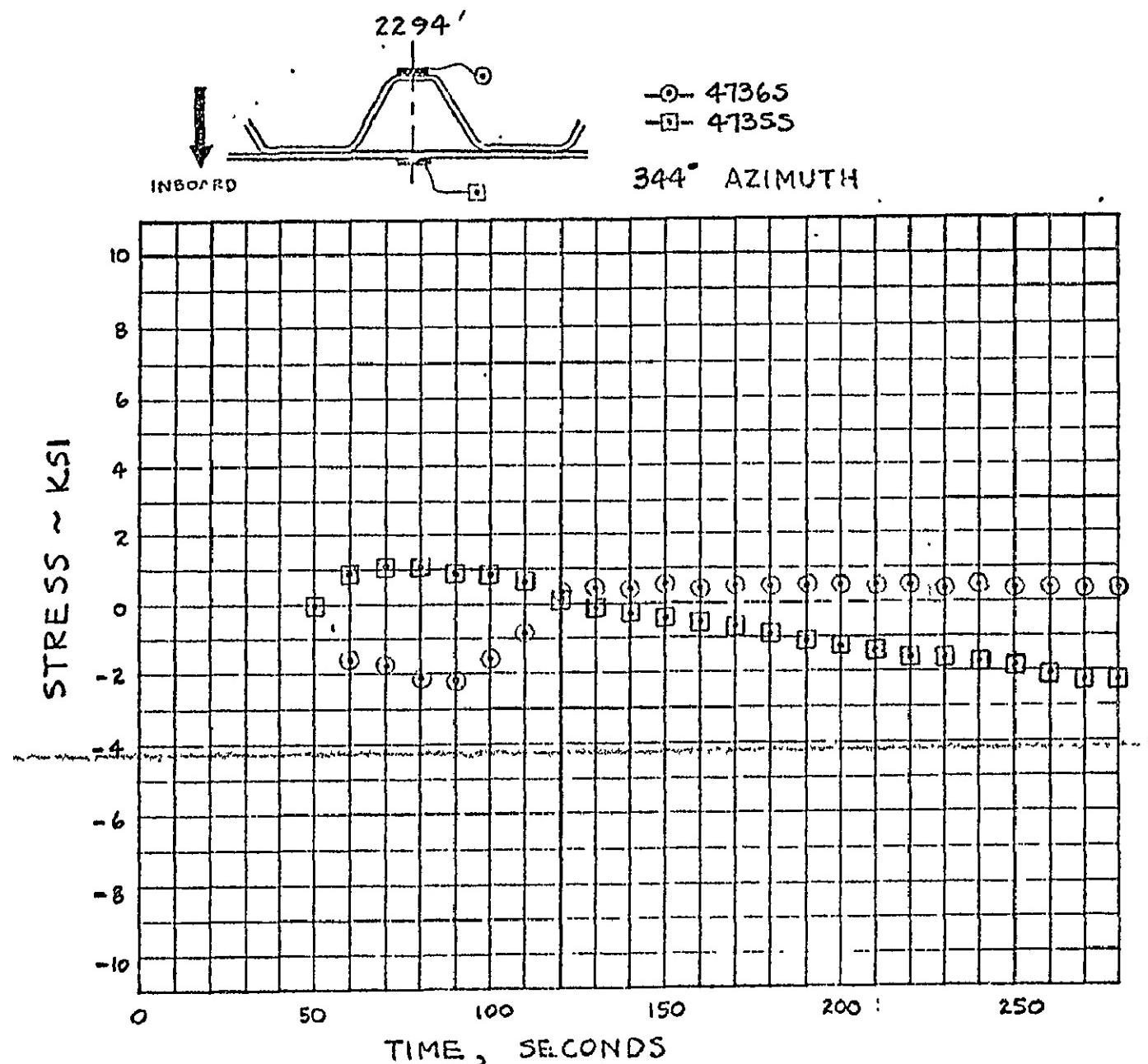


FIGURE VI-C-17 COMPARISON OF CORRUGATION STRESS FOR TEST I

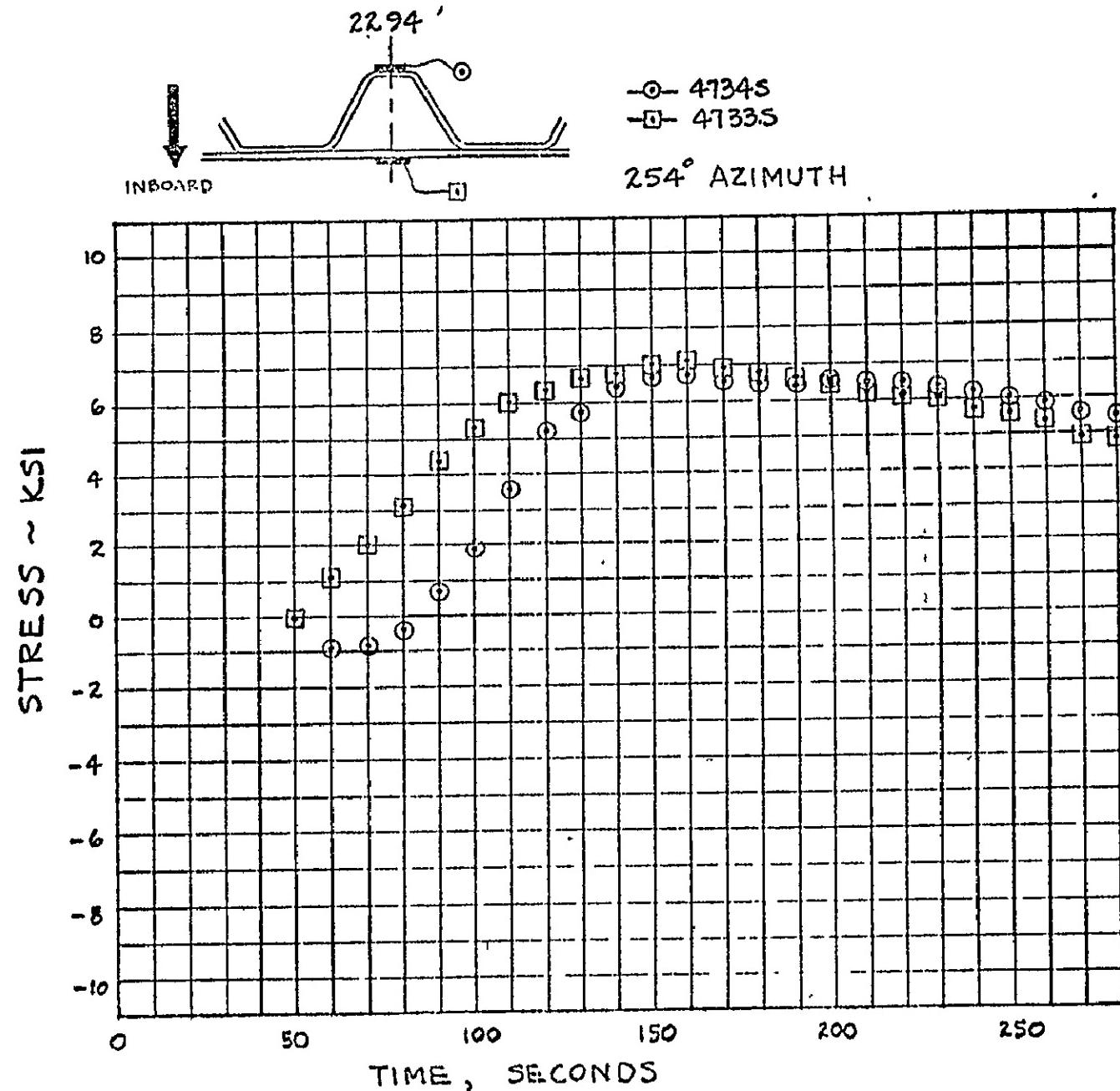


FIGURE IC-18 COMPARISON OF CORRUGATION STRESS FOR TEST 1

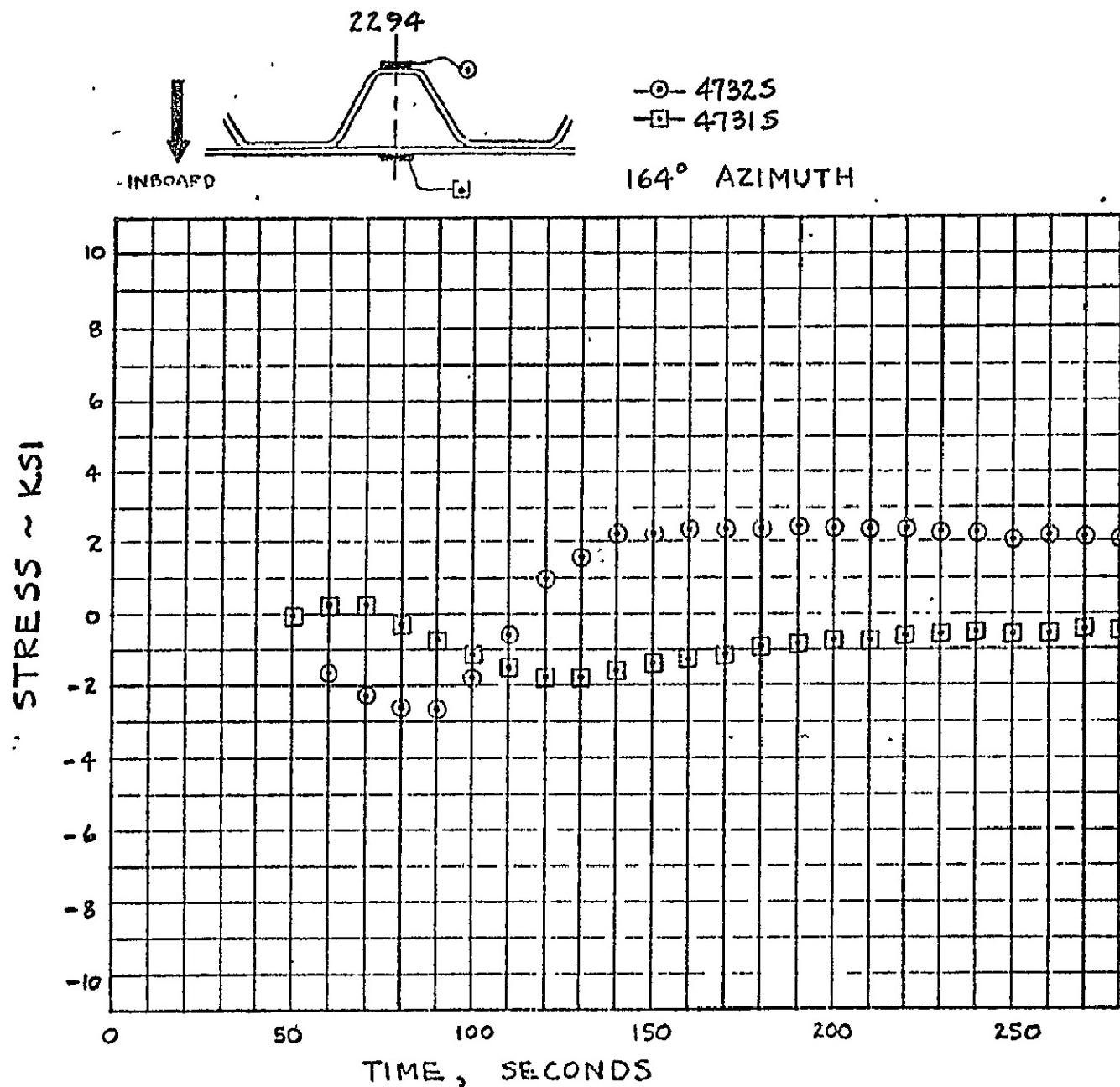


FIGURE VI-C-19 COMPARISON OF CORRUGATION STRESS FOR TEST 1

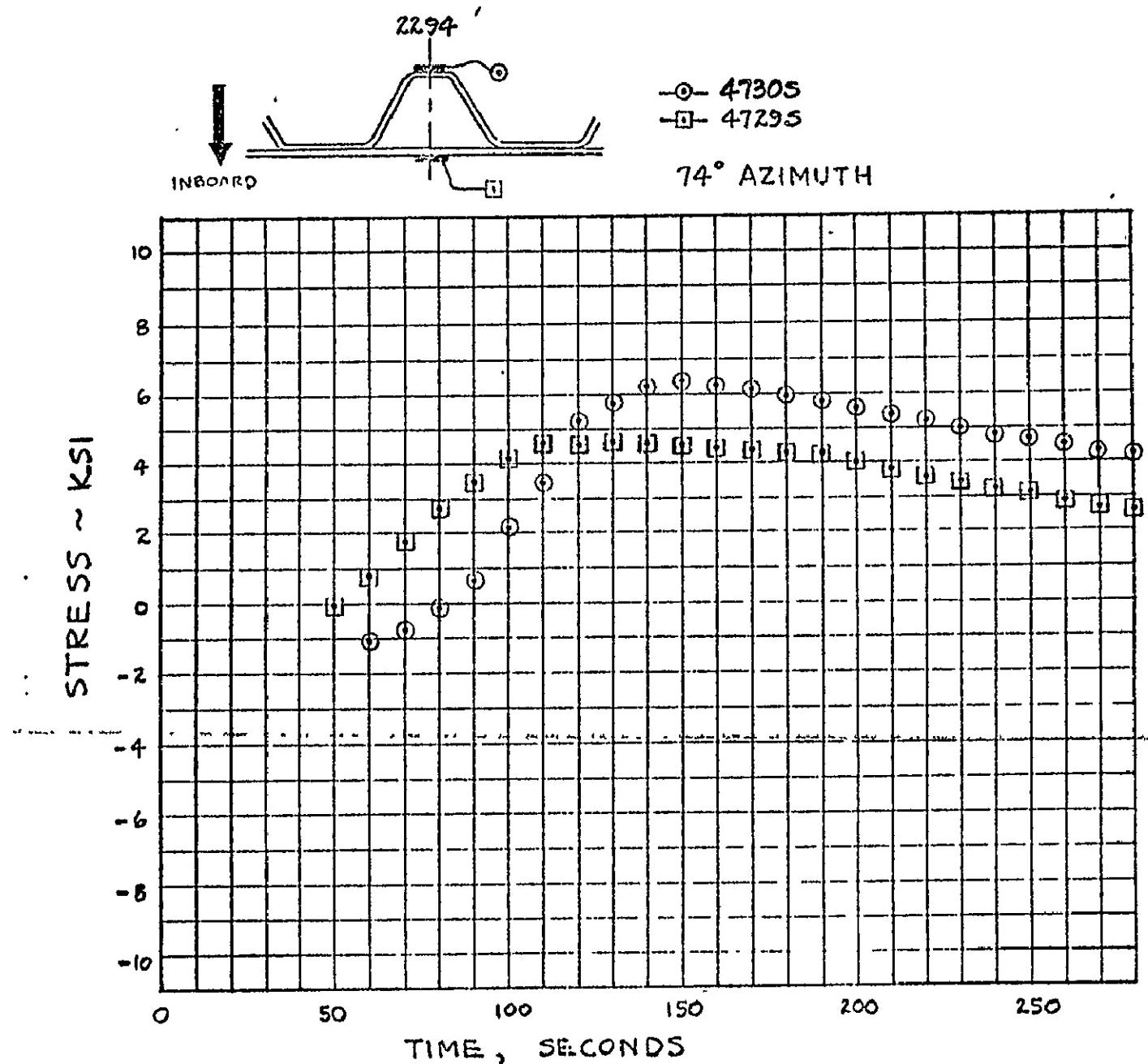


FIGURE V-C-20 COMPARISON OF CORRUGATION STRESS FOR TEST 1

REPRODUCIBILITY OF THE
ORIGINAL PAGE IS POOR.

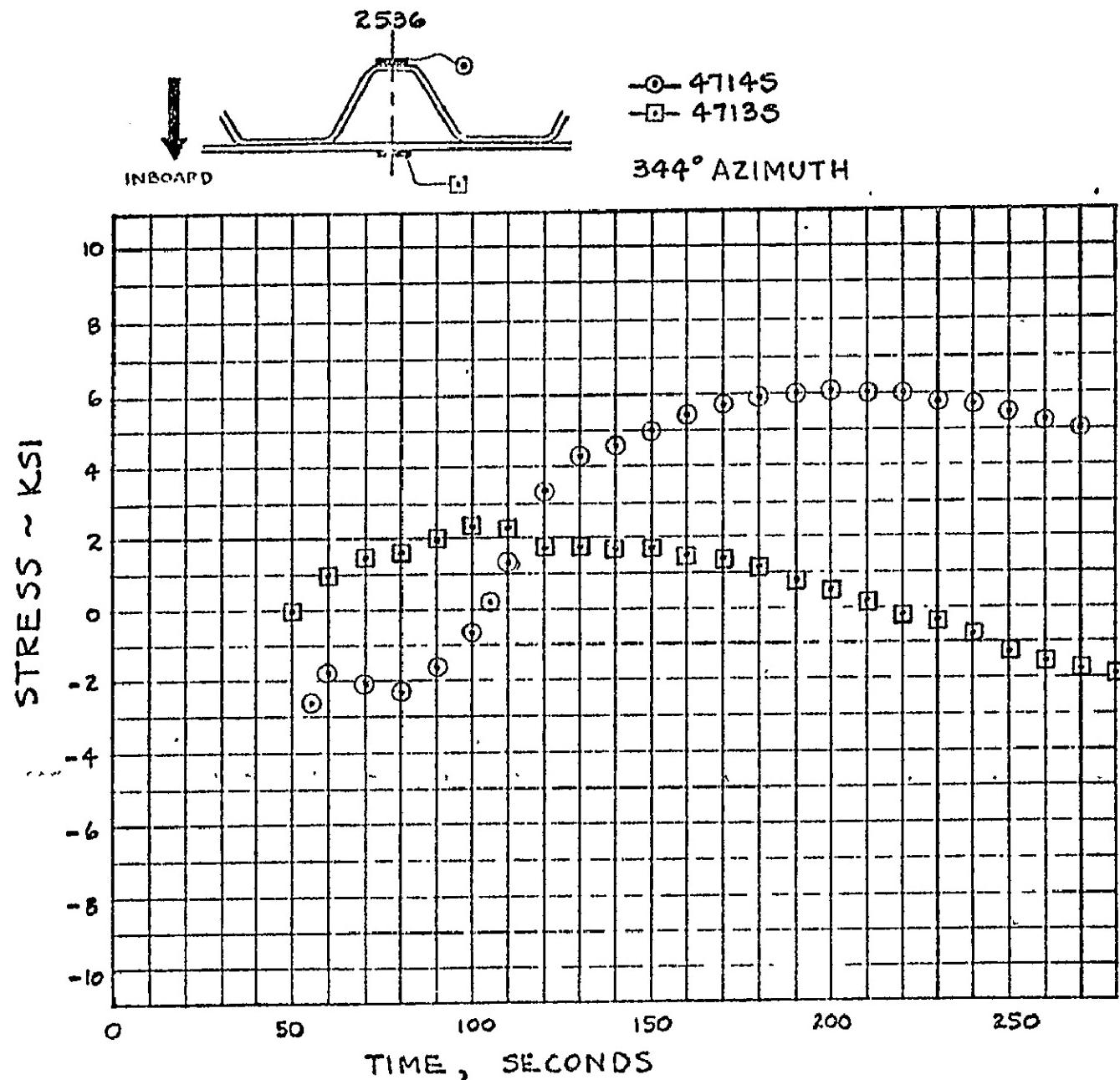


FIGURE IV-C-21 COMPARISON OF CORRUGATION STRESS FOR TEST 2

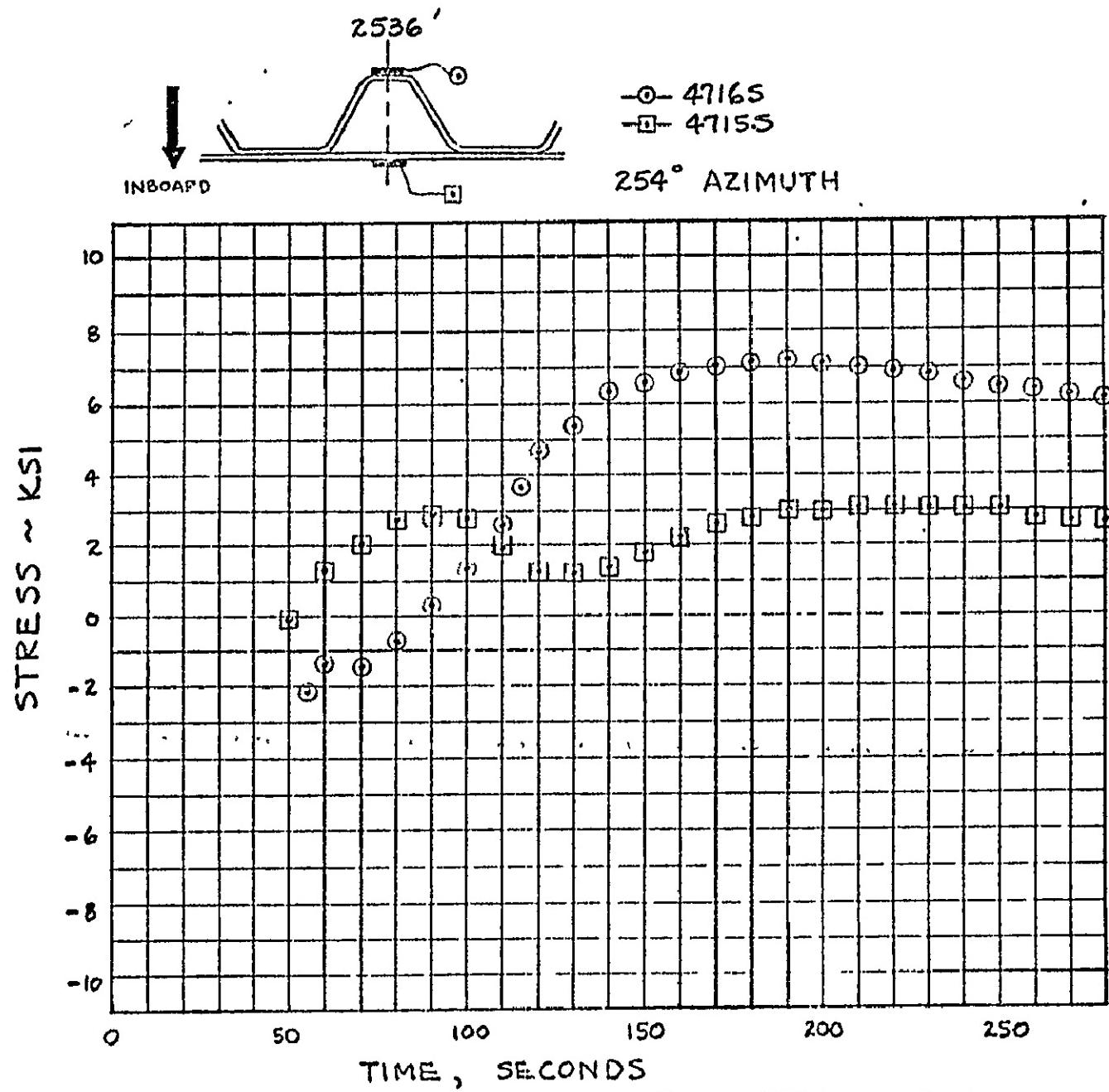


FIGURE VC-22 COMPARISON OF CORRUGATION STRESS FOR TEST 2

L8

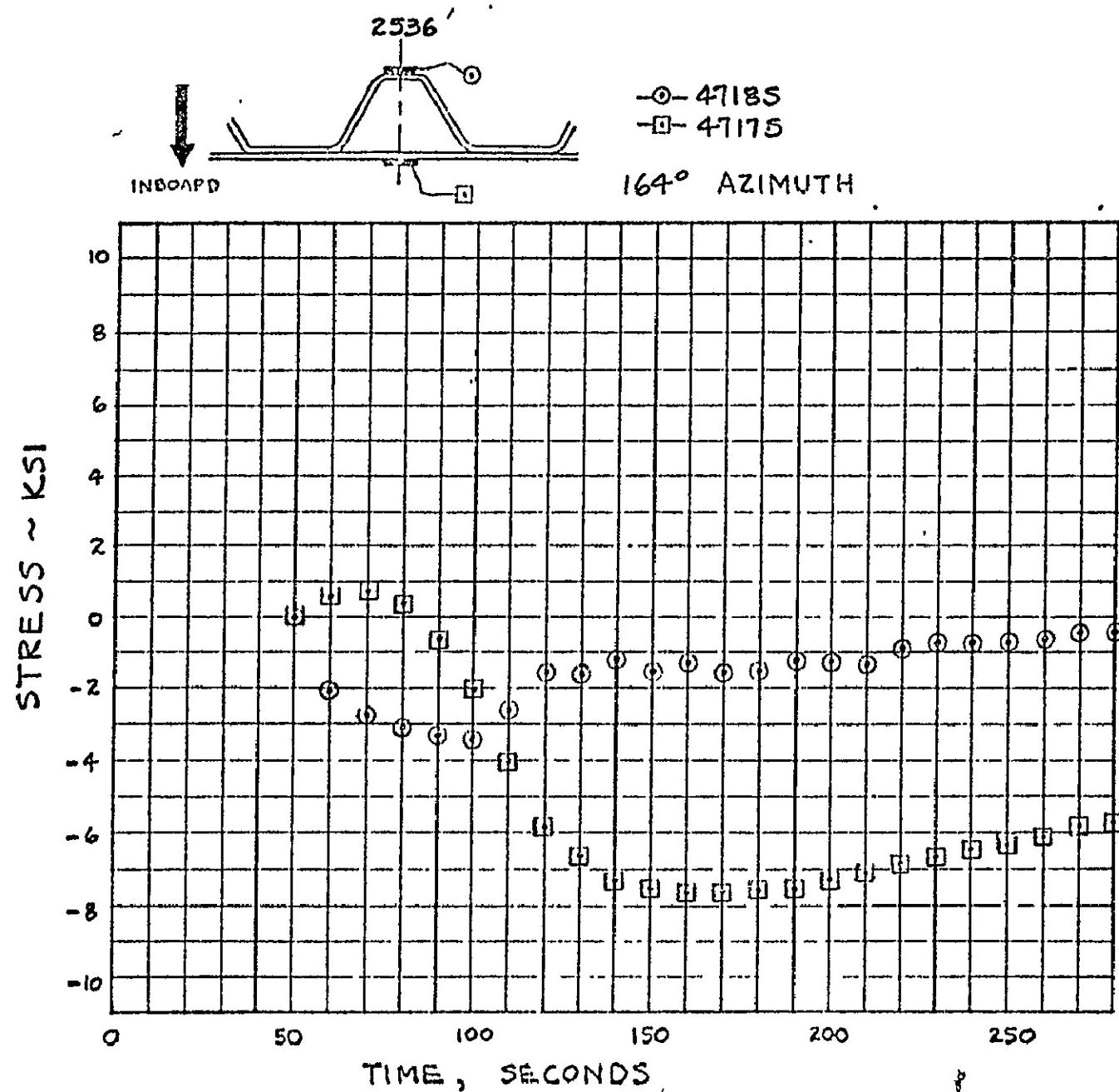


FIGURE IC-23 COMPARISON OF CORRUGATION STRESS FOR TEST 2

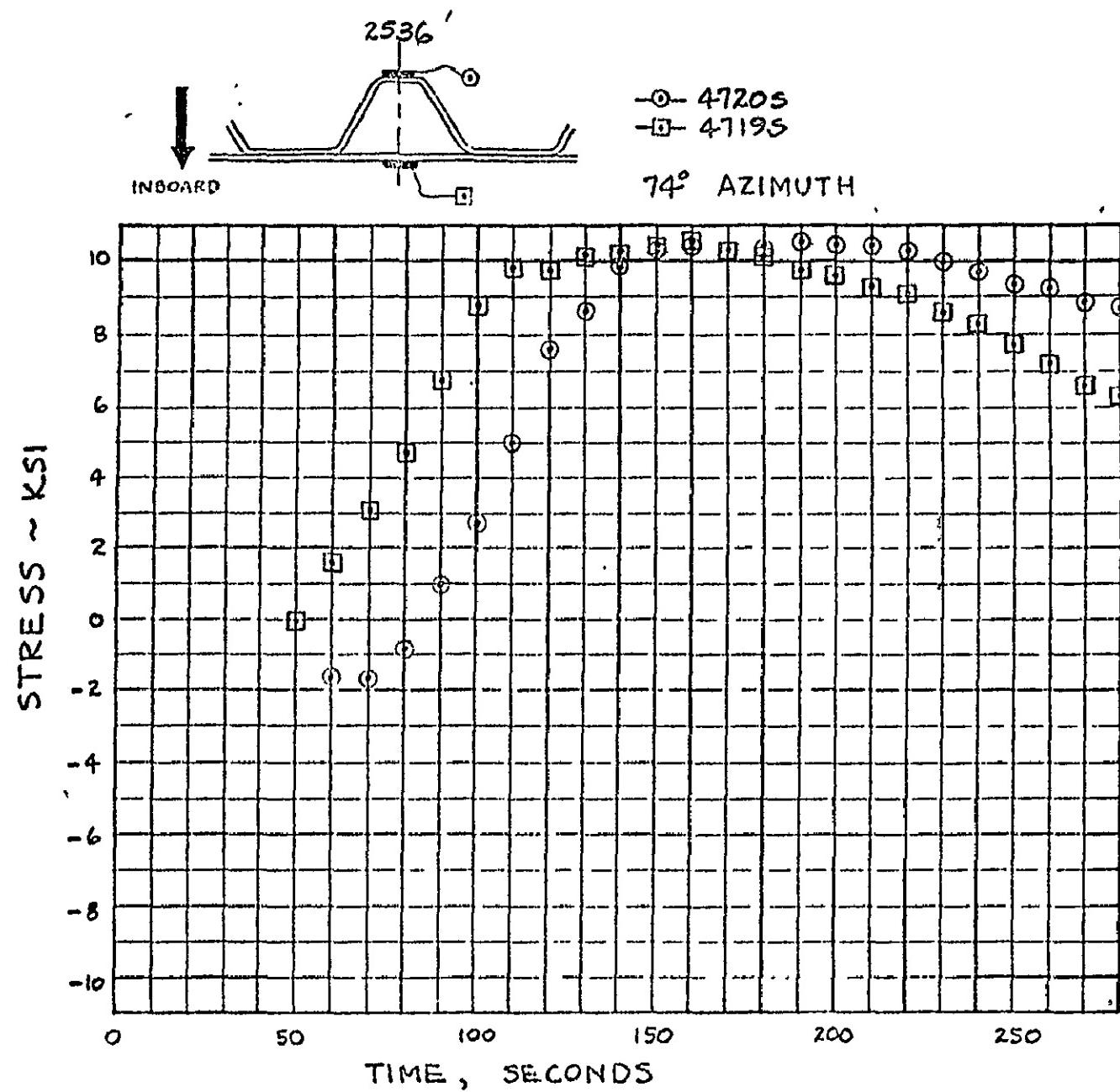


FIGURE IC-24 COMPARISON OF CORRUGATION STRESS FOR TEST 2

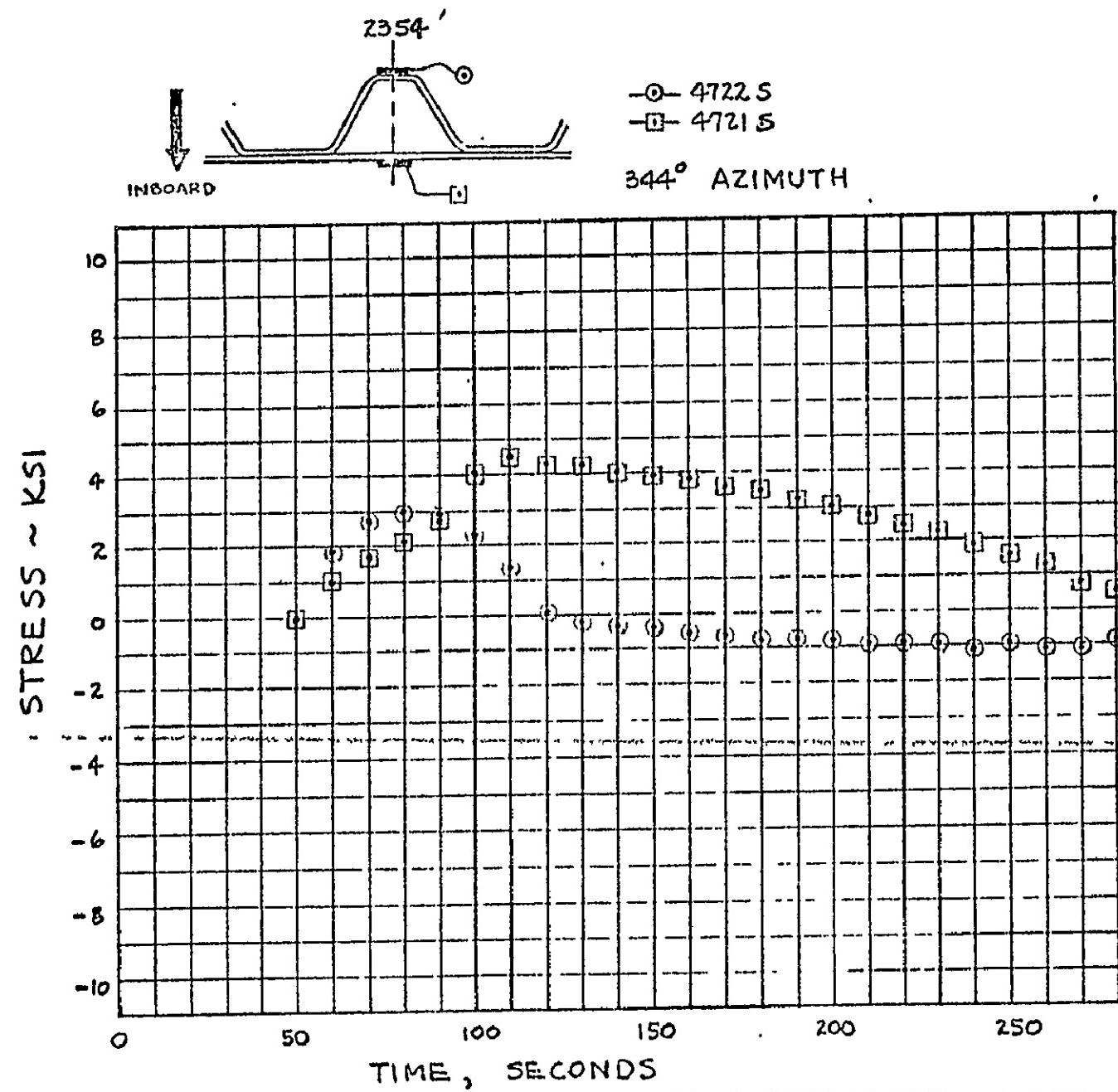


FIGURE TC-25 COMPARISON OF CORRUGATION STRESS FOR TEST 2

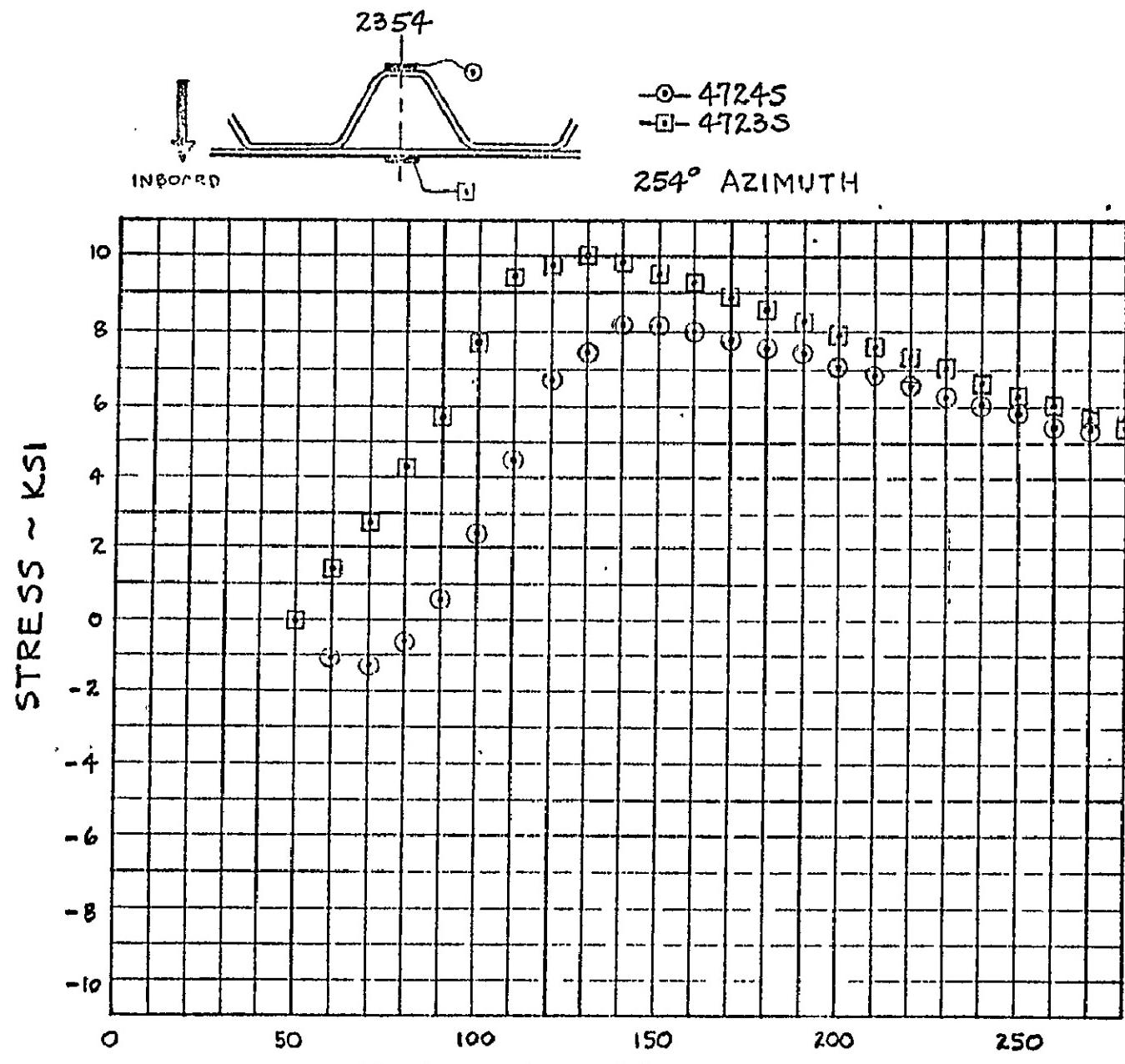


FIGURE IC-26 COMPARISON OF CORRUGATION STRESS FOR TEST 2

16

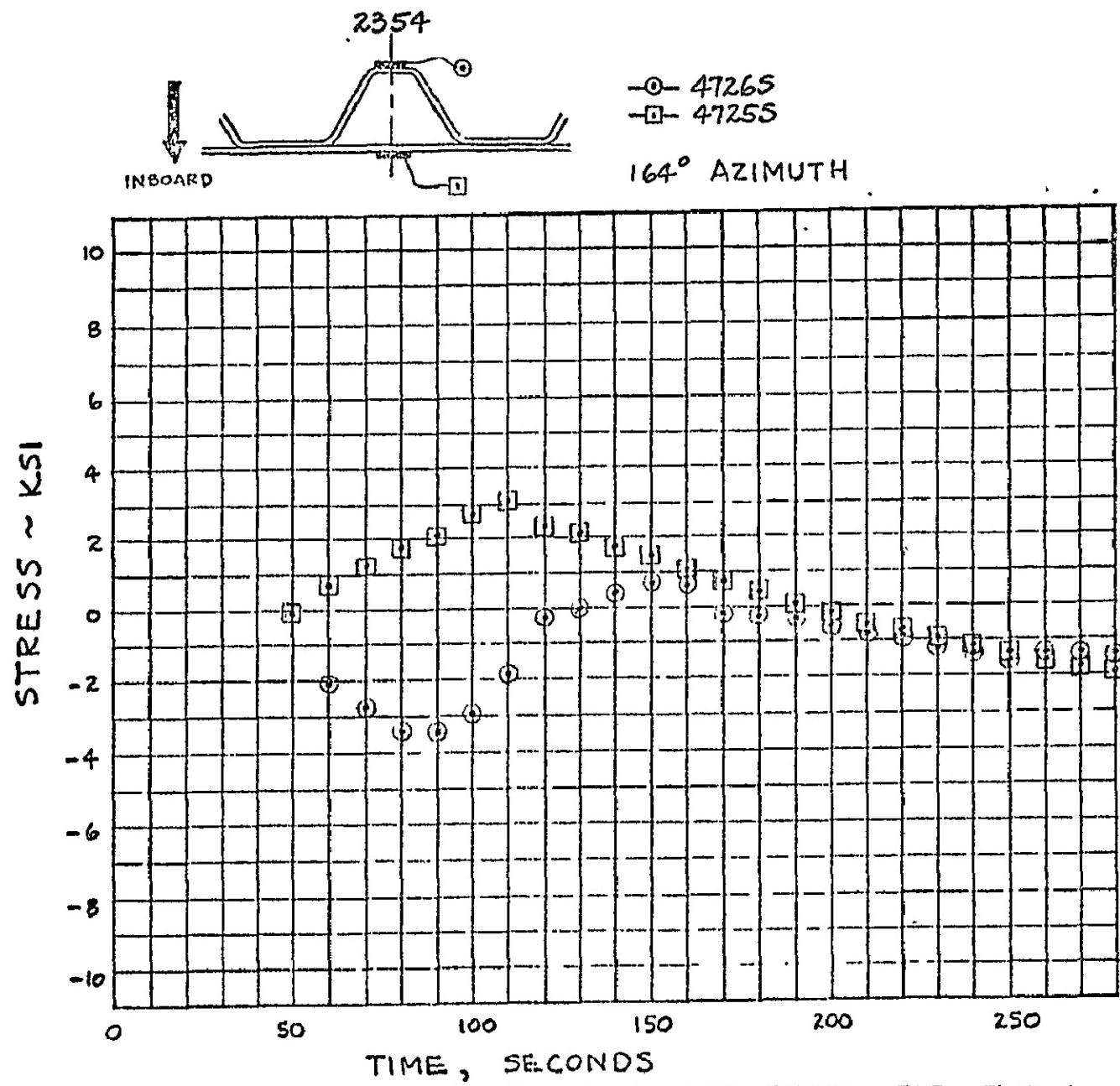


FIGURE IIC-27 COMPARISON OF CORRUGATION STRESS FOR TEST 2

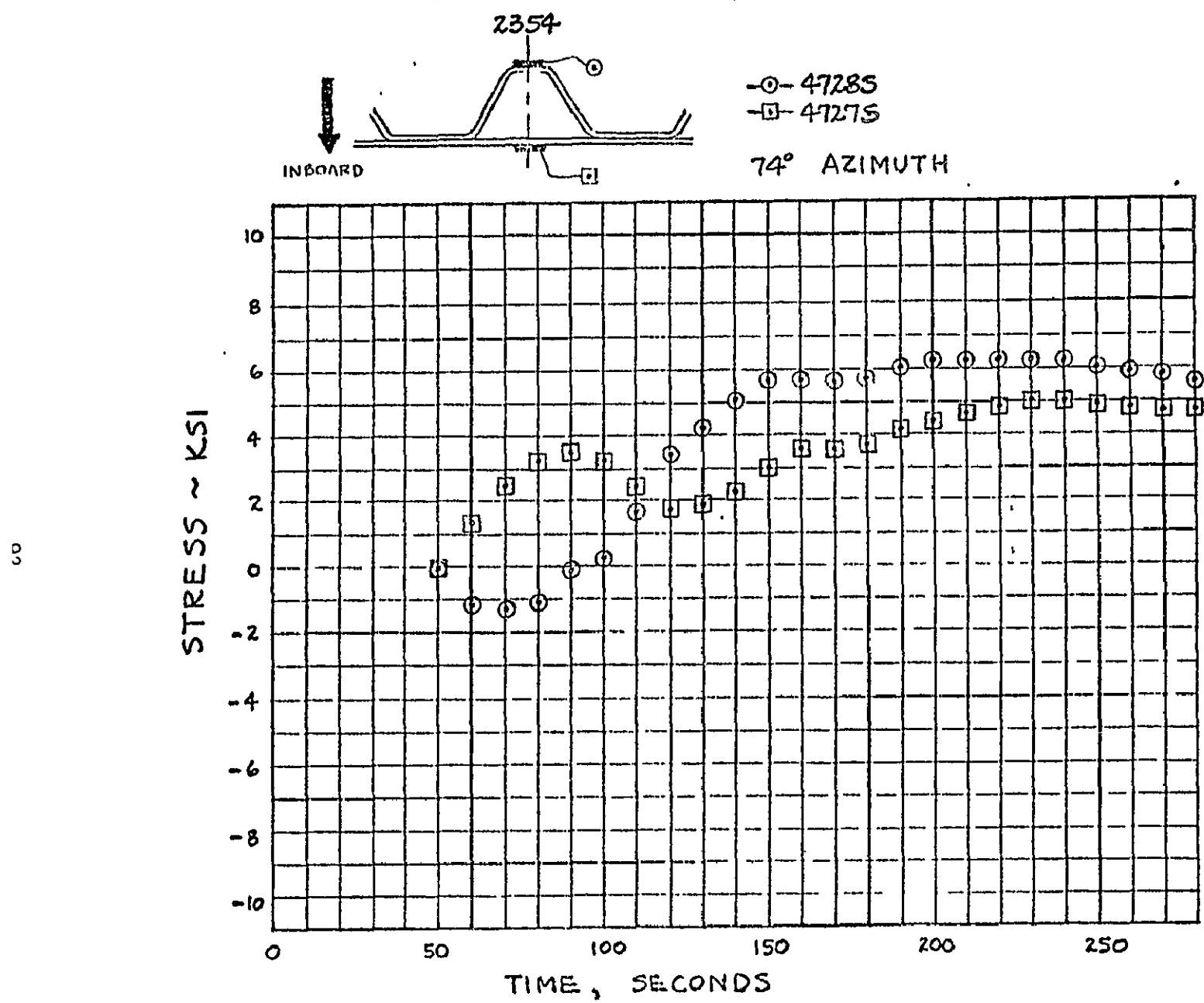


FIGURE IC-28 COMPARISON OF CORRUGATION STRESS FOR TEST 2

V.D. Jettison Stresses, Loads and Boattail Motions

Charles W. Eastwood, Jr., George S. Sarvay, and Richard T. Barrett

One primary objective of the tests was the verification of the CSS structural capability during jettison. Information, which was obtained from strain gages during the two heated tests, was used to determine the thermal effects on the performance of the CSS hardware during jettison. The unheated test served as a reference baseline for measuring the thermal effects and to isolate the purely mechanical factors affecting the jettison performance. Strain-time histories were displayed on Brush strip charts with time zero taken at Super-Zip firing. Stress data is not available for all strain gages because some of the gages failed or their readings are questionable. In general, all the figures show a "zero shift" prior to the firing of the separation system. This shift is attributed to the thermal strain during heating and should be eliminated during the determination of stresses resulting from jettison.

Forward Hinge Longeron Stresses

Each forward hinge longeron was instrumented with four strain gages as shown in figure VD-1a, to determine stress levels during jettison. The test results as shown in figures VD-2 through VD-8 indicate that the outboard flange cap stresses are greater than the inboard values. The stress levels ranged between 12 000 and 16 000 psi during the three tests. These levels are well within the 17-4PH CRES material yield and outboard flange cap buckling allowables (ref. 9).

Aft Hinge Fitting Stresses and Loads

The aft hinge fittings were instrumented with strain gages, as shown in figure VD-1b. The data presented in figures VD-9 through VD-14 are the stress levels during the first 3 seconds of jettison motion. The axial hinge load calculations are based on the data from a single strain gage located on each aft hinge fitting. The gages (item A in figure VD-1b) located on the forward surface of each aft hinge fitting provide the most direct method for estimating axial tension loads. The correlation between the measured stress levels and the applied axial load is (ref. 3):

$$P_x = -0.513 f_A$$

This relationship is valid during the first 0.1 second after CSS separation. The axial loads determined from the three tests did not exceed 8470 pounds which was reached during test 3 at the 103° azimuth hinge. This load represents 46 percent of the design limit load (ref. 9). The loads from this series of tests were somewhat higher than those measured during the third cryogenic-unlatch test (ref. 3).

Station 2209 Ring Stresses

The effects of jettison on the boattail station 2209 ring stresses are presented in figures VD-15 through VD-20. As can be seen from these figures, the maximum stress levels are low and did not exceed 6000 psi, which is equivalent to less than half of the maximum design loads (ref. 9).

Boattail Motions Observed by Cameras during Jettison. - Figure VD-25 shows the deflections which occurred at stations 2209 and 2180 during test 3. The magnitudes were taken from the cyclic traces shown in figures VD-26 through VD-32. Generally, the frequency of boattail motion is about 9-10 Hz for tests 2 and 3. Test 1 was not monitored by cameras.

Simulated Flight Jettison Strain Measurements

CSS flight strain gage data are to be evaluated by comparison with test data. Therefore, the measurements for sensing the strains that were developed in the aft hinge longerons during each of the CSS jettison tests were simulations of the strain gage assemblies designed for the first two Titan/Centaur flight vehicles. The strain gage arrays were located on the webs of the aft hinge longerons. Each array consisted of four uniaxial gages centered on station 2187 and electrically connected to compensate for temperature variations and to give augmented signal voltage output as shown in figure VD-21.

Prior to CSS jettison in tests 1 and 2, the hinge strain measurements on the aft hinge longerons experienced strain changes during the heating cycles. These strain values are attributable to thermal effects in the nonjettisonable boattail section and were not to be included in the subsequent strain data developed from the CSS jettison event. Therefore, the test data were corrected by establishing the strain values at the time of Super-Zip firing as the zero datum levels. The polarity of the measurements on the 103° and 283° longerons has been reversed to correct instrumentation errors. All strains have been converted to stresses.

The stresses indicated by the aft hinge longeron measurements were as predicted. Figures VD-22, VD-23, and VD-24 show that immediately after Super-Zip firing the stresses developed as oscillating tension in each of the four hinge measurements for each of the three tests. The oscillations were approximately 9 Hz, damping to zero by approximately 0.7 seconds. From that time until the two halves of the CSS either separated from the hinges (270° half) or engaged the catch net (90° half), the stresses were low level compression of varying magnitudes. The maximum stress values were:

Hinge location	77°	103°	257°	283°	
Test No. 1 tension	2000	2400	1500	2400	psi
Test No. 2 tension	2200	1800	2000	1700	psi
Test No. 3 tension	2400	--	2700	2300	psi
Test No. 1 compression	400	750	300	500	psi
Test No. 2 compression	500	800	400	700	psi
Test No. 3 compression	600	--	400	800	psi

2
3

The measurement on the 103° longeron in test 3 developed an anomalous offset which appeared to be corrected immediately following Super-Zip firing. However, determination of the actual offset value was questionable so that this set of data are considered unreliable.

Comparison of the jettison test data with data obtained in a prior hinge test program (ref. 2) established a correlation between hinge stress measurements and hinge loads. Since the static load hinge tests were performed at 80 percent of design loads, the values have been proportioned to 100 percent of design values for correlation purposes. The jettison test maximum tension and compression stresses compare with the design load stresses in the aft hinge longeron measurements as follows:

	Altitude Jettison Tests			Static Load Hinge Tests (100% Design Value)	
	No. 1	No. 2	No. 3	Symmetric	Unsymmetric
Max tension (psi)	2400	2200	2700	3400	7500
Max compression (psi)	750	800	800	--	9700

The value of the maximum tension stress for test 3 was 73 percent of the stress produced by the design symmetric loads. The largest stress in a single hinge longeron was a tension stress in test 3. The value was 36 percent of the stress produced in one hinge longeron by the design loads. These maximums occurred approximately 0.06 seconds after Super-Zip firing. The estimated inaccuracy based on the instrumentation and correlation is ± 10 percent. The compression stresses, which occurred approximately 0.7 seconds after Super-Zip firing, were the result of combined axial and radial loading. Inaccuracies are estimated to be ± 20 percent.

The similarity of the data traces as seen in figures VD-22, VD-23, and VD-24 was excellent. This indicates good repeatability and validates the planned use of the measurements in flight for evaluation of jettison loads. The tests did not include forces produced by C.G. offset, limit cycle, and thruster unbalance. As a result, the flight jettison stresses will probably be larger than the test values.

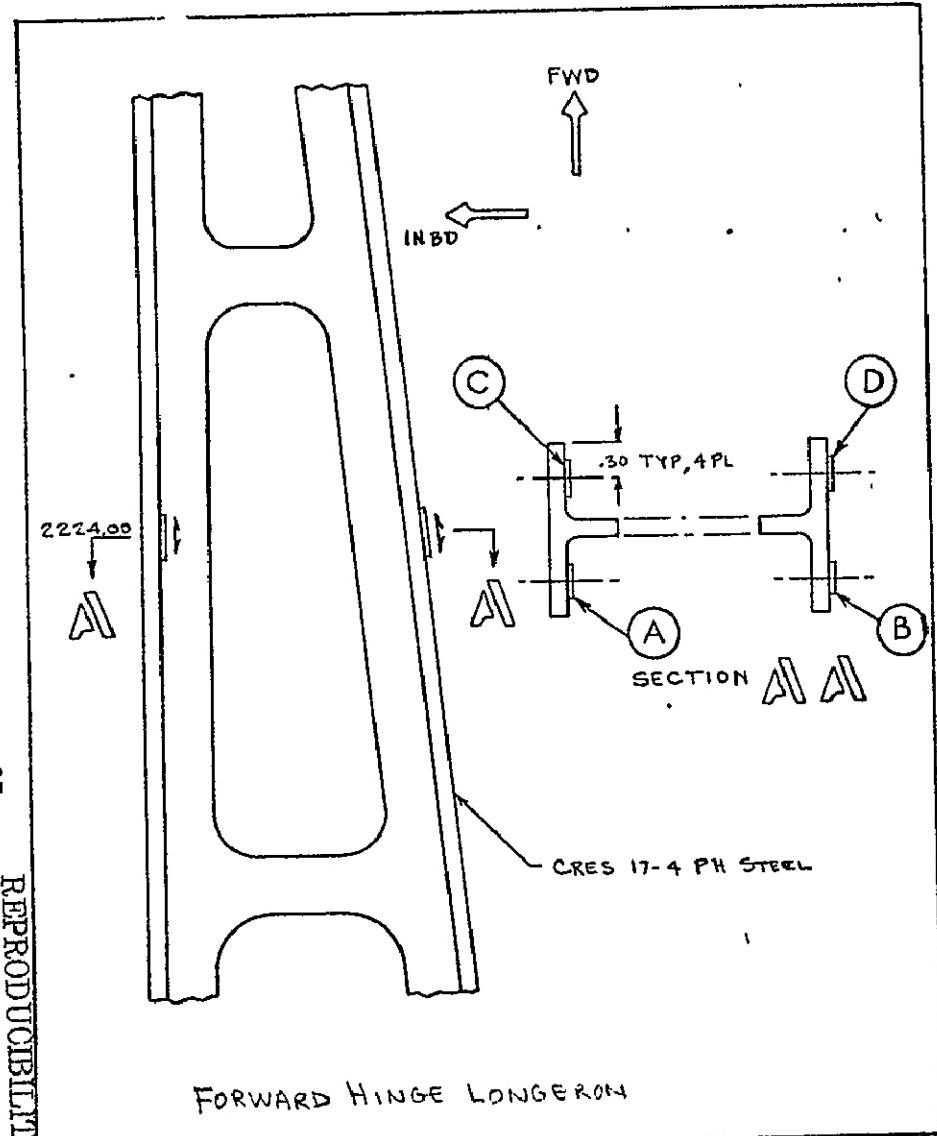
The stresses produced in the aft hinge longerons during CSS jettison as indicated by simulations of the planned flight measurements are of sufficient magnitude and repeatability to yield meaningful flight data.

Interstage Adapter

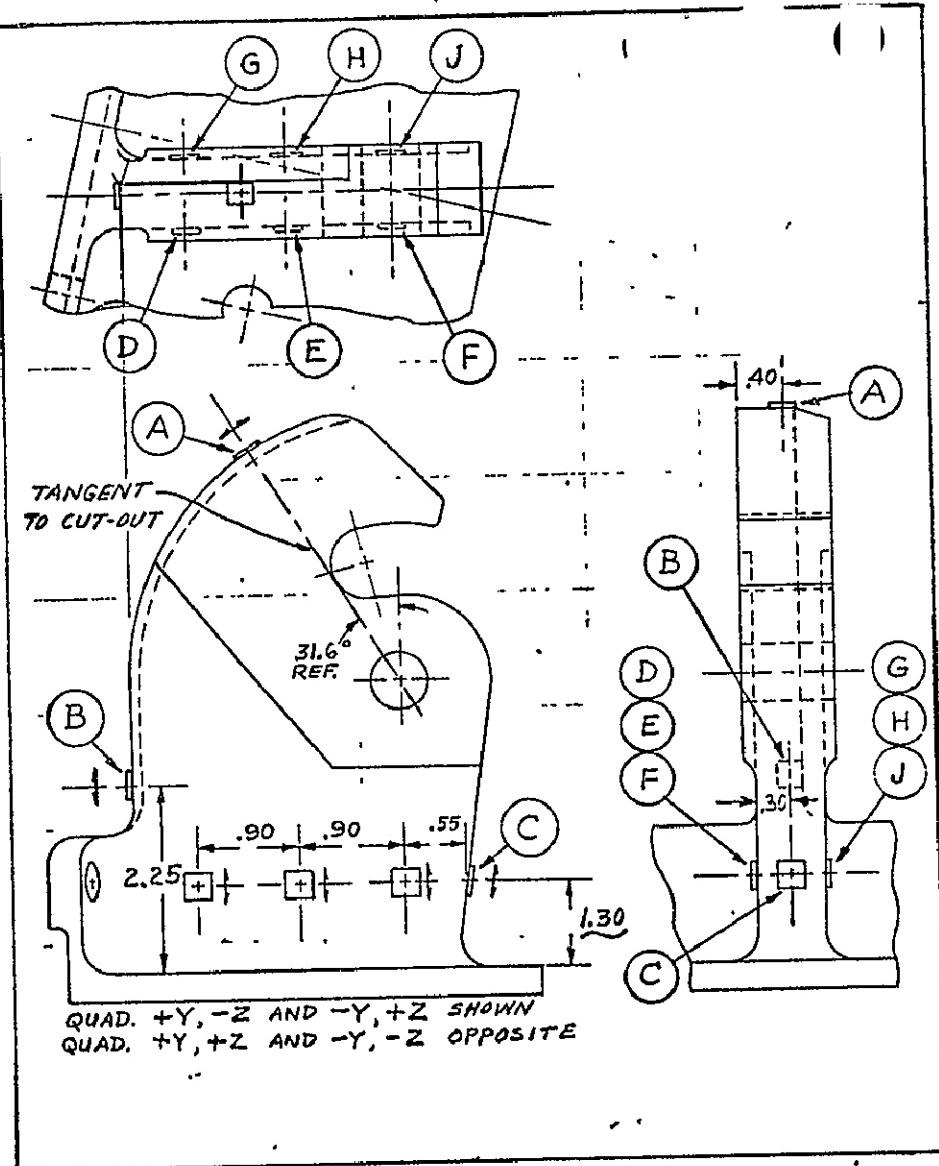
The ISA had 10 strain gages installed for these tests. The CSS support ring (station 2177) was instrumented with both circumferential and axial gages.

Maximum circumferential stress was 6360 psi, which was reached on test 1. The ring is 2219-T852 aluminum, which has a yield stress allowable of 42 000 psi. Maximum axial stress was -12 000 psi on test 1. The next closest reading was -6360 psi, which occurred during test 3. Maximum stringer stresses reached 2880 psi. This compares to a yield allowable of 54 000 psi for the 2024-T81 aluminum stringers.

Since there was no evidence of permanent deformation in noninstrumented areas and very low stress readings on all of the instrumented areas, it can be concluded that CSS jettison is noncritical for ISA design.



(a.)



(b.)

FIGURE ID-1 CSS HINGE STRAIN GAGE INSTALLATIONS

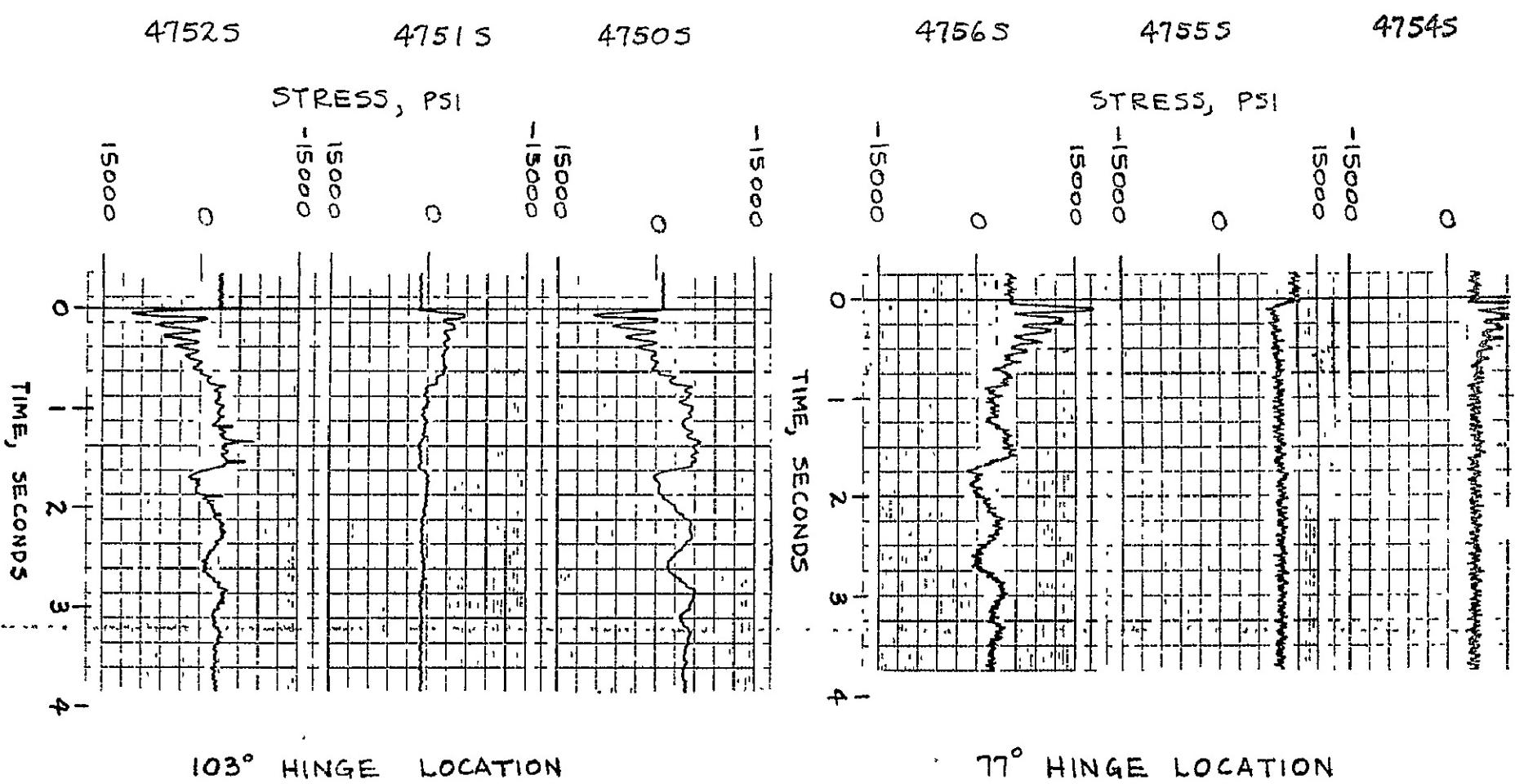


FIGURE IV-2 FWD. HINGE LONGERON STRESSES FOR TEST I

FIGURE ID-3 FWD HINGE LONGERON STRESSES FOR TEST 2

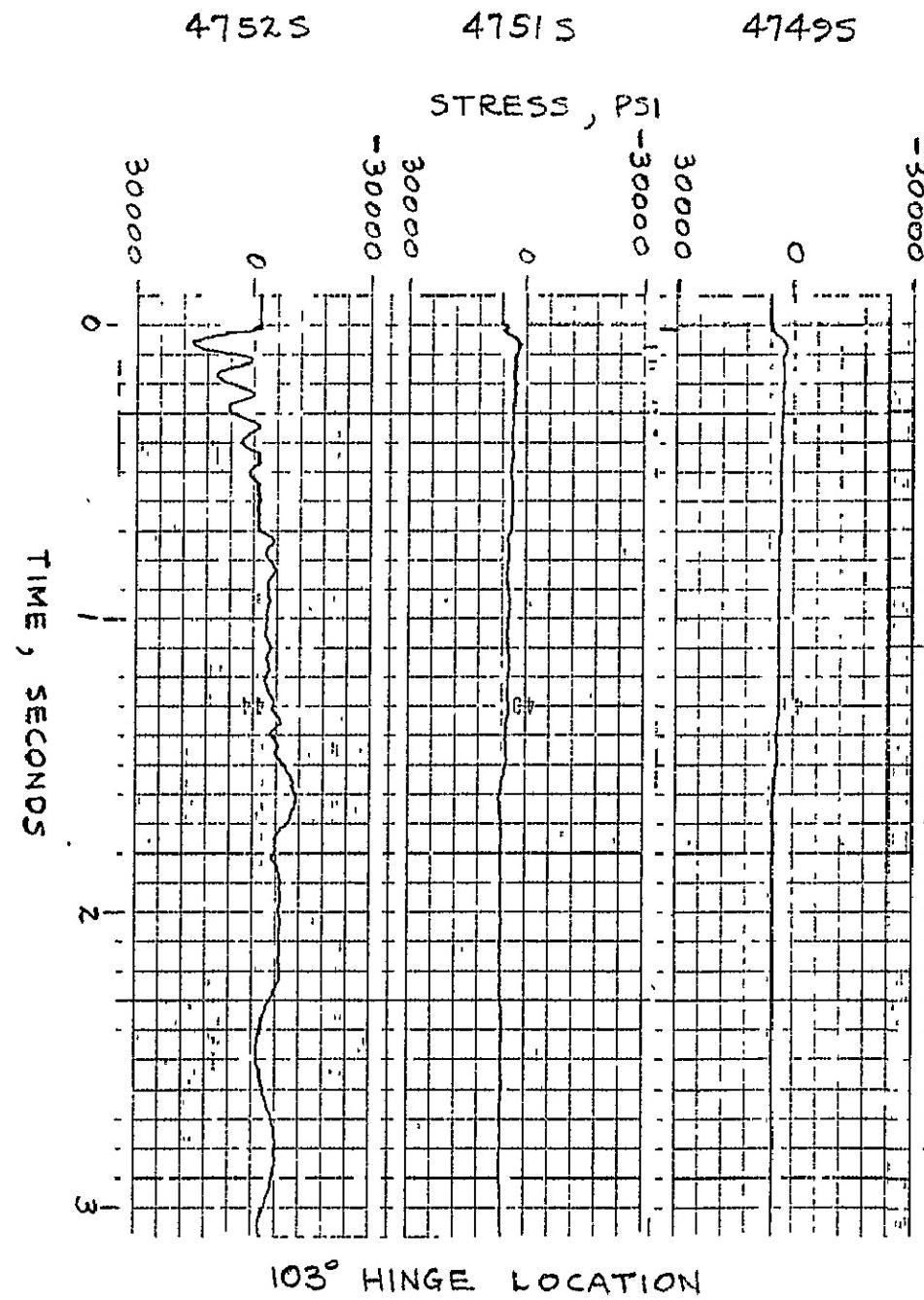


FIGURE IV-4 FWD HINGE LONGERON STRESSES FOR TEST 2

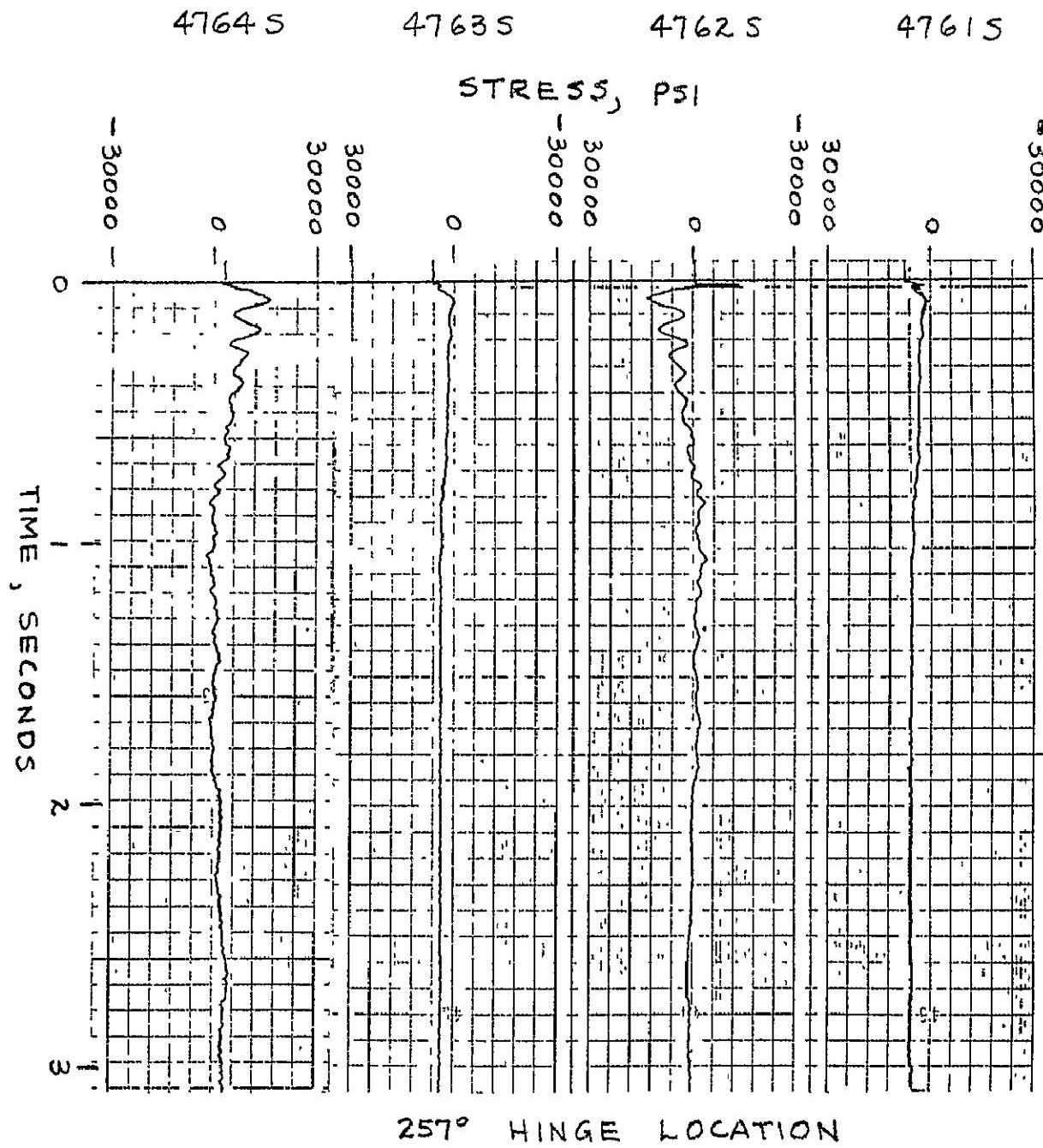


FIGURE EID-5 FWD HINGE LONGERON STRESSES FOR TEST 2

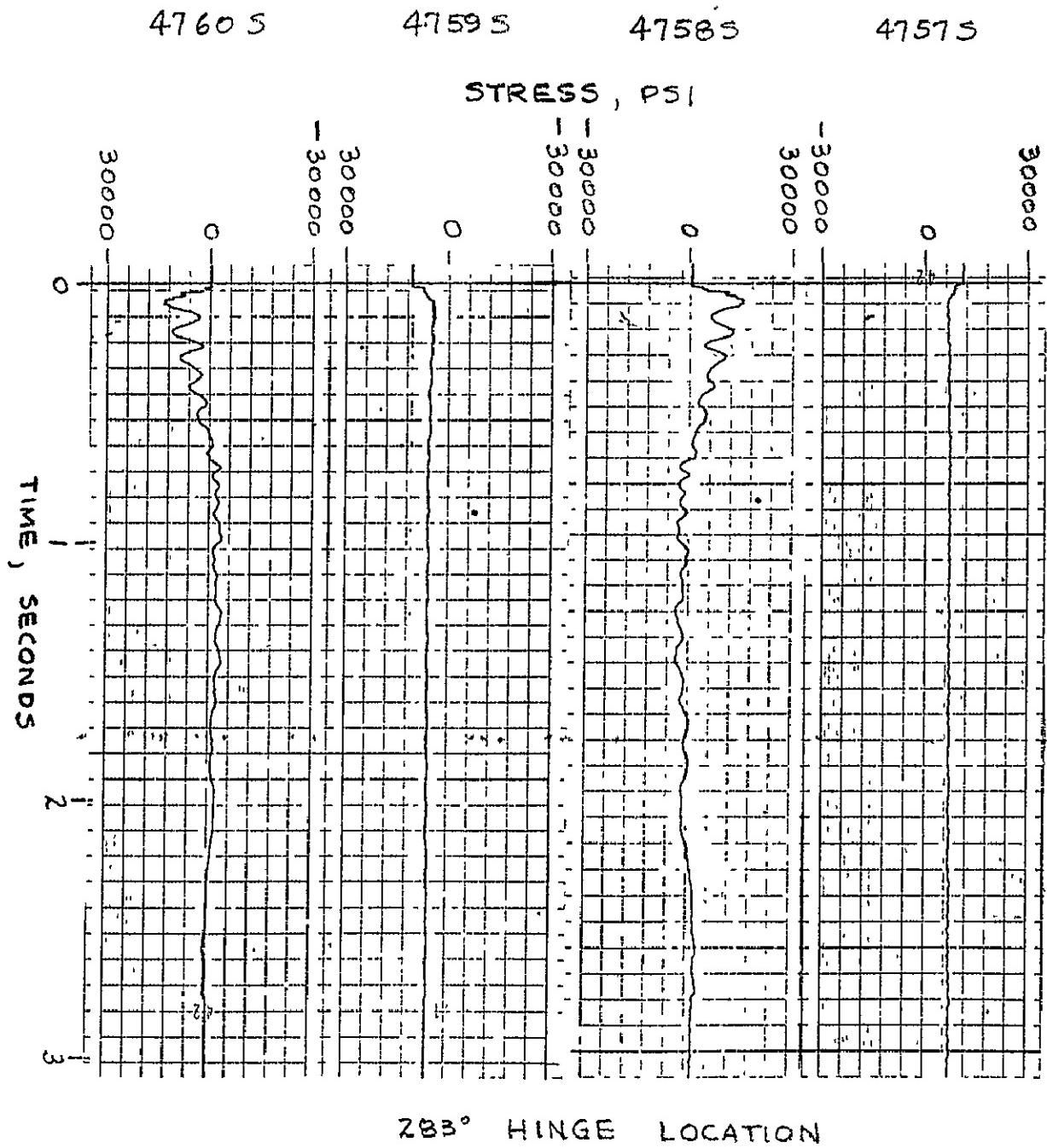


FIGURE IV-6 FWD HINGE LONGERON STRESSES FOR TEST 3

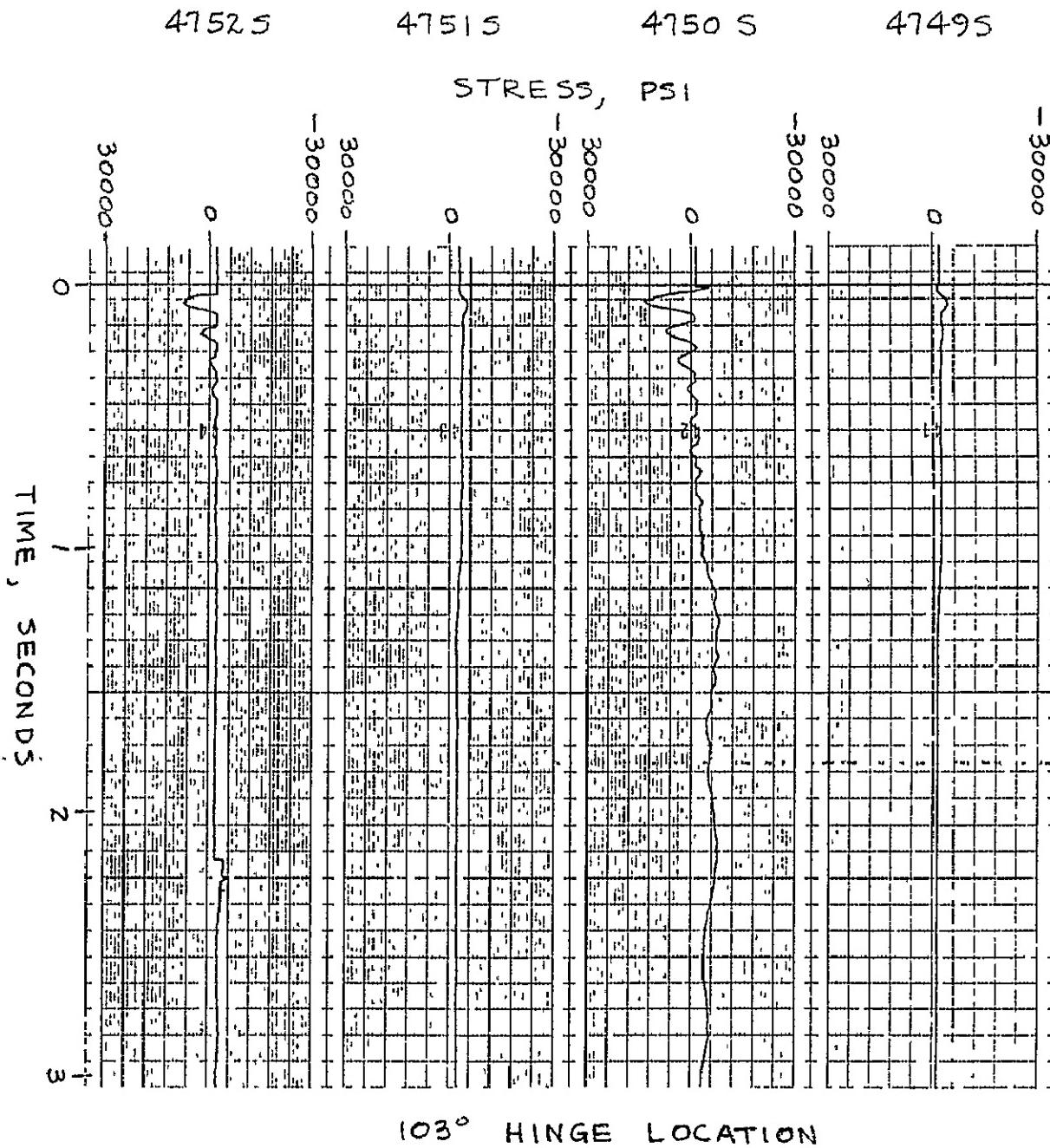
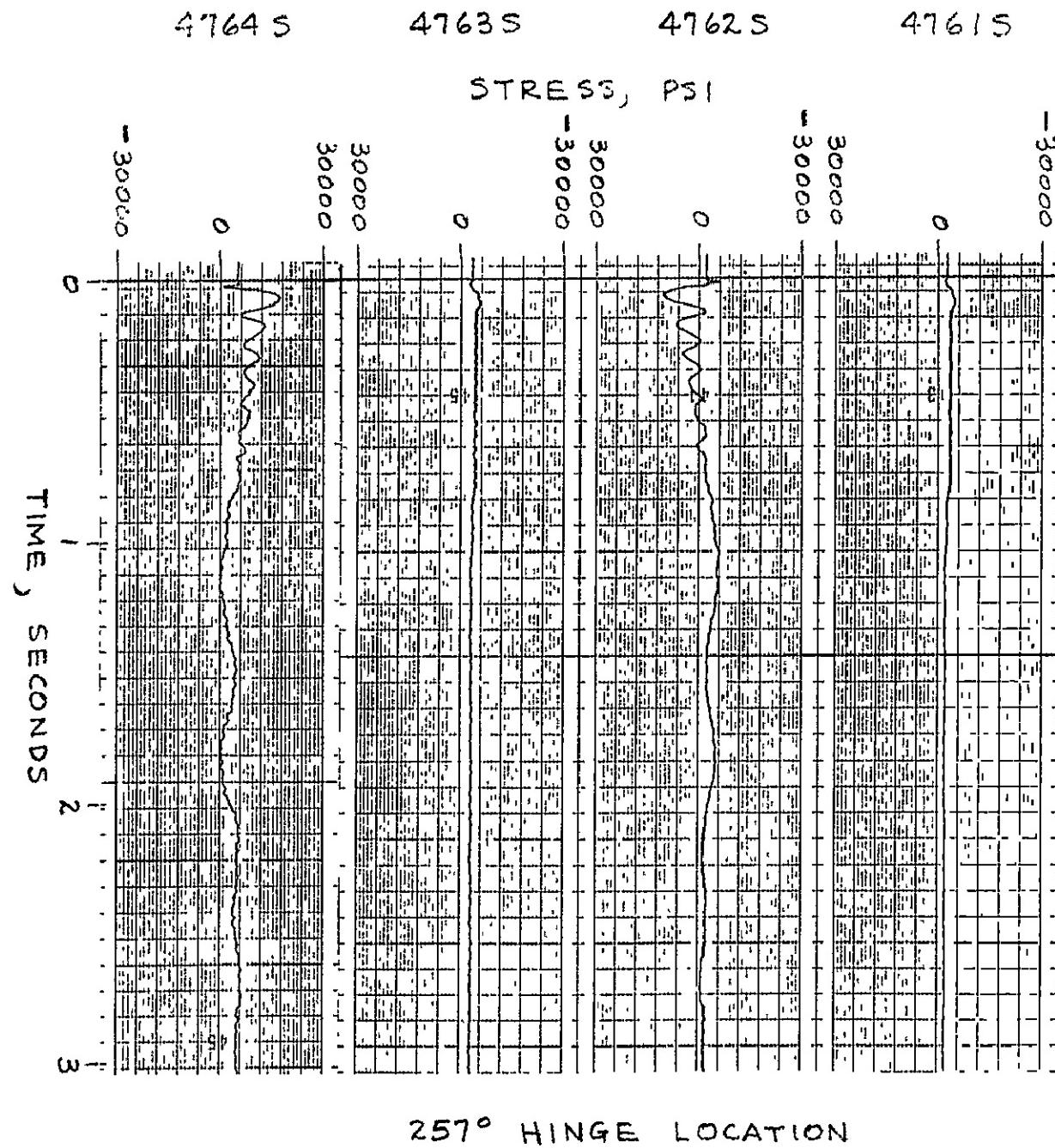


FIGURE VD-7 FWD HINGE LONGERON STRESSES FOR TEST 3



REPRODUCIBILITY OF THE
ORIGINAL PAGE IS POOR

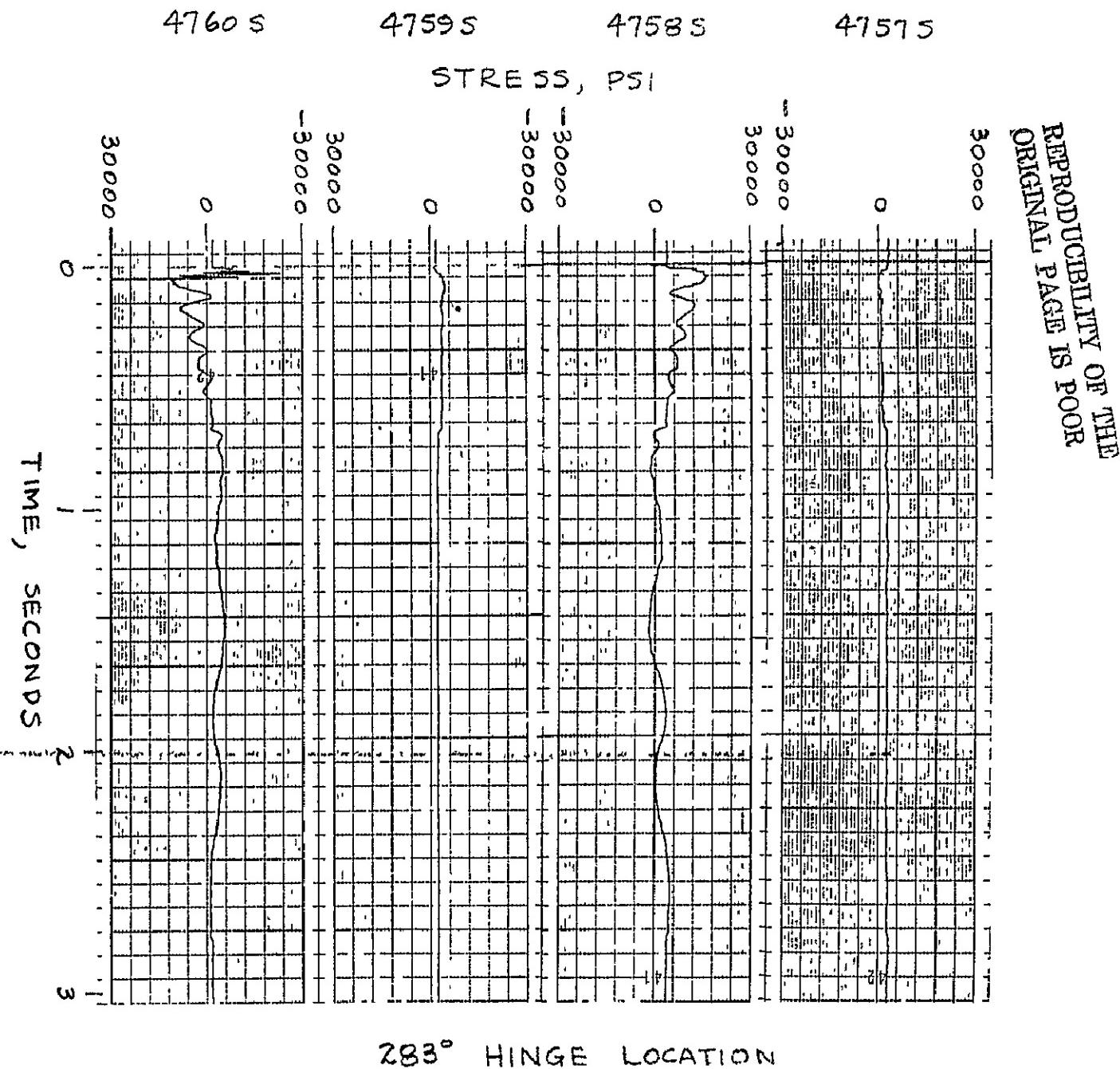


FIGURE ID-8 FWD HINGE LONGERON STRESSES FOR TEST 3

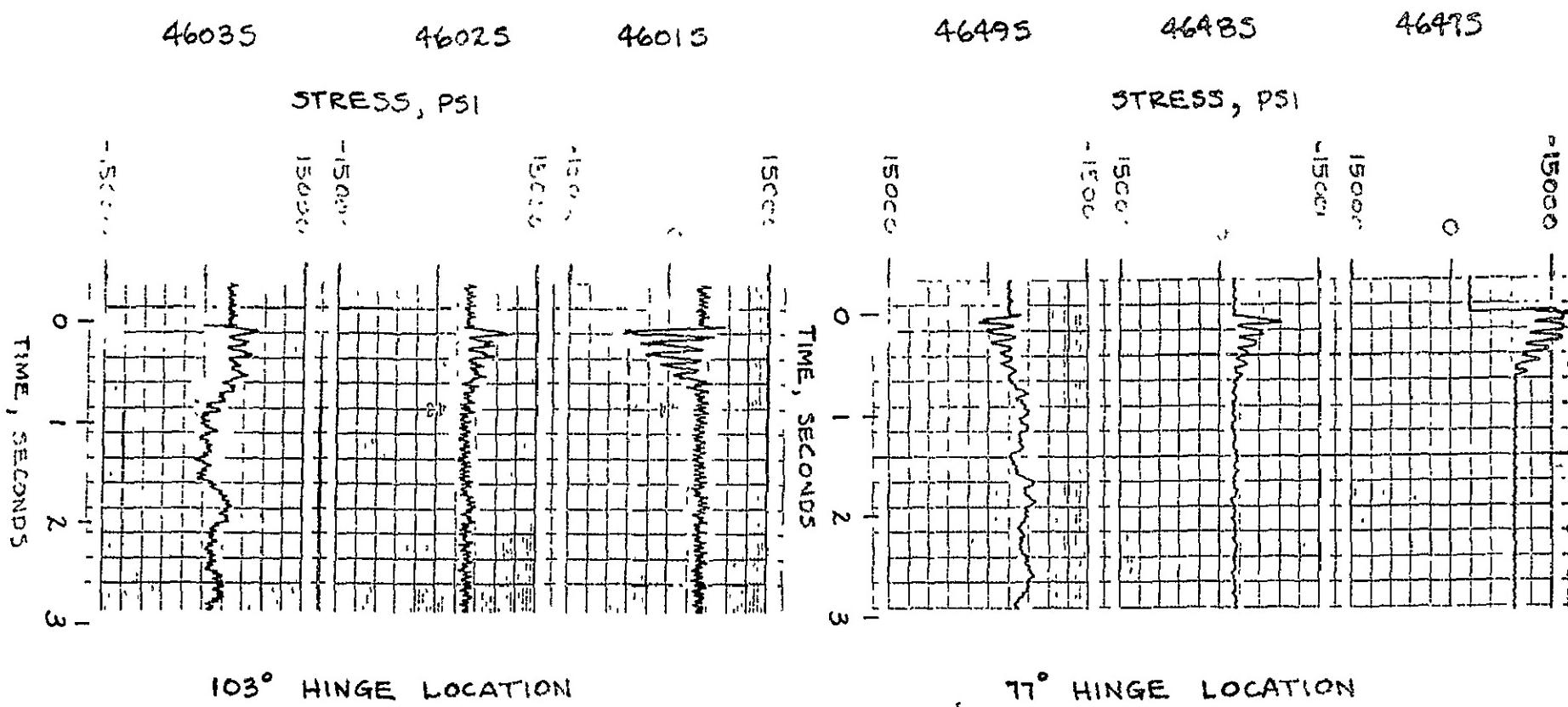


FIGURE ID-9 AFT HINGE FITTING STRESSES FOR TEST I

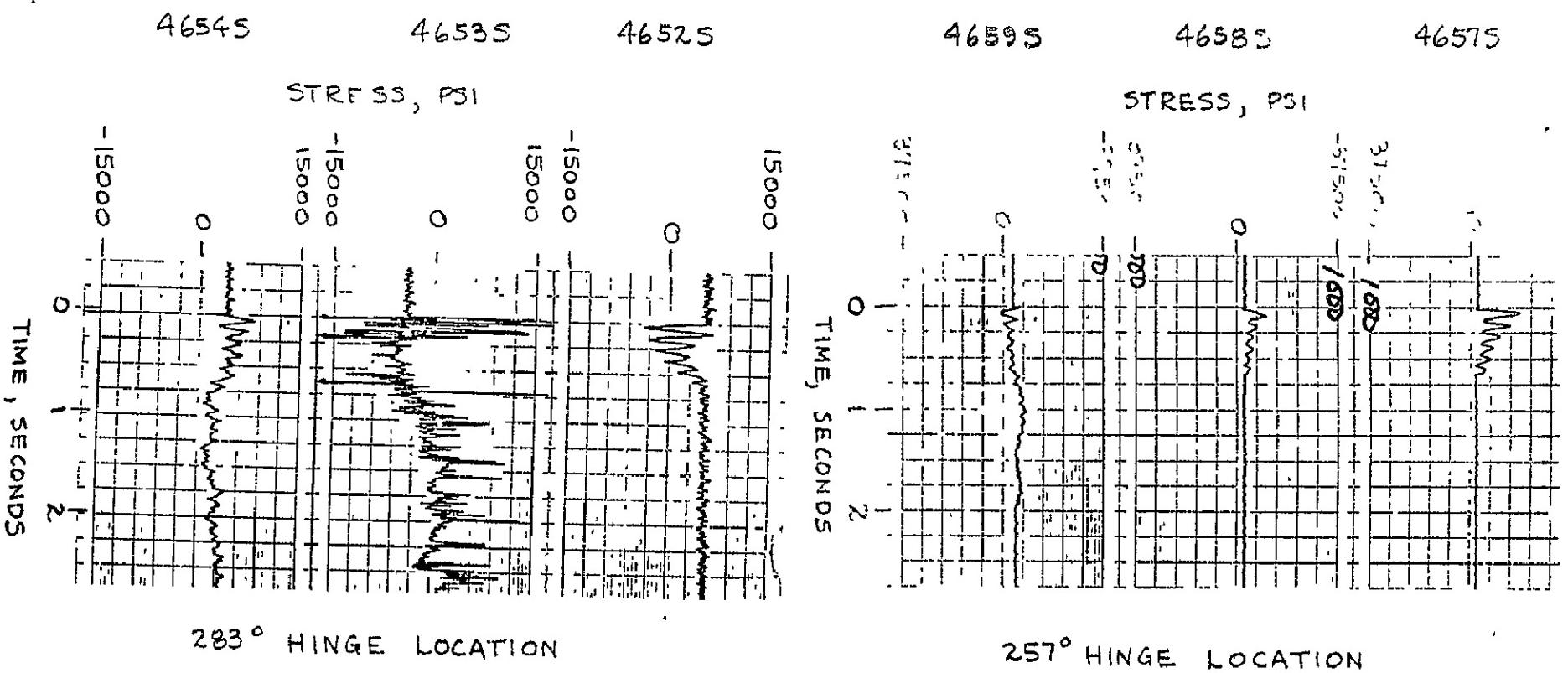


FIGURE D-10 AFT HINGE FITTING STRESSES FOR TEST I

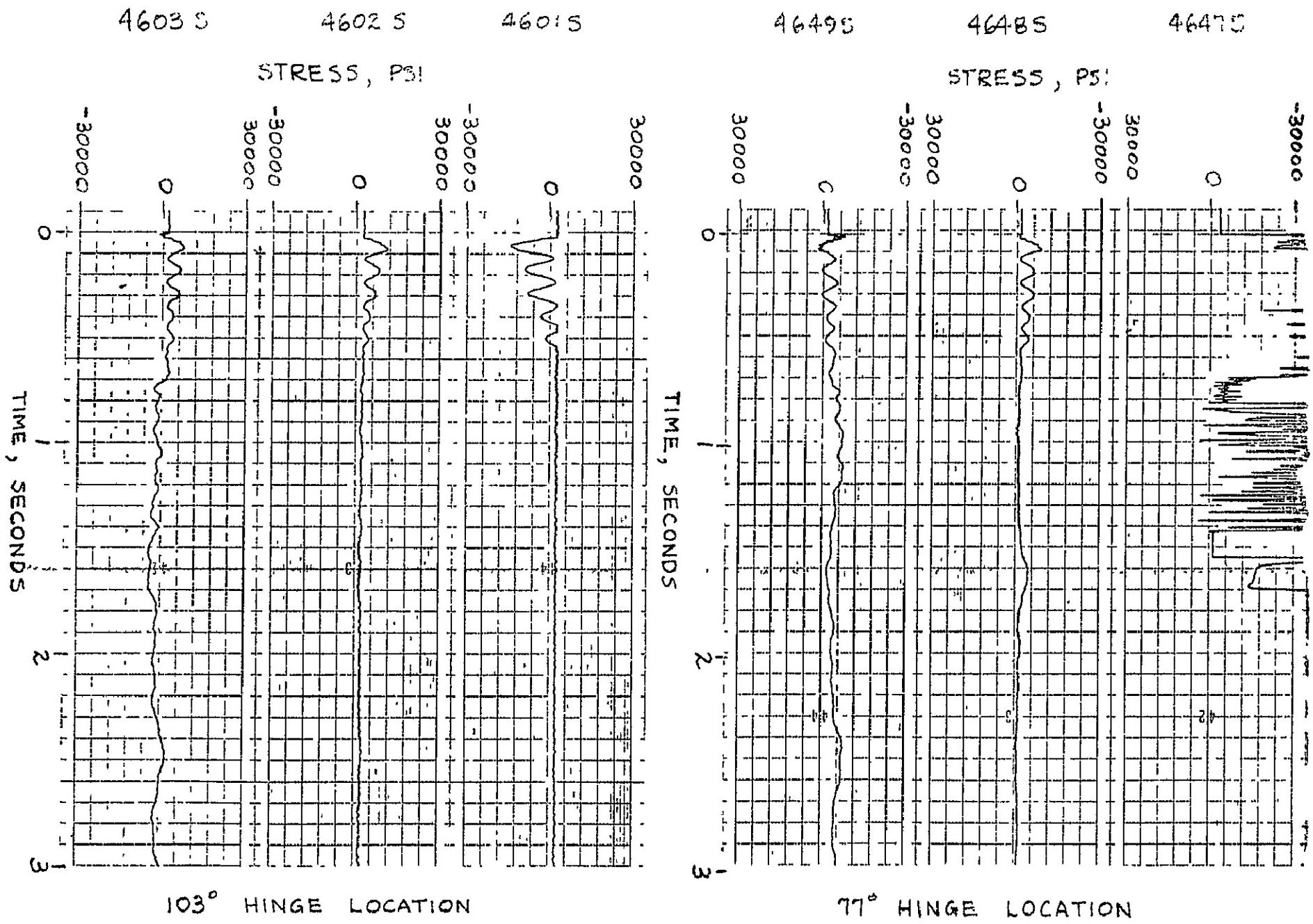
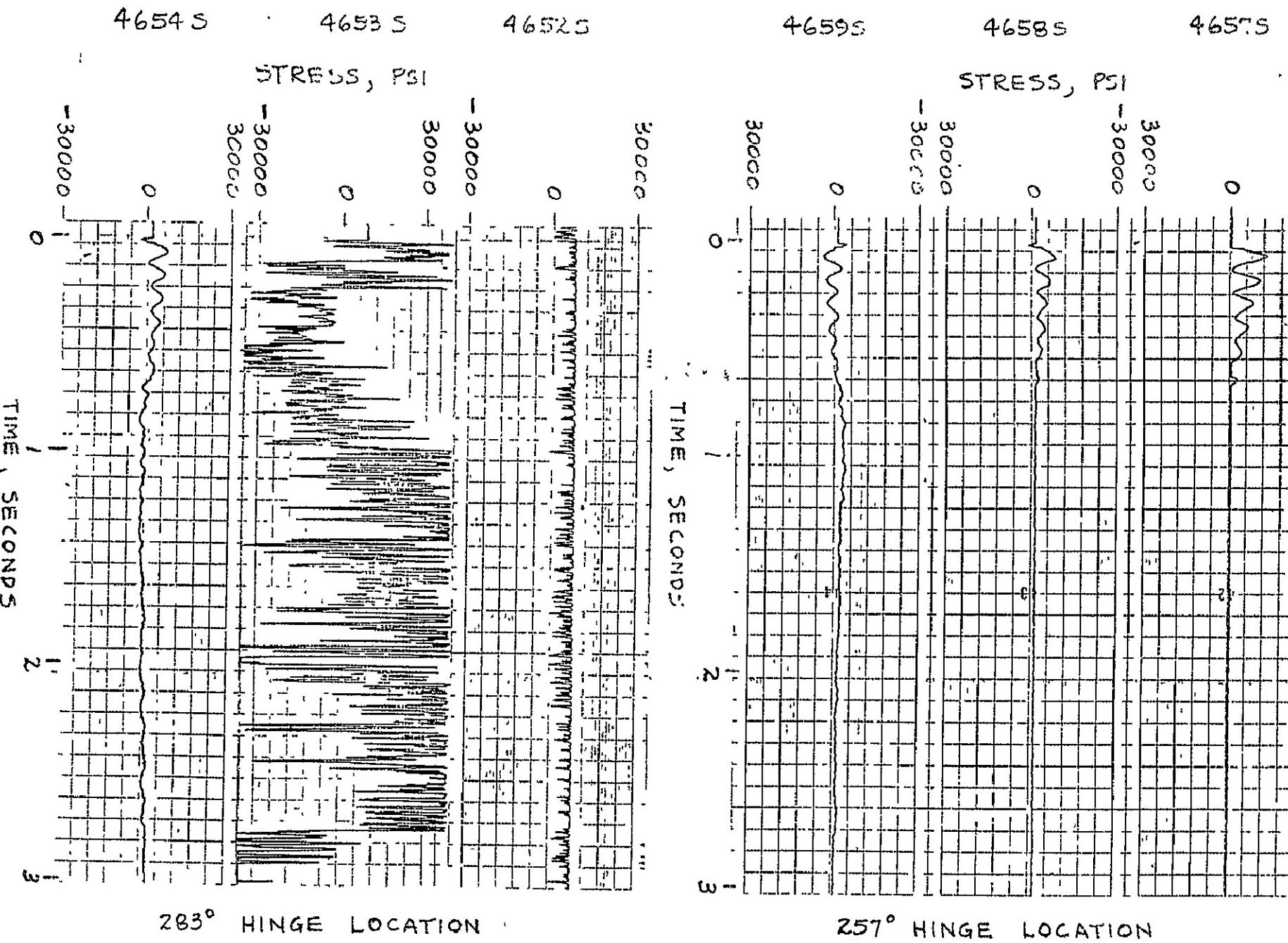


FIGURE II AFT HINGE FITTING STRESSES FOR TEST 2

FIGURE IV-12 AFT HINGE FITTING STRESSES FOR TEST 2

108 REPRODUCIBILITY OF THE

ORIGINAL PAGE IS POOR



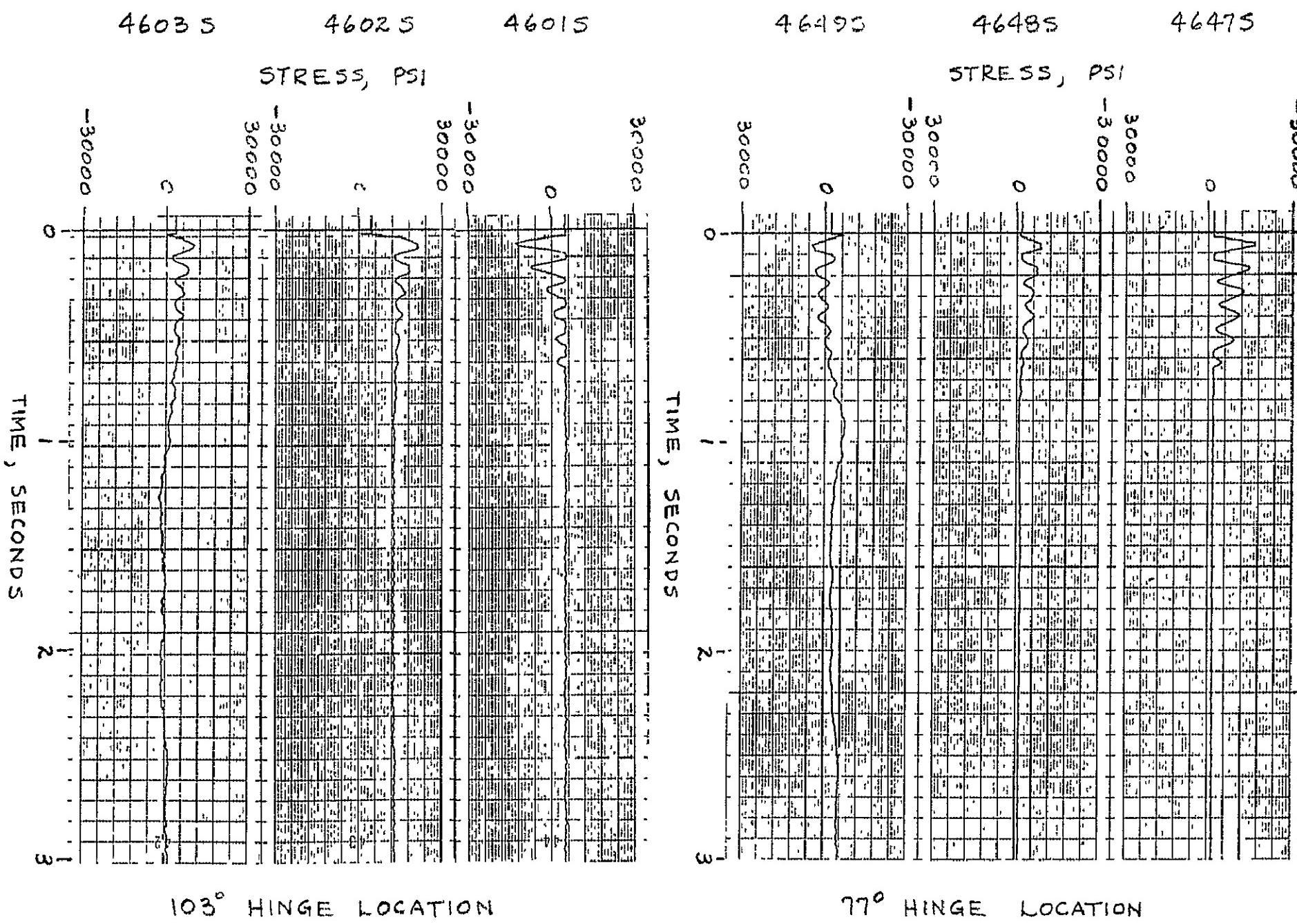


FIGURE D-13 AFT HINGE FITTING STRESSES FOR TEST 3

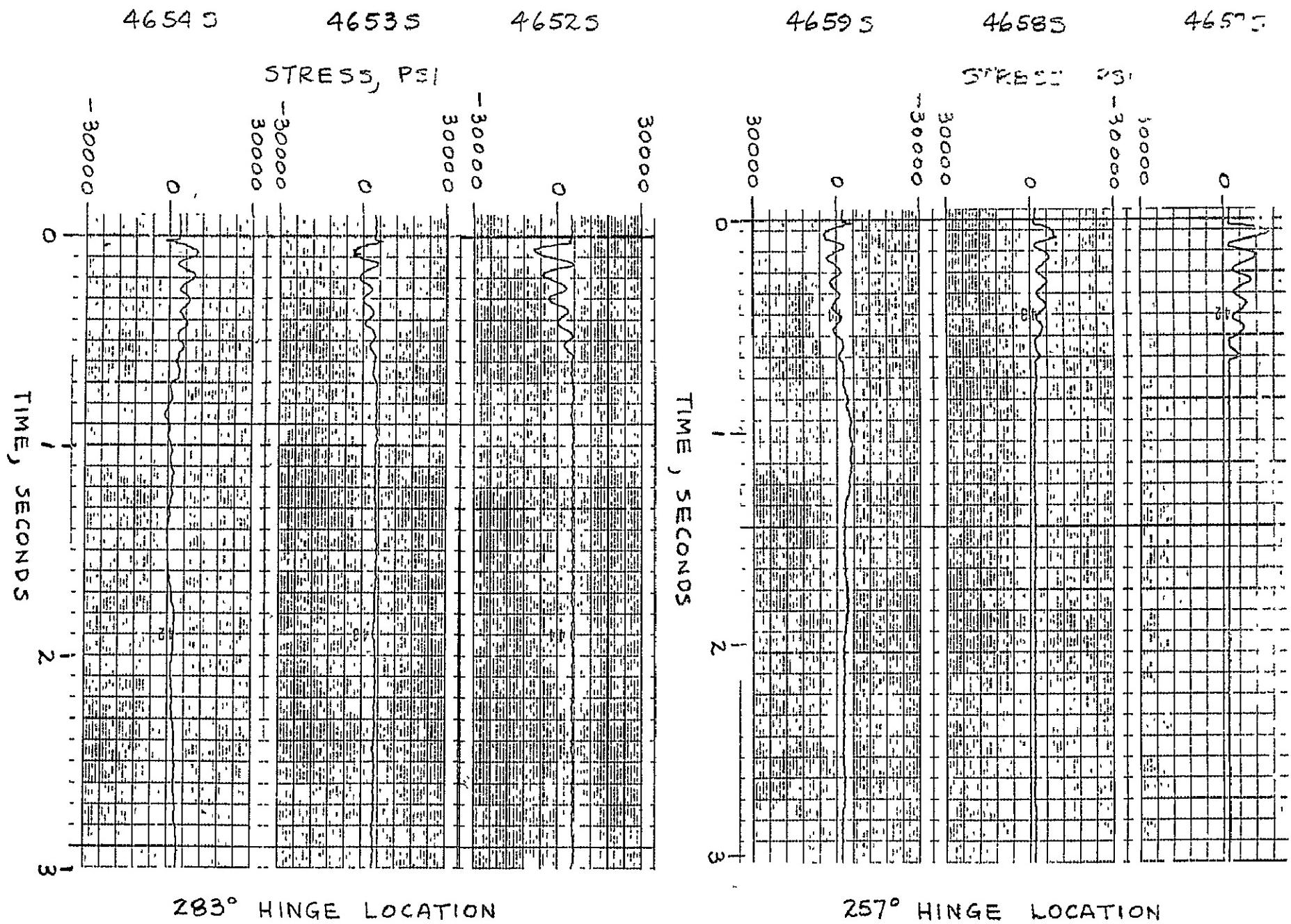


FIGURE ID-14 AFT HINGE FITTING STRESSES FOR TEST 3

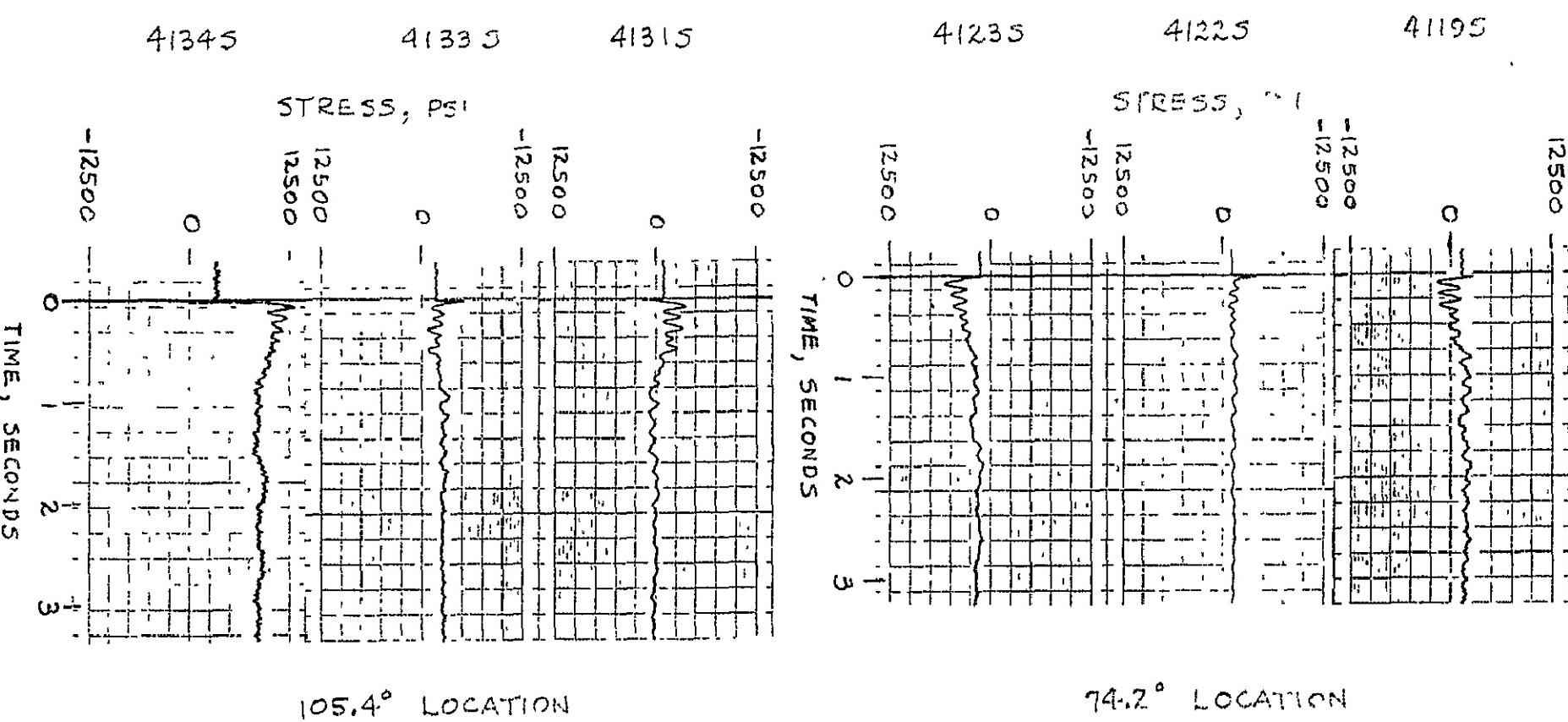
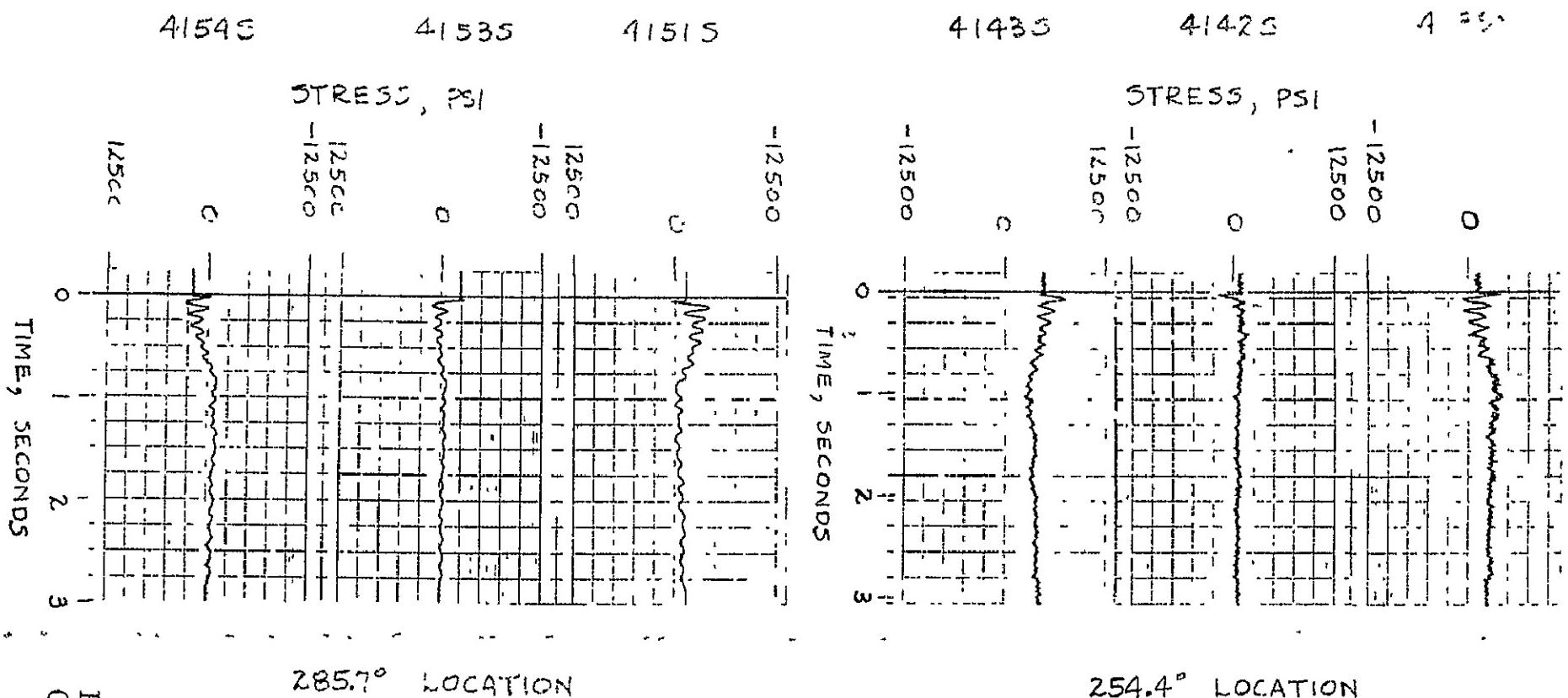


FIGURE II-15 STATION 229 RING STRESSES FOR TEST I



REPRODUCIBILITY OF THE
ORIGINAL PAGE IS POOR

FIGURE VII-16 STATION 2209 RING STRESSES FOR TEST I

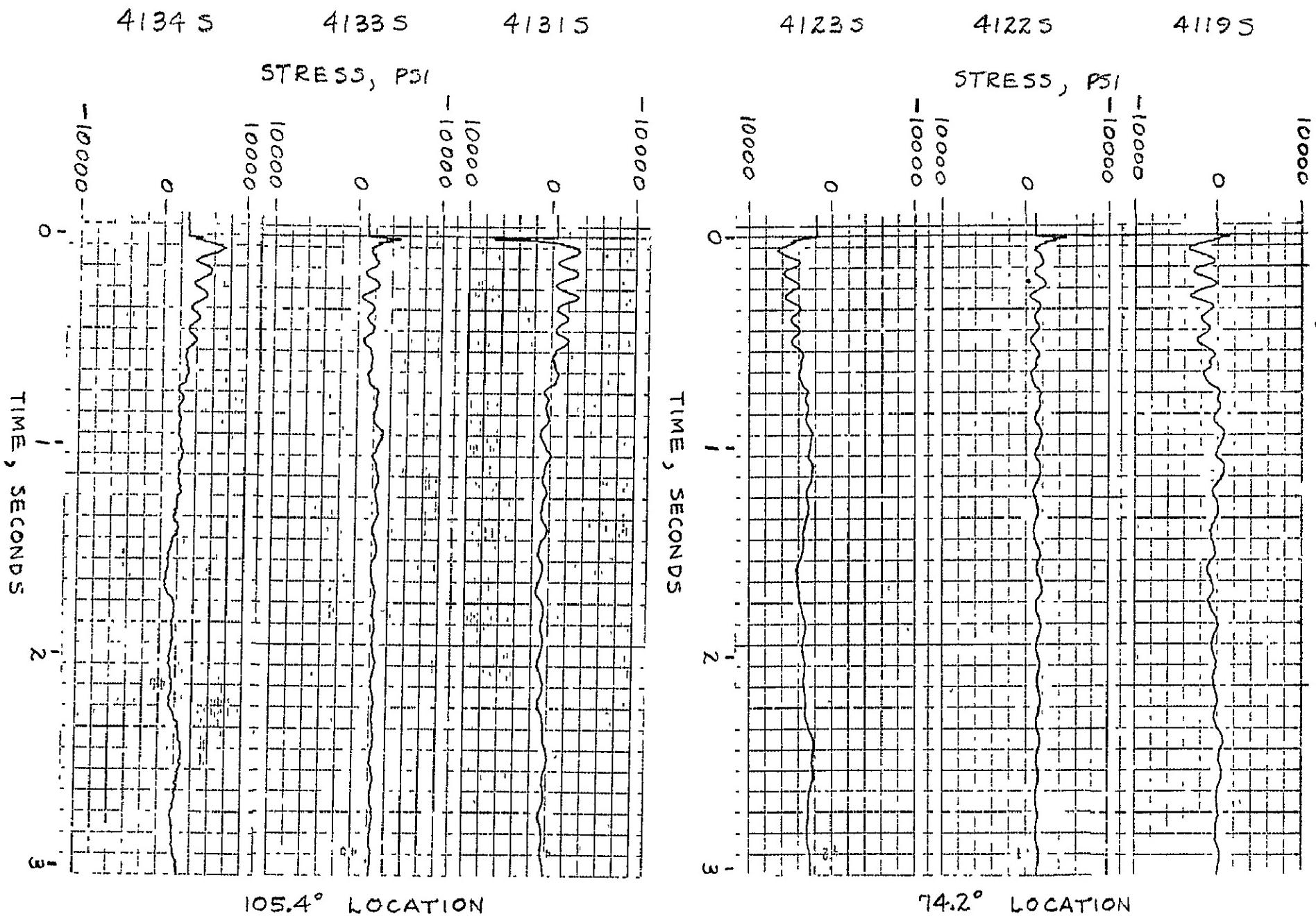


FIGURE II-17 STATION 2209 RING STRESSES FOR TEST 2

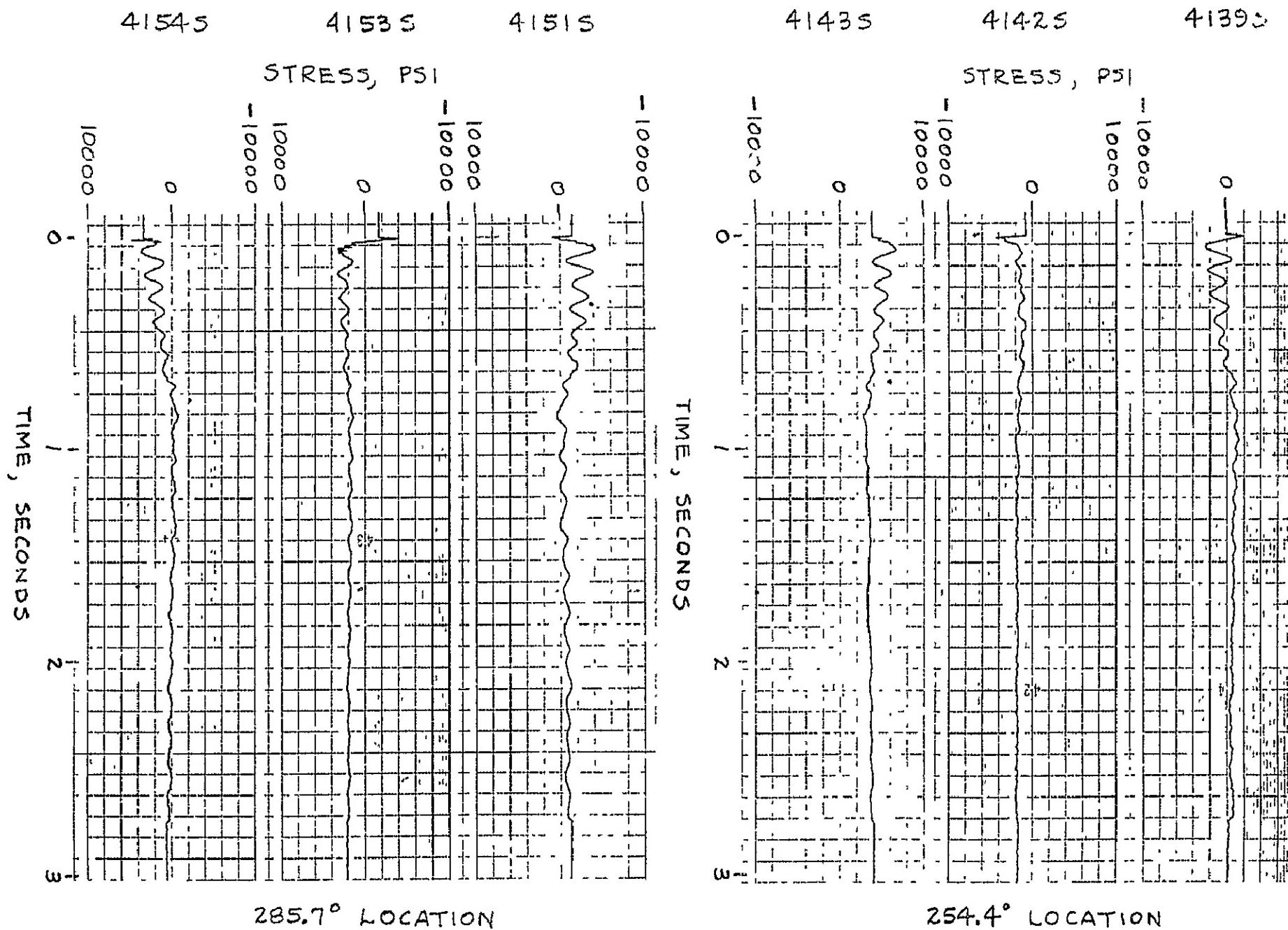


FIGURE D-1B STATION 2209 RING STRESSES FOR TEST 2

FIGURE ID-19 STATION 2209 RING STRESSES FOR TEST 3

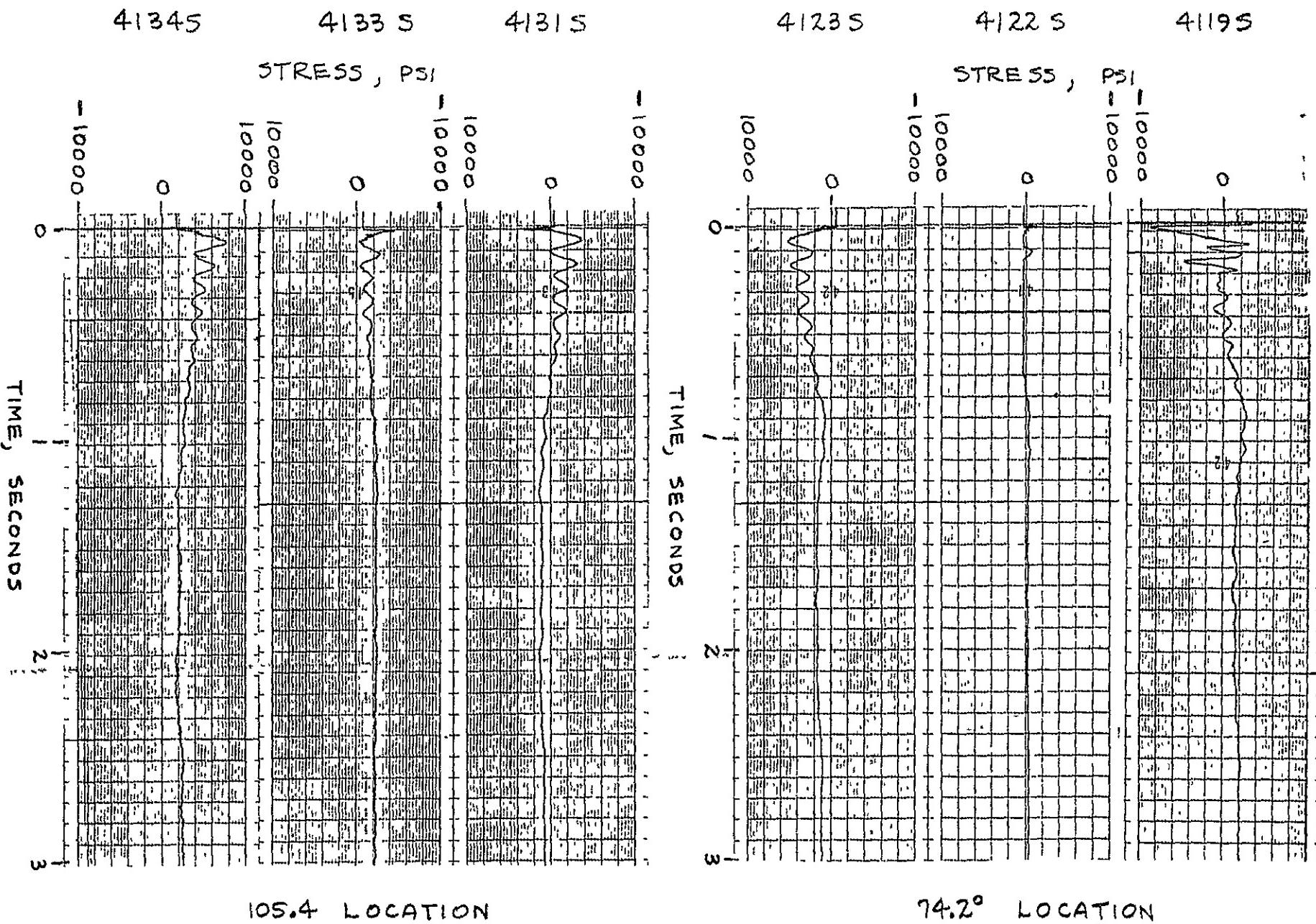
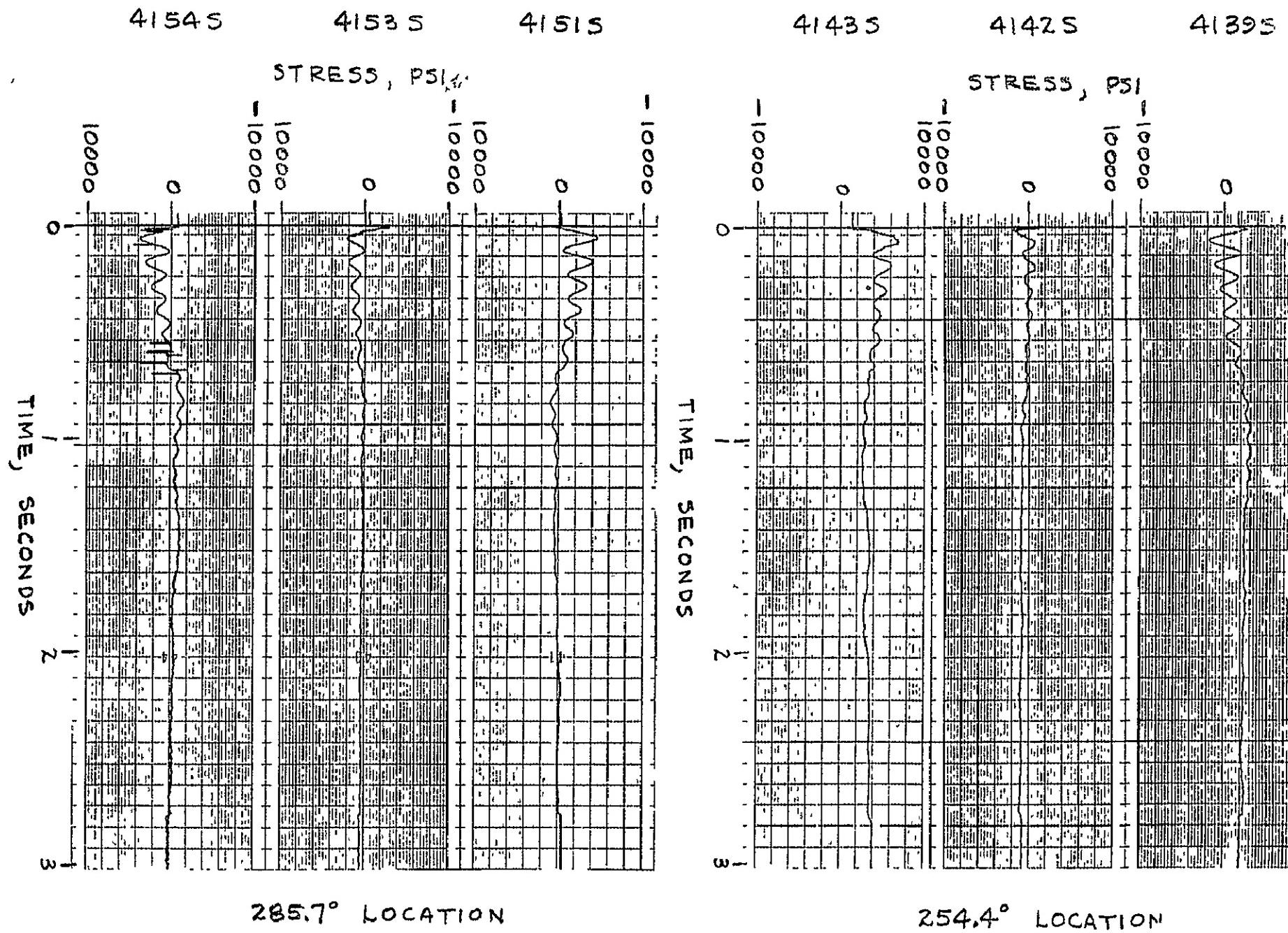


FIGURE D-20 STATION 2209 RING STRESSES FOR TEST 3

116

REPRODUCIBILITY OF THE
ORIGINAL PAGE IS POOR



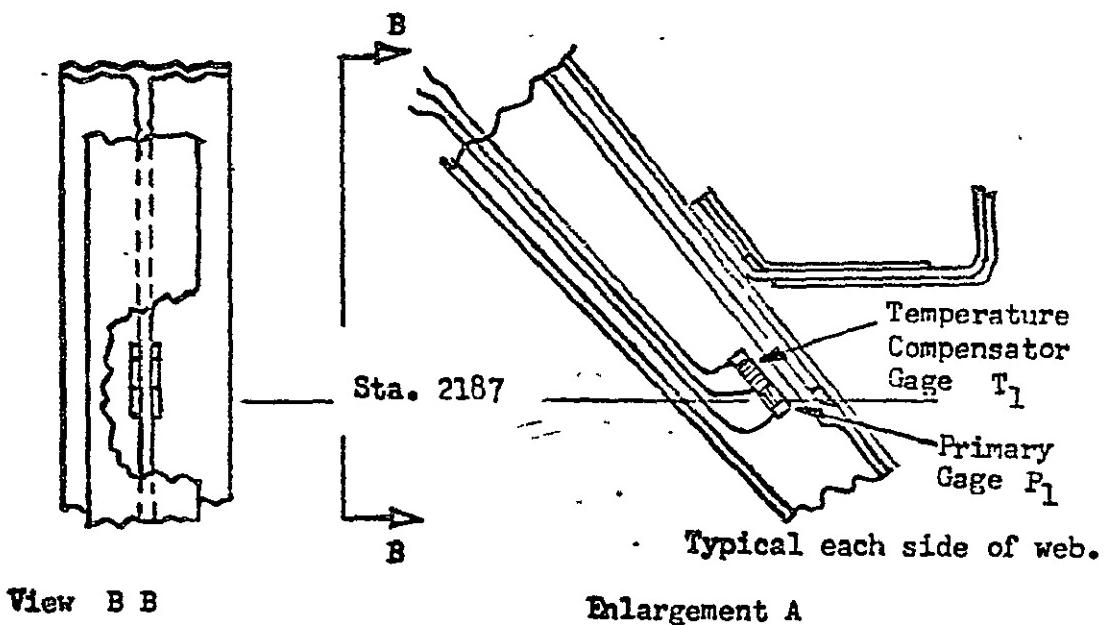
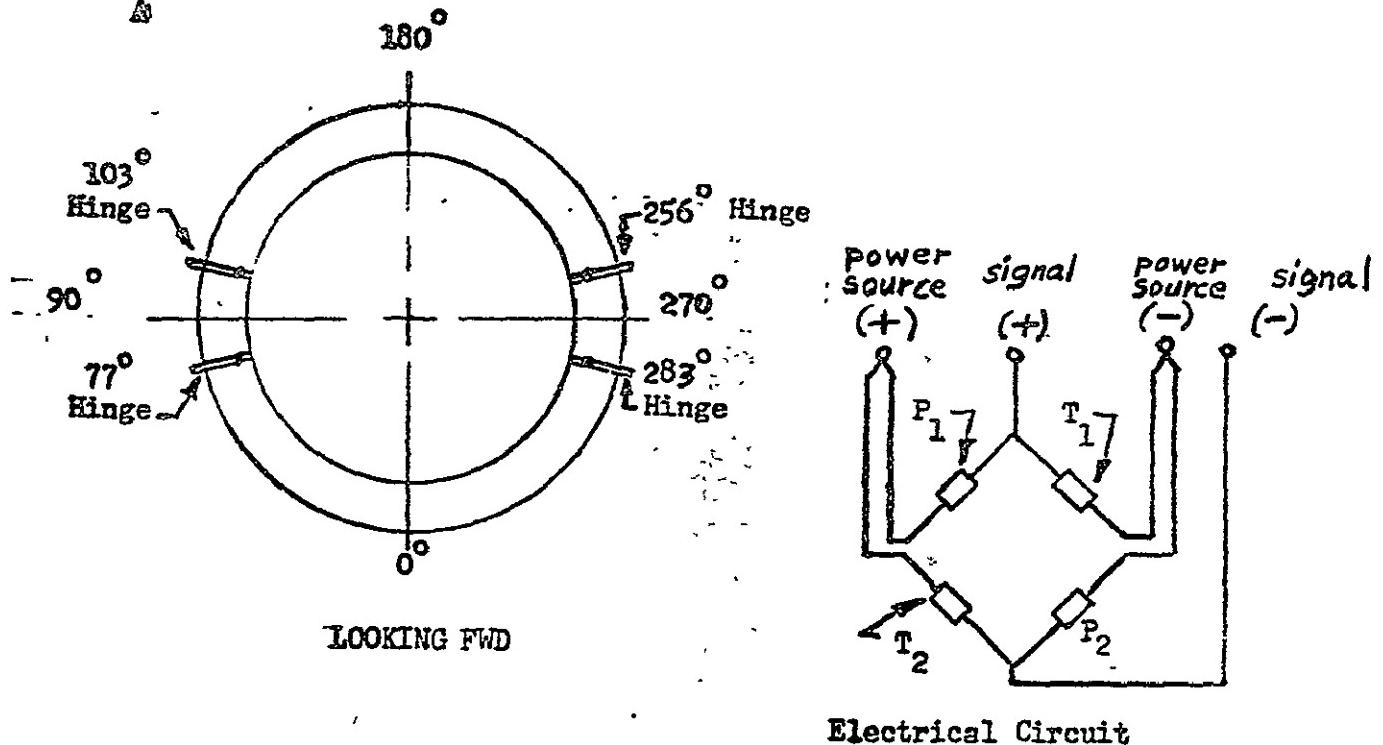
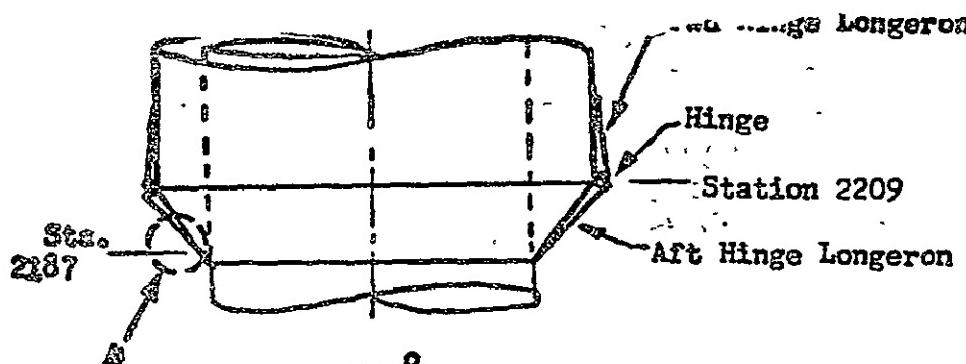


Figure IV-21. Aft Hinge Longeron Strain Gages.

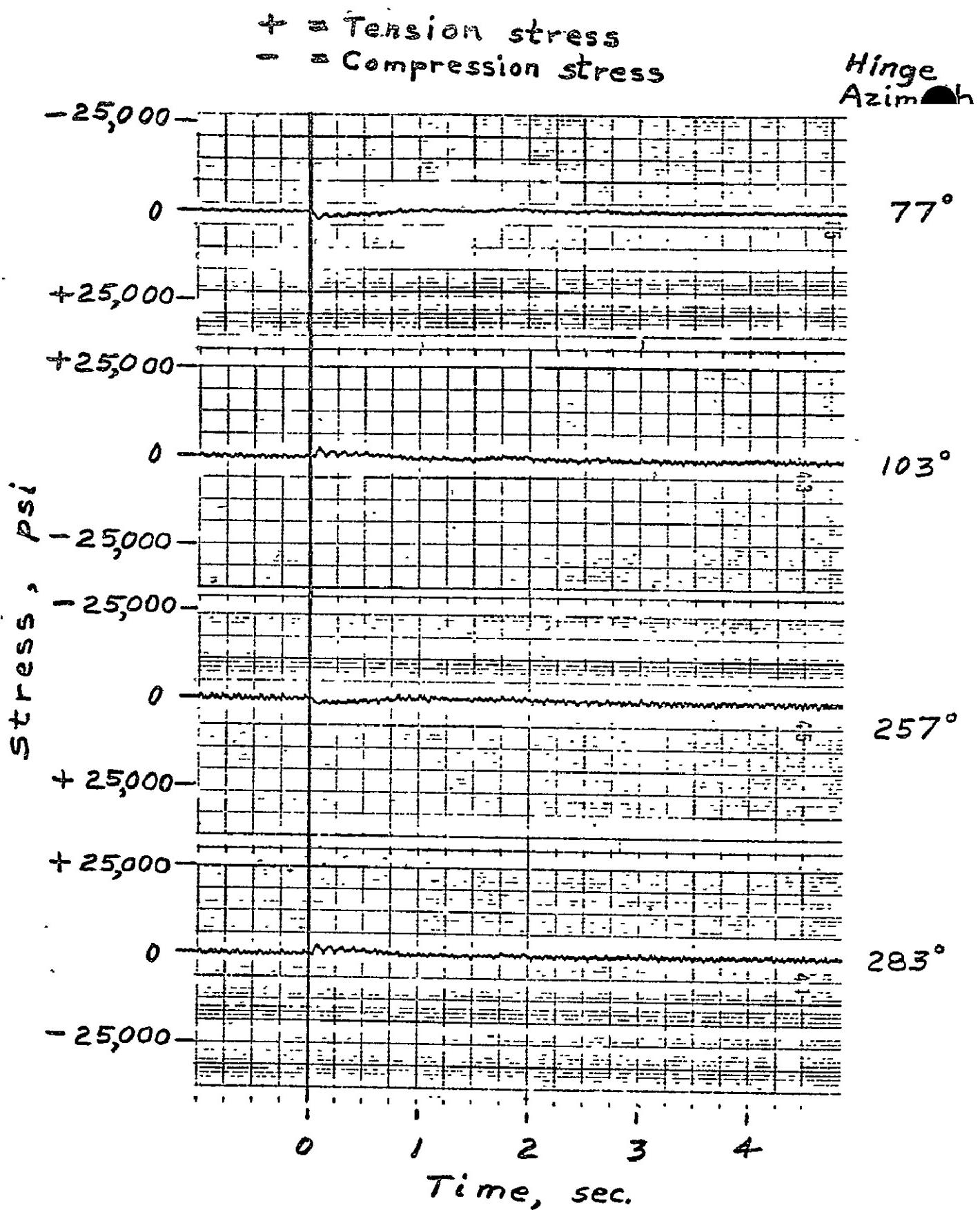


Figure II-D-22. Aft Hinge Longeron Stresses at Station 2187, Test No. 1.

REPRODUCIBILITY OF THE
ORIGINAL PAGE IS POOR

+ = Tension stress
- = Compression stress

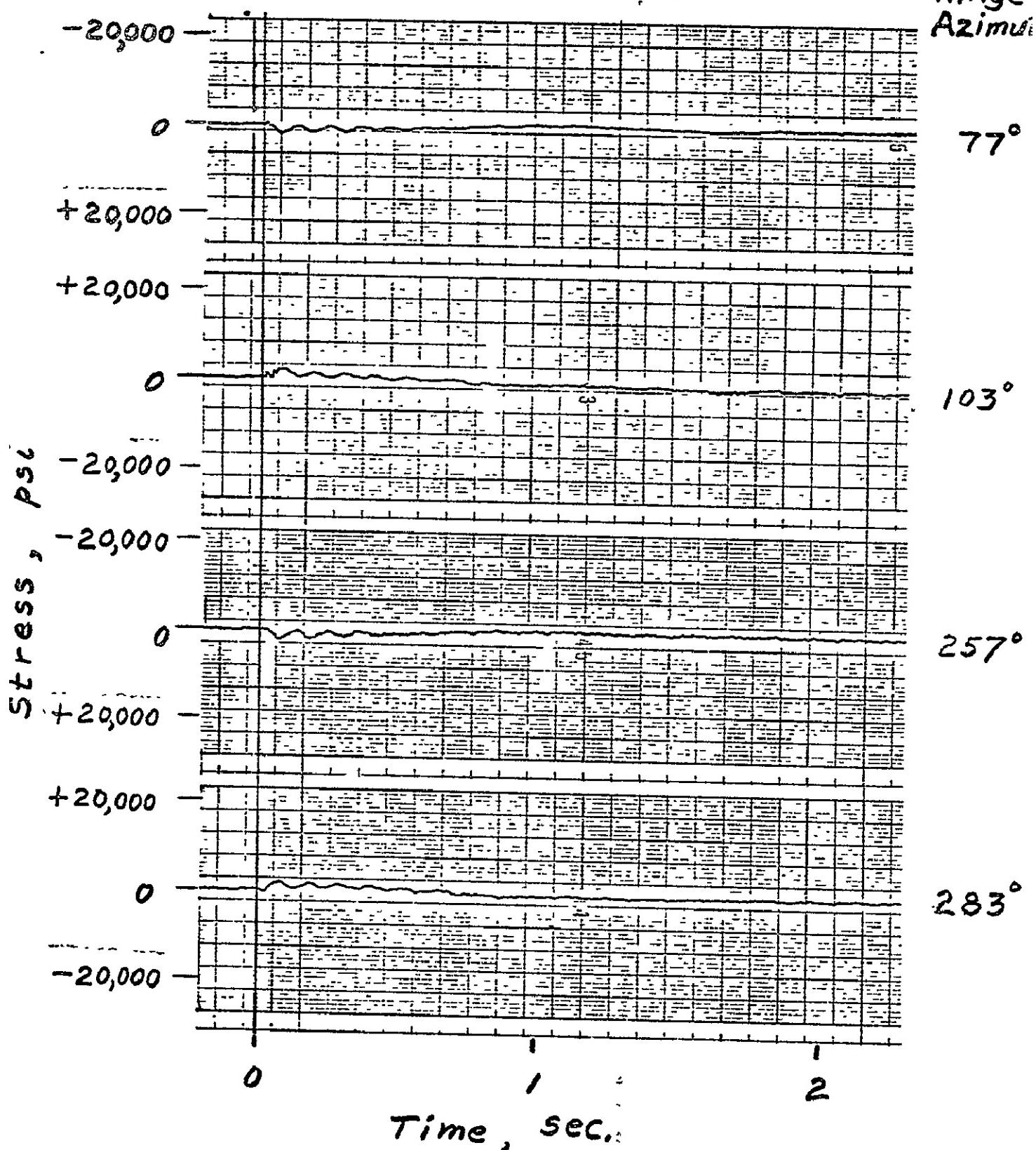


Figure IV-D-23. Aft Hinge Longeron Stresses at Station 2187, Test No. 2.

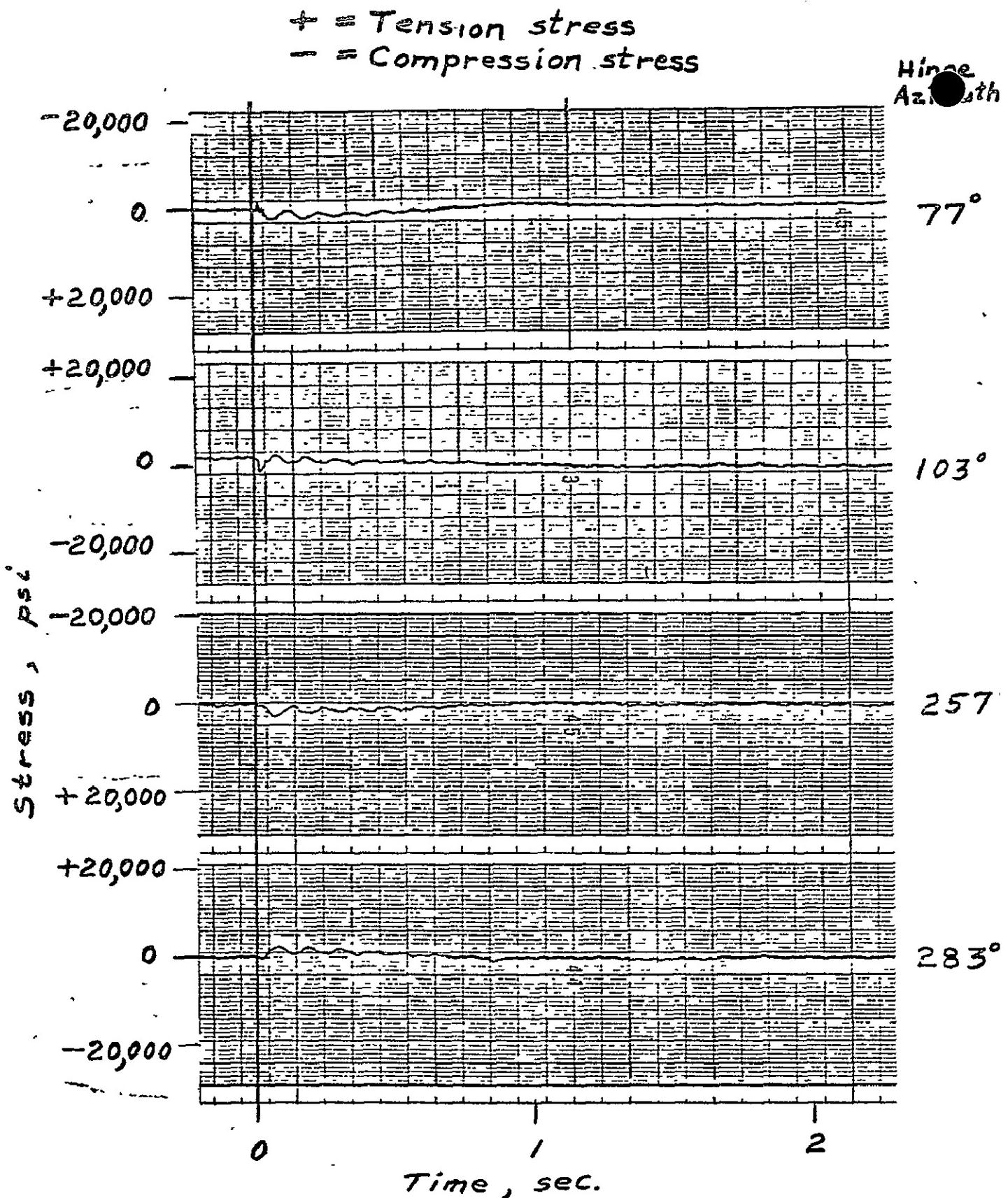


Figure IVD-24. Aft Hinge Longeron Stresses at Station 2187, Test No. 3.

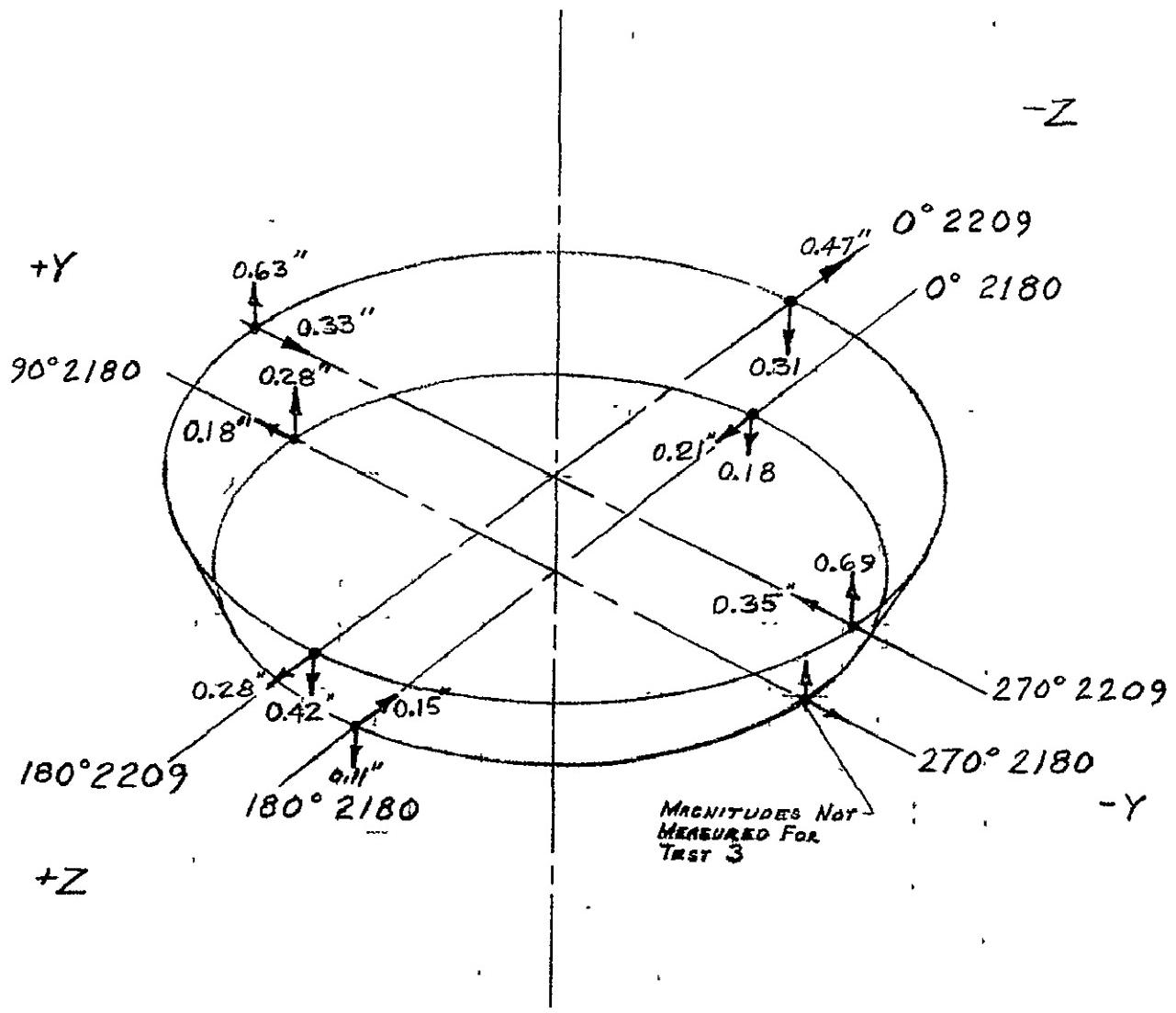


FIGURE XD-25 DIRECTIONS & PEAK DEFLECTIONS OF BOATAIL - TEST 3

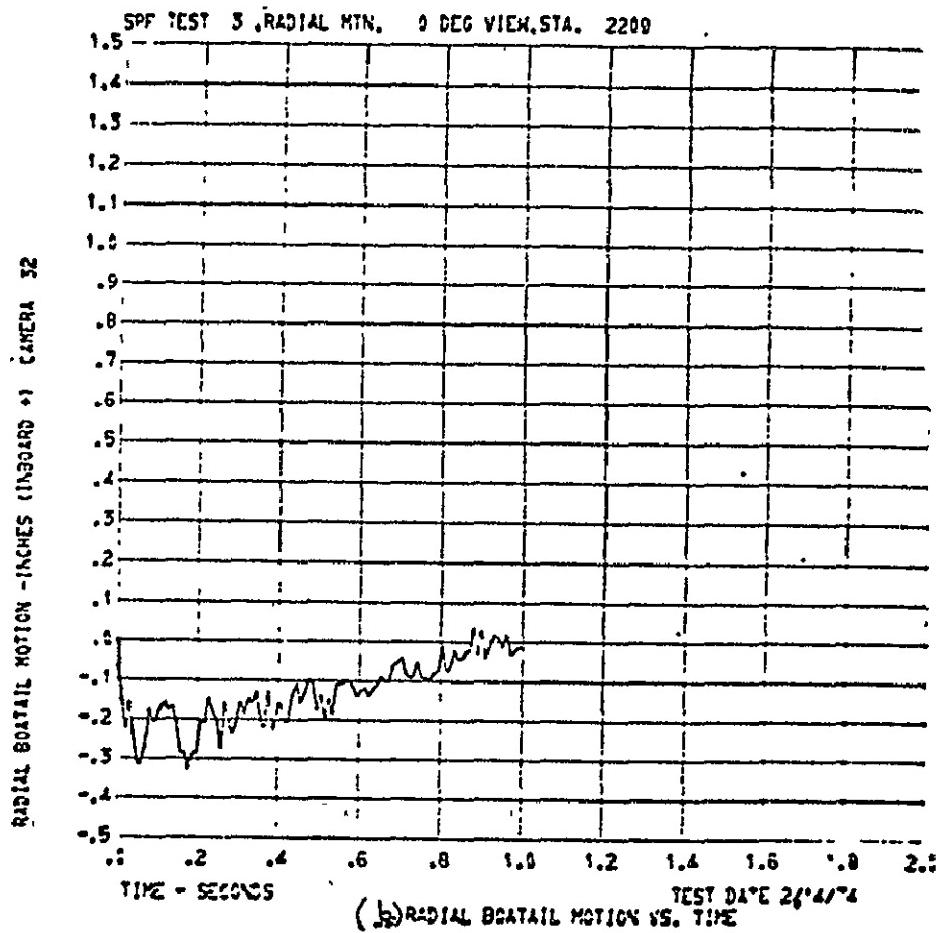
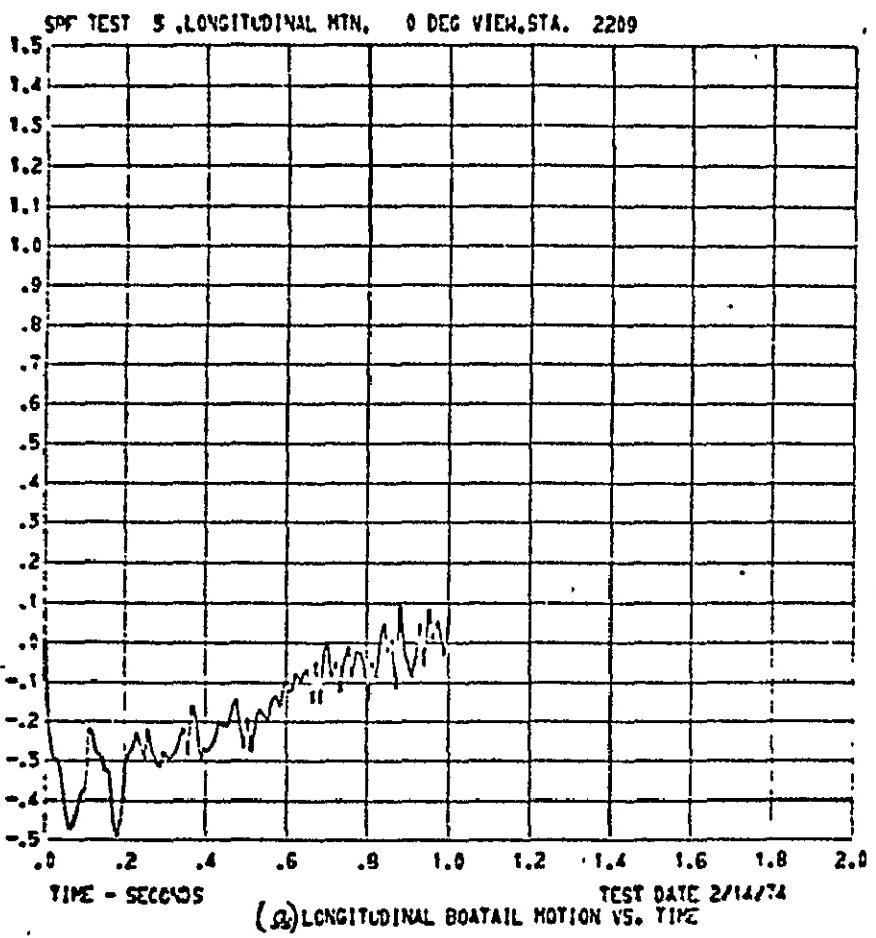


FIGURE II-D-26 BOATTAIL MOTIONS DURING TEST 3

REPRODUCIBILITY OF THE
ORIGINAL PAGE IS POOR

LONGITUDINAL INTERSTAGE MOTION - INCHES / CAMERA 32

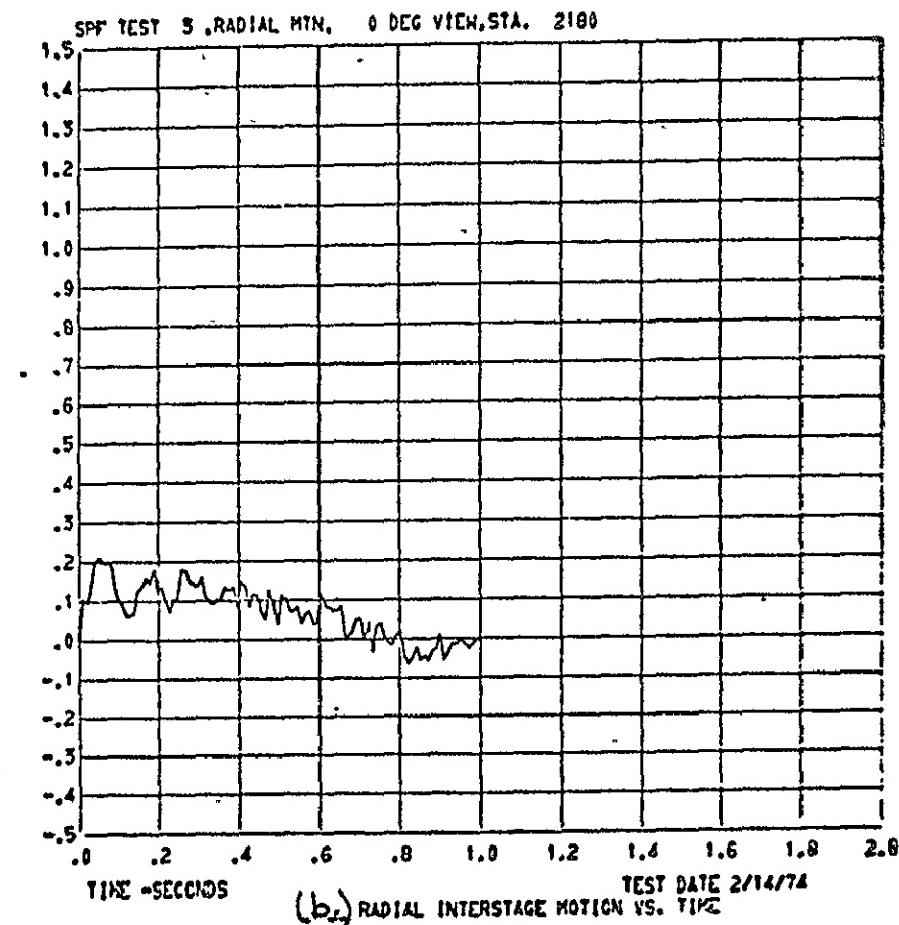
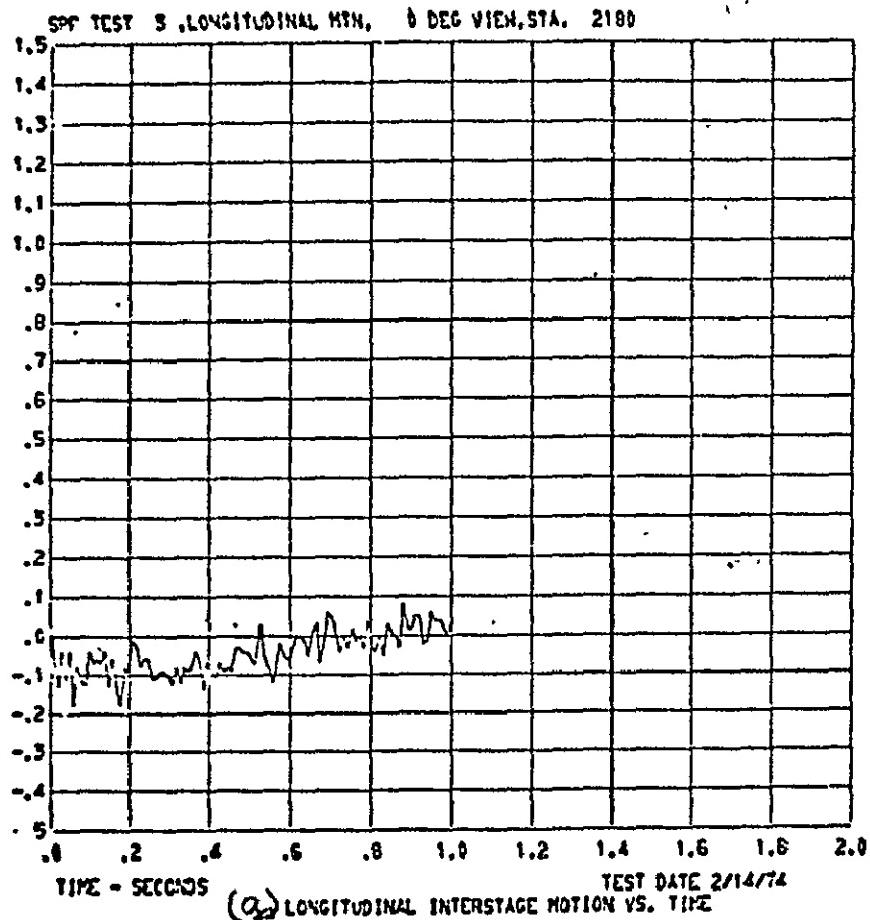


FIGURE ID-27 BOATTAIL MOTIONS DURING TEST 3

124

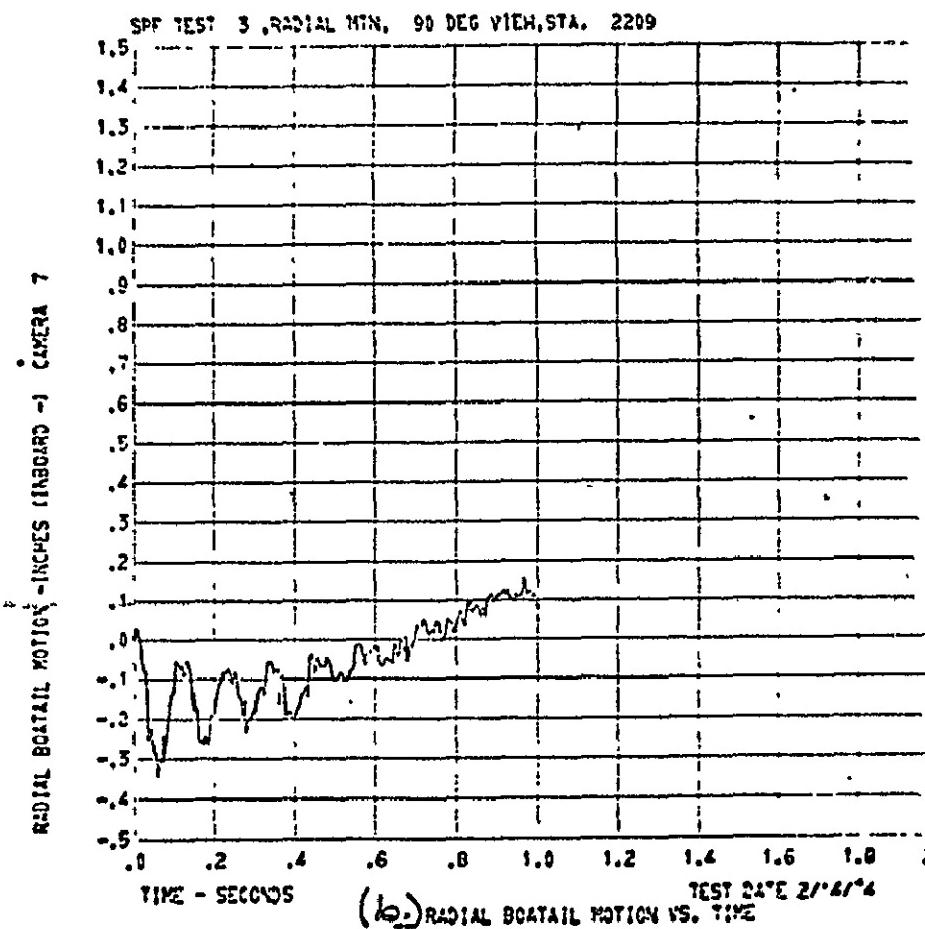
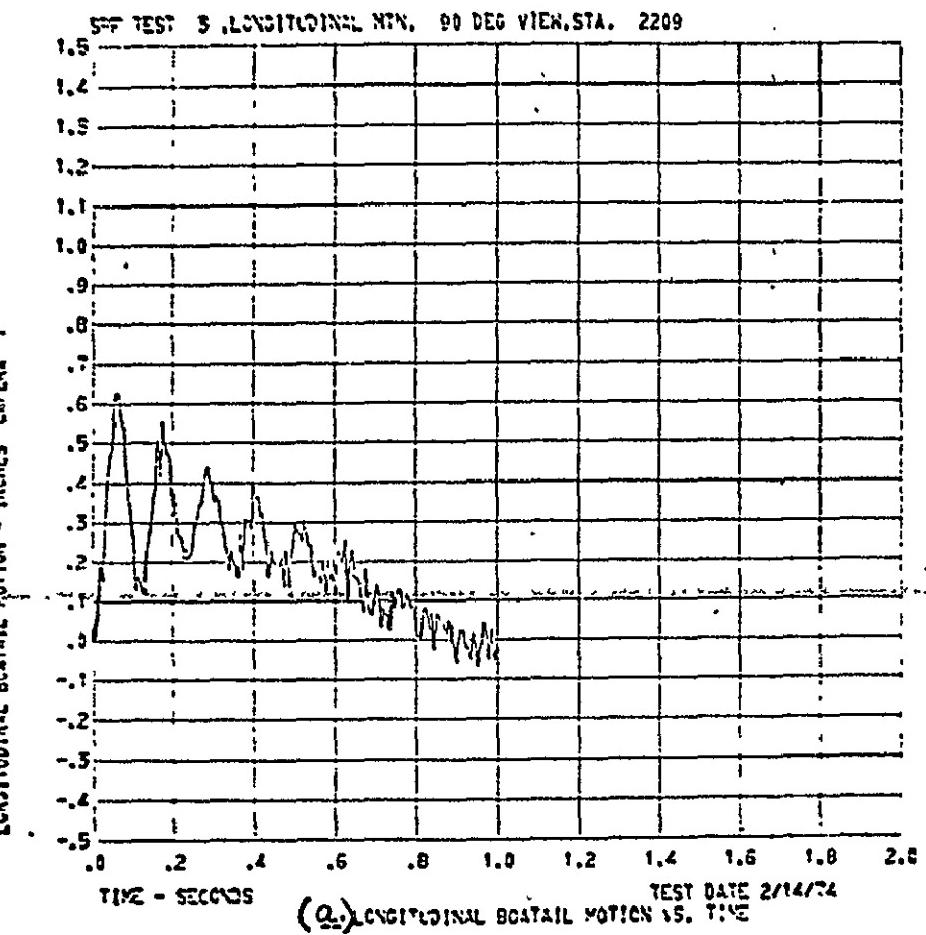


FIGURE IVD-28 BOATTAIL MOTIONS DURING TEST 3

LOG 1

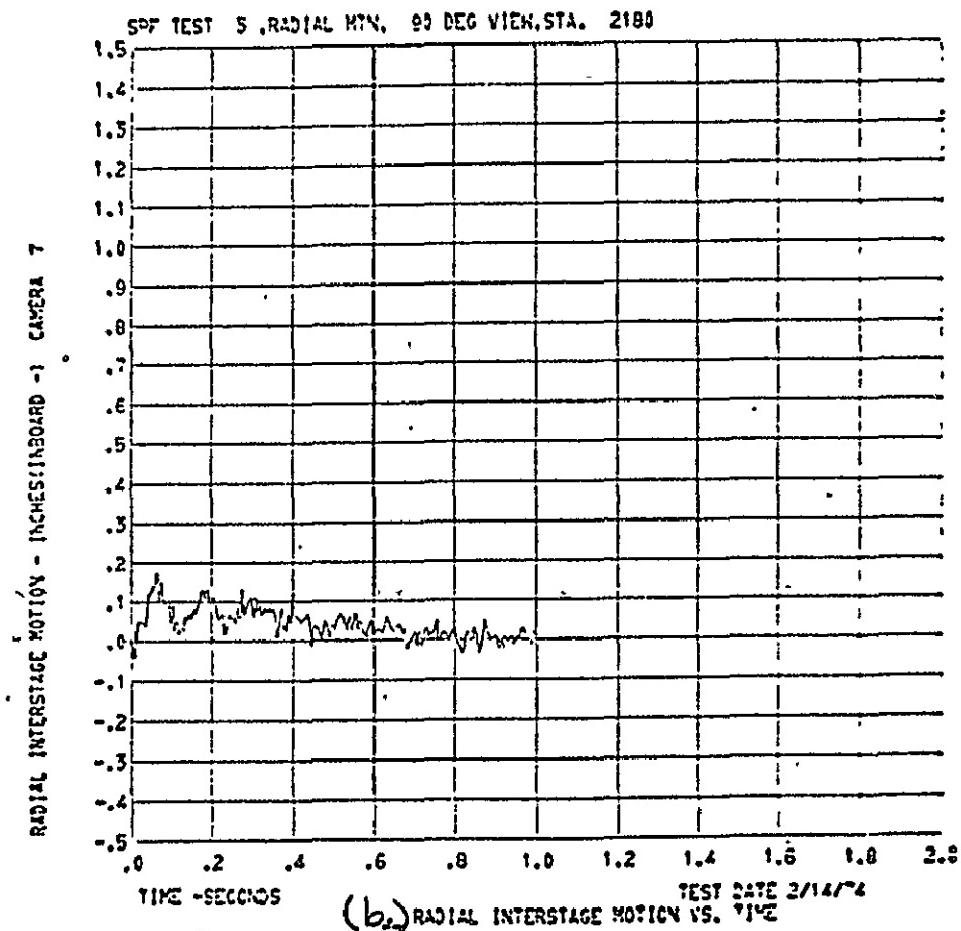
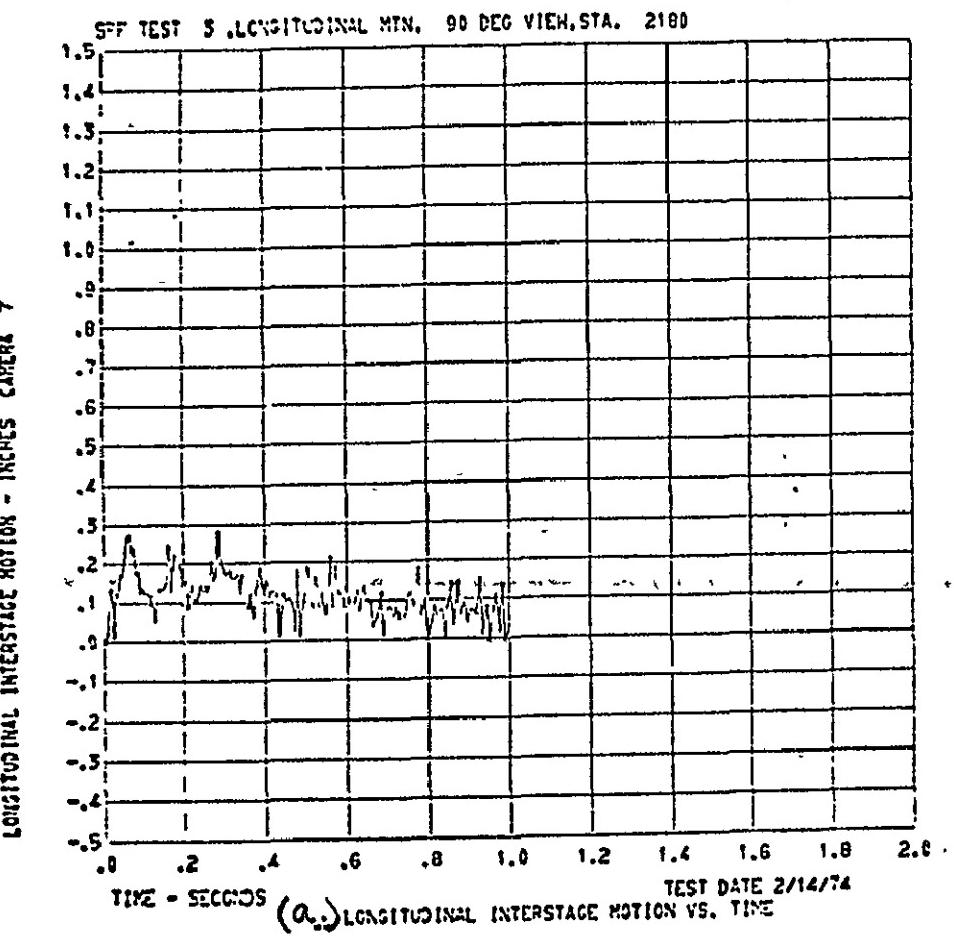


FIGURE IID-29. BOATTAIL MOTIONS DURING TEST 3

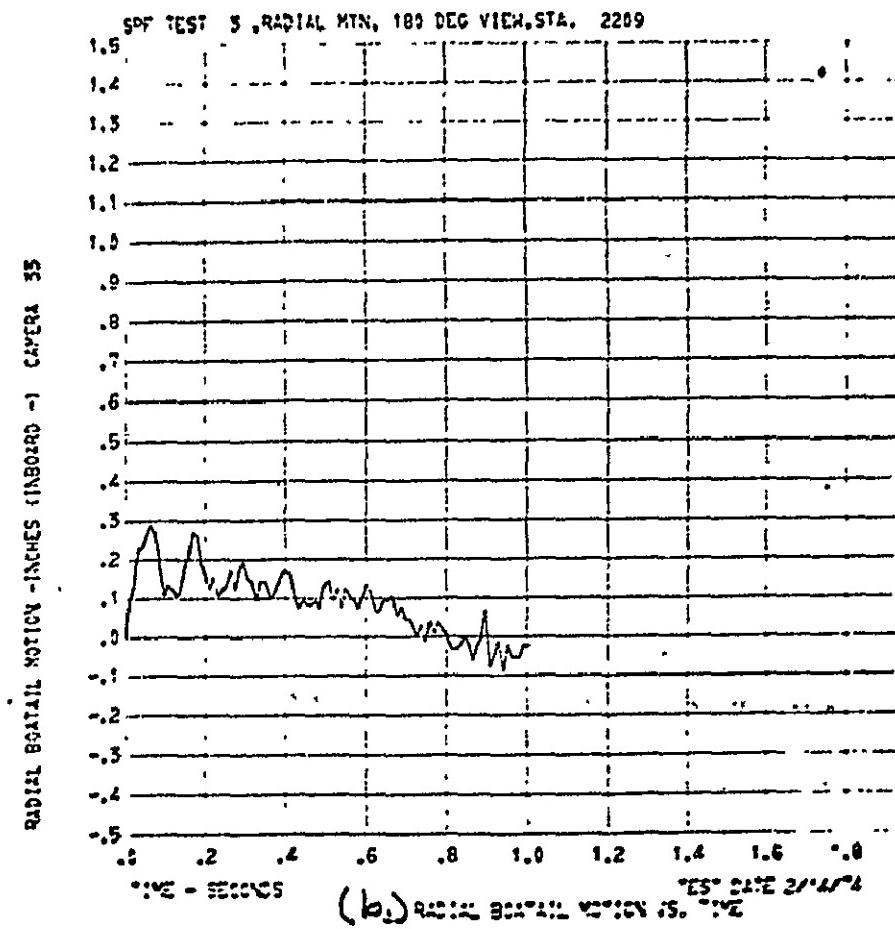
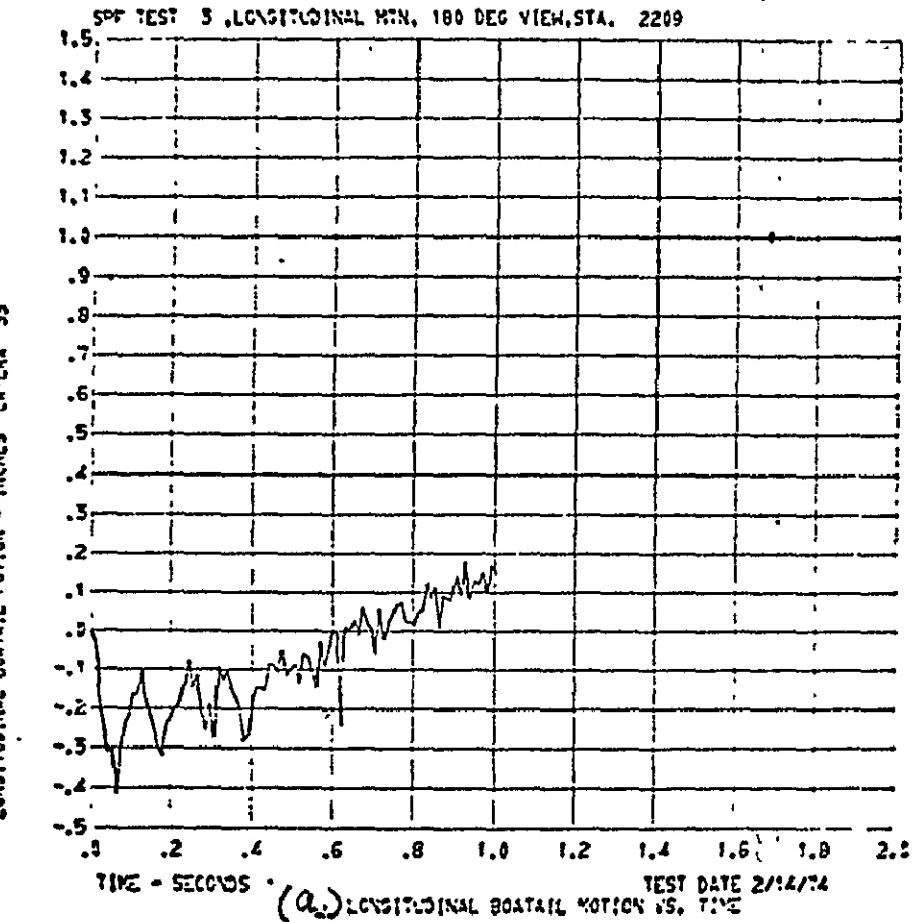
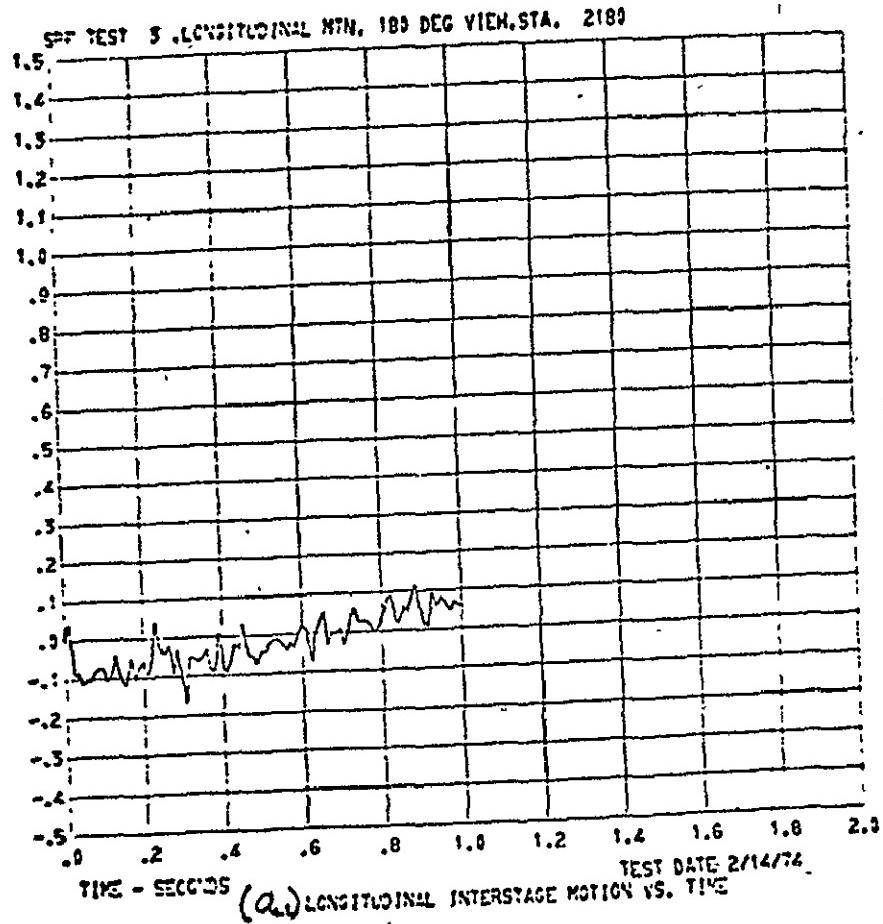


FIGURE VD-30 BOATTAIL MOTIONS DURING TEST 3

LATERAL INTERSTAGE MOTION - INCHES CAVERA 33



RADIAL INTERSTAGE MOTION - INCHES(11 BOARD -1) CAVERA 33

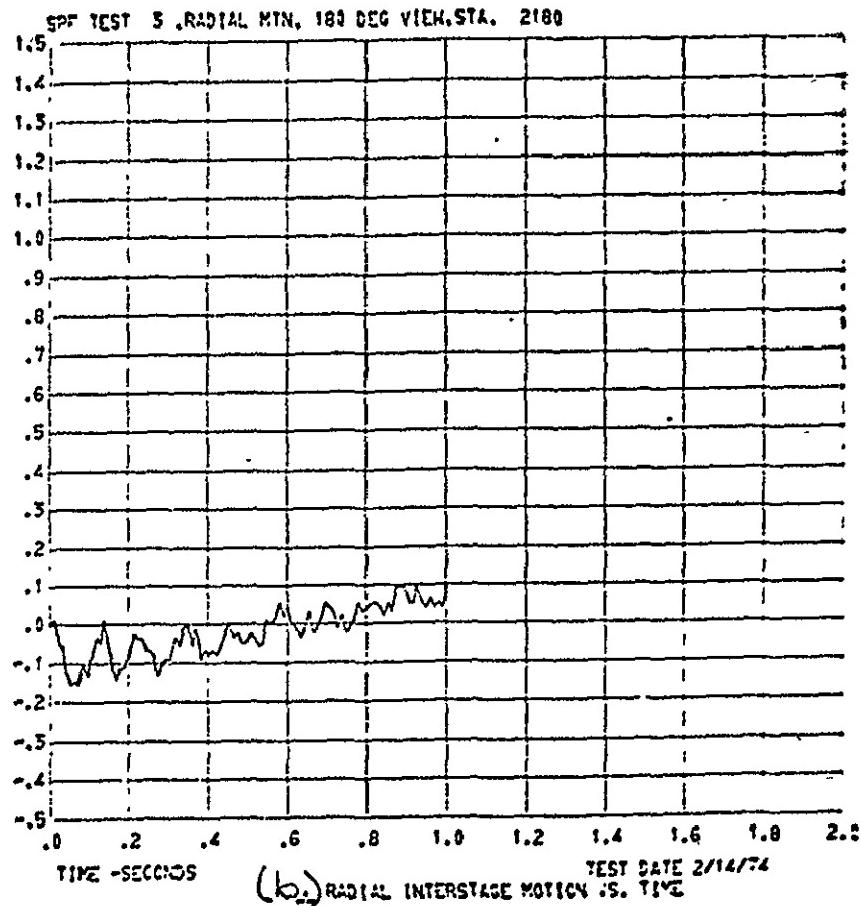


FIGURE IV D - 31 BOATTAIL MOTIONS DURING TEST 3

REPRODUCIBILITY OF THE
ORIGINAL PAGE IS POOR

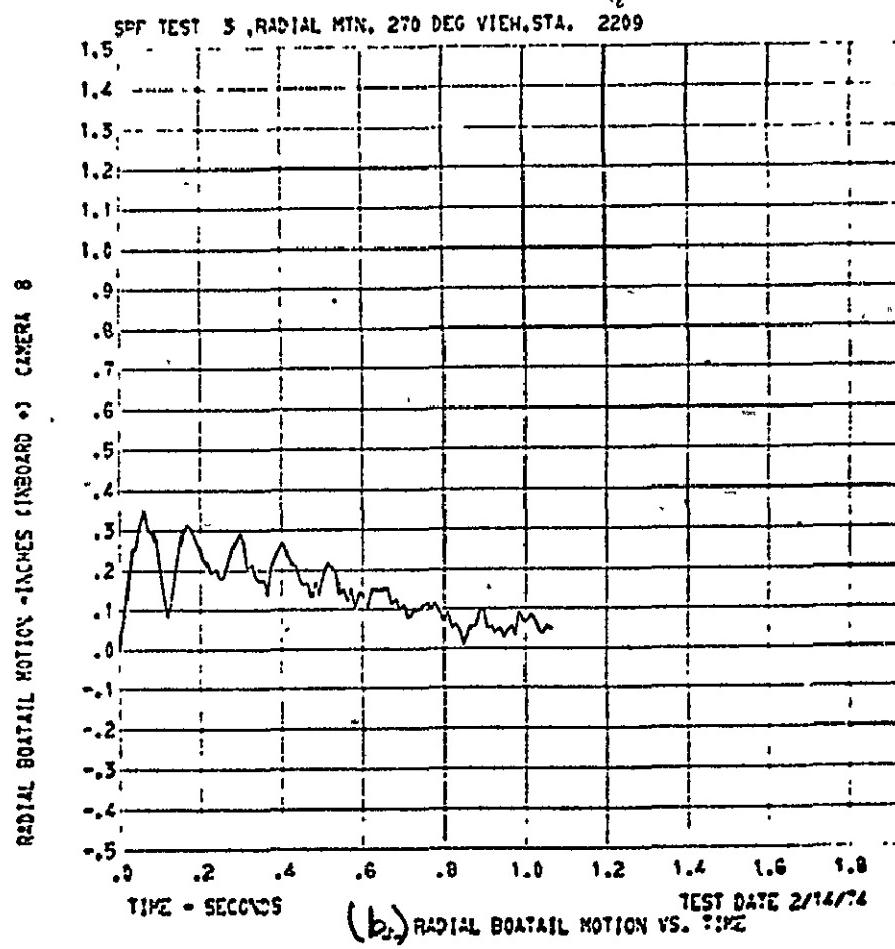
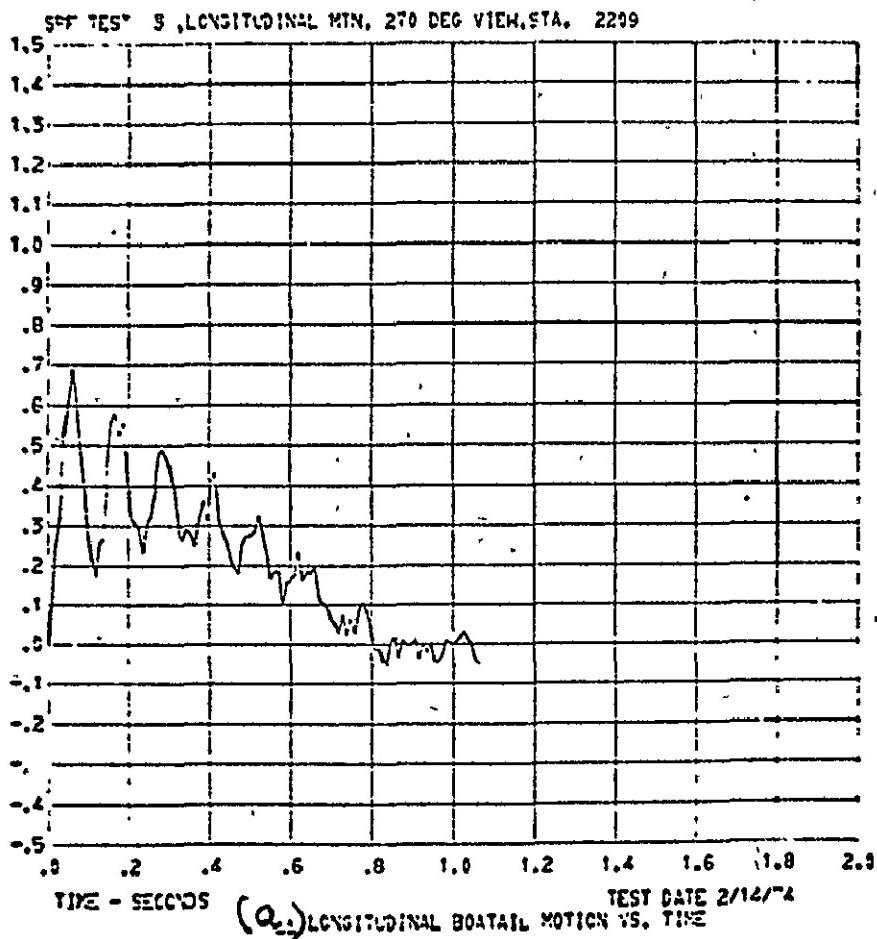


FIGURE IV-D-32 BOATTAIL MOTIONS DURING TEST 3

V.E. CSS Jettison Performance

Thomas L. Seeholzer, John L. Collins, and Theodore W. Porada

Super-Zip System

The primary firing mode of the Super-Zip system was successfully demonstrated in the three jettison tests. However, anomalies relative to the secondary firing mode occurred. These anomalies did not compromise the primary function, but could seriously affect the secondary system. Modifications to the system design were incorporated as a result.

The Super-Zip separation systems, both primary and secondary, are shown in figures VE-1 and VE-2. The systems incorporate a longitudinal and circumferential joint consisting of two explosive cords in a stainless steel tube as shown in figures VE-3 and VE-4. When either cord is ignited, the resultant pressure expands the tube and fractures the doublers, figure VE-4.

Each Super-Zip joint is redundantly activated by electric detonators as shown in figures VE-5 and VE-6. At the payload section, there are detonation transfer lines which bridge the field joint and ignite the cord by means of nonelectric detonators, figure VE-2.

The secondary system in an actual flight is fired 0.5 seconds after primary command only in the event the primary system fails to separate the CSS. Deactivation of the secondary system is accomplished by electrical disconnects located as shown in figure VE-7. For these tests, the secondary system was activated after the primary system had fired and the CSS was in the nets.

Electrical Description. - The electrical system for initiation of the Super-Zip for these tests is shown in figure VE-8. Power to the electric detonators was supplied by a 28-volt battery. The Squib Fire Circuits (SFC's) were supplied with 28 VDC power. The SFC's were activated and allowed current to flow to the detonators when a control signal was applied. This control signal was applied through contacts of a programmer controlled firing relay. Power was routed from the SFC's through resistor packages to the detonators and returned through current shunts. The resistor packages were designed to provide the proper amount of current and to limit the current in the event of a shorted detonator or short circuit. The SFC's and current shunts are Titan flight-type hardware.

Each SFC supplies power to four detonators in the primary system. The secondary system was initiated when the CSS had been jettisoned and in the nets by means of adapter cables at the Titan/CSS interface, and by inserting test cables between the in-flight disconnects.

Test Results. - During the three jettison tests, the Super-Zip primary system successfully separated the CSS.

Tube Ruptures - Tests 2 and 3: Following separation and jettison of the CSS into the nets, the secondary separation system was initiated to verify proper performance. On the first test, no anomalies were noted. In tests 2 and 3, the circumferential tube ruptured. This anomaly, as shown in figure VE-9, was attributed to improper installation of a cushioning tape as shown in figure VE-10.

This tape prevents coining of the tube by tool marks in the adjacent ring which can cause a tube rupture. Two layers of tape are required. Only one layer had been applied.

Verification that the ruptures occurred during secondary system firing was made by performing a pressure check of the Super-Zip system following primary system activation on test 3.

Barrier Anomaly - Test 3: On this test, the secondary system cord in the payload section failed to propagate beyond the detonator blocks. After inspection of the hardware by LeRC and contractor personnel, it was determined that the secondary cord broke at the end of the detonator blocks during primary system firing. This was verified by X-rays of the tubes adjacent to the detonator blocks (fig. VE-11) and inspection of the detonator blocks and tubes (figs. VE-12, VE-13 and VE-14).

It was further determined that the barrier which separates the primary and secondary cord had moved due to a failure of the retaining screw during primary firing. The apex of the barrier (ref. fig. VE-15) cut the secondary cord. The contractor (LMSC) conducted tests which substantiated this mode of failure.

As a result of the above failure investigation, the Super-Zip system was modified as shown in figure VE-16. The modifications were as follows:

1. A steel rivet was added to retain the barrier.
2. The barrier clip retention screw was modified to provide better shear transfer.
3. An anti-rotation feature was added to the clip.

These modifications were successfully qualified at the component and subsystem level by the contractor. The design was then incorporated and successfully flown on the TC-2 flight and is effective on all future Centaur Standard Shrouds.

CSS Vehicle and Payload Electrical Disconnects

In-flight electrical disconnects were located at the E/M, at the CSS boattail, and at the spacecraft model as shown in figure VE-19. The disconnects

at the E/M are shown in figures VE-20 and VE-21. They were located at azimuths 66° and 252°. Electrical, instrumentation, and R.F. connectors were connected from the Centaur vehicle to the CSS at these two points.

Each connector/disconnect had a primary and secondary disconnect mode. The primary mode imposed a 30-pound load on the CSS while the secondary mode imposed approximately a 300-pound load.

At the base of the CSS, as shown in figures VE-22 and VE-23, was an R.F. blackout disconnect. This disconnect was similar to the R.F. connectors on the E/M.

For the Helios missions, and installed on these tests, were disconnects between the CSS and spacecraft (model). This tripod disconnect, as shown in figure VE-24, consisted of two R.F. and one electrical disconnect similar to those at the E/M.

All of the above cables were disconnected at CSS jettison by lanyards attached to each connector at their respective panel.

Electrical Disconnect Anomaly. - A review of the jettison test movies indicated the CSS boattail deflected aft and the CSS itself moved forward immediately following Super-Zip system separation. Premature separation of the electrical disconnects is possible under this condition (See figs. VE-7 and VE-17). The electrical disconnect must remain engaged as long as there is a possible secondary firing mode requirement. In the case of a primary mode longitudinal failure, vertical motion could cause premature disconnect of the secondary firing mode electrical circuit preventing CSS jettison. .

The time of disconnect from flight and jettison test data was less than 0.04 seconds after primary mode actuation.

The electrical disconnect had a mechanical stroke of 0.375 inches. Beyond this, electrical contact is lost. The initial vertical deflection of the CSS, at separation, exceeded this value.

As a result, the disconnect was modified, as shown in figure VE-18, as follows:

1. The stroke was increased by 1.125 inches, giving a total of 1.500 inches prior to disconnect.

2. A spring was added to ensure 1.125-inch bracket motion prior to the 0.375-inch disconnect travel.

3. The retraction spring was removed to eliminate side load.

The contractor (LMSC) successfully conducted bench tests of the modified design. The longer stroke disconnects were incorporated and successfully

flown on the TC-2 flight and are effective on all follow-on Centaur Standard Shrouds. Flight data indicated the time of modified electrical disconnect function was 0.2 seconds after firing of the primary system. This is acceptable since the command for secondary system function is not sent until 0.5 seconds after primary command. Therefore, for a normal separation, the secondary system is properly deactivated.

Titan Vents. - The Titan skirt vent duct bellows disconnects were installed on these tests. These disconnects consist of four fiberglass bellows assemblies, as shown in figures VE-25 and VE-26, installed between the CSS and the ISA. At CSS jettison, the vent ducts disconnect as shown in figure VE-26.

Test Results. - The disconnects separated normally in the primary mode on all three tests. On heated jettison test 2, the lanyard broke on the R.F. disconnect at the 66° E/M panel. This, however, did not impair disconnect function. Failure was attributed to the fact that the lanyard had been subjected to prior tests in the cryogenic unlatch series at Plum Brook (ref. 3).

For the Helios tripod disconnect, a portion of the spacecraft envelope was simulated to verify the assembly properly cleared the spacecraft. Motion picture data from test 1 verified adequate clearance existed.

Motion picture and post-inspection coverage of the Titan vents verified that the disconnect function was normal for these tests. One disconnect was damaged during CSS rebound in the nets on test 1. The damaged disconnect was removed for subsequent tests.

Bolt-ons and Disconnects. -

Forward Purge Gas Seal: (fig. III-23) The forward seal's release and separation were reviewed from camera data. The seal cable retainer released as expected and the cable was very slack. Under the tongue depressors (required by forward bearing reaction struts), the seal did not fall away freely; but as the CSS shell halves moved away, during jettison, the seal then separated easily without any hangup. Post-test inspections revealed no hardware damage.

Aft Purge Gas Seal: (fig. III-22) The aft seal separation was also viewed from camera film. The seal separated smoothly as it has done on all previous testing at Plum Brook and San Diego. Post-test inspection revealed no damage to test hardware.

LH₂ Vent Disconnect: (fig. III-25) When the Super-Zip pyrotechnic was ignited, the CSS moved forward; however, the camera viewing the LH₂ disconnect showed a very clean and smooth separation.

Vent Gas Retainer: The vent gas retainer separation was viewed from camera film and the separation was satisfactory and without any serious problem. The loose fabric in the vent gas retainer brushed the memory plate rods indicating that the extra fabric fell inboard. Post-test inspection did not reveal any seal damage.

Forward and Aft Split Line Seals: The separation of these seals was viewed by cameras at the forward and aft purge seals of the split line areas. The data reveals that the seals separated easily and post-test inspection indicated that all split line seals separated satisfactorily.

Forward Split Line Foam Dams: On the first heated jettison test, these dams were not installed properly, but this was corrected on the subsequent heated jettison test. On both heated jettison tests, the dams separated satisfactorily as determined by post-test inspection and camera data.

CSS Jettison Performance. - Analytical Prediction of Rigid Body Trajectories - Analysis results of the CSS jettison dynamics are shown in figures VE-27 and VE-28 in the form of rotational angle and rate of rotation about the CSS hinge points. The state of the CSS is represented as a rigid body; i.e., elasticity of the CSS or its support was not considered. Mass properties and spring parameters were actual measured values. Disconnect forces, frictional forces, and aerodynamics were not included. Some losses, therefore, were expected between the actual potential energy stored in the springs and the resulting kinetic energy of CSS rotation. The energy conversion efficiency was determined by observing the best match between test data and several computer solutions with spring efficiency as a parameter. A spring efficiency of 80 percent was determined to best fit the test data. This data comparison is shown in figure VE-29.

Trajectory data was obtained by using cameras 9 and 10 which picked up data from targets at station 2241. These were used because the targets at this station were in the view of these cameras for a reasonable length of time.

Figures VE-30, VE-31, and VE-32 show views of angular displacement versus time for all three tests. The $\pm Z$ edges were used and are shown for all tests except test 2 where camera 9 failed to operate. Catch net contact by the +Y half was made at approximately 1.3 seconds for each of the three tests. The trajectories are nearly identical and repeatable for the three tests. As mentioned in the section of tangential displacement versus time, the +Y half on the +Z edge has a slightly higher rate of displacement. This difference in slope or rate on the angular displacement curves supports the fact that the CSS was observed twisting counterclockwise as viewed from above by the overall view motion picture cameras.

- NONCONTAMINATING REDUNDANT SYSTEM
- CENTAUR INITIATES COMMANDS
- TITAN PROVIDES POWER

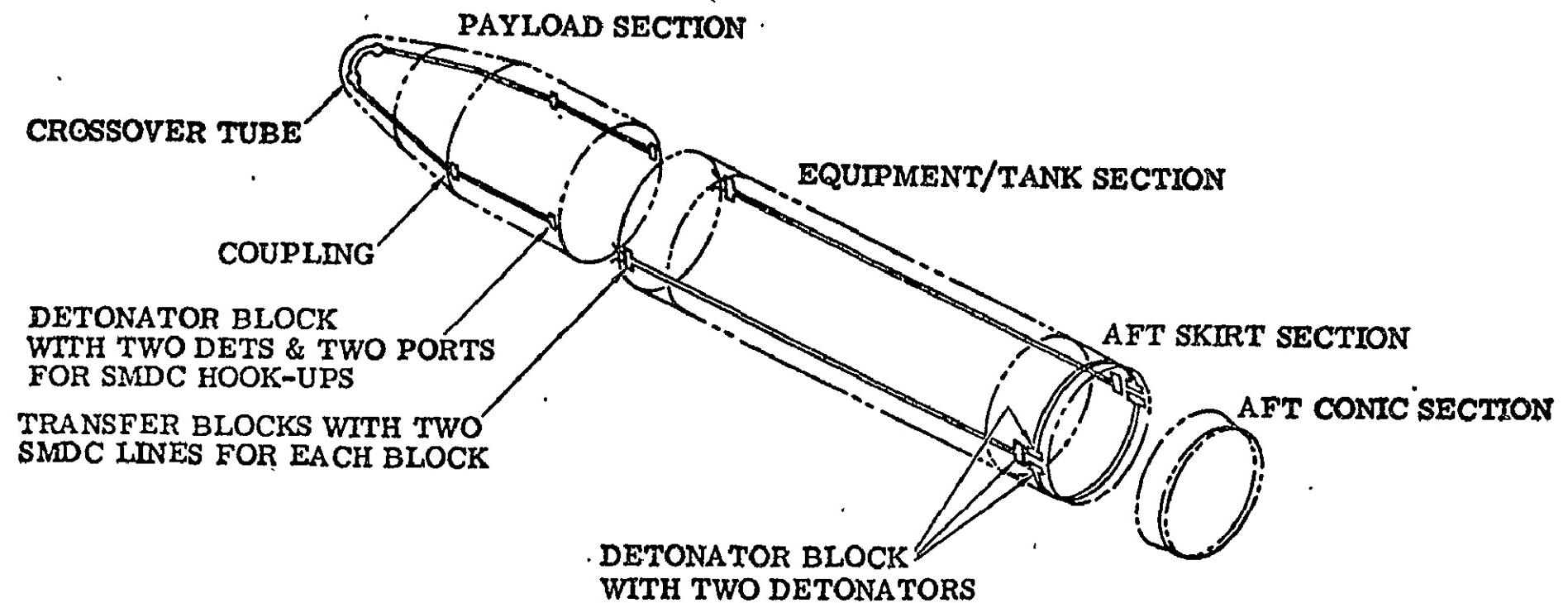
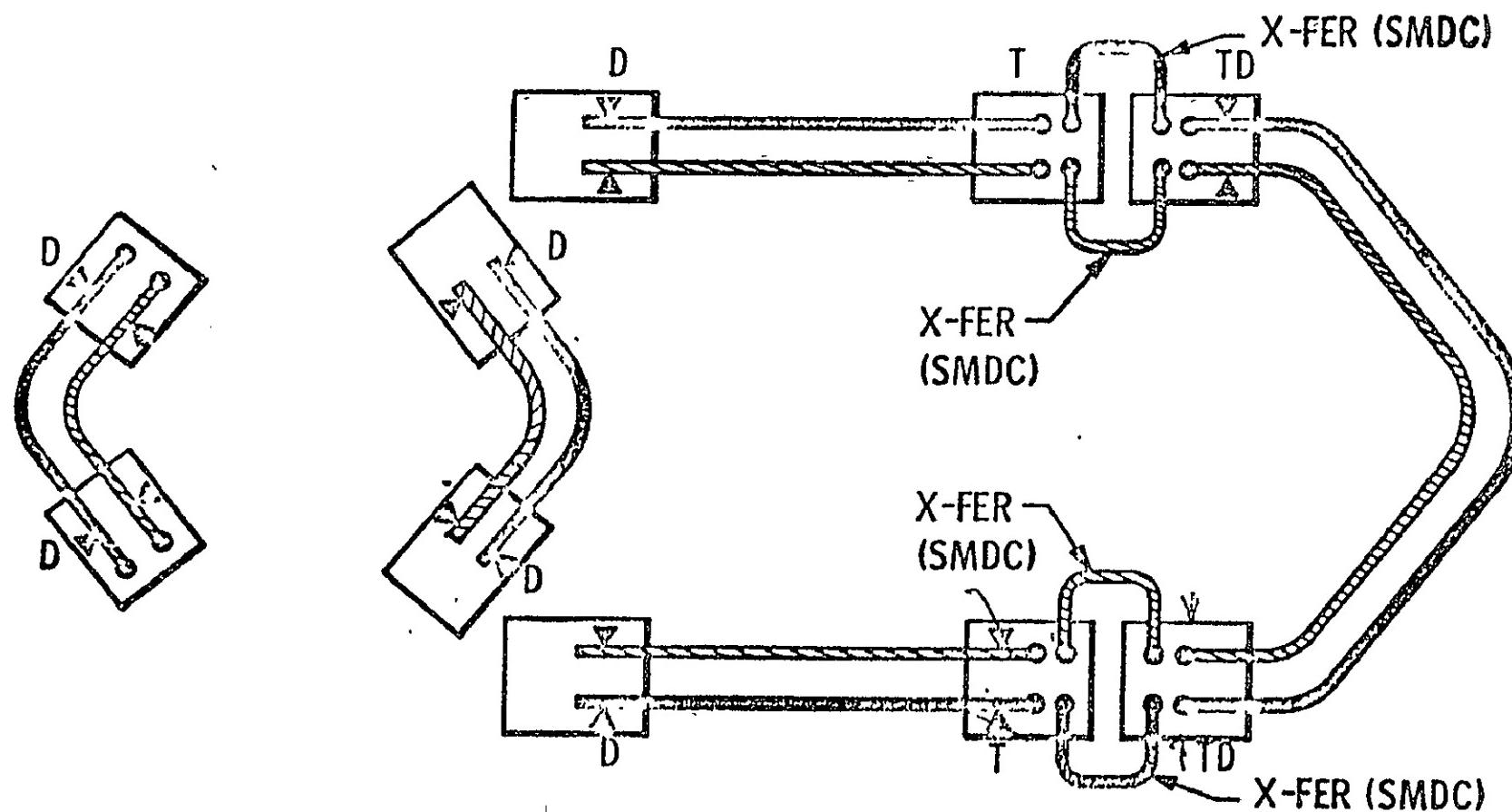
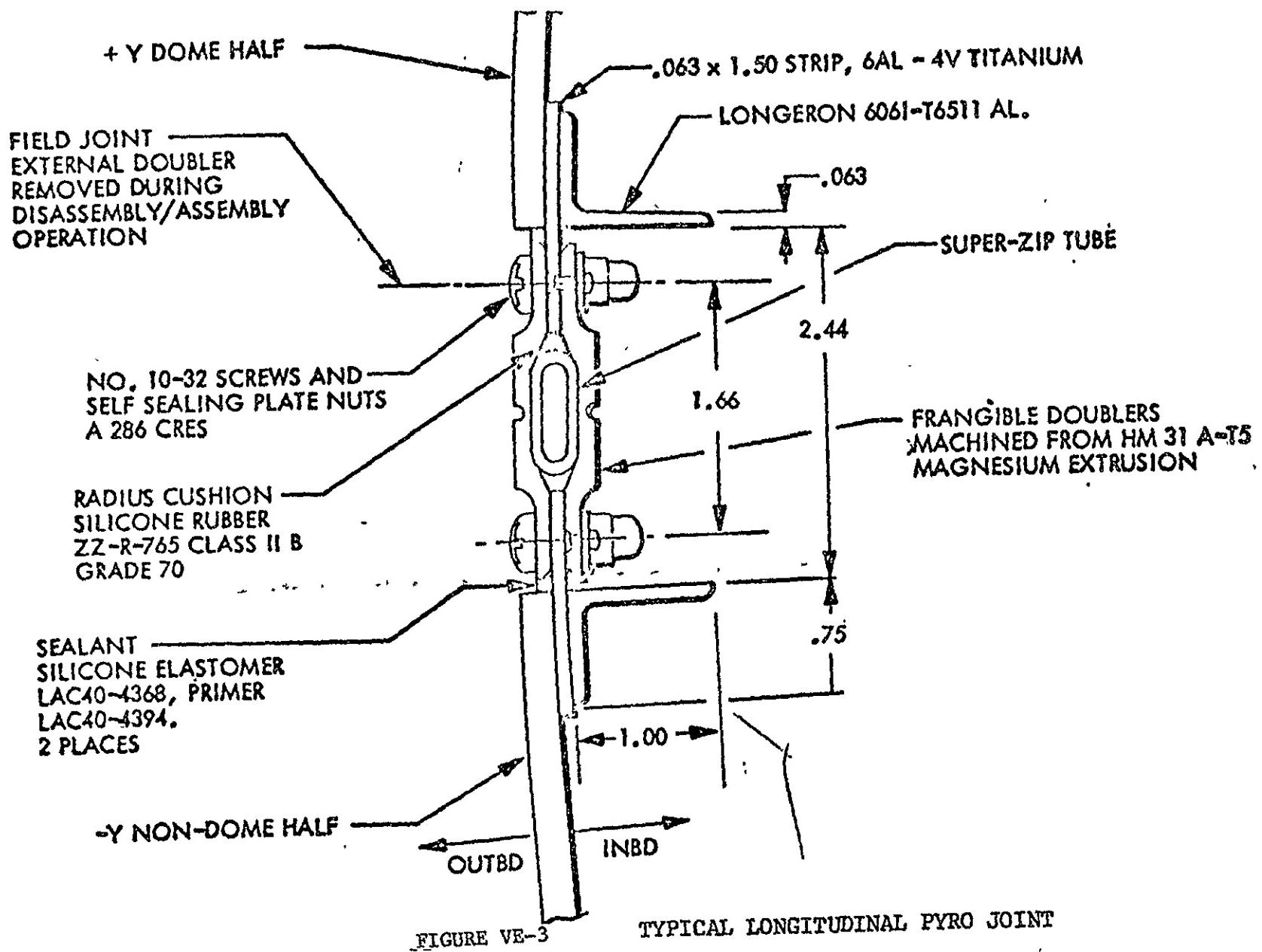


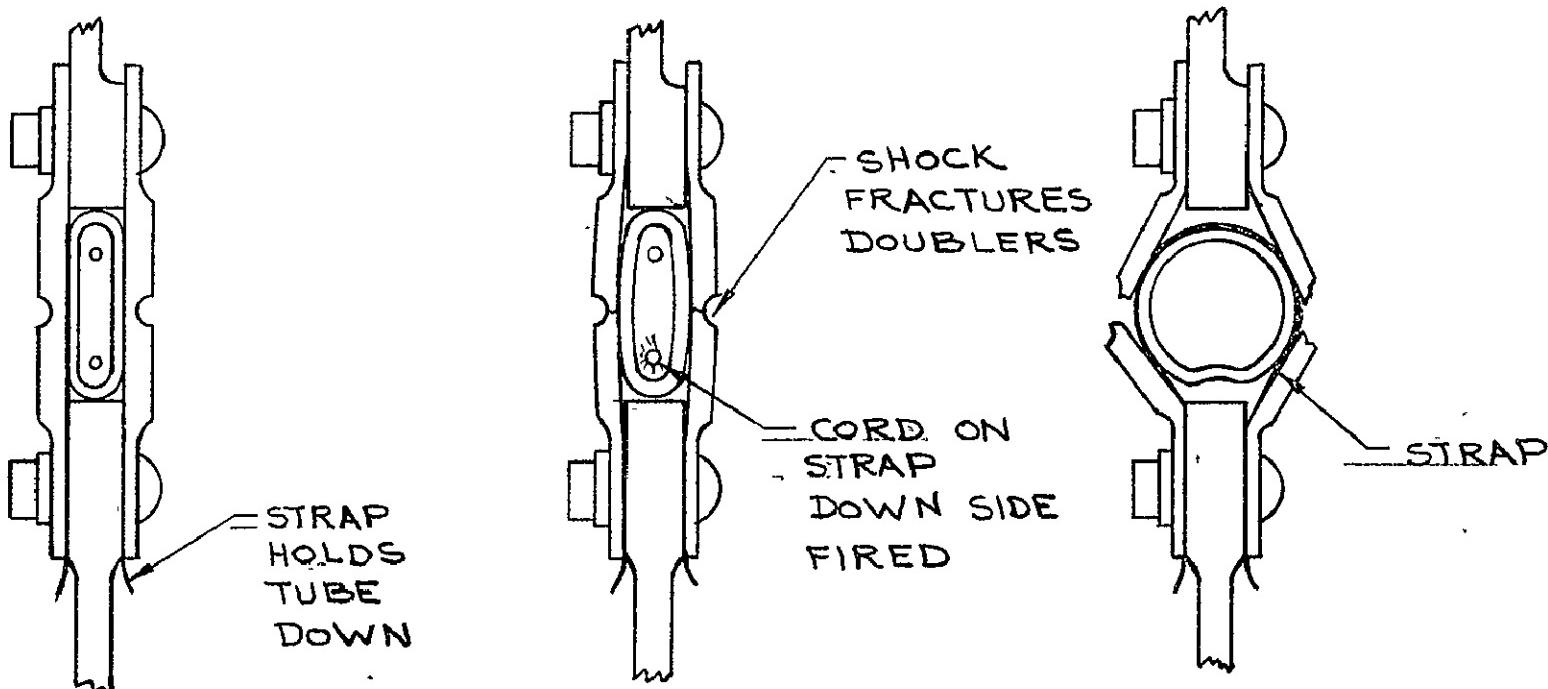
FIGURE VE-1 PYRO SUPER-ZIP JOINT ARRANGEMENT



—	PRIMARY SYSTEM	16
—	SECONDARY SYSTEM	16
◎	NON-ELEC. DET	6
▲	ELECTRIC DETONATOR	2
	X-FER (SMDC)	2
	TRANS DET BLOCKS (TD)	2

FIGURE VE-2 SUPER-ZIP ORDNANCE SYSTEM





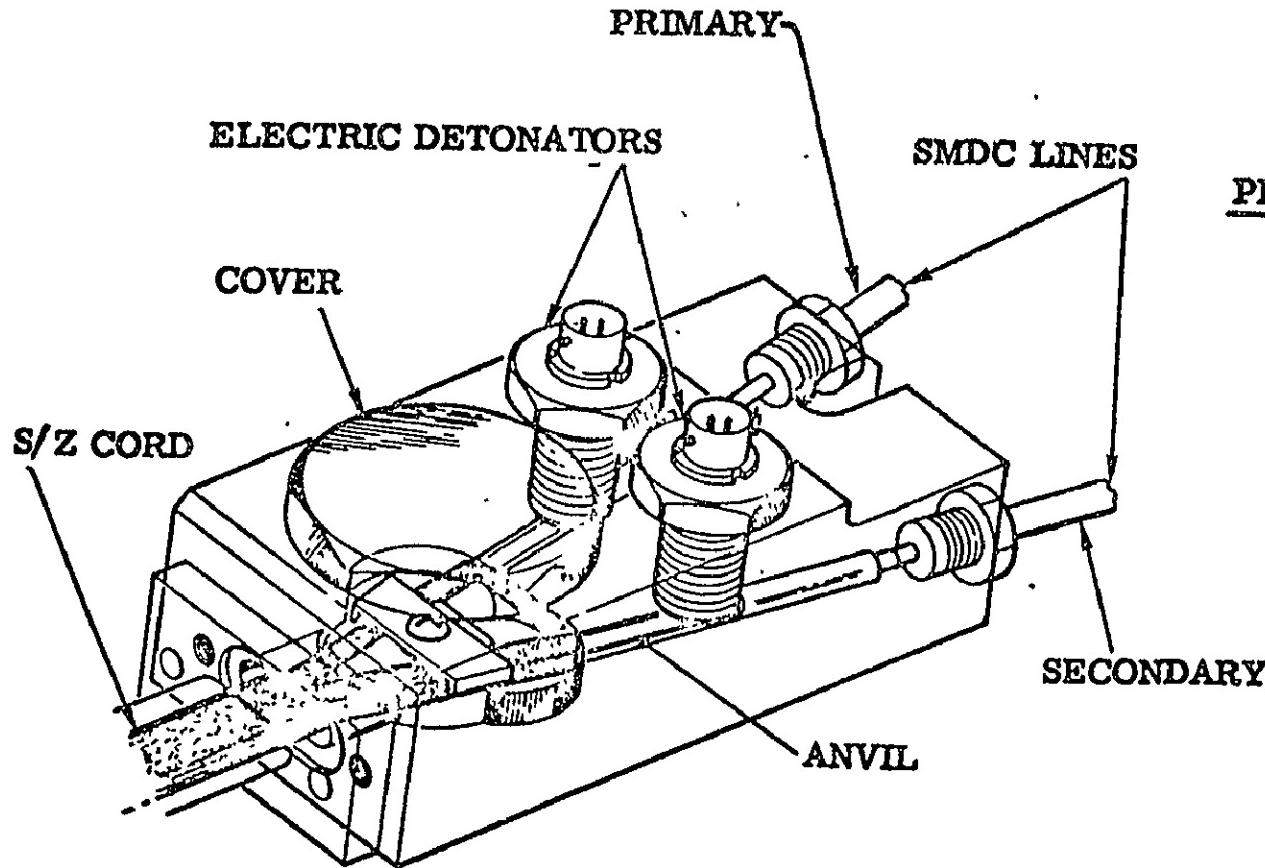
PRE-FIRING
CONFIGURATION

DETONATION

TUBE CIRCULARIZES
DUE TO PRESSURE RISE

FIG. V E-4

SUPER - ZIP OPERATION

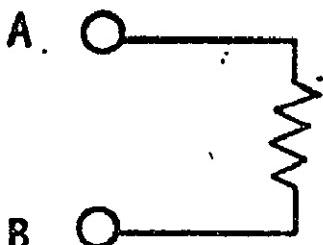


SUPER-ZIP BARRIER MODIFICATION

PROBLEM:

- DURING ALTITUDE JETTISON TEST NO. 3 AT PLUMBROOK, THE PAYLOAD SECTION SECONDARY SYSTEM FAILED TO PROPAGATE
- INVESTIGATION REVEALED CORD PROPAGATED ONLY WITHIN TRANSFER/DETONATOR BLOCKS

FIGURE VE-5 SUPER-ZIP DETONATOR BLOCK



PRIMARY SYSTEM

- STANDARD CLOCKING ON INITIATOR END
- RIGHT HAND THREADS ON OUTPUT END

SECONDARY SYSTEM

- "W" CLOCKING ON INITIATOR END
- LEFT HAND THREADS ON OUTPUT END

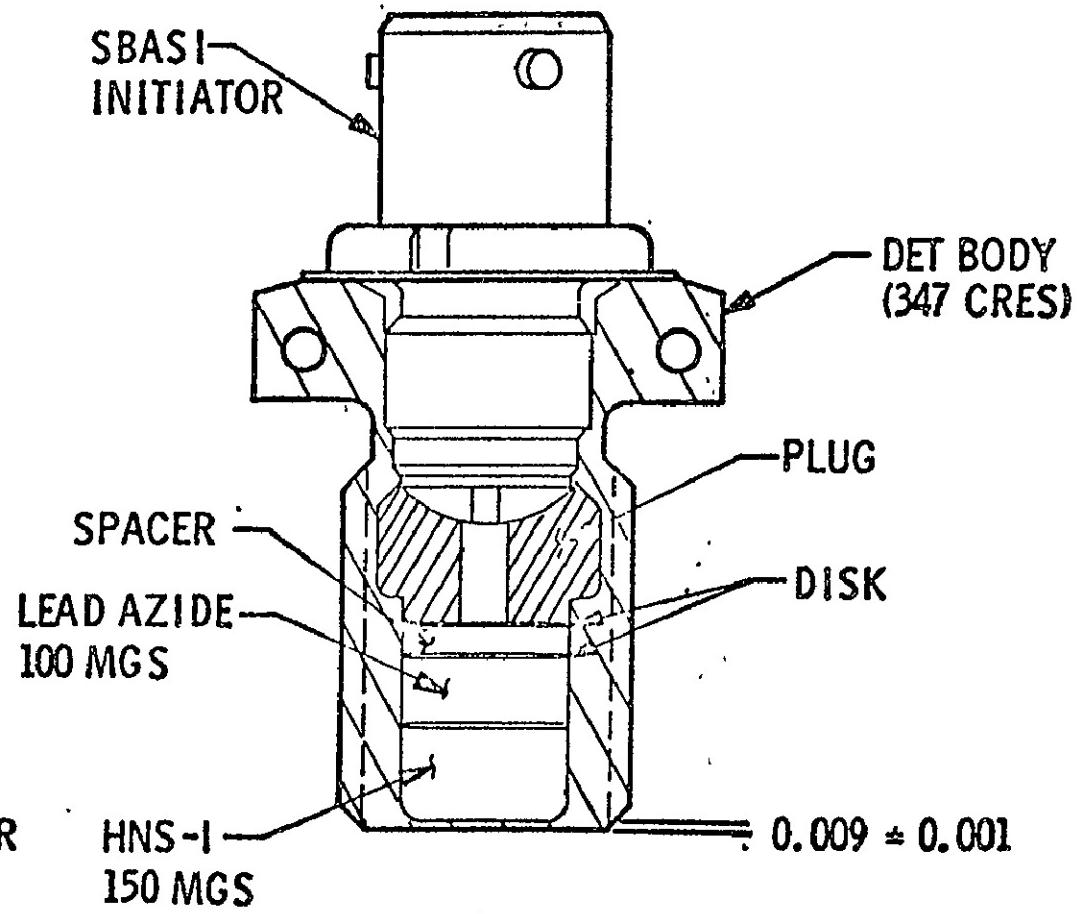


FIGURE VE-6 ELECTRIC DETONATOR

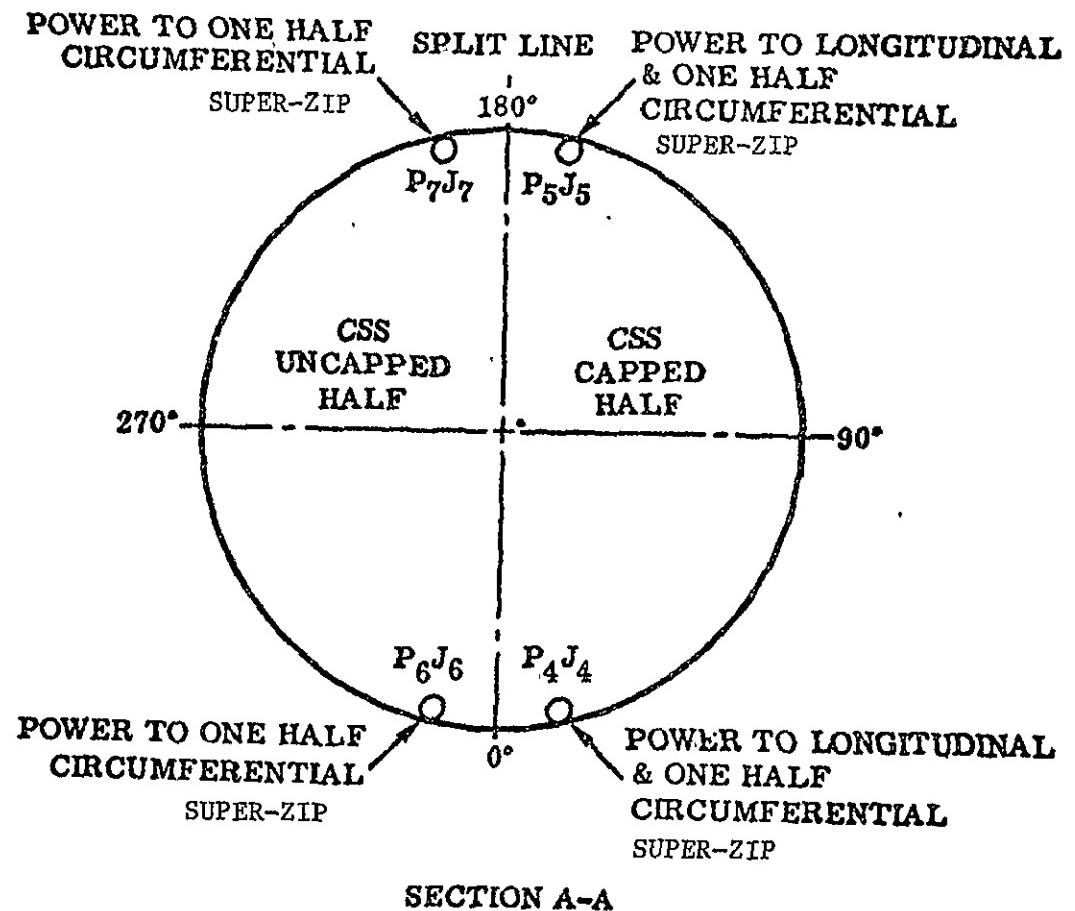
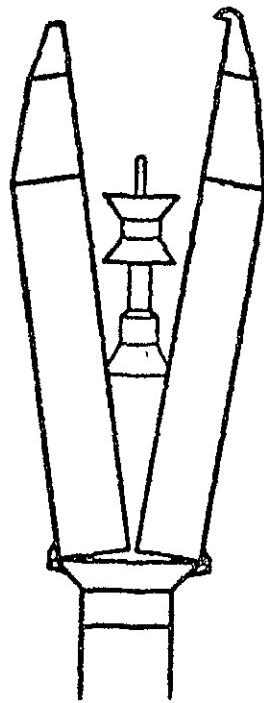
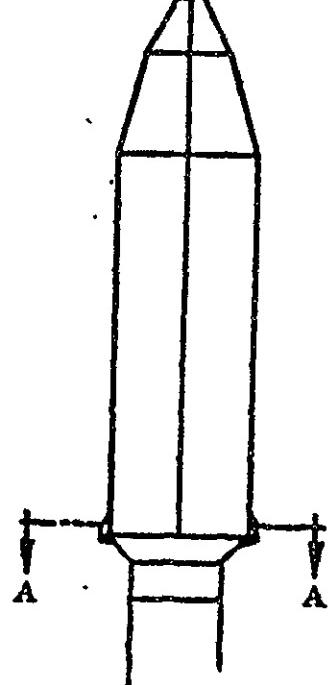


FIGURE VE-7 CSS SUPER-ZIP SYSTEM ELECTRICAL DISCONNECTS

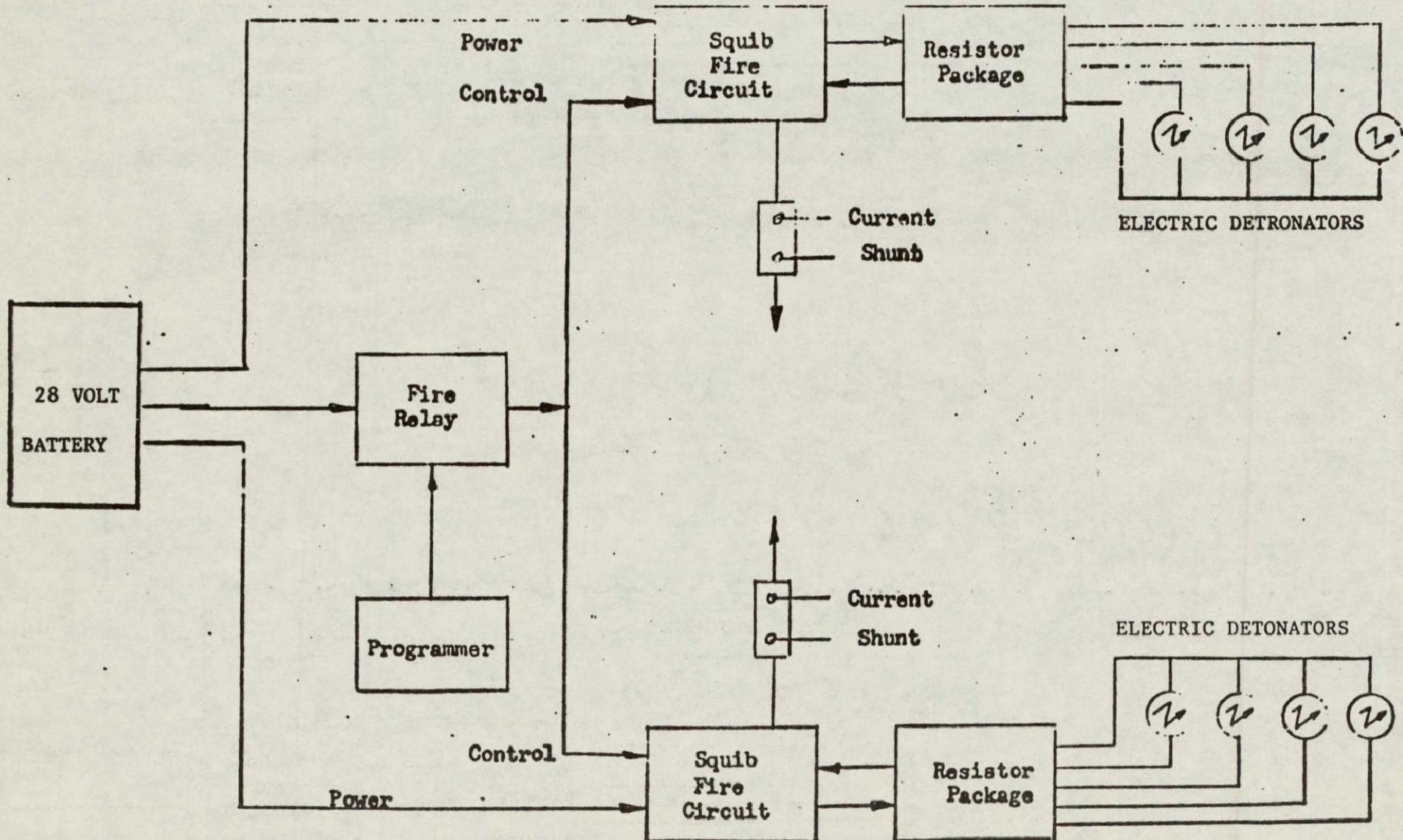


FIGURE VE-8 SCHEMATIC OF SUPER-ZIP ELECTRICAL FIRING CIRCUIT USED DURING CSS HEATED ALTITUDE JETTISON TESTS

1-24-74 HJT #2

CIRCUMFERENTIAL
SUPER-ZIP TUBE (FWD)

+ Y HALF
60" FROM 180° END

142

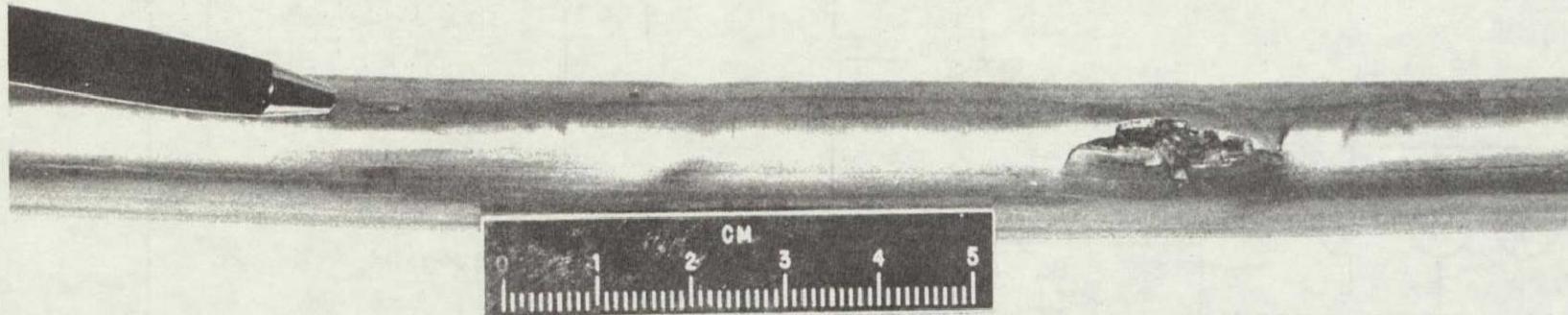


FIGURE VE-9 FAILED CIRCUMFERENTIAL TUBE AFTER HJT #2

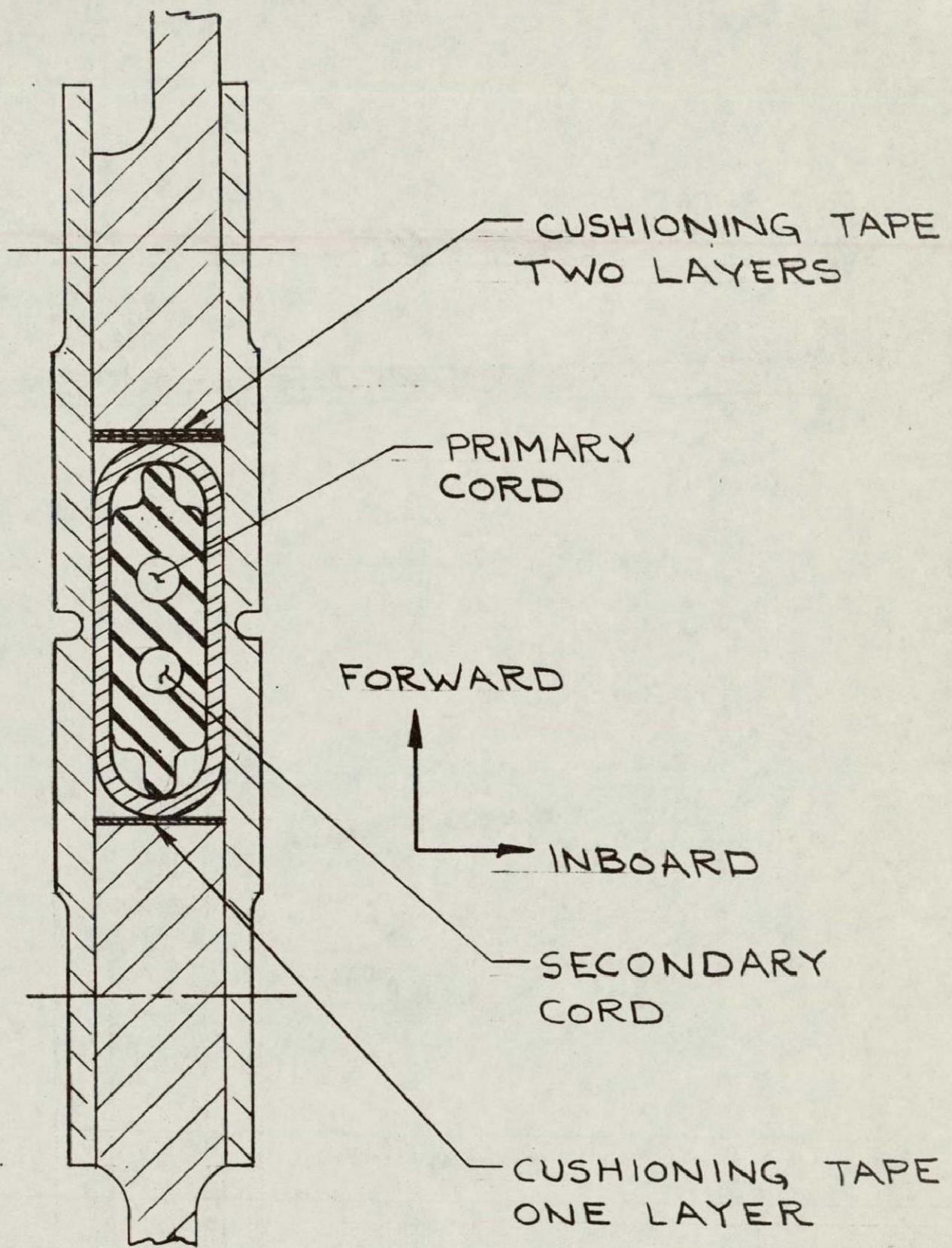
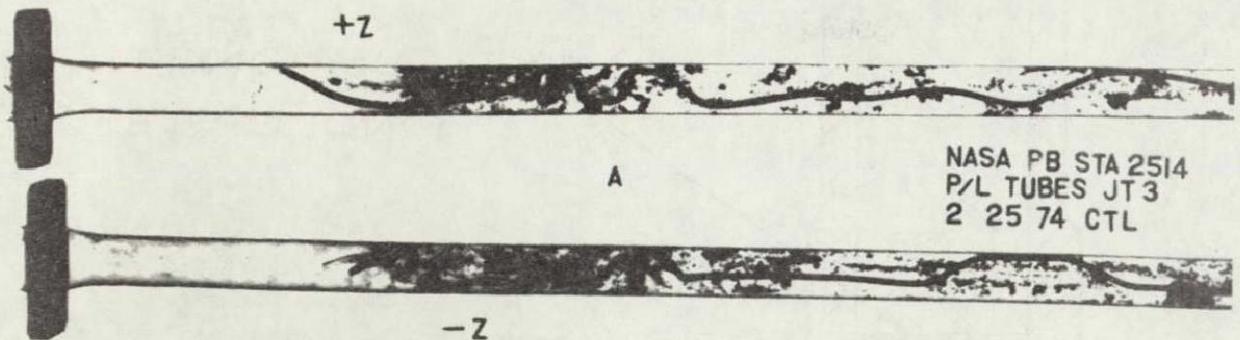
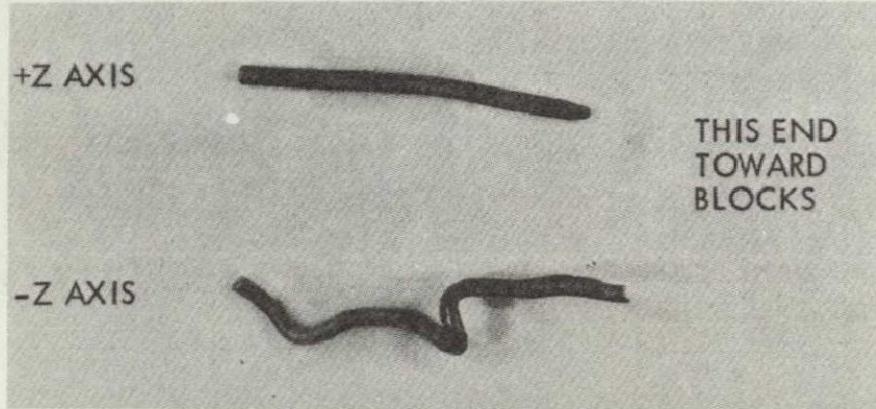


FIGURE VIE-10 SUPER-ZIP SYSTEM CIRCUMFERENTIAL JOINT



X-Ray of Detonating Cord Before Removal From Tube

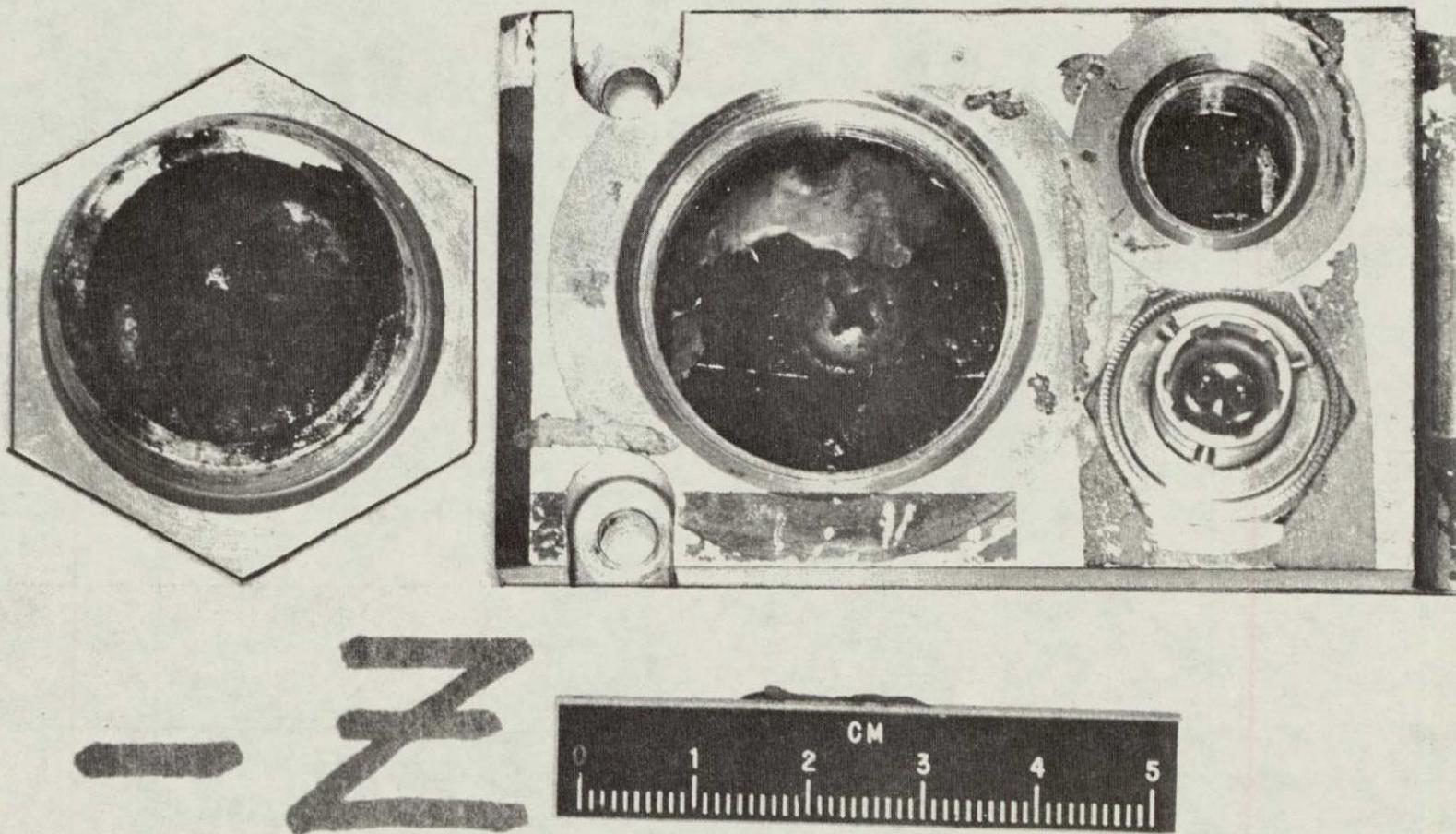


Ends of Detonating Cord Removed From Tube

FIGURE VE-11

144

REPRODUCIBILITY OF THE
ORIGINAL PAGE IS POOR



REPRODUCIBILITY OF THE
ORIGINAL PAGE IS POOR

FIGURE VE-12 PAYLOAD SECTION DETONATOR BLOCK AFTER TEST #3

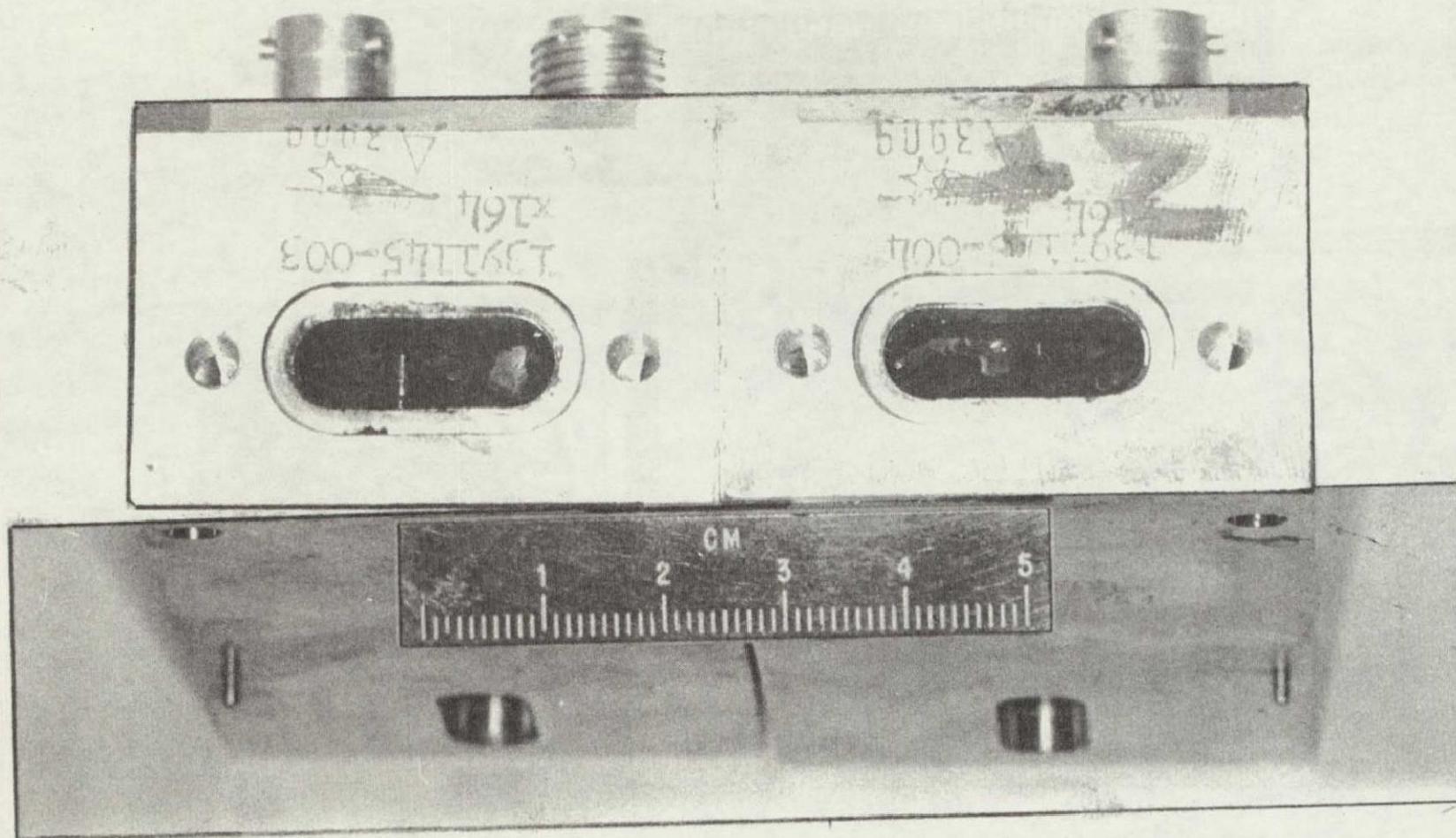


FIGURE VE-13 PAYLOAD SECTION DETONATOR BLOCKS AFTER TEST #3
SHOWING BARRIER APEX MOVEMENT

E-8508

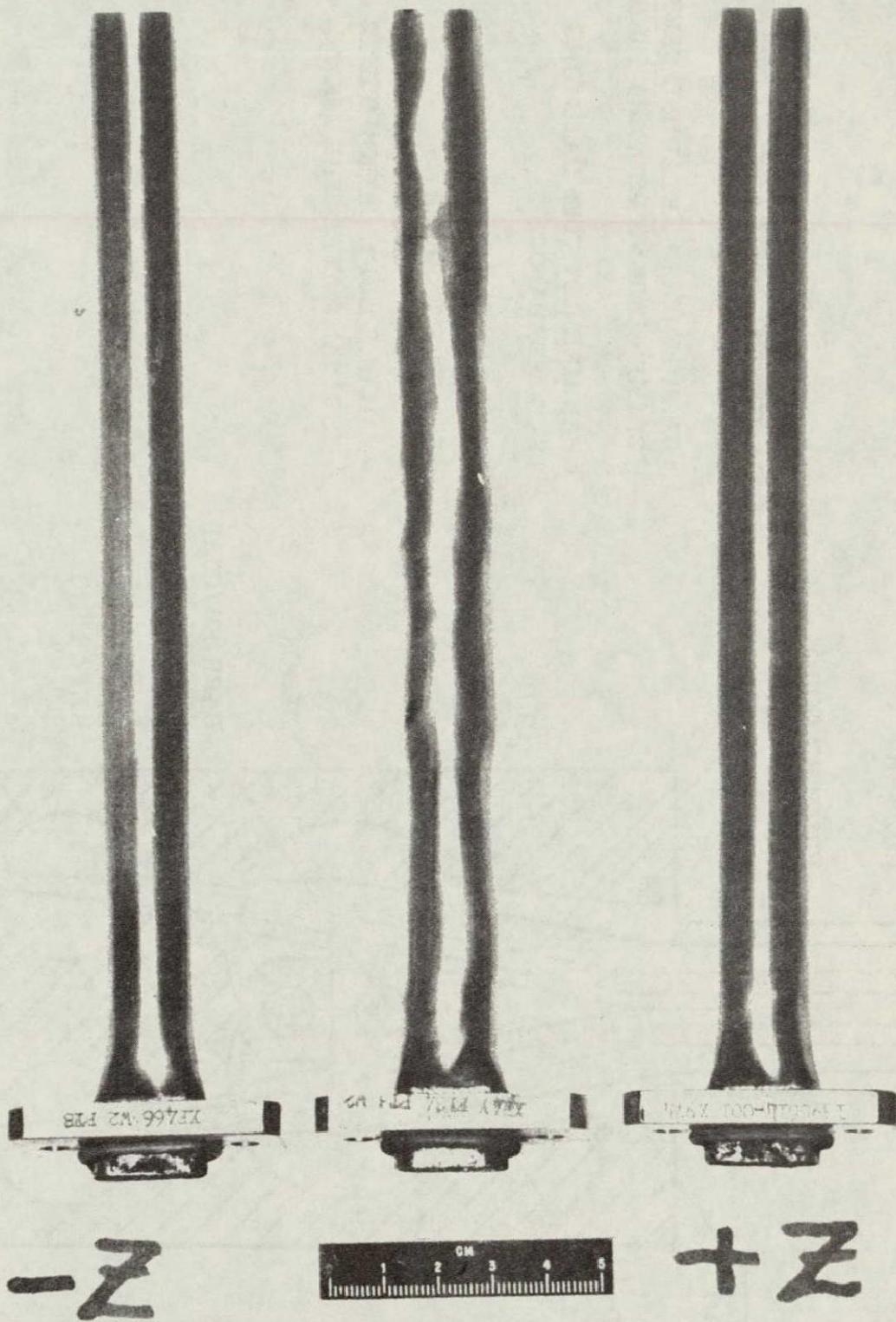


FIGURE VE-14 PAYLOAD SECTION TUBES AFTER TEST #3,
COMPARED TO TUBE SUBJECTED TO PRIMARY & SECONDARY FIRINGS (CENTER)

147

NASA-Lewis-Com'l

REPRODUCIBILITY OF THE
ORIGINAL PAGE IS POOR

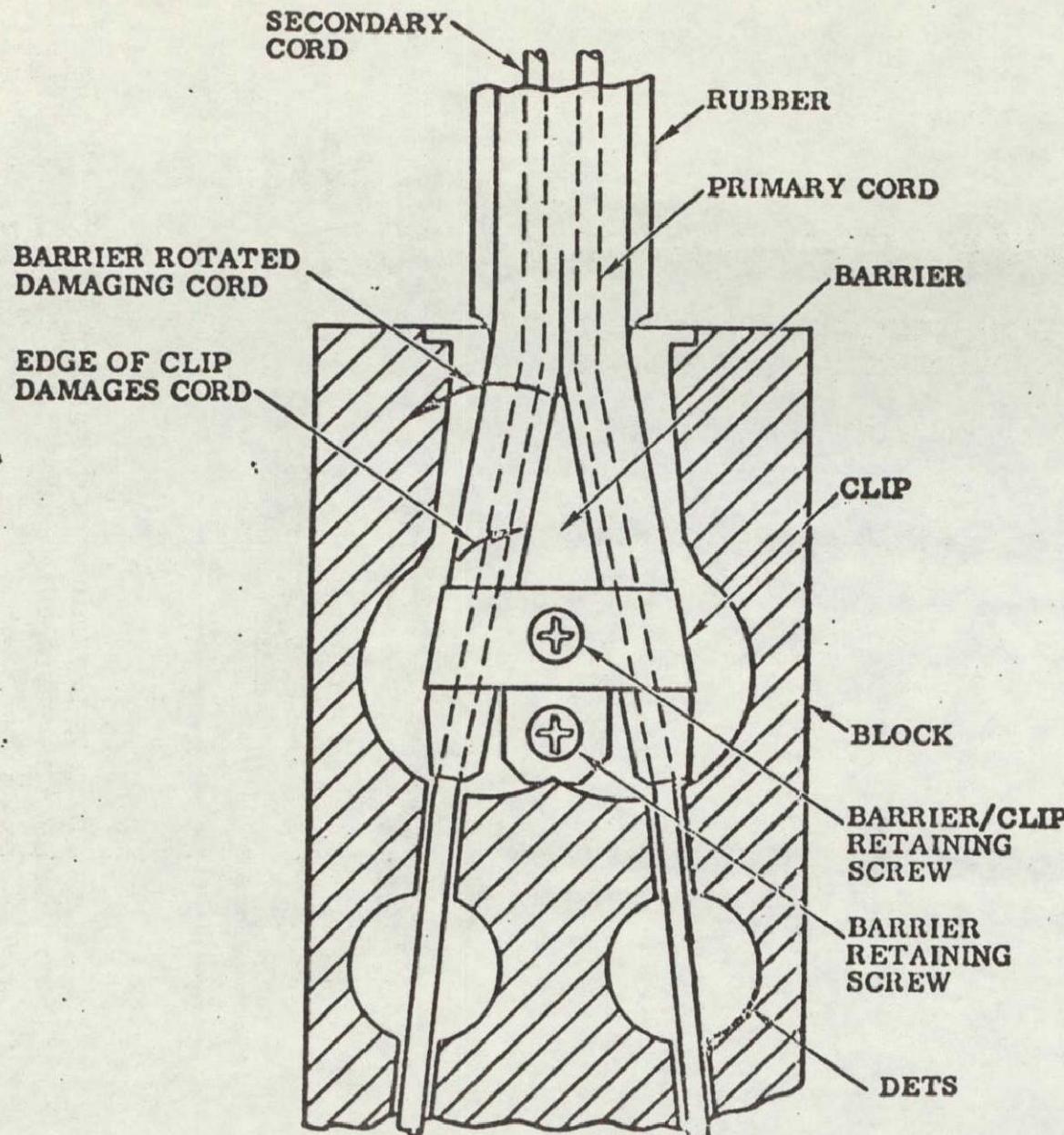
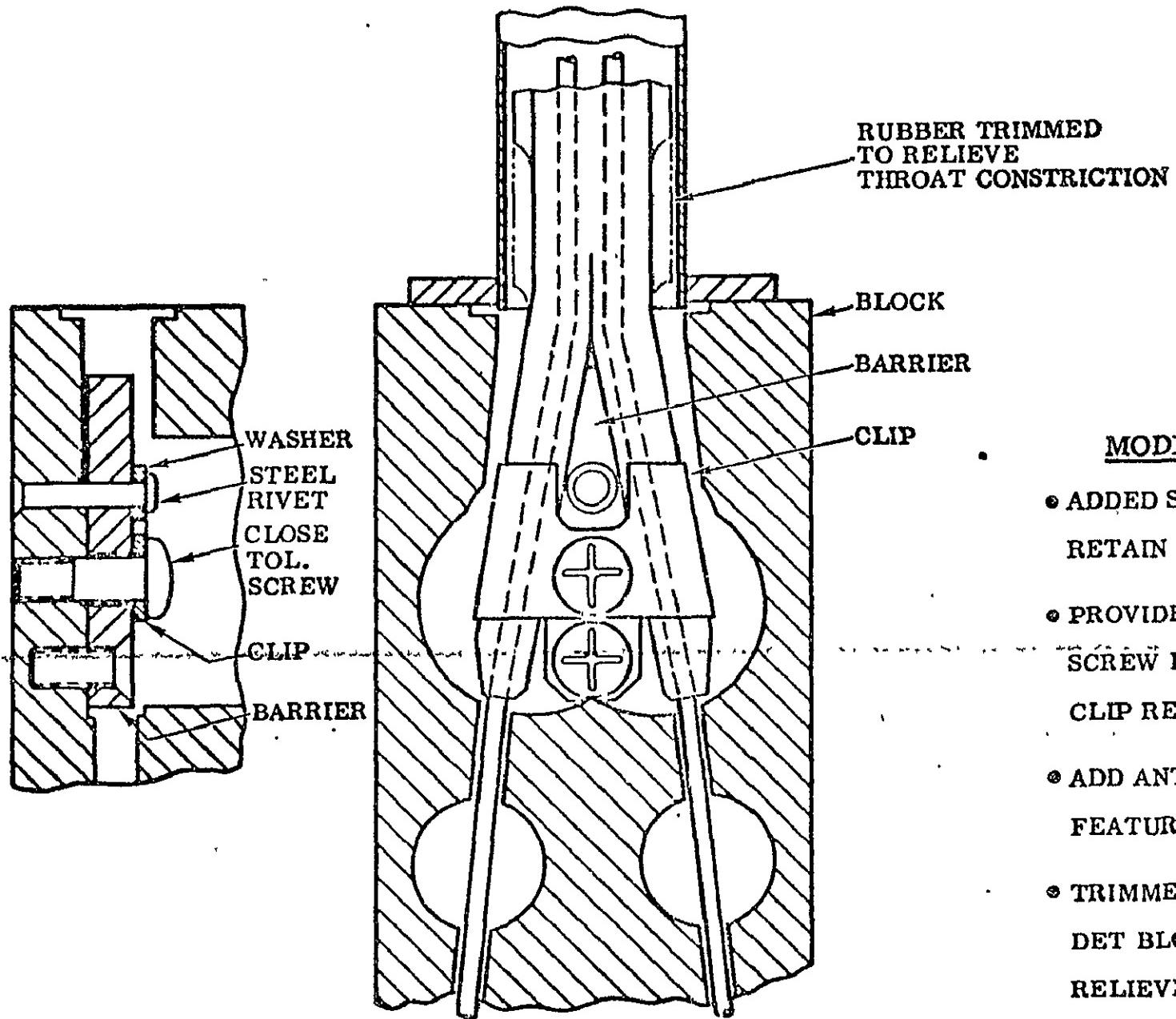


FIGURE VE-15 SUPER-ZIP DET BLOCK ASSEMBLY (TC-1 CONFIGURATION)

FAILURE INVESTIGATION RESULTS

- BARRIER/CLIP RETAINING SCREW BREAKS DURING PRIMARY FIRING.
- BARRIER ROTATES DAMAGING SECONDARY CORD.
- CLIP ROTATES OR COMES FREE OF BARRIER.
- FAILURE DUPLICATION TESTS SUBSTANTIATED THE ABOVE.



MODIFICATIONS

- ADDED STEEL RIVET TO RETAIN BARRIER.
- PROVIDED CLOSE TOL. SCREW FOR BARRIER/CLIP RETENTION.
- ADD ANTI-ROTATION FEATURE TO CLIP.
- TRIMMED RUBBER AT DET BLOCK THROAT TO RELIEVE CONSTRICION.

FIGURE VE-16 SUPER-ZIP DET BLOCK ASSEMBLY (TC-2 AND ON CONFIGURATION)

DATA FROM CSS JETTISON TESTS CONDUCTED AT PLUM BROOK AND TC-1 INDICATE THE FOLLOWING:

UPON PRIMARY SYSTEM ACTUATION, RELATIVE VERTICAL MOTION OF THE CSS TO BOATTAIL EXCEEDS THE DISCONNECT ENGAGEMENT.

IN THE REMOTE CASE OF A PRIMARY SYSTEM LONGITUDINAL FAILURE, VERTICAL MOTION COULD CAUSE PREMATURE DISCONNECT OF SECONDARY SYSTEM ELECTRICAL CIRCUIT, PREVENTING SYSTEM FUNCTION.

150

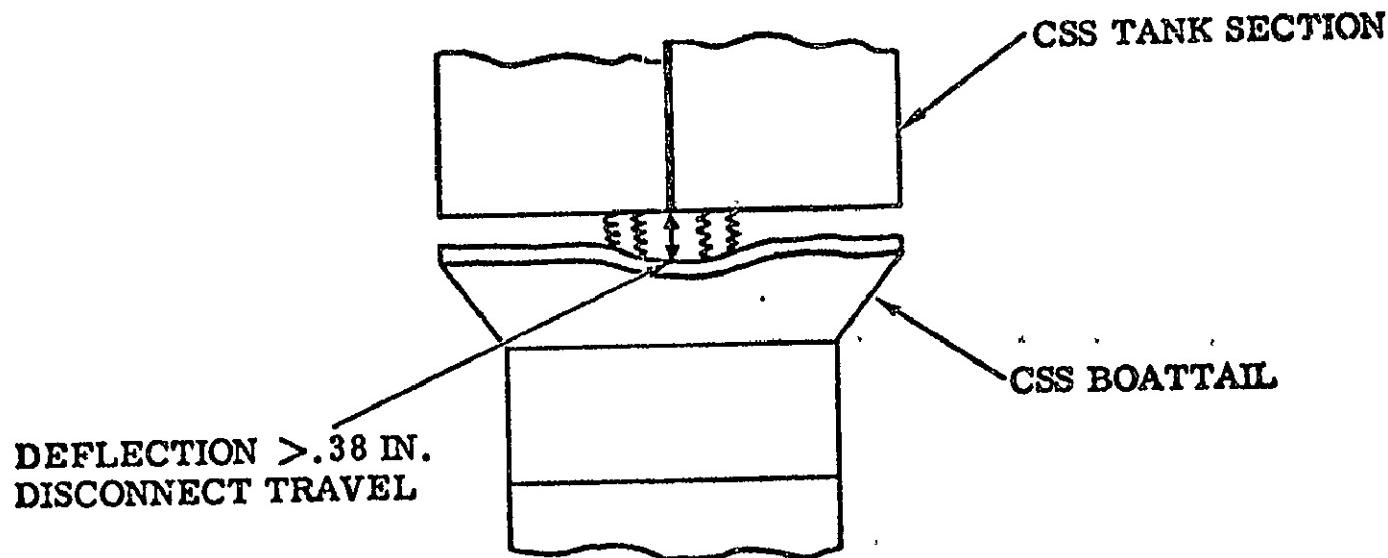
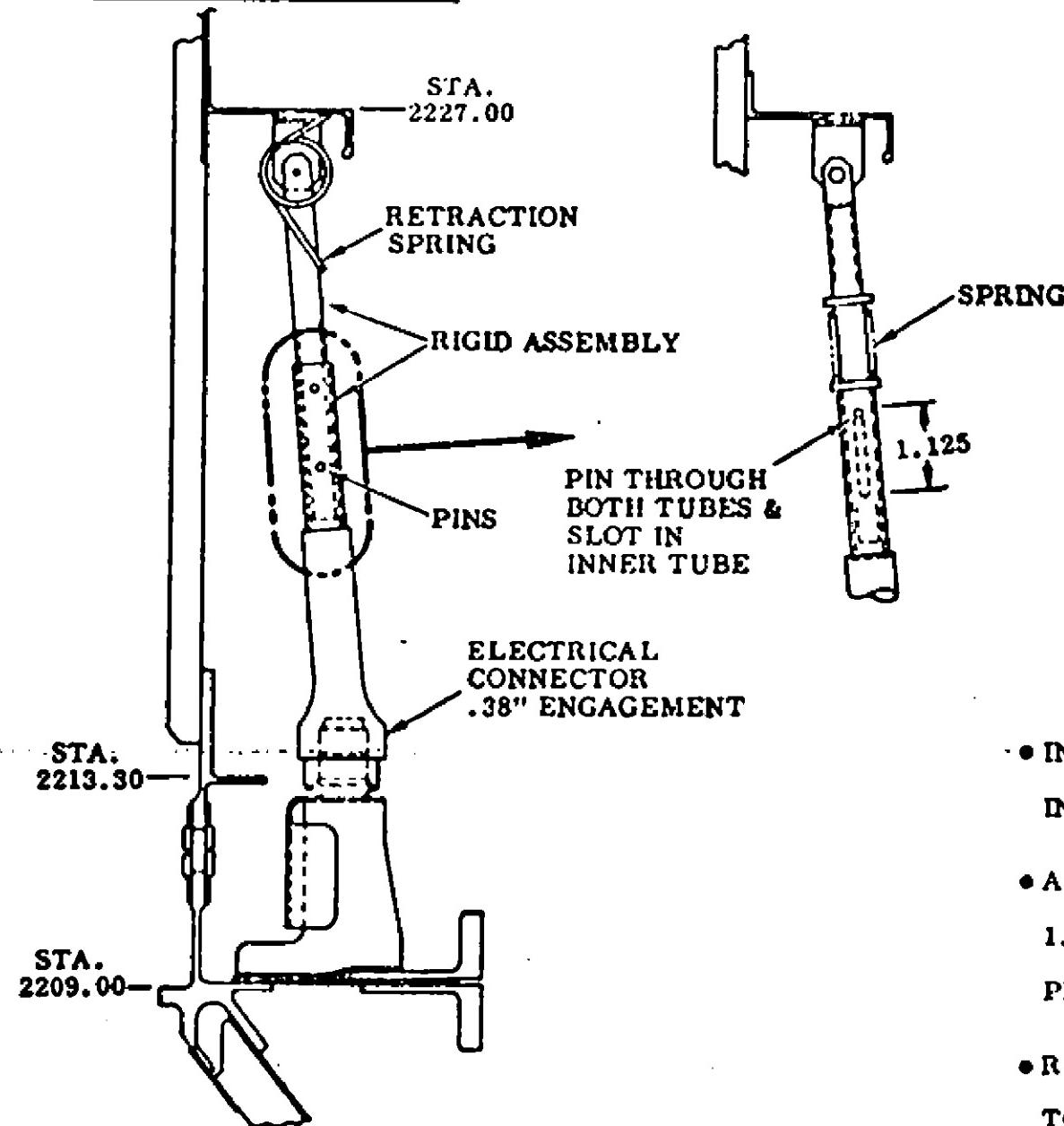


FIGURE VE-17 SUPER-ZIP ELECTRIC DISCONNECT PROBLEM

TC-1 CONFIGURATION



MODIFICATIONS

- INCORPORATE 1.125 IN. STROKE IN BRACKET ASSY.
- ADDED SPRING TO ENSURE 1.125 IN. MOTION OF BRACKET PRIOR TO .38 IN. DISCONNECT TRAVEL.
- RETRACTION SPRING REMOVED TO ELIMINATE SIDELOAD.

FIGURE VE-18 CSS ELECTRICAL DISCONNECT MODIFICATIONS (TC-2 AND ON CONFIGURATION)

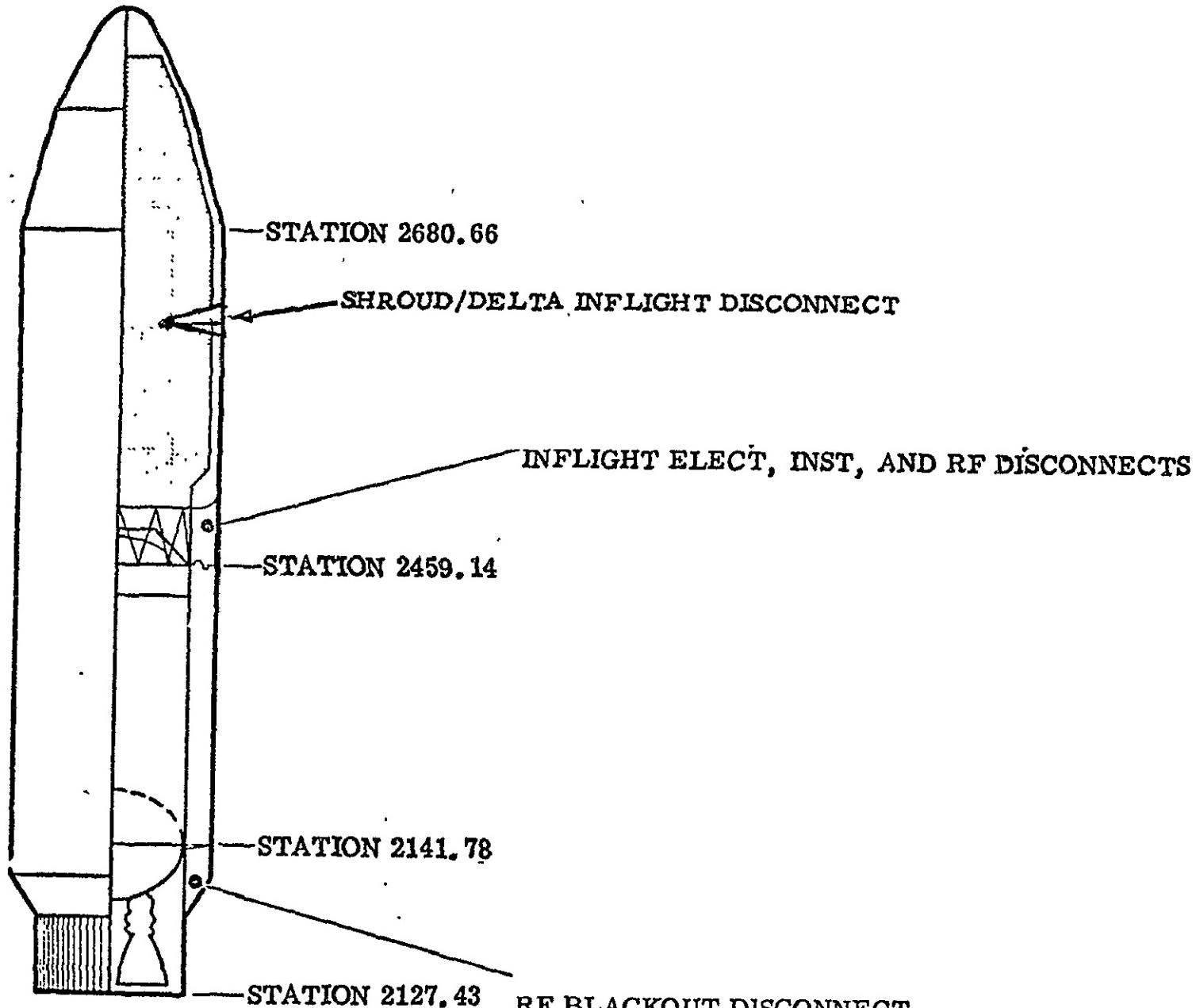


FIGURE VE-19 CSS DISCONNECTS

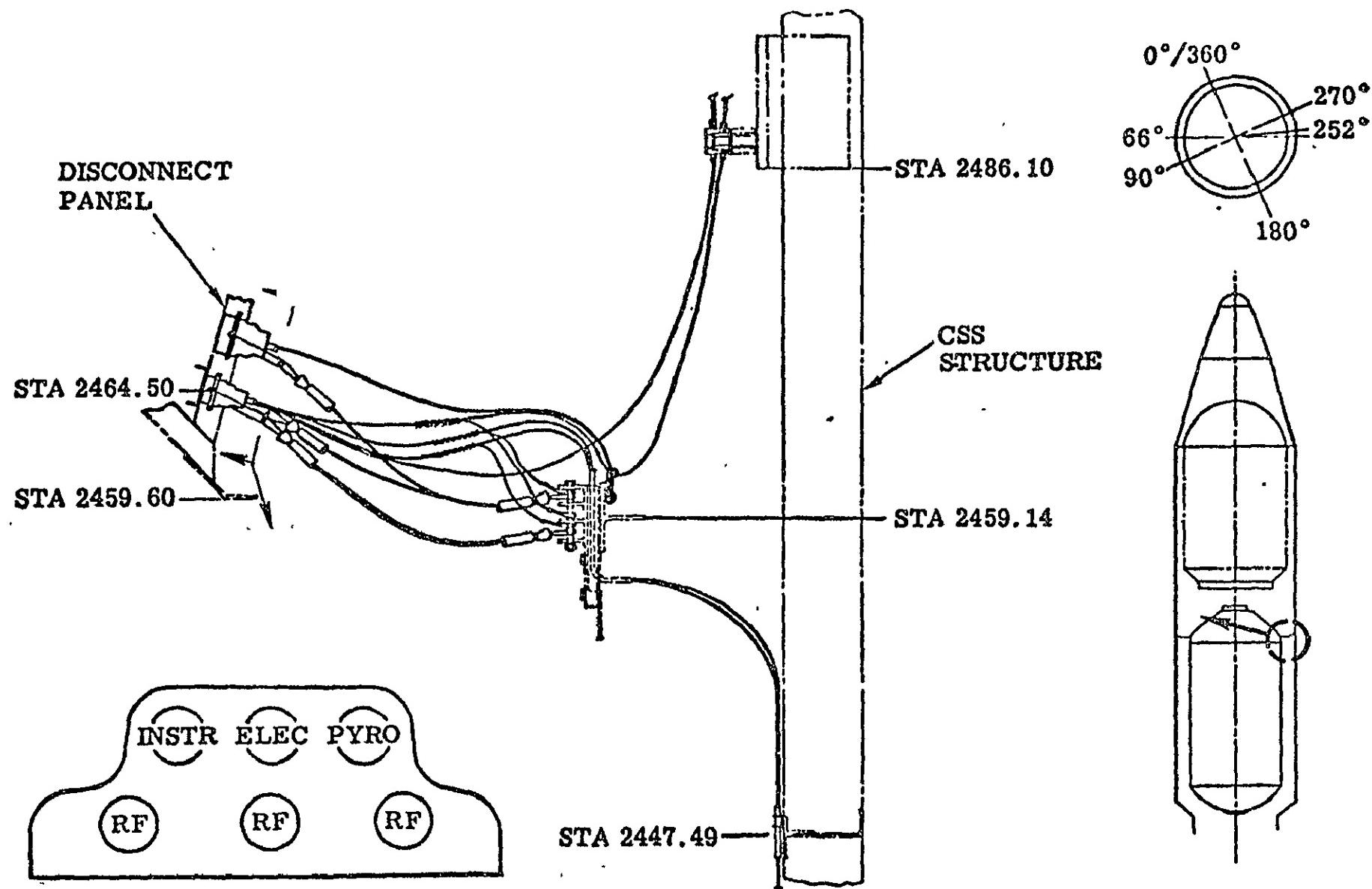


FIGURE VE-20 IN-FLIGHT DISCONNECTS

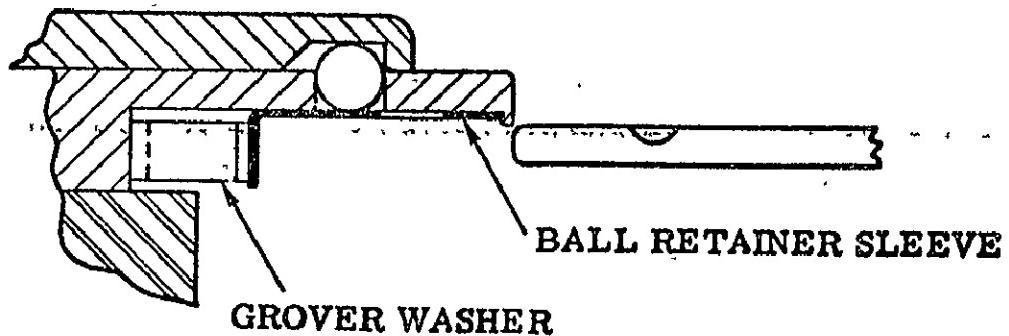
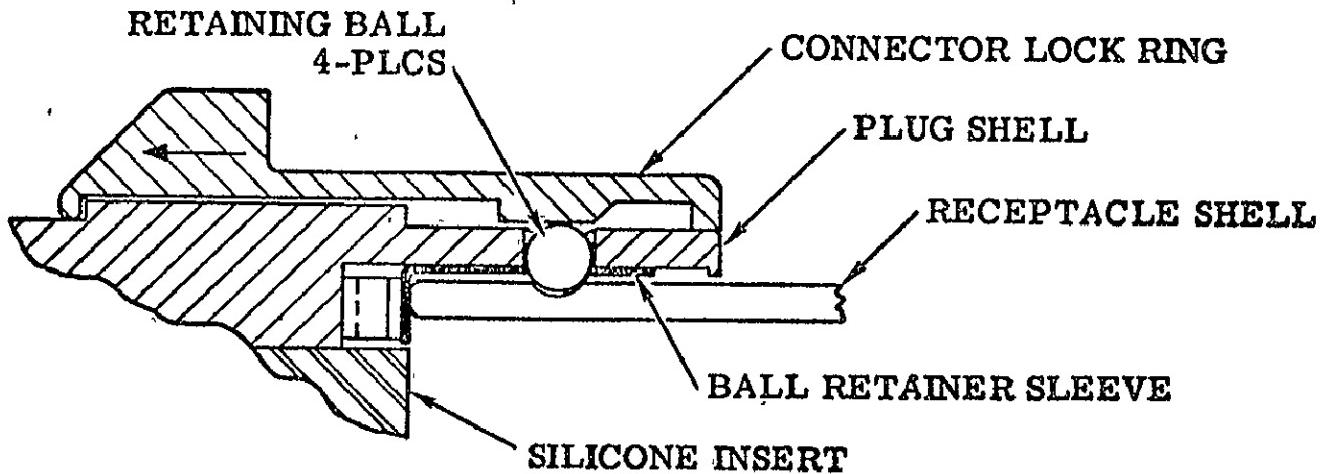


FIGURE VE-21 ELECTRICAL DISCONNECT PRIMARY RELEASE

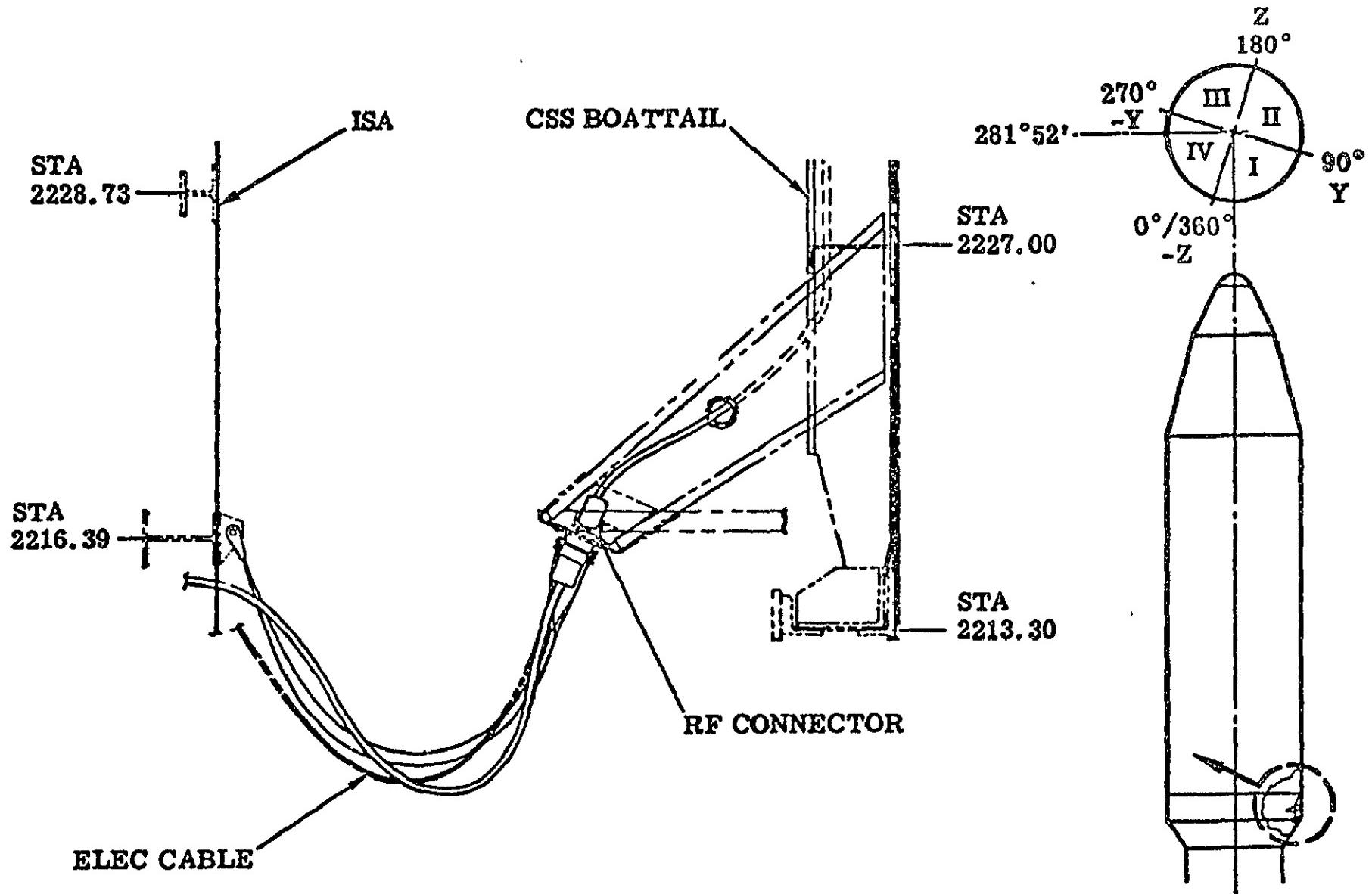
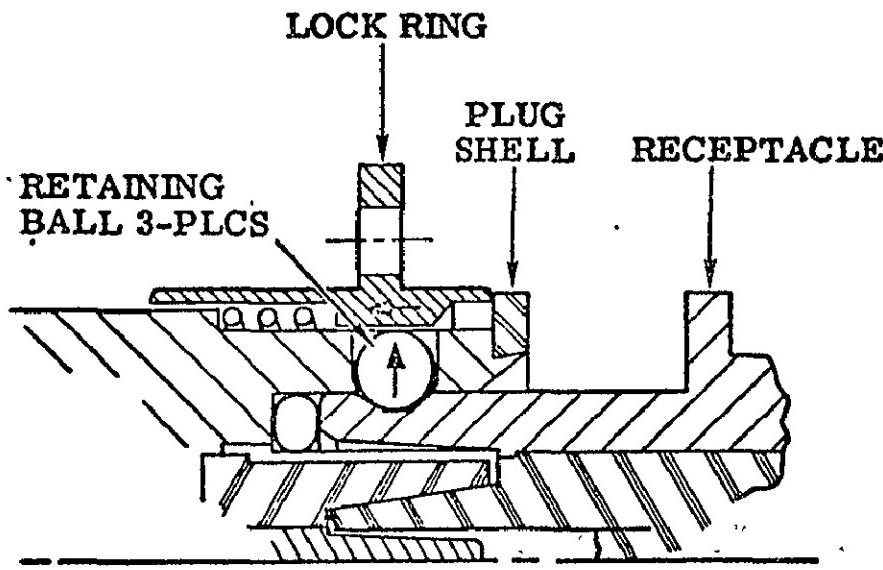
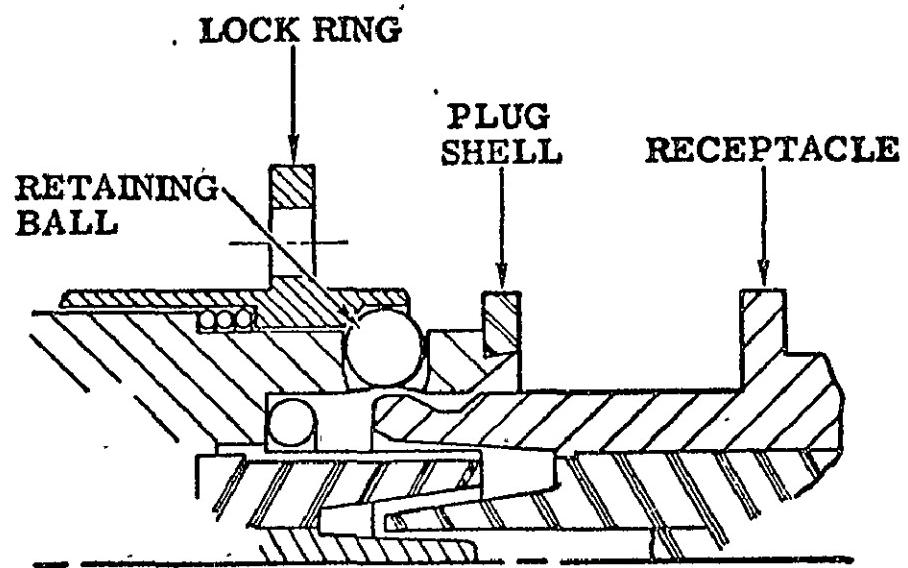


FIGURE VE-22 R.F. BLACKOUT DISCONNECT



MATED POSITION



RELEASE POSITION

FIGURE VE-23 R. F. DISCONNECT PRIMARY RELEASE

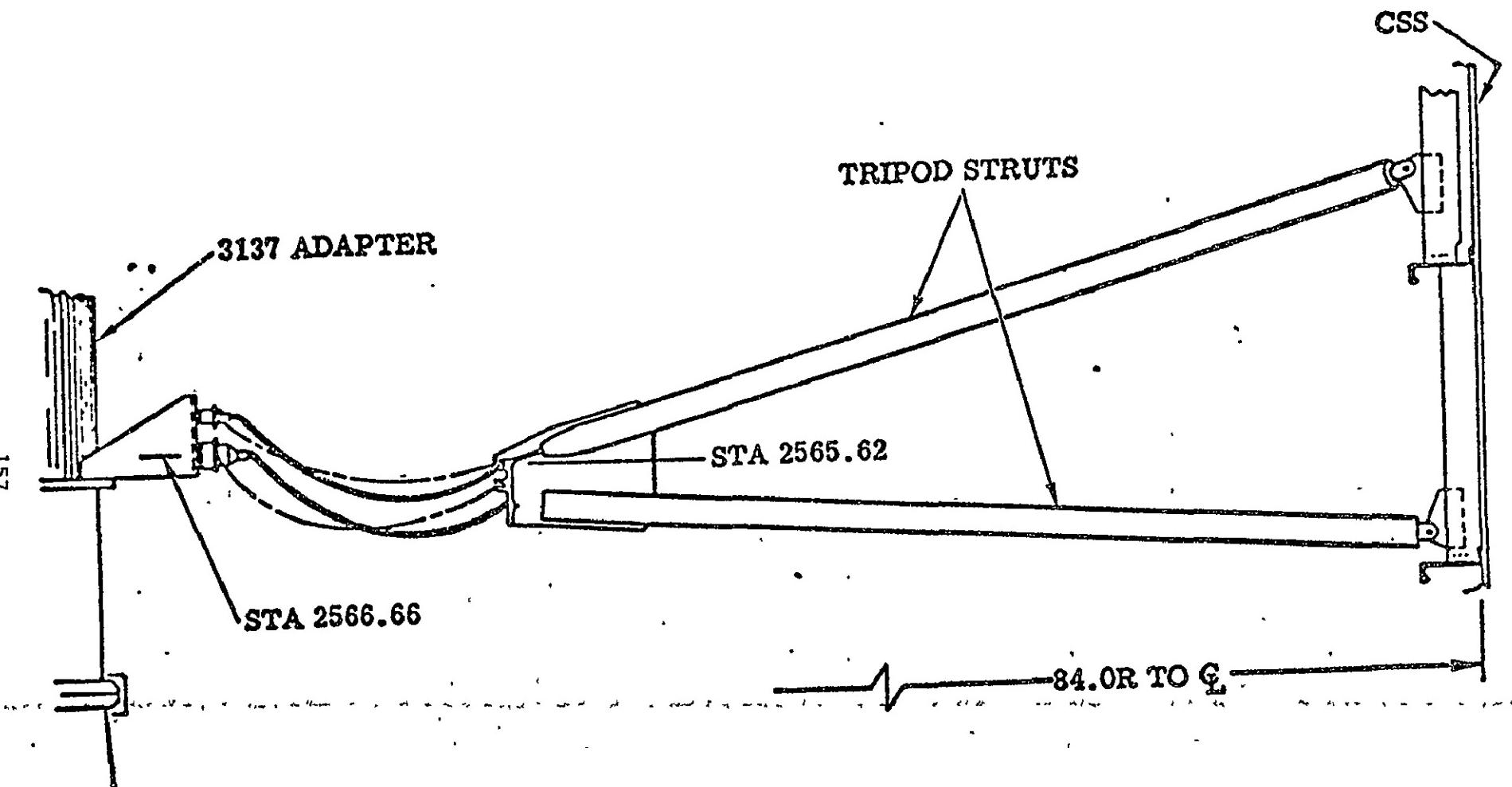


FIGURE VE-24 ELECTRICAL DISCONNECT TRIPOD INSTALLATION

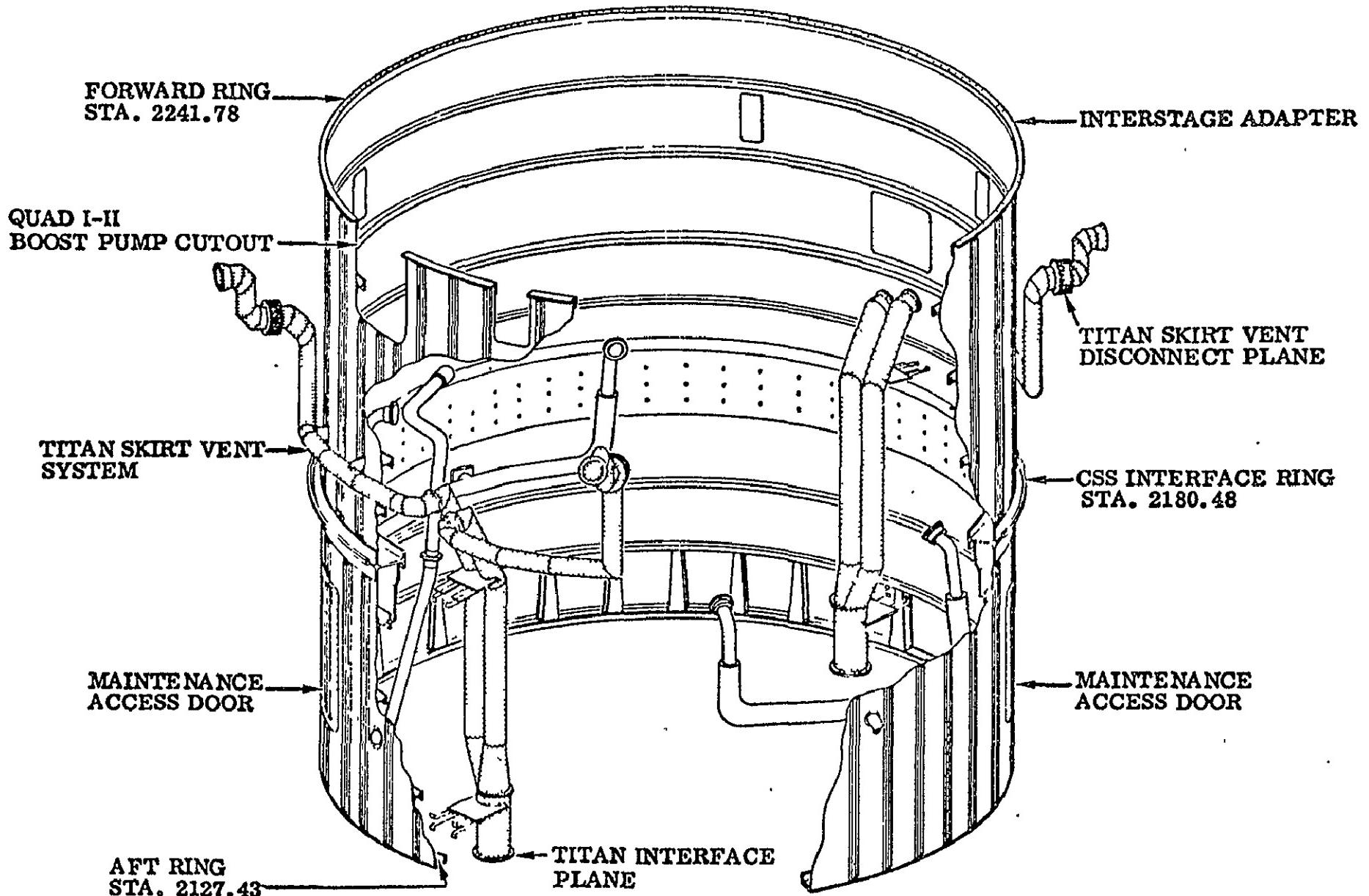


FIGURE VE-25 TITAN SKIRT VENT SYSTEM

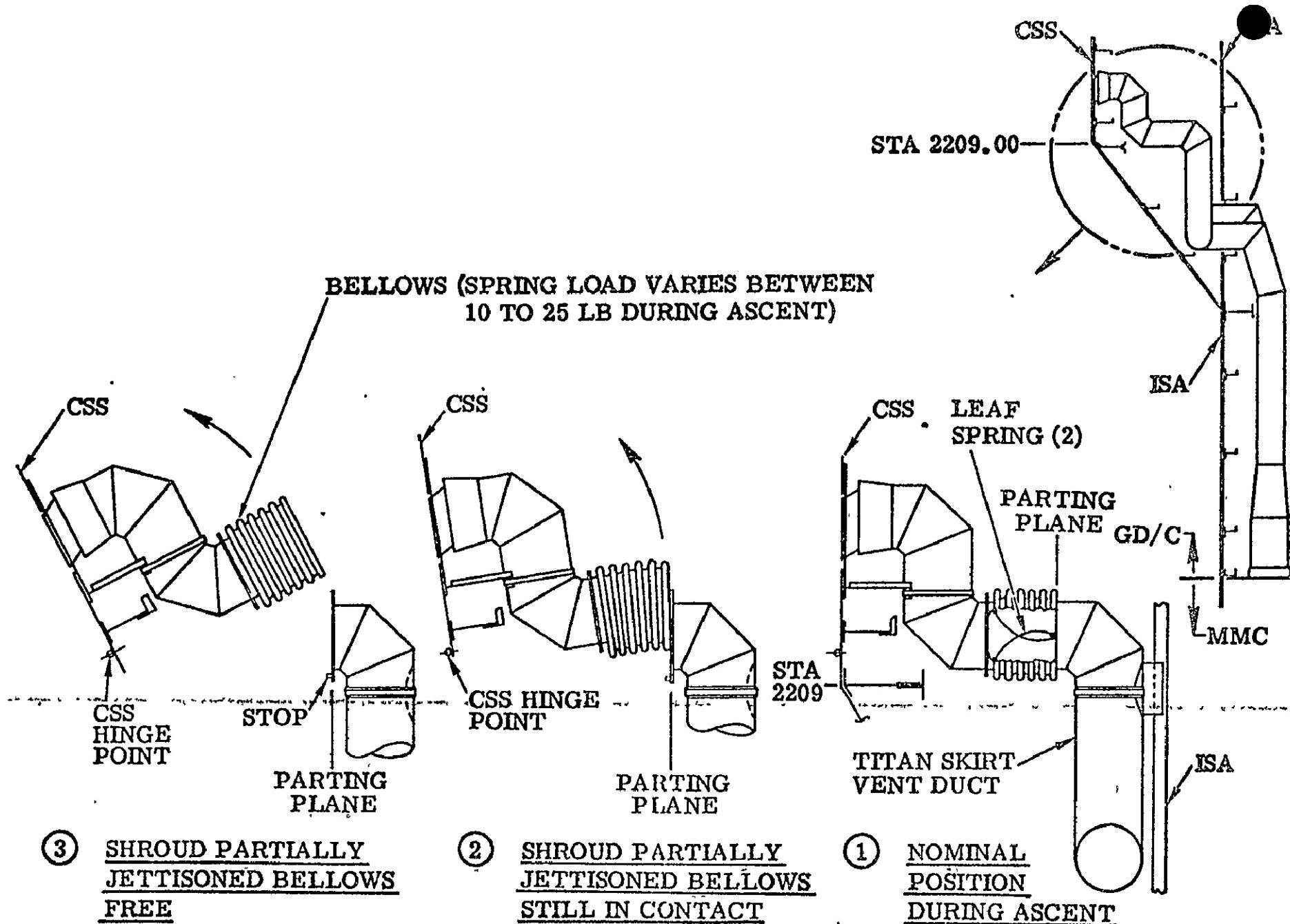


FIGURE VE-26 TITAN SKIRT VENT BELLOWS

GSS JETTISON ANALYSIS

RATE OF ANGEL VS TIME

DOSE (RAD) HALF

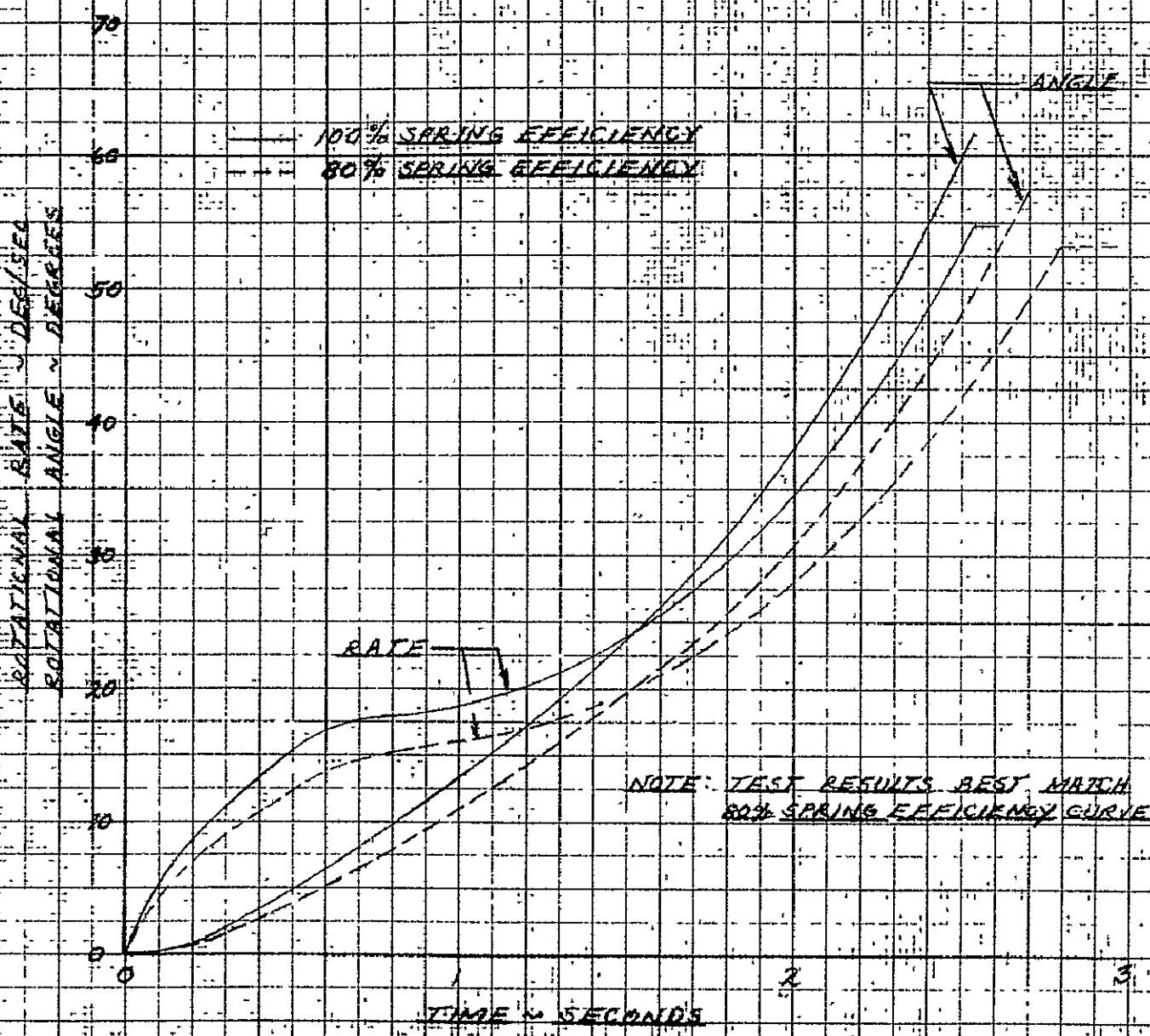


FIGURE N.F.-27

CSS JETTISON ANALYSIS

RATE VS ANGLE VS TIME

New Data ($-y$) HAF

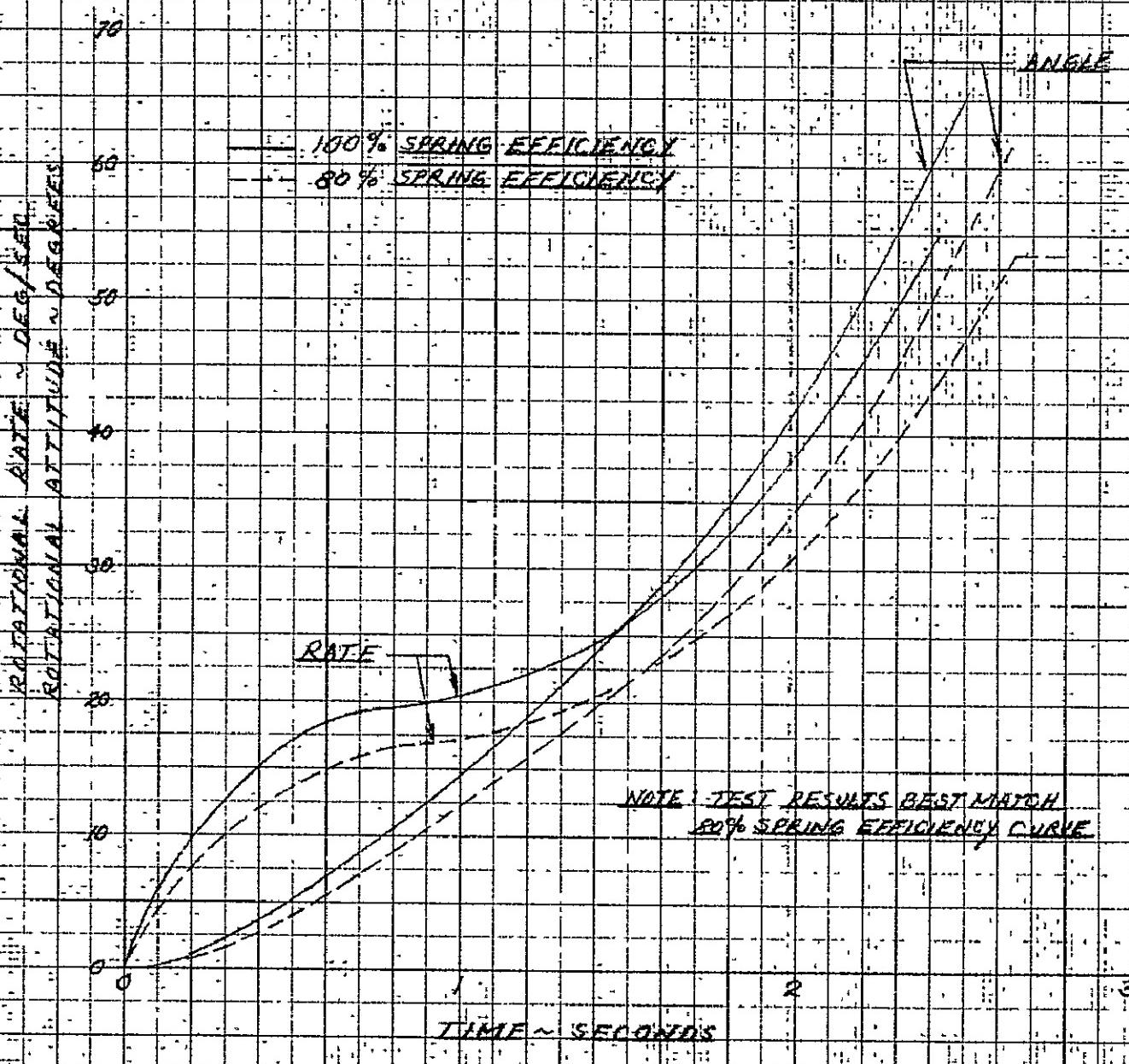
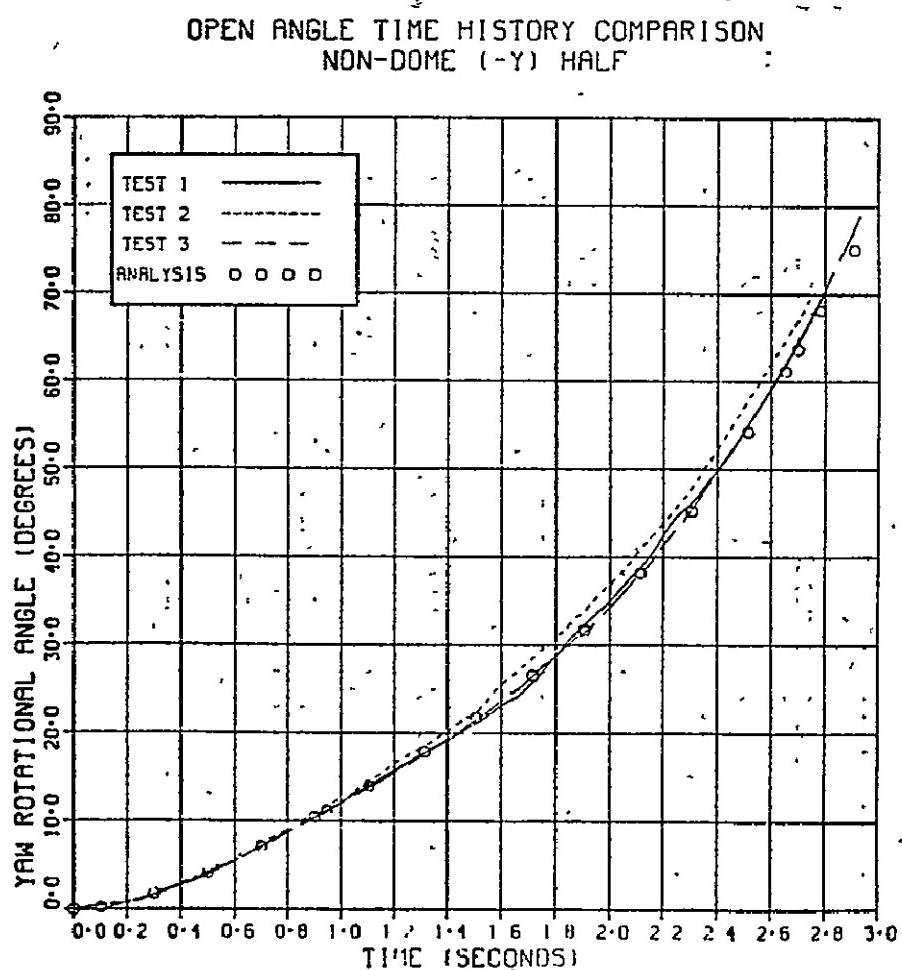
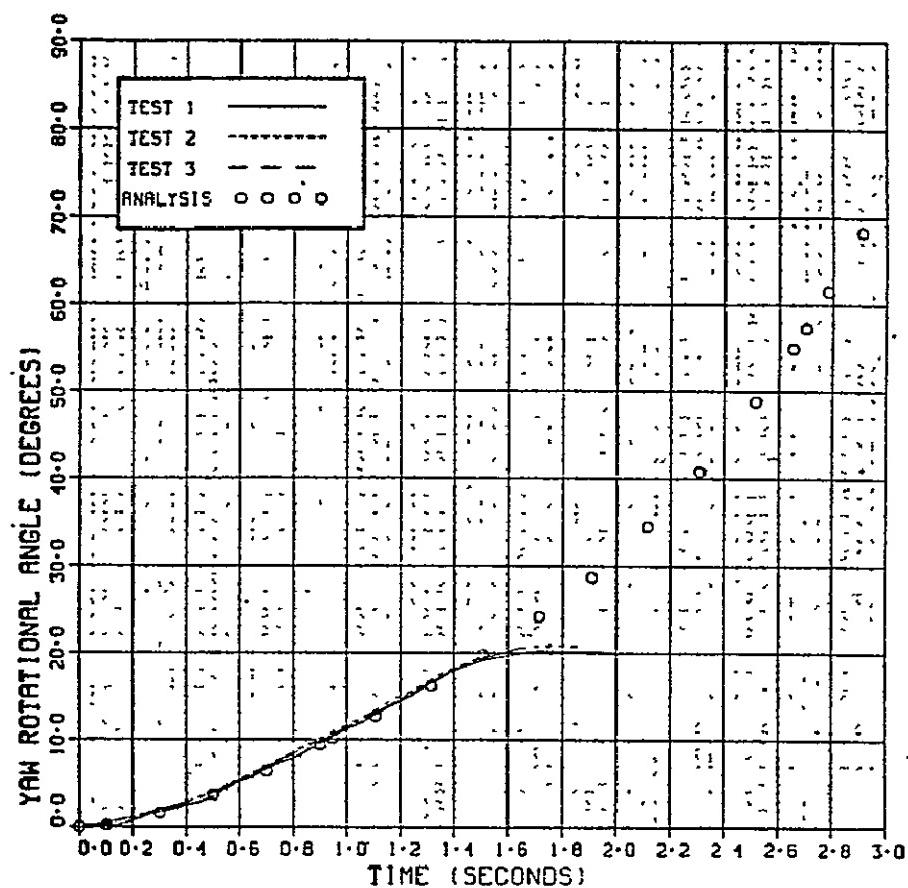


FIGURE I-E-28

FIGURE YE-29 CSS JET TISON TEST
OPEN ANGLE TIME HISTORY COMPARISON
DOME (+Y) HALF



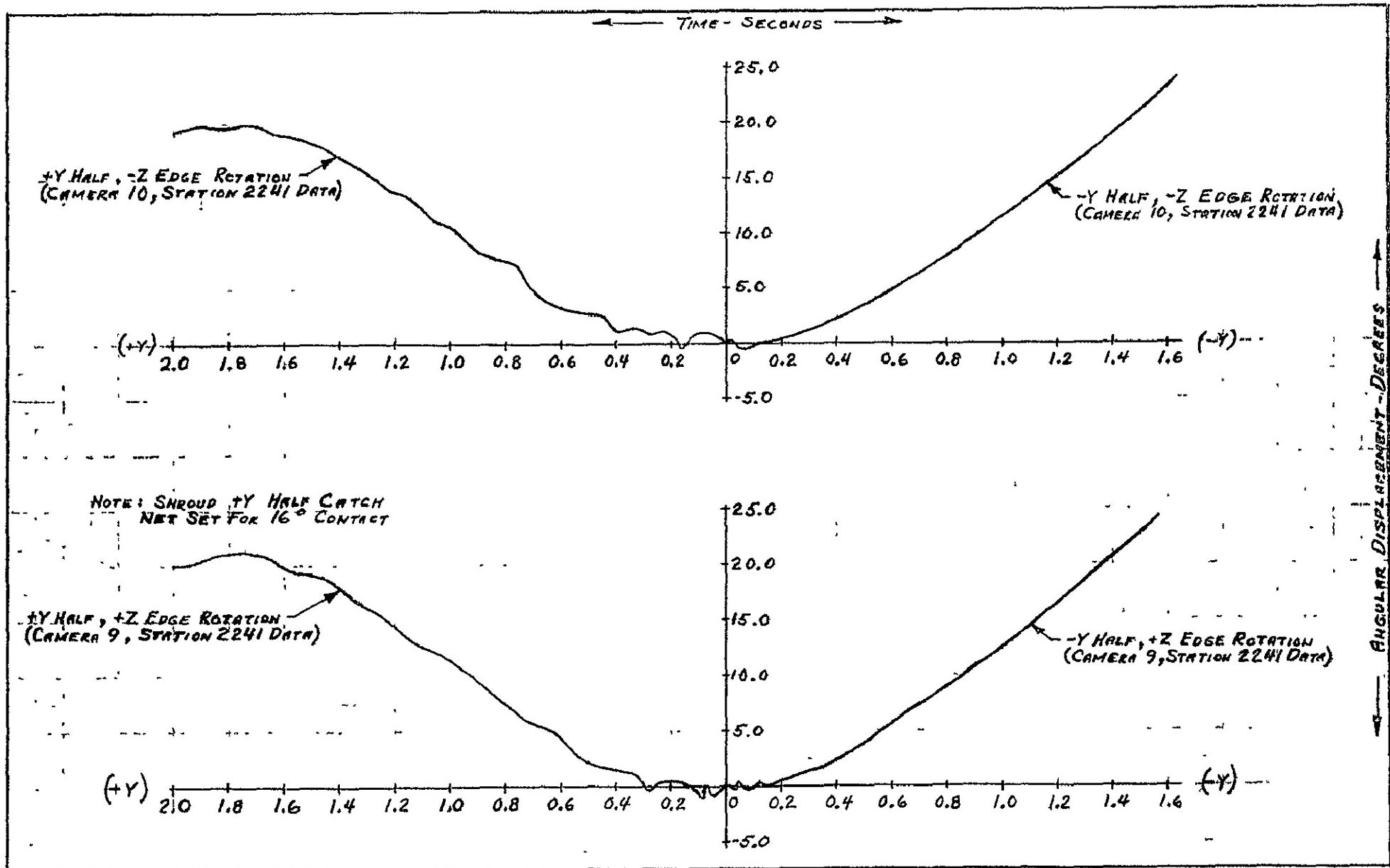


FIGURE VI-E-30 CSS EDGE ROTATION VS. TIME - STATION 2241, TEST 1

NOTE: SHROUD +Y HALF CATCH
NET SET FOR 16° CONTACT

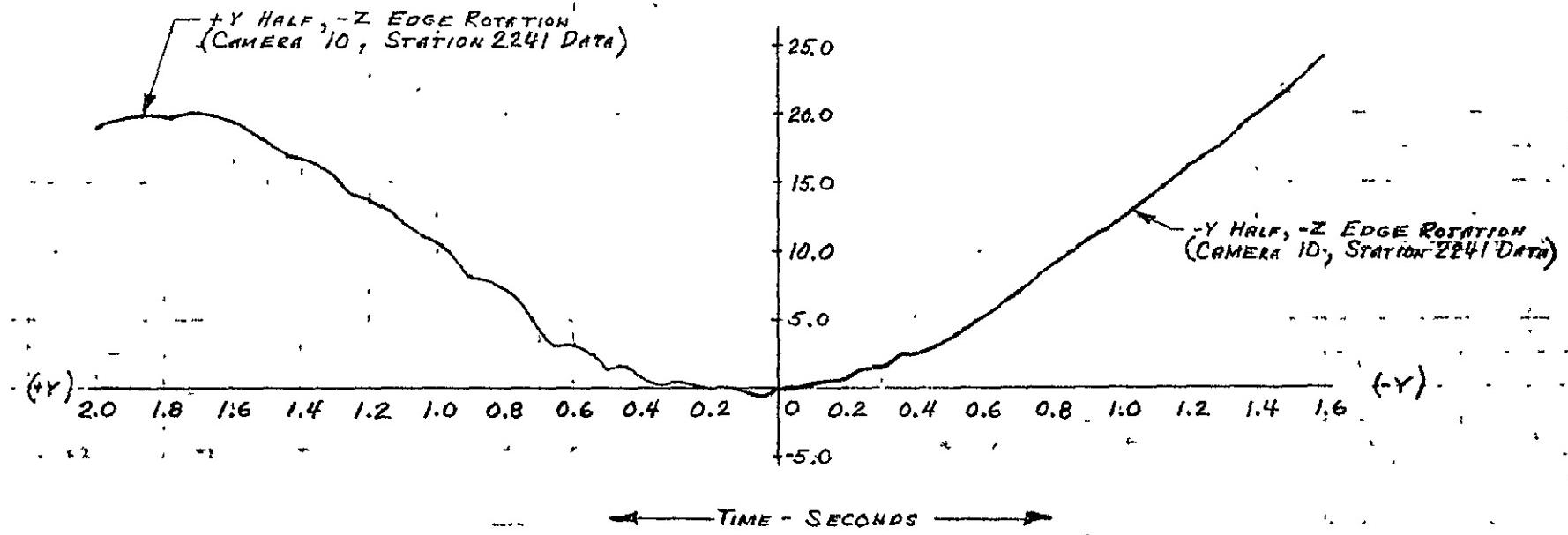


FIGURE II-31 CSS EDGE ROTATION VS. TIME - STATION 2241, TEST 2

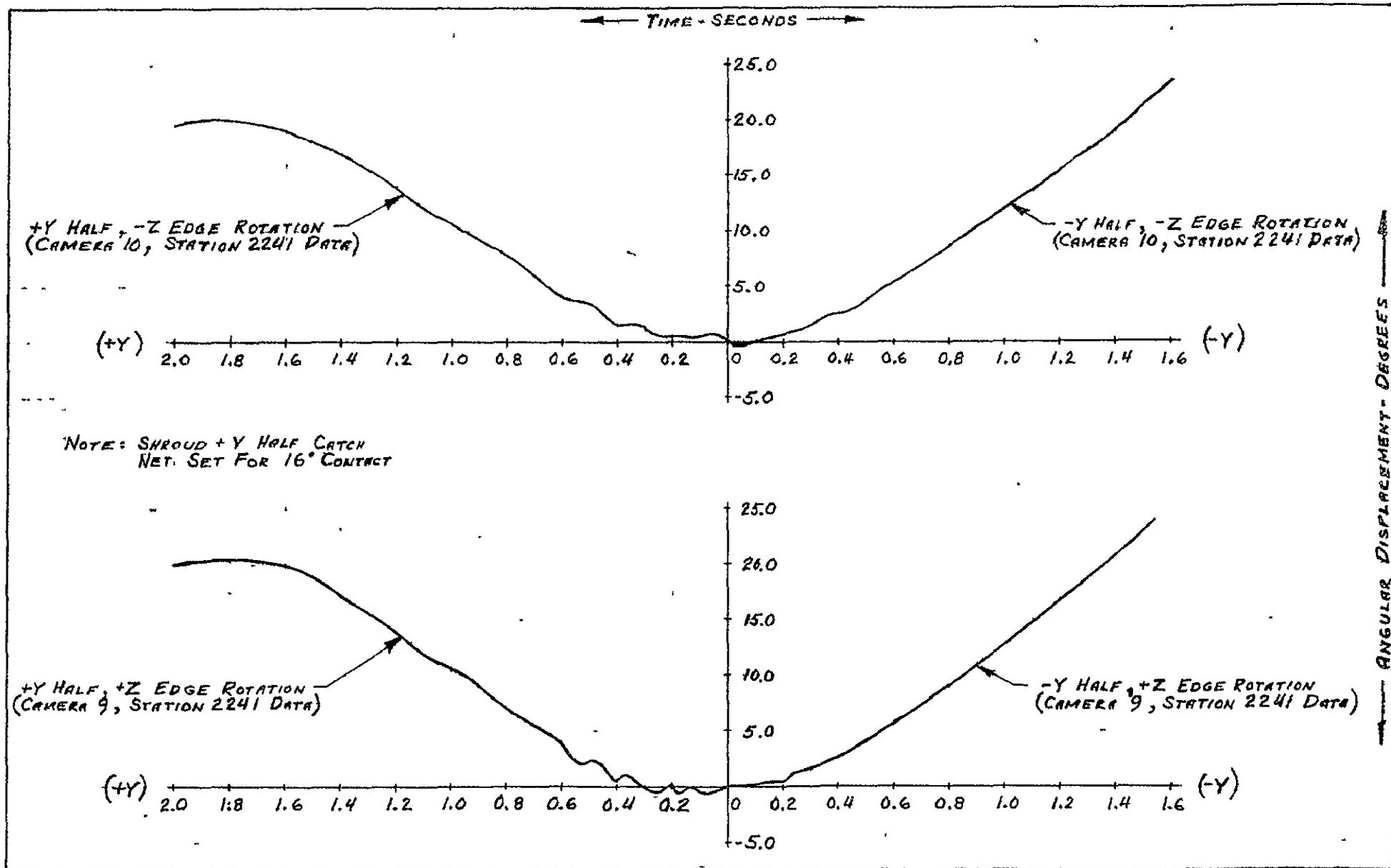


FIGURE VII-32 CSS EDGE ROTATION VS. TIME - STATION 2241, TEST 3

V.F. CSS Edge Motions

Eugene J. Cieslewicz

Payload Envelope Clearance

The Titan/Centaur payload envelope is shown in figure VF-1. There was no violation of the payload envelope by the CSS edges during any of the three tests. This is illustrated in figures VF-2 through VF-7. These figures show how the CSS edge motion looked from above. CSS edge radial displacement is plotted against the CSS edge tangential displacement as the time after jettison increased from zero to approximately 0.3 seconds. On all the curves this is the time necessary to complete two inboard movements of the CSS edges just after the firing of the Super-Zip. Radial displacement and the corresponding tangential displacement within the mentioned two cycles of edge motion inboard are the two parameters most significantly affecting possible payload envelope violation. The edge motion frequencies are approximately constant for the entire payload compartment length, but tangential displacements are greater with time near the CSS shoulder where amplitudes of radial motion were highest. The closest the CSS came to impinging upon the payload envelope was 1.77 inches at station 2680 during test 2. This is shown in figure VF-4. In general, for all three tests, the radial displacements were maximum at station 2680. Aft of this station, amplitudes decrease and at the bottom of the payload compartment (station 2514) have become too small to cause payload clearance problems.

It should be noted that for both heated jettison tests, the first displacements of any magnitude were inboard, and for the unheated test, first displacements were outboard. These effects are discussed in more detail in the following section. Further, the curves show offsets from pretest zero positions because of heating. The displacement directions correspond well with what was expected, away from the highest temperature inputs. The test 3 data of figures VF-6 and VF-7 for stations 2680 and 2664 show the pretest zero position as expected.

Typical Edge Motions, and Comparison with Predicted Motions

As mentioned in the Introduction, test 3 was performed in order to isolate the mechanical factors affecting jettison performance. The results of test 3 were used to verify the effects of these factors in the LMSC dynamic analysis computer programs. The model used for the program included all known forcing functions, and was updated to use the mass properties of the -Y non-dome shell half of the Plum Brook test CSS and the most accurate force-time histories of springs and disconnects. The forcing functions are:

- Spring thrusters
- Base acceleration
- Super-Zip impulse

Center-of-gravity offsets
Disconnect forces
Seal forces

A complete description of the program inputs and results is given in reference 8. For the edge motions computed for these tests, the spring force tolerances and center-of-gravity offsets were input only in directions to match the twisting motion observed in all three tests.

Figures VF-8 through VF-11 show the radial motions of the four edges at station 2664 during test 3. (In each figure, as well as many of the following figures, one or more portions show the test results, while the last portion shows the motion predicted by the LMSC computer programs. Also, the predictions are based on a model having mass properties of the -Y non-dome CSS half; thus, the frequency predictions for the +Y dome half always will be higher than the test results.) In these figures, the computer predictions are well matched to the test data in edge motions and in the twist motion. The twist motion, which was observed in all three tests, appeared as a counterclockwise rotation of the CSS halves when viewed from above. The computer program predicts this motion as an oscillation, having a frequency of 0.16 Hz, excited principally by unsymmetric mechanical forces such as separation of the LH₂ vent disconnect.

As described previously in section VB, the CSS tends to bend away from the MTL because of axial and circumferential thermal gradients ("hot-dog" distortion), and also tends to pinch into a figure eight shaped cross section because of radial thermal gradients in the rings and geometry of construction at the Super-Zip joints. When the Super-Zip is severed, the strain energy is released and the free edges of the CSS halves spring outboard and then begin an oscillatory radial motion which can reduce payload clearance on the inboard excursions. The CSS edge motions for tests 1 and 2, along with the motions predicted by the LMSC computer programs for test 2, are shown in figures VF-12 through VF-17. For these figures, the predicted results are obtained completely by analyses, beginning with temperatures and temperature gradients expected from the modified RH7588 trajectory. The whole method of analysis is described in Appendix A. Predictions are available only for test 2 (MTL at 0° azimuth) because of a critical computer program modification, made during analysis of these test results, which is difficult to make for other cases (See ref. 8). The radial edge deflections at station 2680 (figs. VF-12 through VF-15) are typical of the data obtained for stations in the payload compartment. The data show that the motion is approximately a 5.8 Hz oscillation on the -Y half and 5.4 Hz oscillation on the +Y half superimposed on a twist motion. Because of the combined effects of "hot-dog" deflection and twist motion, the inboard radial movement is greatest for the -Z edge of the -Y half. The stiff structural ring at station 2459 acts as a node point, and very little 5.8 Hz oscillation occurs below this station. Instead, a higher frequency, lower-amplitude mode is predominant. This mode has a frequency of approximately 9 Hz, and amplitude less than 0.4 inches peak-to-peak.

The test results did not show significant rocking motion in any of the tests. In all cases, the LMSC predictions are well matched with the test data. In the payload compartment, the frequency of edge motion is calculated within 0.2 Hz, and motion toward the payload envelope is calculated within 0.5 inches.

Table VF-1 summarizes the test data and is presented in graphical form with additional discussion in reference 8.

Comparison of Edge Motion from Camera and Accelerometer Data

Figure VF-18 shows a plot of accelerometer and camera data. They are shown plotted together as if the edges of station 2664 were viewed from above. The camera data shown indicates that all four of the edges were oscillating peak-to-peak about 2.50 inches at approximately 6 Hz. Three of the four accelerometers operated for the test and yielded frequencies which corresponded to that determined by the movie data. Two of the three also provided a good comparison on amplitudes. The camera data is probably more accurate since it is directly reduced. The accelerometer data had to undergo two integration operations to yield displacements for comparison. The method used to process the accelerometer data is described in Appendix D.

TABLE VF-1
CSS RADIAL EDGE MOTIONS & FREQUENCIES SUMMARY

STATION	+Z EDGE				-Z EDGE			
	+Y HALF		-Y HALF		+Y HALF		-Y HALF	
	* AMPLITUDE (In.)	FREQUENCY (Hz)	AMPLITUDE (In.)	FREQUENCY (Hz)	AMPLITUDE (In.)	FREQUENCY (Hz)	AMPLITUDE (In.)	FREQUENCY (Hz)
TEST 1								
2680	3.20	5.21	2.70	5.56	2.80	5.26	3.80	6.00
2664	2.77	5.30	2.40	5.71	2.60	5.37	2.40	6.02
2596	1.60	5.48	1.50	5.88	1.90	5.41	1.65	6.25
2514	0.65	5.20	0.95	5.75	1.00	5.26	1.00	6.17
2459	0.30	5.20	0.10	5.77	0.50	5.70	0.40	6.06
2241	0.60	10.00	0.30	9.30	0.50	8.30	0.40	10.00
2214	N.A.	N.A.	0.40	9.40	N.A.	N.A.	0.70	10.20
TEST 2								
2680	3.10	5.40	3.00	5.84	3.90	5.40	3.80	5.84
2664	3.20	5.42	2.50	5.88	3.40	5.41	3.60	5.88
2596	2.10	5.41	1.80	5.88	2.10	5.48	2.10	6.00
2514	1.20	5.48	1.00	5.77	0.90	5.41	1.10	6.02
2459	0.50	5.48	0.60	Random	0.40	5.22	0.40	6.12
2241	0.60	9.09	0.40	9.09	Small	Random	Small	Random
2214	N.A.	N.A.	1.00	8.00	N.A.	N.A.	Small	Random
TEST 3								
2680	1.20	5.00	0.80	5.81	1.10	4.88	1.20	5.78
2664	1.10	5.13	1.00	6.02	1.10	5.00	1.20	5.63
2596	0.60	4.82	0.50	5.71	0.70	5.00	0.80	5.56
2514	0.40	5.13	0.40	Random	0.20	Random	0.20	Random
2459	0.30	Random	0.20	Random	0.40	Random	0.40	Random
2241	0.80	8.70	0.40	8.57	0.70	10.12	0.50	10.00
2214	N.A.	N.A.	0.80	8.54	N.A.	N.A.	0.90	8.33

* Amplitudes Listed Are Peak-To-Peak Amplitudes

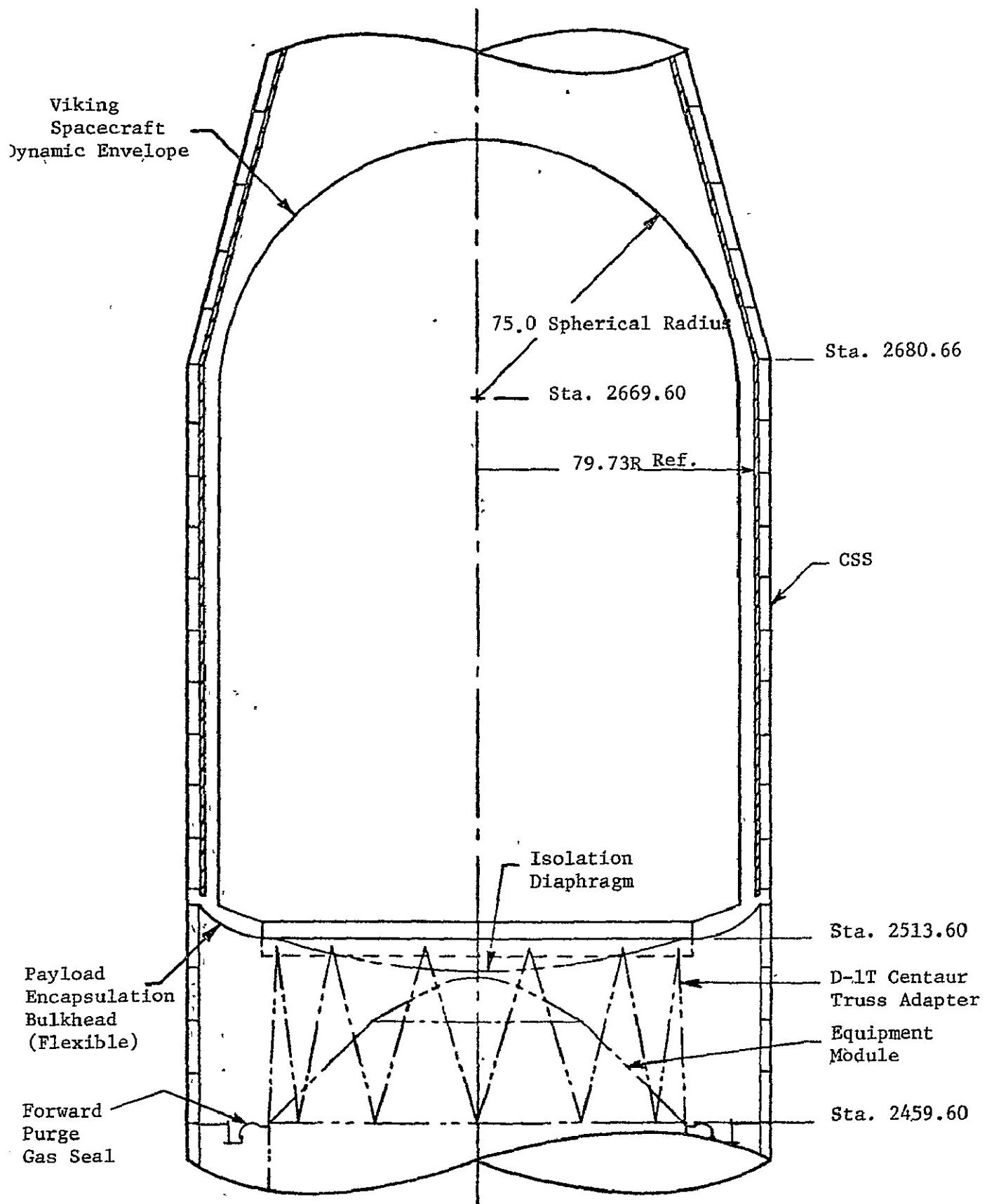
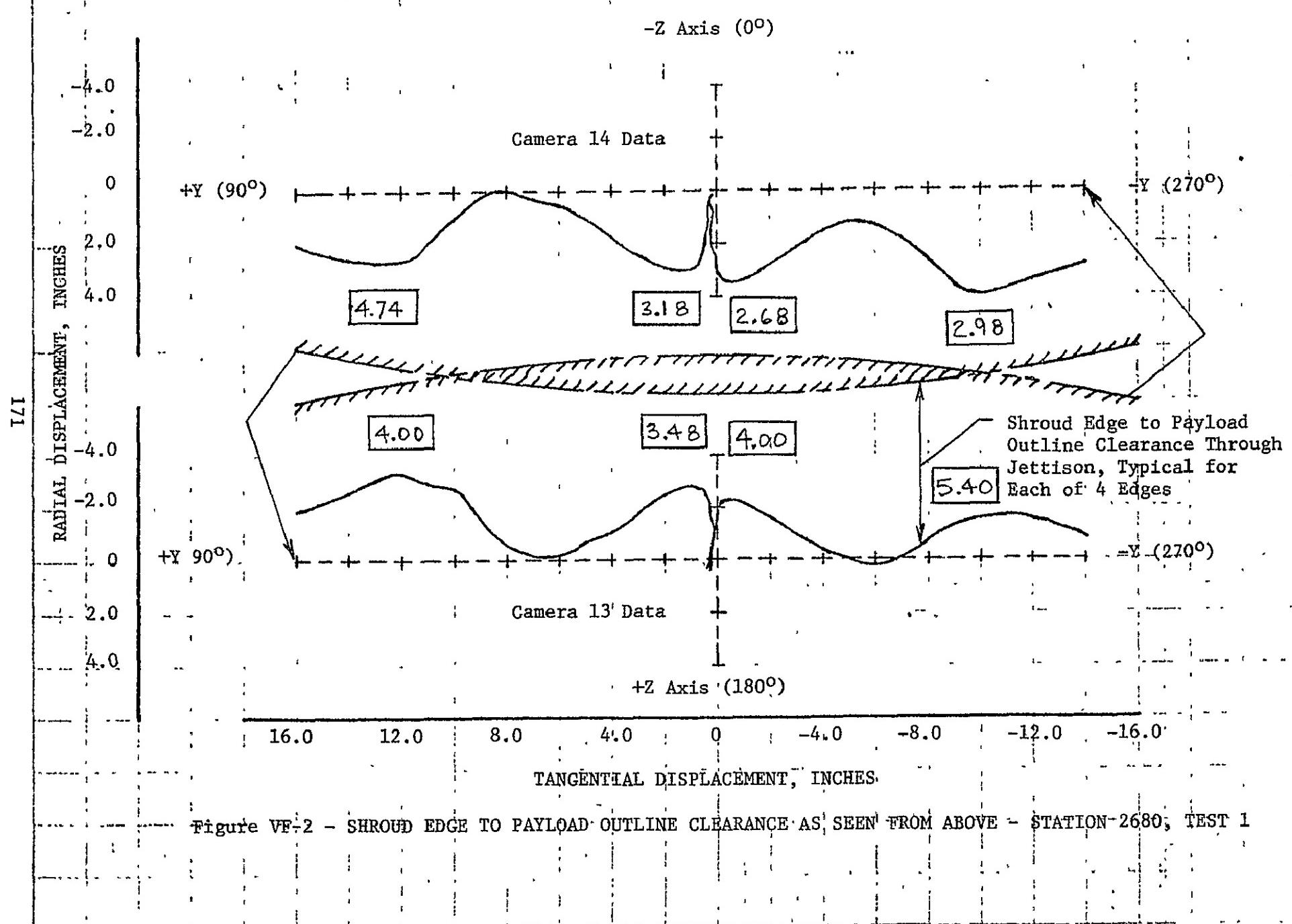
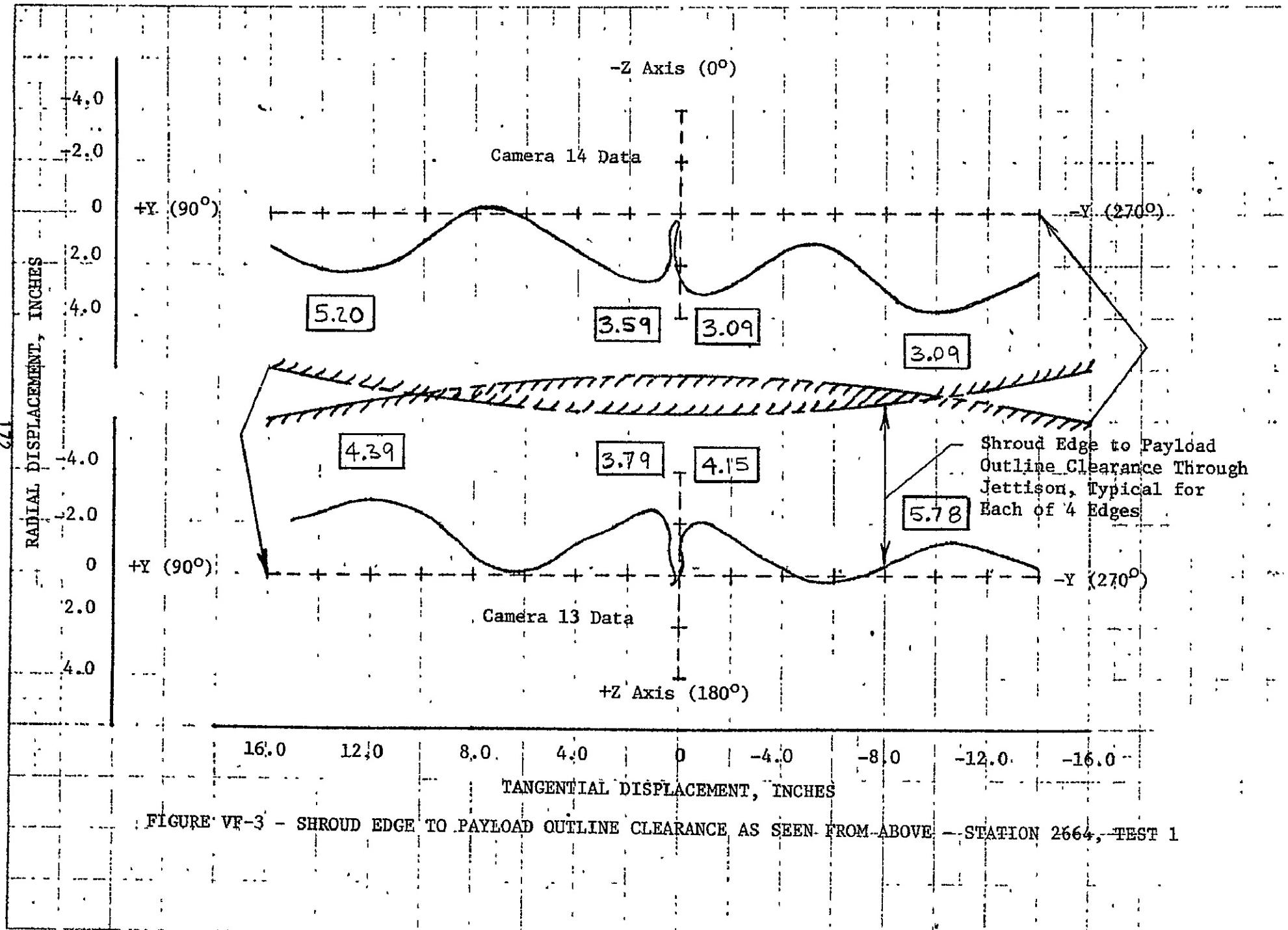


Figure VF-1 VIKING SPACECRAFT DYNAMIC ENVELOPE SHOWING CLEARANCE TO CSS





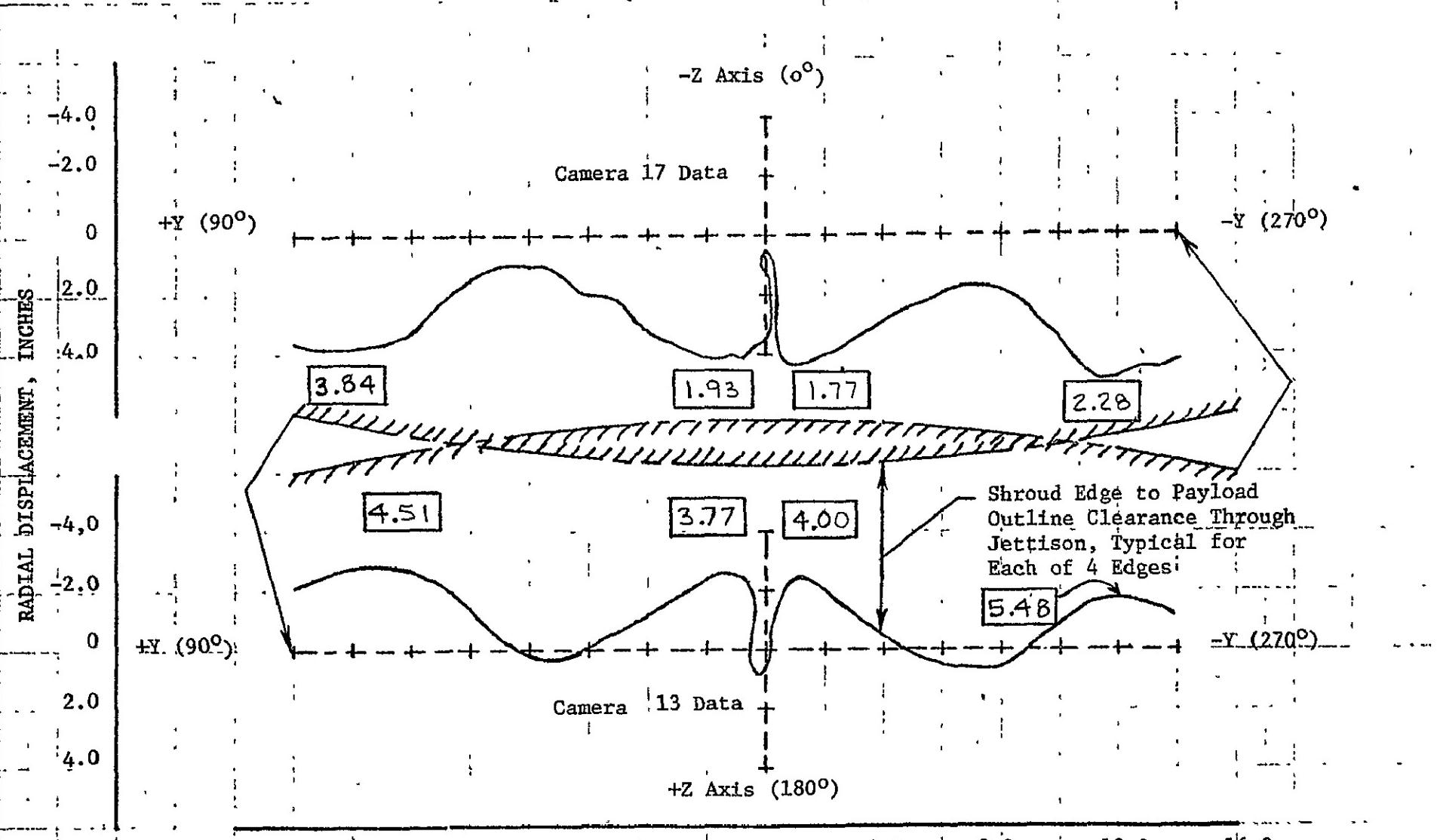
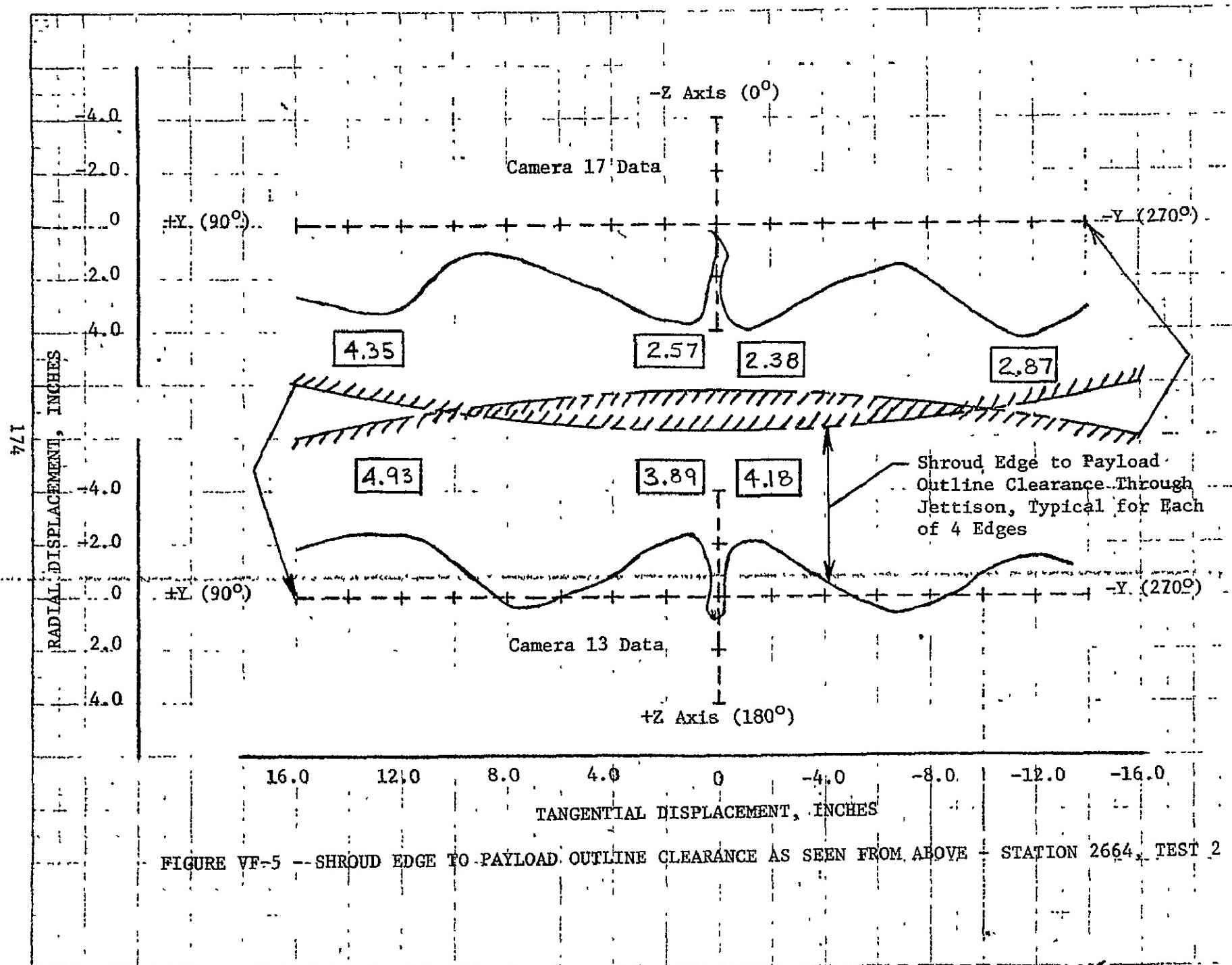
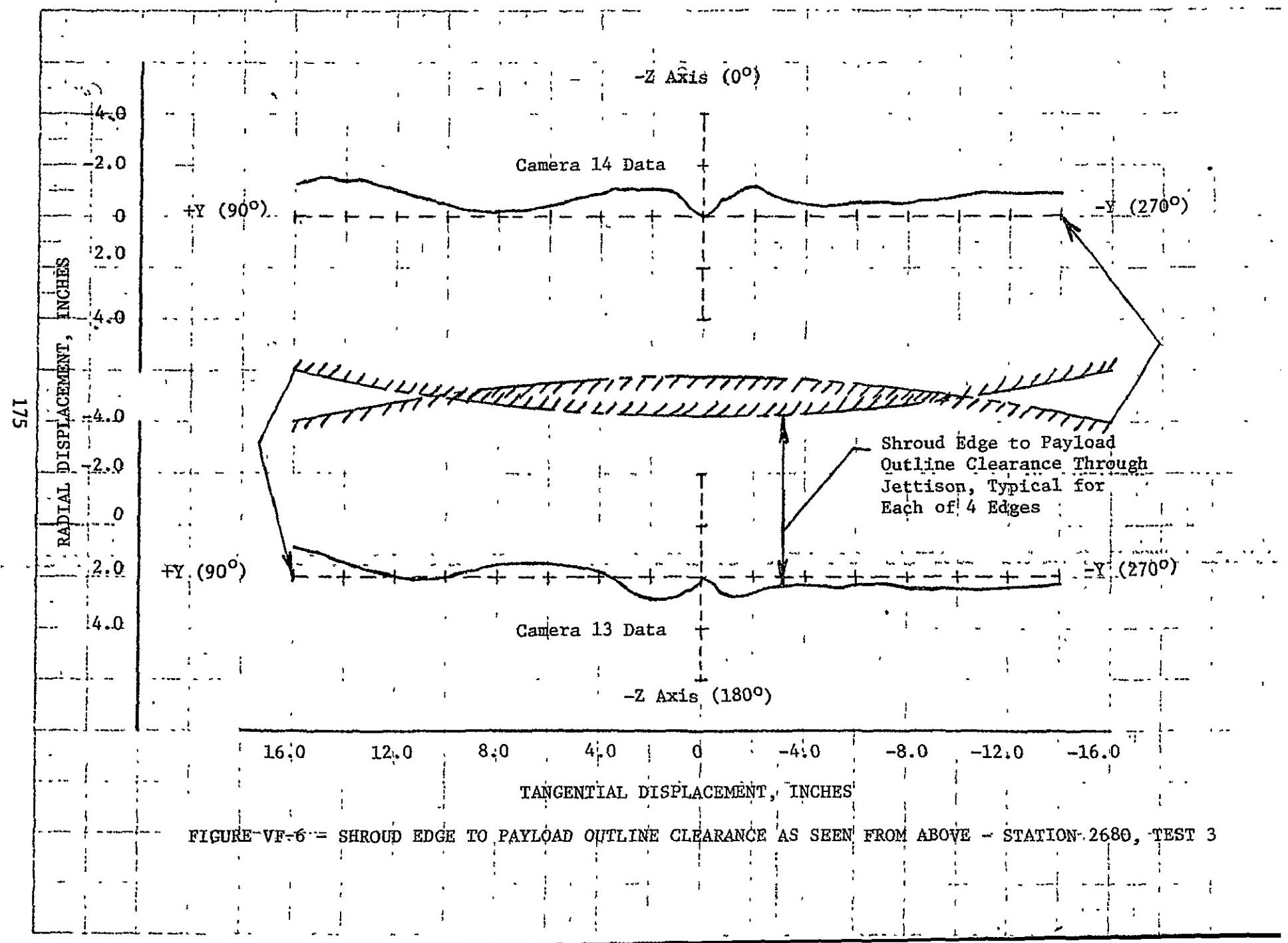
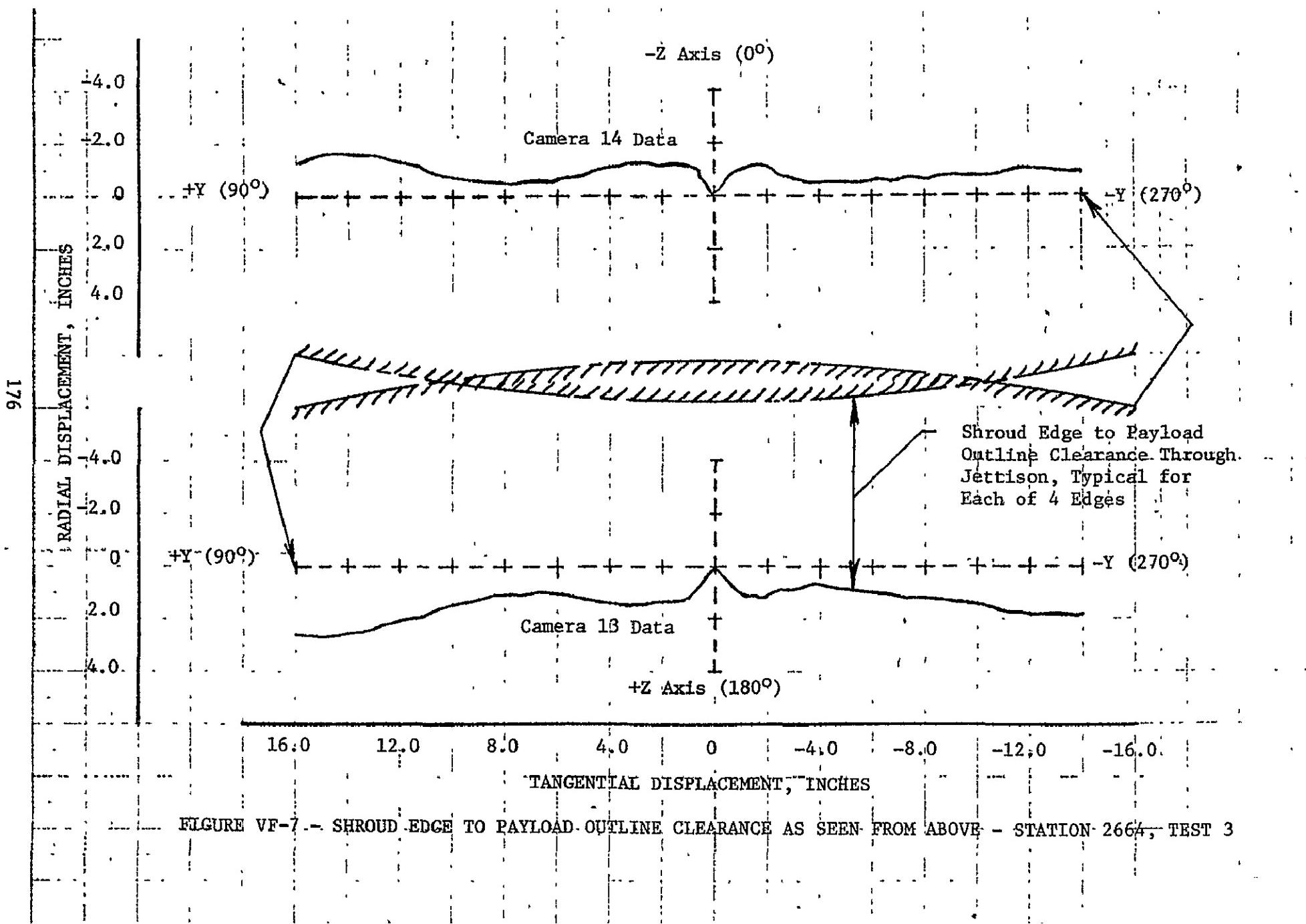


FIGURE VF-4 - SHROUD EDGE TO PAYLOAD OUTLINE CLEARANCE AS SEEN FROM ABOVE - STATION 2680, TEST 2







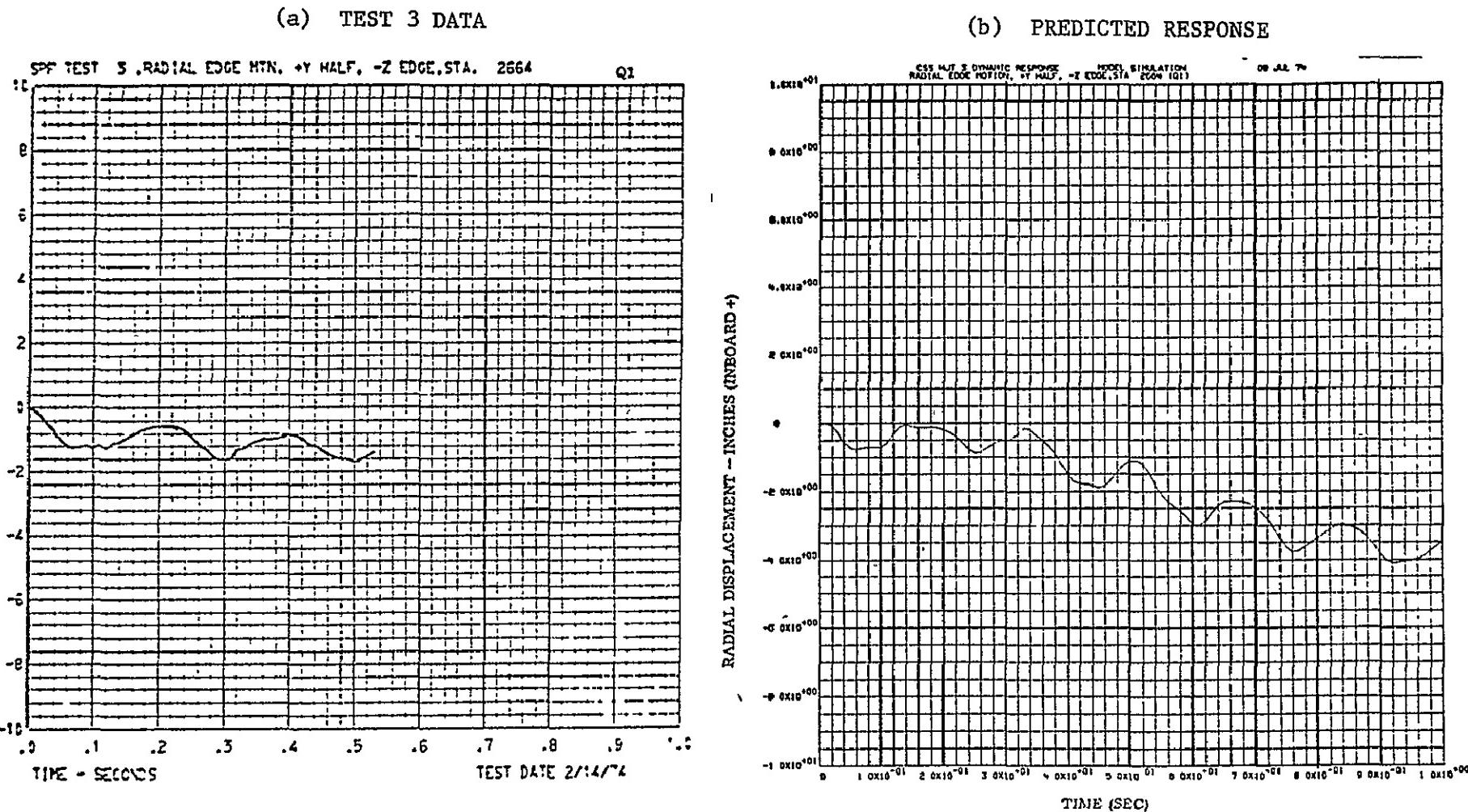


FIGURE VF-8 - RADIAL EDGE MOTION +Y HALF, -Z EDGE, Q1, STATION 2664

8/1

RADIAL DISPLACEMENT - INCHES (INBOARD -1) CAMERA 15

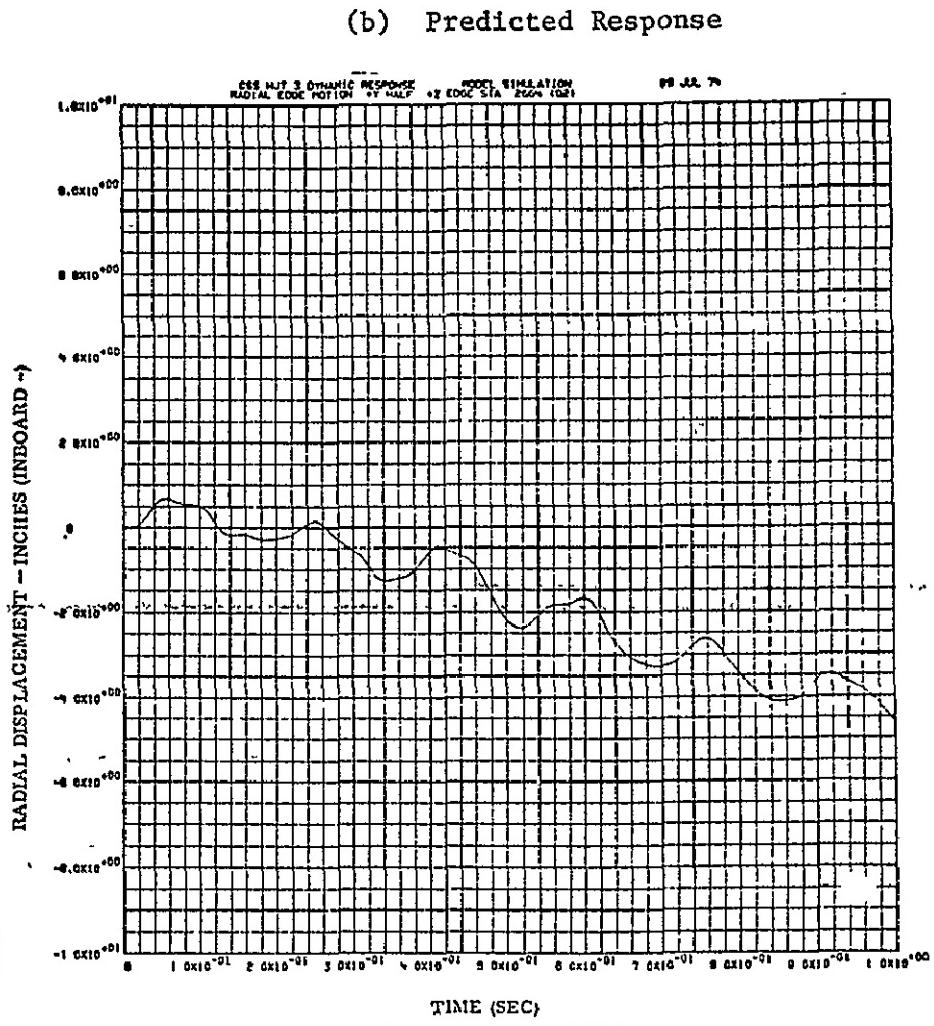
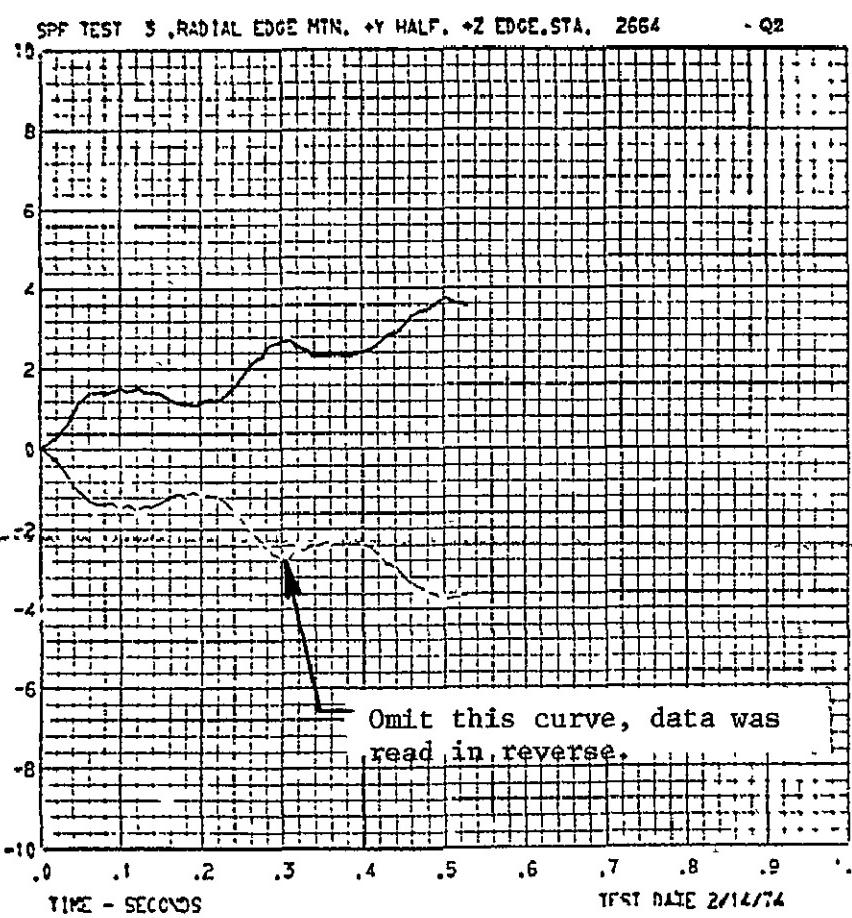
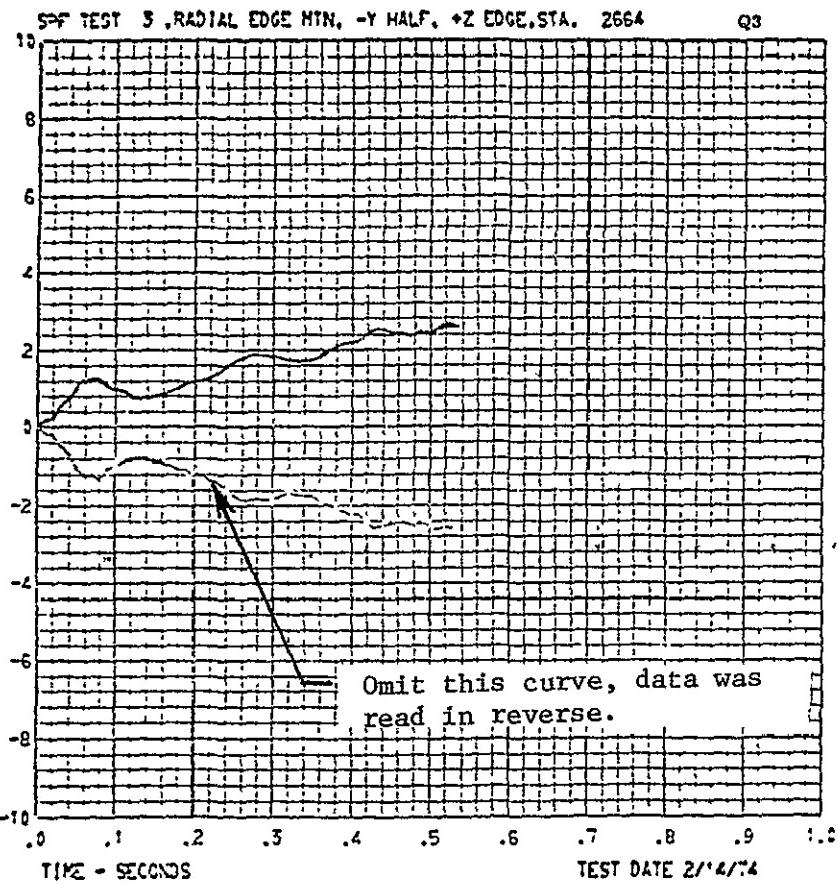


FIGURE VF-9 RADIAL EDGE MOTION +Y HALF, +Z EDGE, Q2, STATION 2664

(a) TEST 3 DATA



(b) PREDICTED RESPONSE

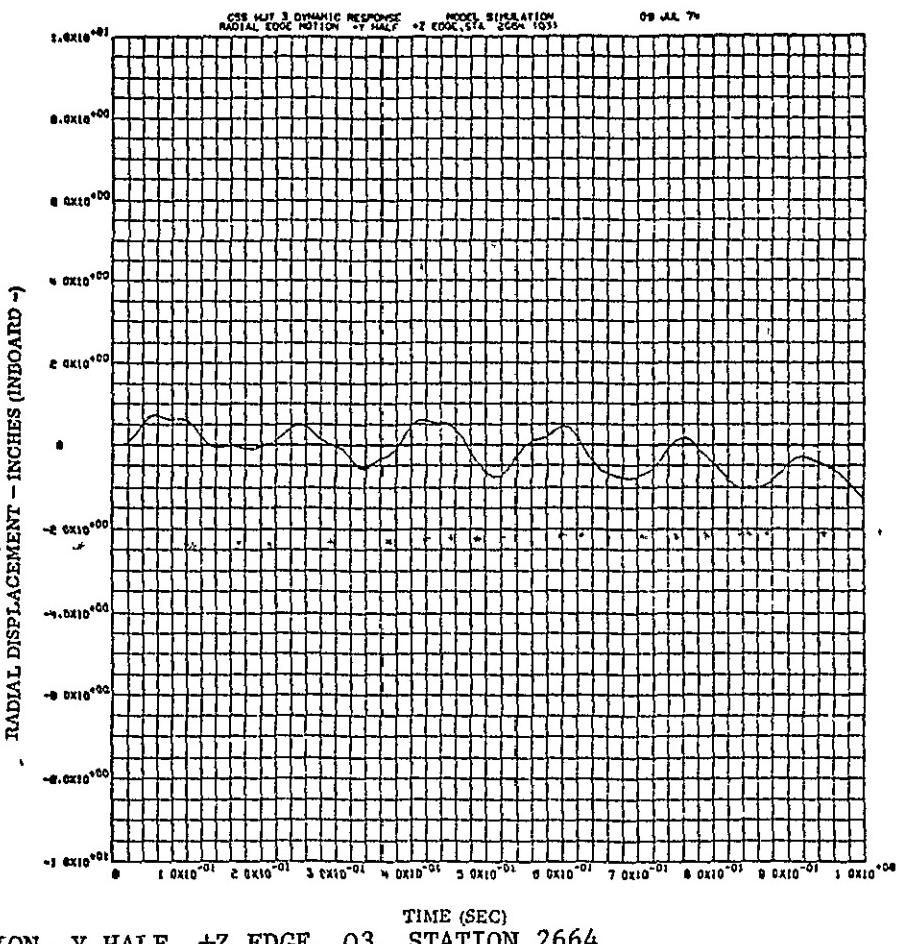
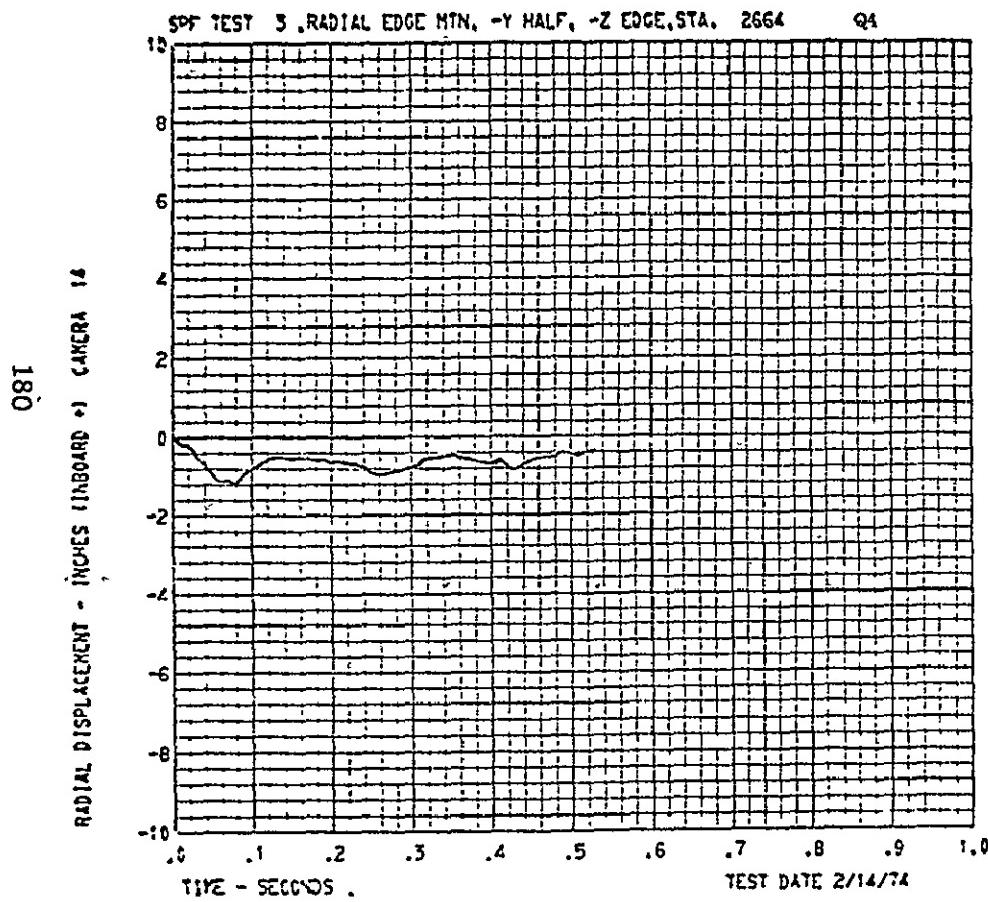


FIGURE VF-10 RADIAL EDGE MOTION -Y HALF, +Z EDGE, Q3, STATION 2664

(a) TEST 3 DATA



(b) PREDICTED RESPONSE

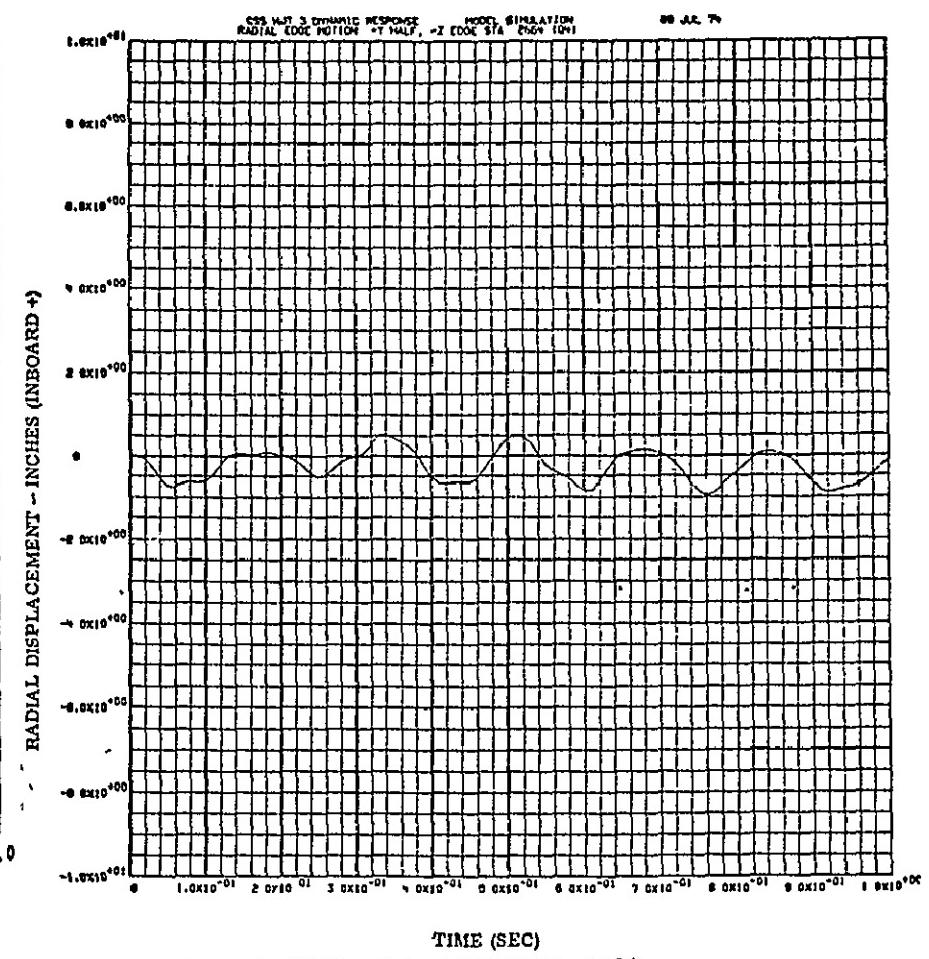


FIGURE VF-11 RADIAL EDGE MOTION -Y HALF, -Z EDGE, Q4, STATION 2664

RADIAL DISPLACEMENT - INCHES
(INBOARD +)

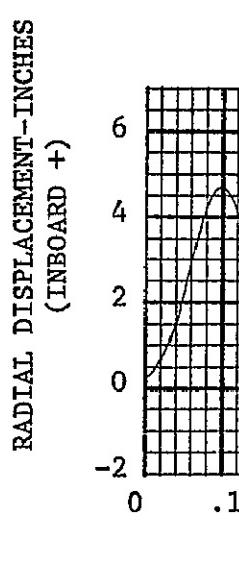
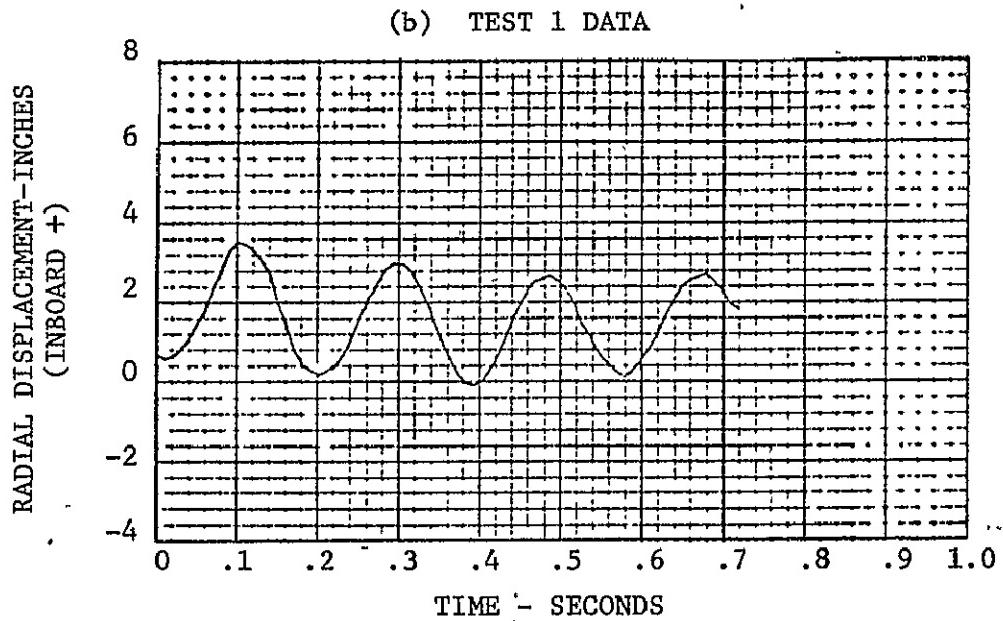
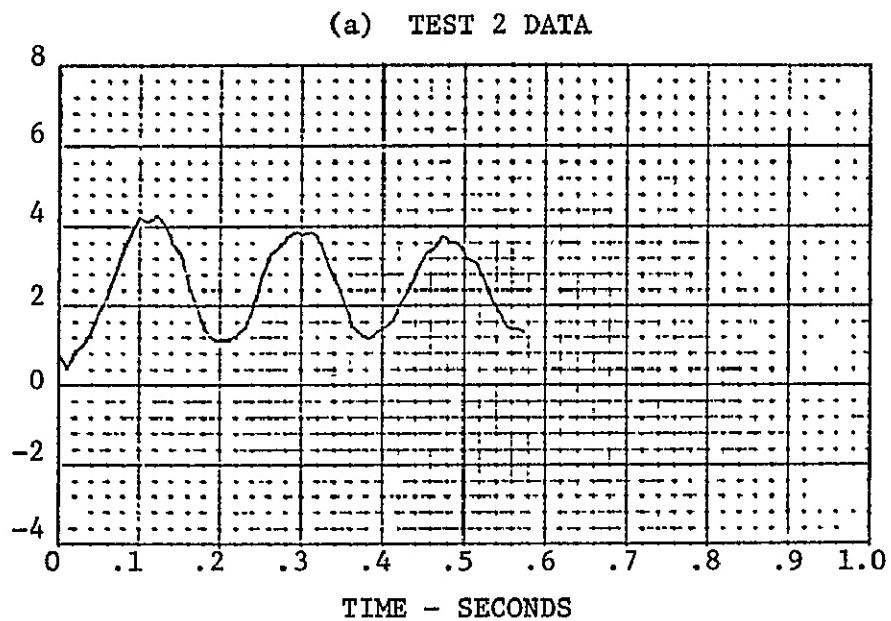
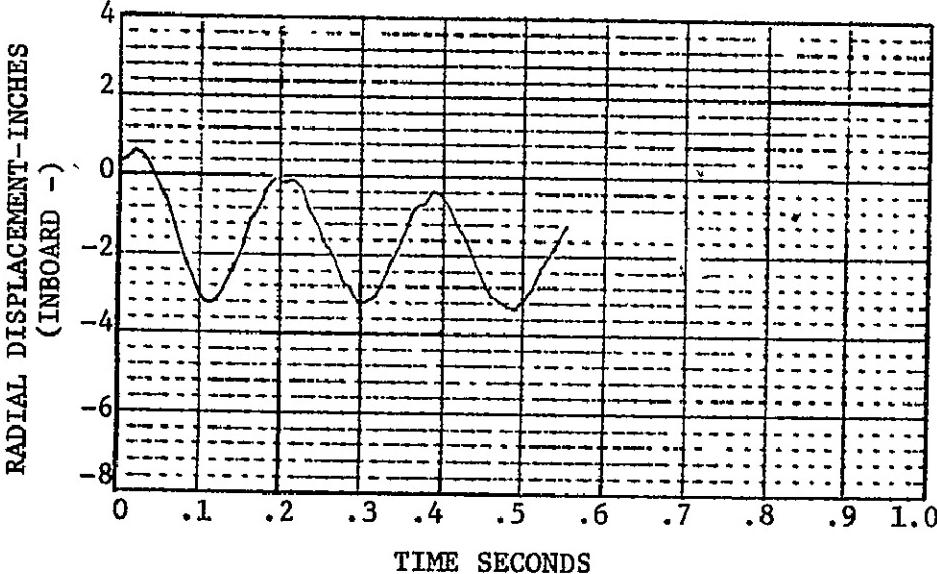
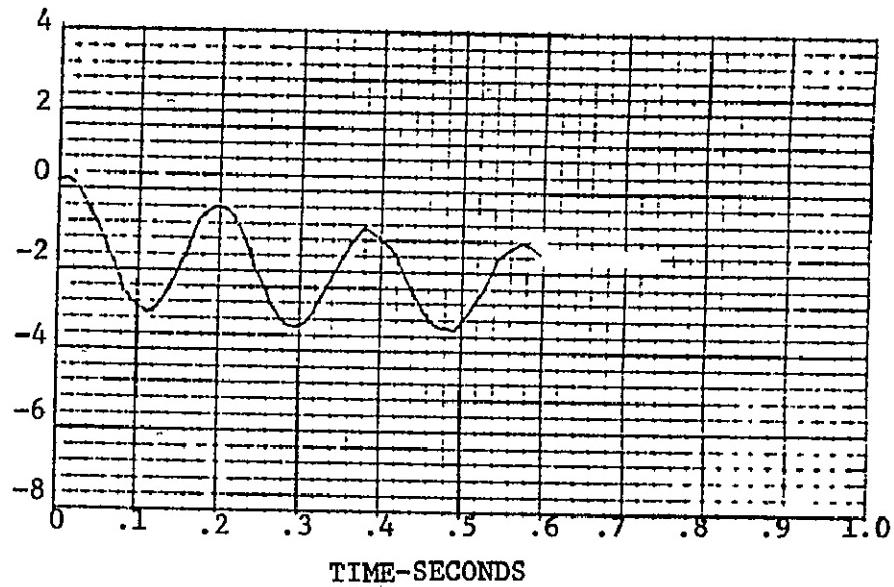


FIGURE VF-12 RADIAL EDGE MOTION +Y HALF, -Z EDGE, Q1, STATION 2680

(a) TEST 2 DATA



(b) TEST 1 DATA



(c) PREDICTED RESPONSE

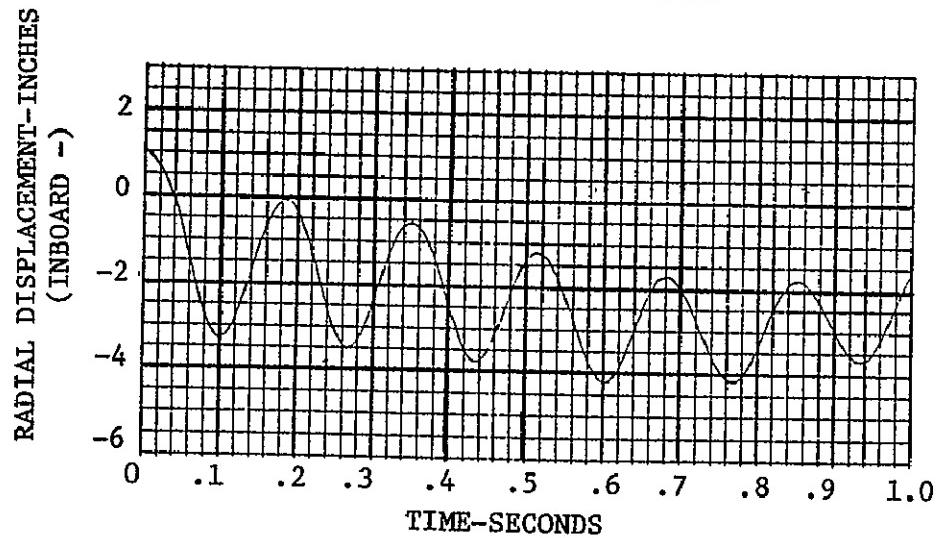
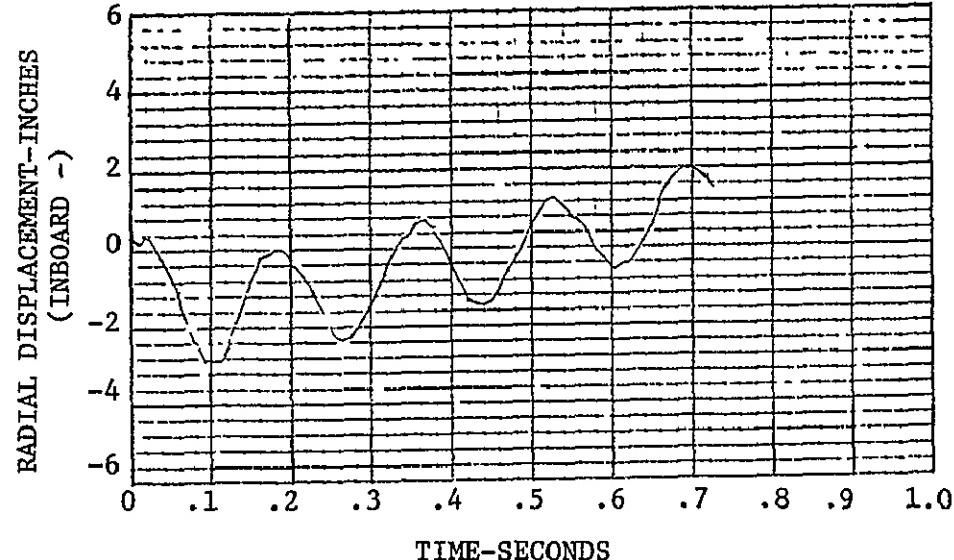


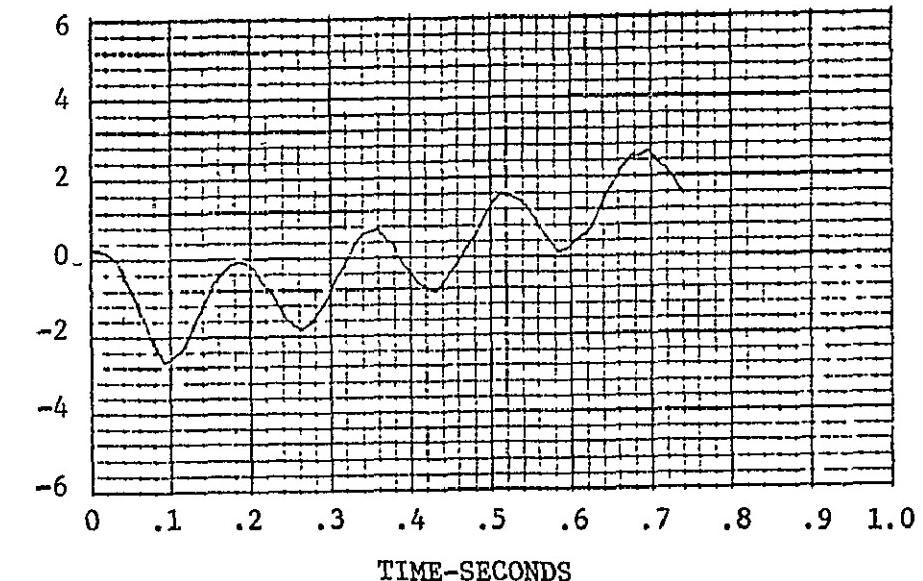
FIGURE VF-13 RADIAL EDGE MOTION +Y HALF, +Z EDGE, Q2, STATION 2680

REPRODUCIBILITY OF THE
ORIGINAL PAGE IS POOR

(a) TEST 2 DATA



(b) TEST 1 DATA



(c) PREDICTED RESPONSE

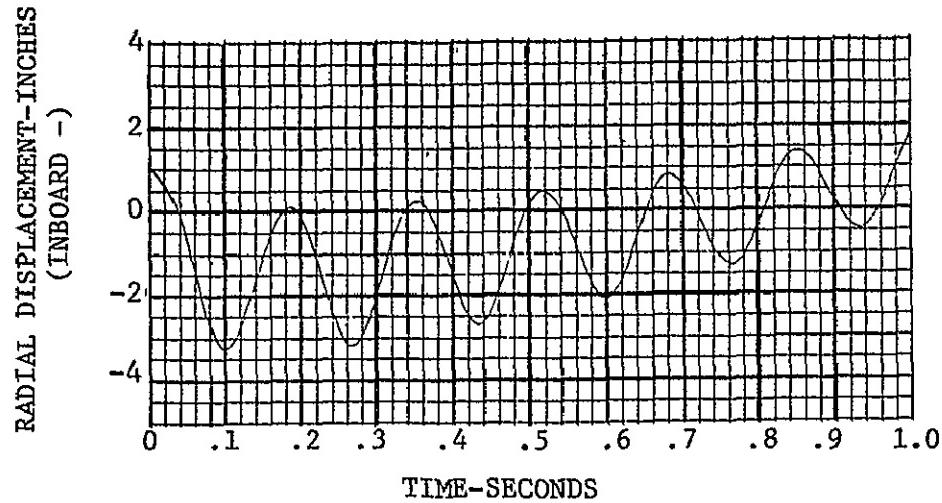
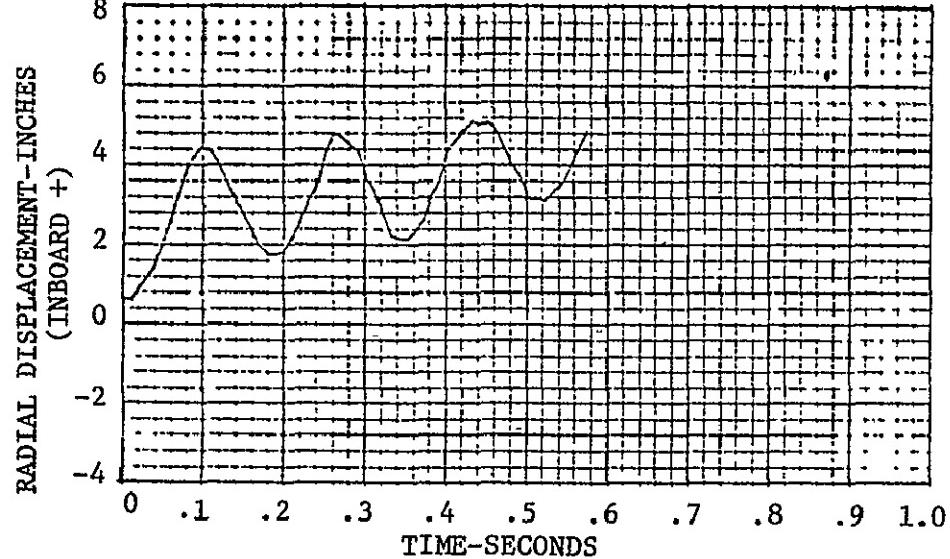
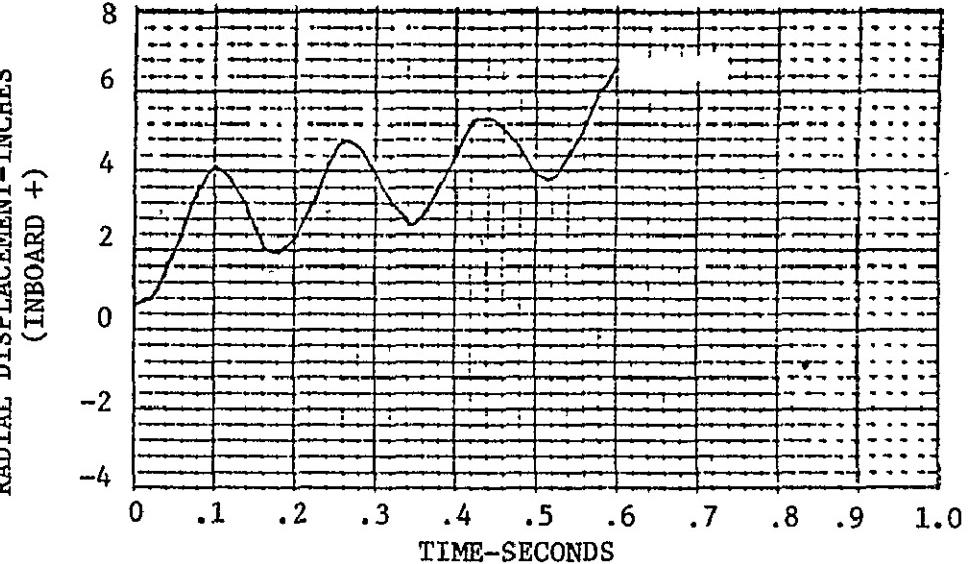


FIGURE VF-14 RADIAL EDGE MOTION -Y HALF, +Z EDGE, Q3, STATION 2680

(a) TEST 2 DATA



(b) TEST 1 DATA



(c) PREDICTED RESPONSE

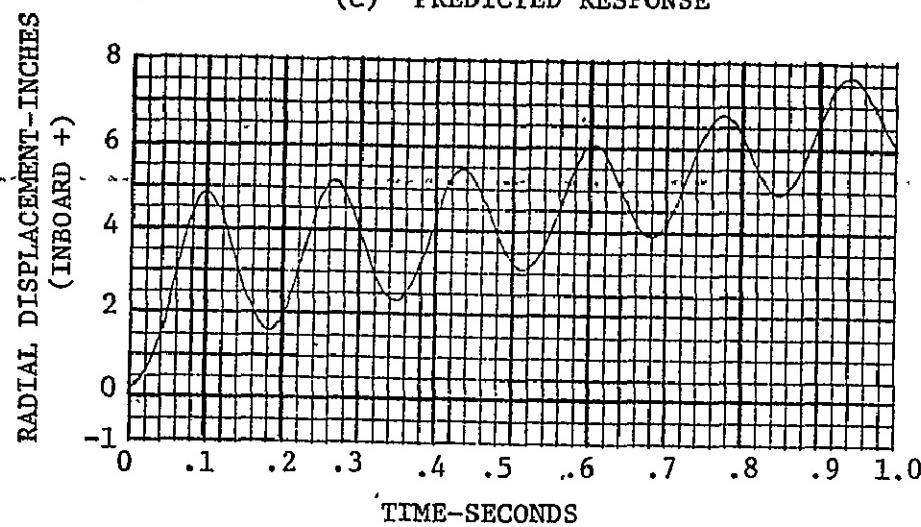
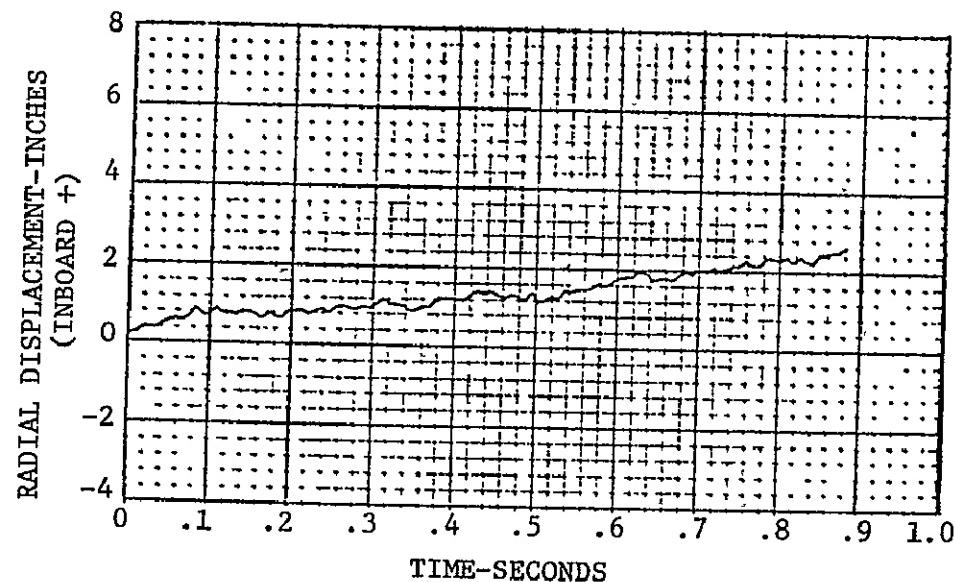
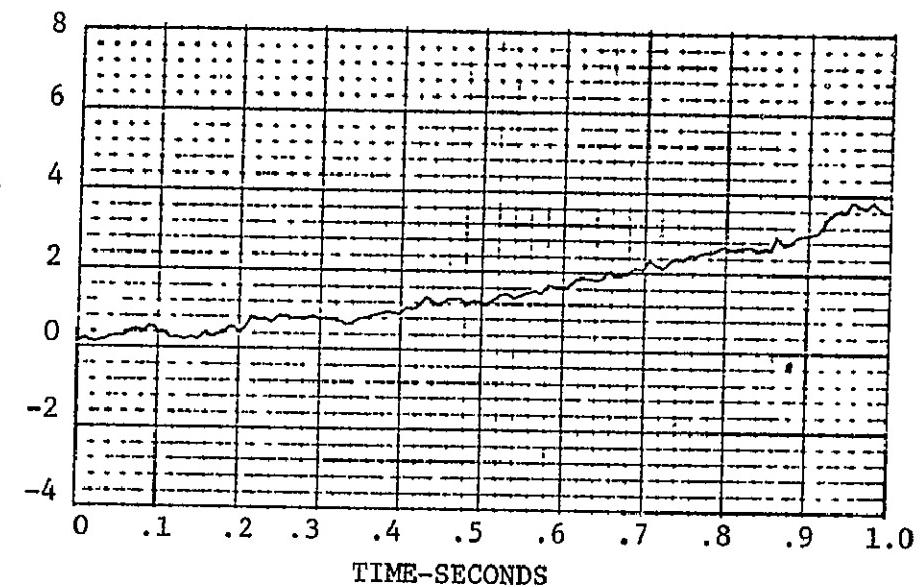


FIGURE VF-15 RADIAL EDGE MOTION -Y HALF, -Z EDGE, Q4, STATION 2680

(a) TEST 2 DATA



(b) TEST 1 DATA



(c) PREDICTED RESPONSE

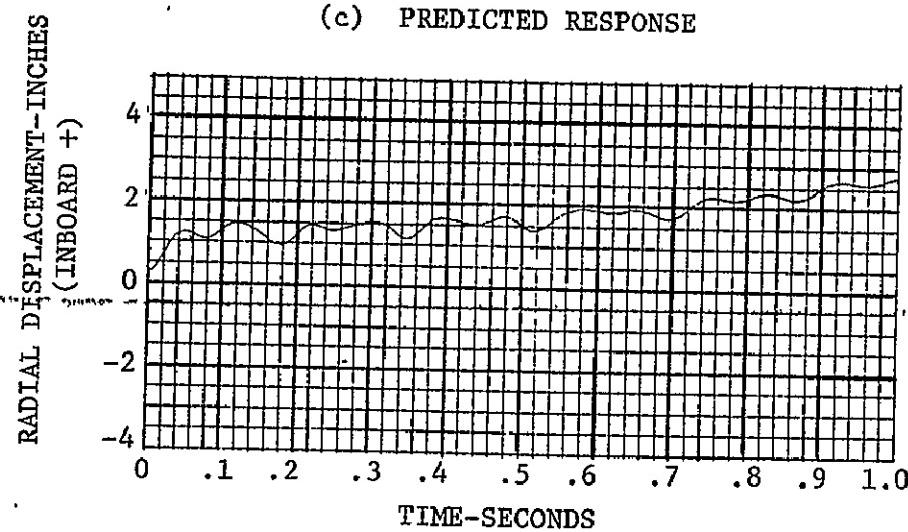
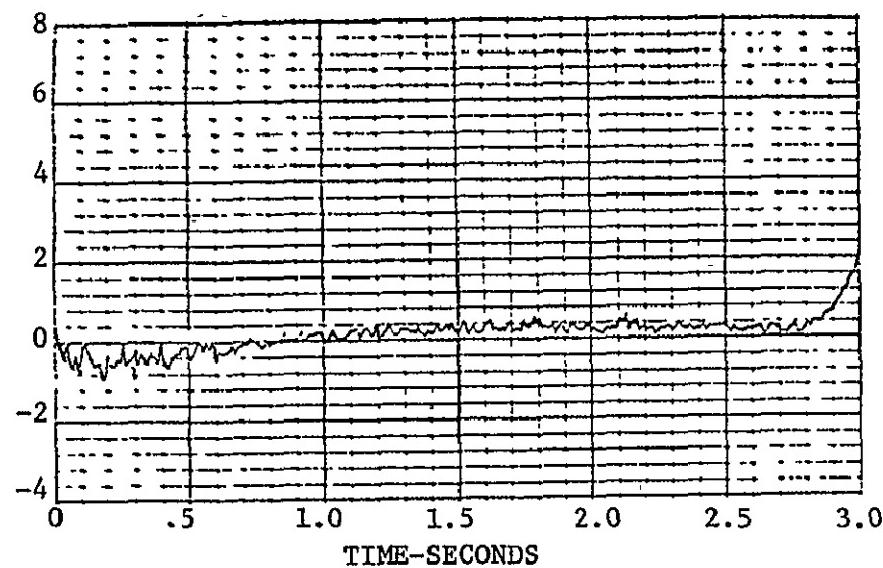


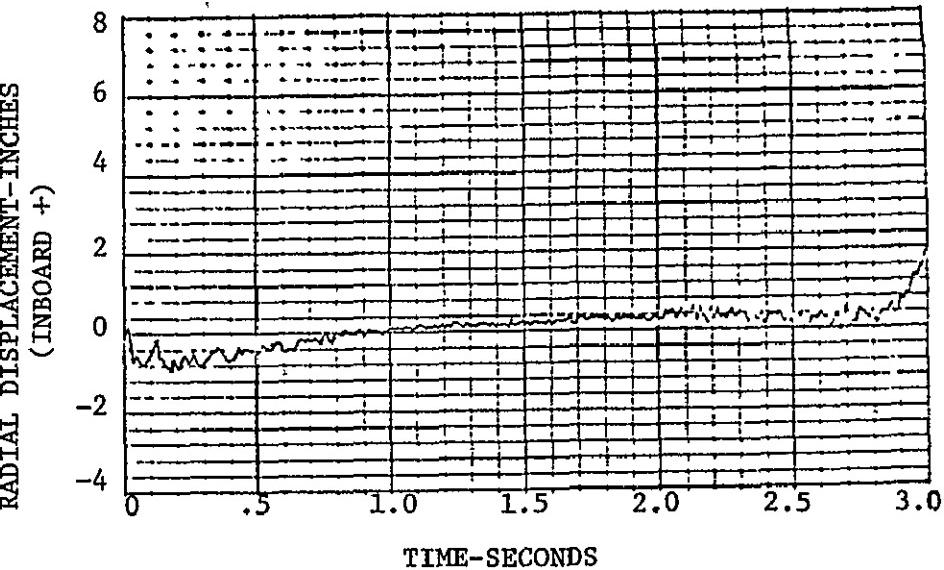
FIGURE VF-16 RADIAL EDGE MOTION -Y HALF, -Z EDGE, Q4, STATION 2459

RADIAL DISPLACEMENT-INCHES
(INBOARD +)

(a) TEST 2 DATA



(b) TEST 1 DATA



(c) PREDICTED RESPONSE

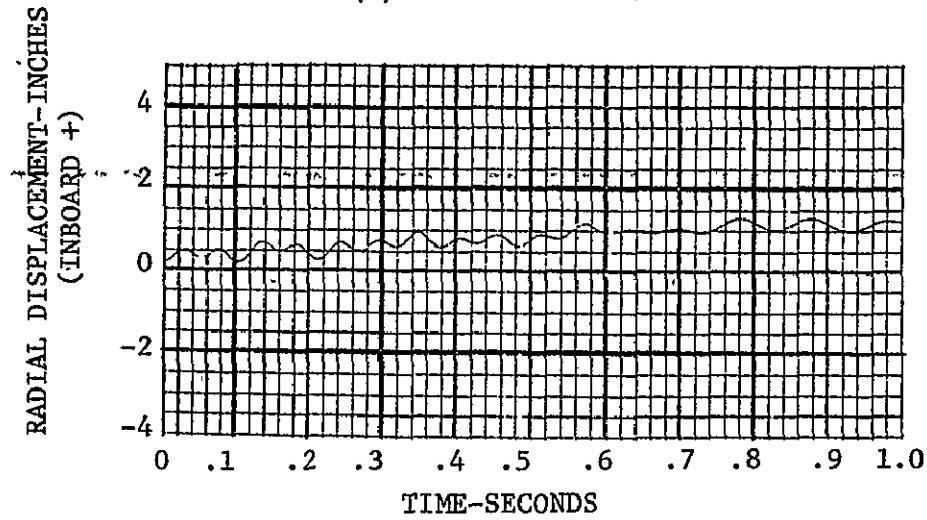


FIGURE VF-17 RADIAL EDGE MOTION -Y HALF, -Z EDGE, Q4, STATION 2214

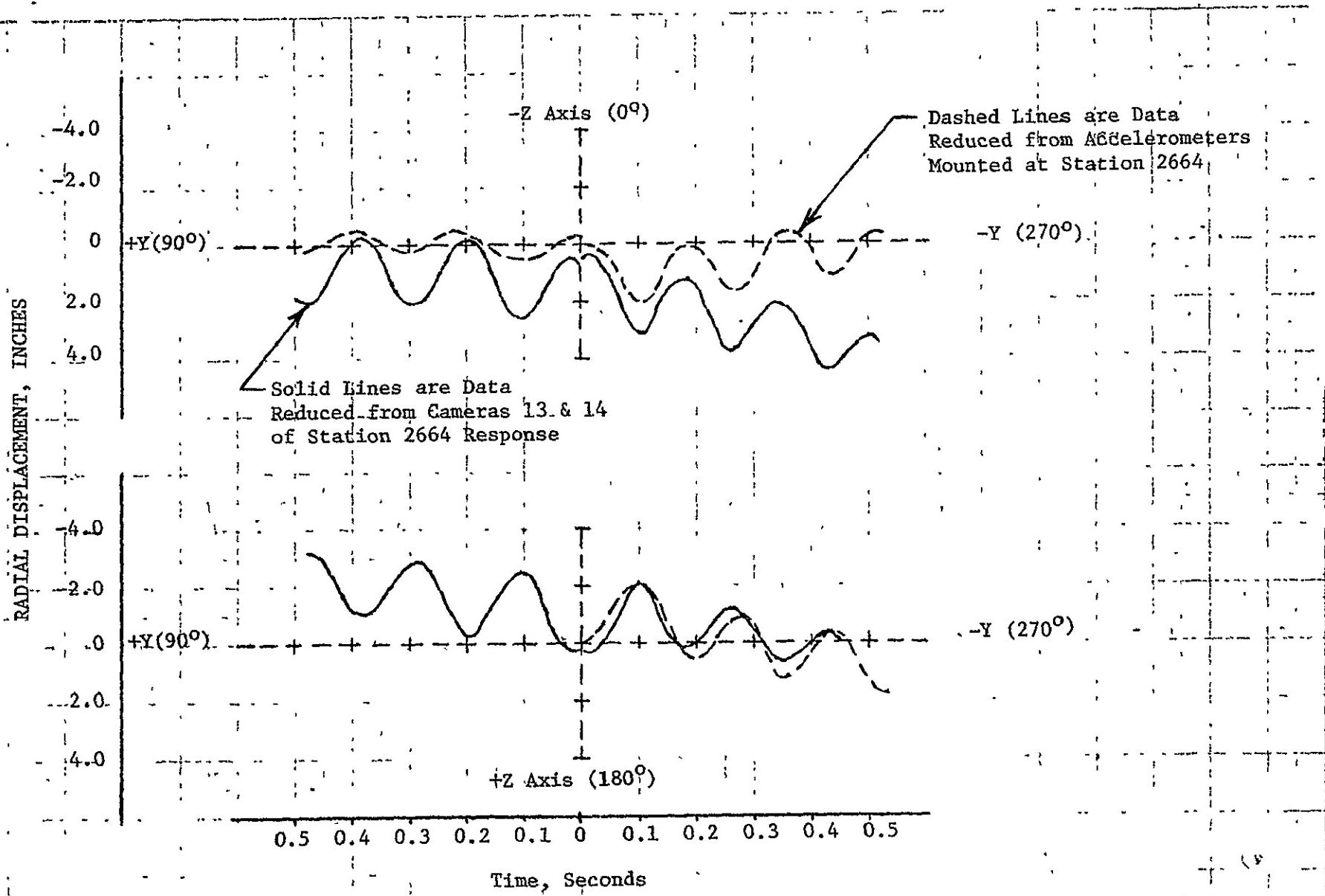


FIGURE VF-18 COMPARISON OF CAMERA AND ACCELEROMETER DATA AT STATION 2664, TEST 1

VI. CONCLUDING REMARKS.

by Thomas F. Niezgoda

This test series has proven the functional and structural capability of the CSS to jettison successfully at altitude pressures after being subjected to maximum flight aerodynamic heating. Useful data has been obtained to verify analytical tools used to predict CSS dynamic motions, trajectories, and thermal stress distributions during flight conditions, both prior to and during jettison. All test objectives were successfully accomplished.

The General Dynamics Convair Division (GDC) maximum design heating trajectory, RH758B, was used to program the heating fixture control thermocouples to produce the required temperature profile history. Actual test temperatures followed the programmed values within $\pm 15^{\circ}\text{F}$. The cone and cylinder rings had radial temperature gradients of 30° to 65°F at the MTL at the time of jettison. The distortions due to heating ("hot-dogging") matched predicted deflections very well. These deflections were about 0.50 inch to 0.65 inch at station 2664, which is near the CSS cone-cylinder joint.

Stresses due to heating were low throughout the CSS nose cone and cylindrical sections. Both meridional and circumferential stresses in the nose cone skin and rings agreed well with LMSC predictions, but the cylindrical meridional stresses showed poor agreement, probably due to a nonuniform stiffness in the cylindrical shell in this area. Boattail hinge and longeron stresses indicated that no rocking loads were experienced by the CSS jettison hinges. Peak hinge loads occurred at 0.06 to 0.08 second after Super*Zip firing, and the maximum load of 8470 pounds on the 103° hinge occurred during jettison test 3. This value is about 46 percent of design values. The interstage adapter interface ring at station 2177 experienced stresses of only 15 percent of yield while the stringers below the ring experienced even lower values.

The primary firing mode of the CSS Super*Zip separation system was successfully demonstrated in all three jettison tests. However, some anomalies did occur in the secondary firing mode requiring design changes to improve this system's reliability. Electrical disconnects on the Centaur stage Equipment Module (E/M) panel and the Helios tripod disconnect separated normally, although a lanyard broke on the 66° E/M panel. This failure was attributed to damage due to overuse in many previous tests. The Centaur stage forward purge gas seal, aft purge gas seal, LH_2 vent disconnect, and the vent gas retainer all functioned properly during the tests.

The CSS rotational time history followed a curve which an analysis had predicted for an 80 percent jettison spring efficiency. The 20 percent loss in efficiency was due to frictional and aerodynamic effects, which tended to slow the rotation of the CSS. Complete separation of the -Y half of the CSS occurred at about 2.6 seconds and 60° of rotation.

Initial edge motions of the CSS split line were radially inboard for the heated tests and radially outboard for the cold test. The inboard edge motion was a result of the thermal gradient in the CSS rings which forced the rings to pinch inward at the split line since the outboard flanges of the rings were much warmer than the inboard flanges. The CSS moved to within 1.77 inches of the payload envelope at station 2680 during test 2. The dynamic response of the upper CSS halves was at a frequency of 5.3 to 6.0 Hz while the lower boattail frequencies were at 8.0 to 10.0 Hz.

APPENDIX A

Calculations of CSS Edge Motions

John C. Estes

The pre-separated thermal distortions of the CSS are discussed in Section VB. At separation, the thermal stresses in the CSS release stored strain energy. The separated shell halves tend to seek new equilibrium positions based on the thermal distributions in the shell halves. The edges of the shell halves vibrate due to the released strain energy as the shell halves go from one equilibrium position to the other. These vibrations, when superimposed on the rigid-body rocking of the CSS about its hinges, make up the post-separated edge motions of the CSS discussed in Section VF.

One of the major objectives of the CSS heated jettison tests was to determine whether the contractor could accurately predict the magnitude and phasing of the CSS edge motions during jettison. This prediction capability is extremely important in order to insure an accurate assessment of the CSS-spacecraft clearances during jettison under extreme flight conditions. The heated jettison tests did not fully simulate an extreme flight situation, even though the test heating conditions did simulate the external heating effects of a worst-case trajectory at high altitude. As discussed elsewhere, test radial temperature distributions varied somewhat from flight conditions because the test chamber could not achieve the full vacuum condition of flight. The test was, of course, conducted in a 1.0 g earth environment, but a worst-case condition for edge motions would be predicted for a jettison at an acceleration of 0.6 g (the minimum considered for design). In addition, an extreme CSS jettison would be assumed to occur during a specified level of limit cycle oscillation of the booster vehicle. No limit cycle effects were simulated in the heated jettison tests.

Since the test conditions did not include all extreme flight conditions, the test results could not be directly compared with previous worst-case edge motion predictions. In order to make direct comparisons, new prediction cases were run using the exact conditions simulated in the three jettison tests. New structural models were prepared to update earlier models and to include pre-test predictions of the actual CSS masses and centers of gravity.

The LMSC analytical structural model of the CSS was a finite element representation of the interstage adapter, CSS boattail, CSS cylindrical section, and biconic nose. The CSS has two planes of symmetry, along the separation plane and perpendicular to the separation plane. The two planes of symmetry permitted use of a one-quadrant (90°) analytical model. Responses in all four quadrants were calculated by applying combinations of symmetric and antisymmetric boundary conditions to this one-quadrant model. This single general model precluded local openings, doors, or mass concentrations from being considered in the model. Nose sections of the CSS were modeled as ring-stiffened structures of isotropic membranes and bending plates. Ring-stiffened orthotropic membranes and bending plates were used to model the interstage adapter and the corrugated cylindrical

section of the CSS. The longitudinal stiffeners of the CSS boattail were "smeared" with the conic skin to obtain equivalent orthotropic properties. Node points were included at 15° intervals around the circumference, and all rings were included. The resulting model had 926 nodes and 2628 degrees of freedom. Table A-1 shows the node point locations. Figures A-1 and A-2 depict the model graphically. The base of the interstage adapter was fixed. Otherwise, the model could move elastically in 6 degrees of freedom. It could rotate as a rigid body about the hinges.

Mass properties for the model were taken from the -Y CSS half, since the -Y half rotated completely off its hinges in the tests. These mass properties were considered:

	<u>+Y Half</u>	<u>-Y Half</u>
Weight (lb.)	-	2971.0
X c.g. (Station)	-	2476.0
Z c.g. (Inches)	4.2	-0.5

Table A-2 shows predicted frequencies for 11 symmetric and 6 antisymmetric post-separated modes. Also shown are predicted frequencies for the earlier cryo-unlatch tests and observed frequencies which LMSC was able to detect for both the cryo-unlatch and heated jettison tests. The first symmetric (pendulum) mode was virtually rigid-body rotation. The second, third, and fourth symmetric modes involved "breathing" motions of the shell edges. It will be noted that their observed frequencies were an excellent match to analytic predictions. Frequencies for the observed antisymmetric modes were very difficult to match with predictions, because the primary modes had very low frequencies, and the test observations covered a very short time span. LMSC did conclude that observed second antisymmetric mode (rocking) frequencies were considerably lower than predicted. However, very little contribution was predicted or observed from this mode.

Figures A-3 and A-4 show the post-separated equilibrium positions predicted for the CSS edges for heated jettison tests 1 and 2. The difference between these post-separated positions and the pre-separated positions discussed in Section VB was input as initial conditions in the LMSC dynamic response program, DRILLS. In addition to these thermo-elastic forces, all known mechanical forces were added to the dynamic response simulation. This included the main, lateral, and nose thruster forces shown in table A-3. Actual thruster tolerances from detail and assembly drawings were used. Table A-4 summarizes all other mechanical forces included in the simulation. Base acceleration, pyro impulses, center of gravity offsets, disconnect and seal forces are included. The direction of the net force unbalance from these sources is unpredictable. Therefore, the mechanical forces were applied in a direction to best fit twisting responses from the tests in order to obtain a test-analysis comparison. A worst-case prediction for flight could only envelope such unsymmetric response. All thermo-elastic and mechanical forces for each test condition were superimposed to obtain total predictions directly comparable with test data.

Radial motions for the 0° skew test 2 were originally predicted to be about 50 percent larger than test observations showed. After some investigation, LMSC concluded that this analytical error was due to the assumption that the edges of the CSS halves are tangentially free from the instant of separation. In fact, however, the test data showed a significant initial edge interference in the tangential direction. To account for this, LMSC devised a procedure to model nonlinear tangential compression springs at four stations on each split line. The springs had no tension resistance. This was done in a nonlinear dynamic response program, SCAB, which operates only in generalized coordinates. DRILLS was used to convert the structural model to generalized coordinates, which were then input to SCAB for the nonlinear response analysis. SCAB computed nonlinear spring forces as a function of time. Those force time histories were then transferred back to DRILLS to obtain nodal response which could be compared with test data. This process is summarized in figure A-5. Only the 0° skew test 2 was remodelled in this fashion. The unsymmetric case would have required a model containing both shell halves. The laborious transfer of data back and forth between DRILLS and SCAB was judged to be excessive for the additional results which could have been obtained.

Comparisons of prediction and test have been made in Section VF. A summary comparison for test 2 is shown in figure A-6. Excellent frequency comparison is shown. Amplitudes observed in the test were slightly lower than the final prediction. The prediction was, therefore, slightly conservative.

TABLE A -1 (ref. 8),

MODEL NODE LOCATIONS

<u>Node Number</u>	<u>Station</u>	<u>Remarks</u>
<u>Edge</u>	<u>Backbone</u>	
1	7	25° cone
8	14	25° cone
15	21	25° cone
22	28	25° cone
29	35	25° cone
36	42	15° cone
43	49	15° cone
50	56	15° cone
57	63	15° cone
64	70	15° cone
71	77	cylinder
78	84	bioshield
85	91	cylinder
92	98	cylinder
99	105	cylinder
106	112	cylinder
113	119	cylinder
120	126	cylinder
127	133	cylinder
134	140	cylinder
141	147	cylinder
148	154	fwd. enc. bulkhead
709	715	cylinder
155	161	cylinder
162	168	cylinder
169	175	FBR outer edge
509	515	FBR inner edge
176	182	cylinder
183	189	cylinder
190	196	cylinder
197	203	cylinder
204	210	cylinder
211	217	cylinder
218	224	cylinder

- continued -

TABLE A-1 (CONT'D)

MODEL NODE LOCATIONS

<u>Node Number</u>	<u>Station</u>	<u>Remarks</u>
<u>Edge</u>	<u>Backbone</u>	
225	231	2347.78
232	238	2331.78
239	245	2316.78
246	252	2301.78
253	259	2286.78
260	266	2271.72
267	273	2256.78
274	280	2241.78
614	620	2241.78
284	287	2226.78
288	294	2214.00
677	683	2209.00
684	690	2197.25
691	697	2188.25
908	926	2180.48
749	755	2228.73
756	762	2216.39
763	769	2198.73
770	776	2188.31
777	795	2177.90
796	802	2166.15
803	809	2151.34
810	816	2136.53
817	823	2127.43

TABLE A-2 (ref. 8)

VIBRATION MODES OF CSS POST-SEPARATED HALF SHELL
(-Y SHELL HALF)

SYMMETRIC MODES

Mode Number	Frequency (Hz)			
	Cryo-Unlatch Prediction	HJT Prediction	Cryo-Unlatch Results	HJT Results
1 (Pendulum)	0.33	0.31		
2 (1st Breathing)	5.90	5.97	5.2	6.0
3 (2nd Breathing)	11.17	9.87	9.3	10.0
4	12.33	11.42		11.4
5	13.64	13.29		
6		13.87		
7		15.88		
8		19.80		
9		23.41		
10		27.61		
11		29.95		

ANTISYMMETRIC MODES

Mode Number	Frequency (Hz)			
	Cryo-Unlatch Prediction	HJT Prediction	Cryo-Unlatch Results	HJT Results
1 (1st Twist)	0.18	0.16		
2 (Rocking)	1.09	1.40	0.65	0.83
3 (2nd Twist)	4.34	4.31		
4	6.61	6.81		
5	11.54	11.51		
6		15.62		

Note: For the 0° skew non-linear dynamic response calculation, only 4 symmetric and 4 antisymmetric modes were used to simplify the analysis. For all other dynamic response calculations 11 symmetric and 6 antisymmetric modes were used.

Table A-3 (ref. 8)

SPRING THRUSTER AND MASS PROPERTIES
USED IN CSS EDGE MOTION ANALYSIS

<u>Azimuth (deg)</u>	<u>Rate (lb/in)</u>	<u>Stroke (in.)</u>	<u>Precompression (in.)</u>
<u>Main Thrusters</u>			
12.5	213.3	10.5±.065	0.5±.18
17.5	214.2	10.5±.065	0.5±.18
162.5	210.8	10.5±.065	0.5±.18
167.5	215.0	10.5±.065	0.5±.18
192.5	213.3	10.5±.065	0.5±.18
197.5	215.0	10.5±.065	0.5±.18
342.5	215.0	10.5±.065	0.5±.18
347.5	215.0	10.5±.065	0.5±.18
<u>Lateral Thrusters</u>			
0	133.0	6.0±.03	.13±.15
180	133.0	6.0±.03	.13±.15
<u>Nose Thrusters</u>			
0	100.0	0.9	0.03
180	100.0	0.9	0.03

TABLE A-4 (ref. 8)
S-S MECHANICAL FORCING FUNCTIONS

FORCING FUNCTION								NODE & DIR	COMMENTS
TIME FORCE	0.0 0.0	.01 386.0	1.0 386.0					C.G.-Z	BASE ACCEL. (1G)
TIME FORCE	0.0 0.0	.01 4707.	1.0 4707.					275-Z	MAIN THRUSTER FORCE ON SHROUD
TIME FORCE	0.0 0.0	.01 -4707.	1.0 -4707.					678-Z	MAIN THRUSTER FORCE ON BOATTAIL
TIME FORCE	0.0 815.3	.02 803.9	.06 716.7	.08 643.0	.12 445.5	.16 199.7	.187 20.0	169-Y	LATERAL THRUSTER FORCE
TIME FORCE	0.0 0.0	.305 -75.5	.306 -75.5	.307 -480.	.325 -480.	.326 0.0		188-Y	LH ₂ VENT
TIME FORCE	0.0 -40.	.20 -40.						509-Y	FBR RING S/L SEAL
TIME FORCE	0.0 0.0	.285 0.0	.290 -27.9	.305 -27.9				614-Y	AFT SEAL
TIME FORCE	0.0 0.0	.305 0.0	.310 -54.3	.345 -54.3				615-Y	AFT SEAL
TIME FORCE	0.0 0.0	.345 0.0	.350 -51.8	.395 -51.8				616-Y	AFT SEAL
TIME FORCE	0.0 0.0	.395 0.0	.400 -47.5	.445 -47.5				617-Y	AFT SEAL
TIME FORCE	0.0 0.0	.445 0.0	.450 -41.8	.490 -41.8				618-Y	AFT SEAL

continued --

NOTE: S-S is force symmetric about splitline, symmetric about backbone

Table A-4 (Cont.)

FORCING FUNCTION					NODE & DIR	COMMENTS		
TIME FORCE	0.0 0.0	.490 0.0	.495 -36.1	.510 -36.1	619-Y	AFT SEAL		
TIME FORCE	0.0 0.0	.510 0.0	.515 -16.8		620-Y	AFT SEAL		
TIME FORCE	0.0 0.0	.285 0.0	.290 -9.3	.305 -9.3	614-Z	AFT SEAL		
TIME FORCE	0.0 0.0	.305 0.0	.310 -22.6	.345 -22.6	615-Z	AFT SEAL		
TIME FORCE	0.0 0.0	.345 0.0	.350 -28.0	.395 -28.0	616-Z	AFT SEAL		
TIME FORCE	0.0 0.0	.395 0.0	.400 -34.8	.445 -34.8	617-Z	AFT SEAL		
TIME FORCE	0.0 0.0	.445 0.0	.450 -41.5	.490 -41.5	618-Z	AFT SEAL		
TIME FORCE	0.0 0.0	.490 0.0	.495 -46.5	.510 -46.5	619-Z	AFT SEAL		
TIME FORCE	0.0 0.0	.510 0.0	.515 -24.2		620-Z	AFT SEAL		
TIME FORCE	0.0 0.0	.005 +5.0	.080 +5.0	.085 0.0	162-Y	A/C DUCT		
TIME FORCE	0.0 .465 .550 0.0 1.0 -150.0	.425 .515 .560 0.0 0.0 -150.0	.430 .520 .565 -60.0 -150.0 0.0	.435 .530 .570 0.0 -150.0 0.0	.455 .535 .575 0.0 0.0 -150.0	.460 .545 .585 -180.0 0.0 -150.0	513-Y	ELECT AND INSTRUMENTA- TION DISCONNECTS

Note: S-S is force symmetric about splitline, symmetric about backbone.

TABLE A 4 (CONT'D)

A-S & S-A MECHANICAL FORCING FUNCTIONS

A-S FORCING FUNCTION												NODE & DIR	COMMENTS
TIME	FORCE	0.0	0.1	0.2	0.3	0.4	0.5	0.6	0.7	0.8	0.902		
TIME	FORCE	-13.5	-13.3	-12.7	-11.7	-10.4	-8.7	-6.8	-4.7	-2.4	0.0	275-Z	MAIN THRUSTER FORCE UN-BALANCE DUE TO KNOWN SPRING RATE VARIATION
TIME	FORCE	13.5	13.3	12.7	11.7	10.4	8.7	6.8	4.7	2.4	0.0	678-Z	MAIN THRUSTER FORCE UN-BALANCE DUE TO KNOWN SPRING RATES (REACTION ON BOATTAIL)

S-A FORCING FUNCTION												NODE & DIR	COMMENTS	
TIME	FORCE	0.0	0.1	0.2	0.3	0.4	0.5	0.6	0.7	0.8	0.902			
TIME	FORCE	146.5	143.6	137.7	127.5	112.8	93.8	73.3	51.3	26.4	0.0	275-Z	MAIN THRUSTER FORCE UN-BALANCE DUE TO C.G. OFFSET & KNOWN SPRING RATE VARIATION	
TIME	FORCE	-146.5	-143.6	-137.7	-127.5	-112.8	-93.8	-73.3	-51.3	-26.4	0.0	678-Z	MAIN THRUSTER FORCE UN-BALANCE (REACTION ON BOATTAIL)	
TIME	FORCE	0.0	.01	.02	.04	.06	.08	.10	.12	.14	.16	.187	169-Y	LATERAL THRUSTER UN-BALANCE DUE TO C.G. OFFSET
TIME	FORCE	19.9	19.8	19.6	18.8	17.4	15.6	13.3	10.6	7.7	4.5	0.0	169-Y	UNBALANCE DUE TO LATERAL THRUSTER TOLERANCES
		0.0	.187											
		-20.4	-20.4											

NOTE: A-S is force antisymmetric about splitline, symmetric about backbone

S-A is force symmetric about splitline, antisymmetric about backbone

TABLE A-4 (CONT'D)
A-A MECHANICAL FORCING FUNCTIONS

FORCING FUNCTION											NODE & DIR	COMMENTS	
TIME FORCE	0.0 109.	0.1 107.4	0.2 102.5	0.3 94.5	0.4 83.6	0.5 70.3	0.6 54.8	0.7 37.6	0.8 19.4	0.902 0.0	275-Z	MAIN THRUSTER FORCE UNBALANCE DUE TO C.G. OFFSET	
TIME FORCE	0.0 -109.	0.1 -107.4	0.2 -102.5	0.3 -94.5	0.4 -83.6	0.5 -70.3	0.6 -54.8	0.7 -37.6	0.8 -19.4	0.902 0.0	678-Z	MAIN THRUSTER FORCE UNBALANCE DUE TO C.G. OFFSET (REACTION ON BOATTAIL)	
TIME FORCE	0.0 25.1	.01 25.0	.02 24.7	.04 23.7	.06 21.9	.08 19.7	.10 16.8	.12 13.4	.14 9.7	.16 5.7	.187 0.0	169-Y	LATERAL THRUSTER UN- BALANCE DUE TO C.G. OFFSET
TIME FORCE	0.0 0.0	.305 +75.5	.306 +75.5	.307 +480.0	.325 +480.0	.326 0.0						188-Y	LH ₂ VENT
TIME FORCE	0.0 -10.	.20 -10.										509-Y	FBR RING S/L SEAL
TIME FORCE	0.0 0.0	.285 0.0	.290 -7.0	.305 -7.0								614-Y	AFT SEAL
TIME FORCE	0.0 0.0	.305 0.0	.310 -13.6	.345 -13.6								615-Y	AFT SEAL
TIME FORCE	0.0 0.0	.345 0.0	.350 -12.9	.395 -12.9								616-Y	AFT SEAL
TIME FORCE	0.0 0.0	.395 0.0	.400 -11.9	.445 -11.9								617-Y	AFT SEAL
TIME FORCE	0.0 0.0	.445 0.0	.450 -10.4	.490 -10.4								618-Y	AFT SEAL
TIME FORCE	0.0 0.0	.490 0.0	.495 -9.0	.510 -9.0								619-Y	AFT SEAL

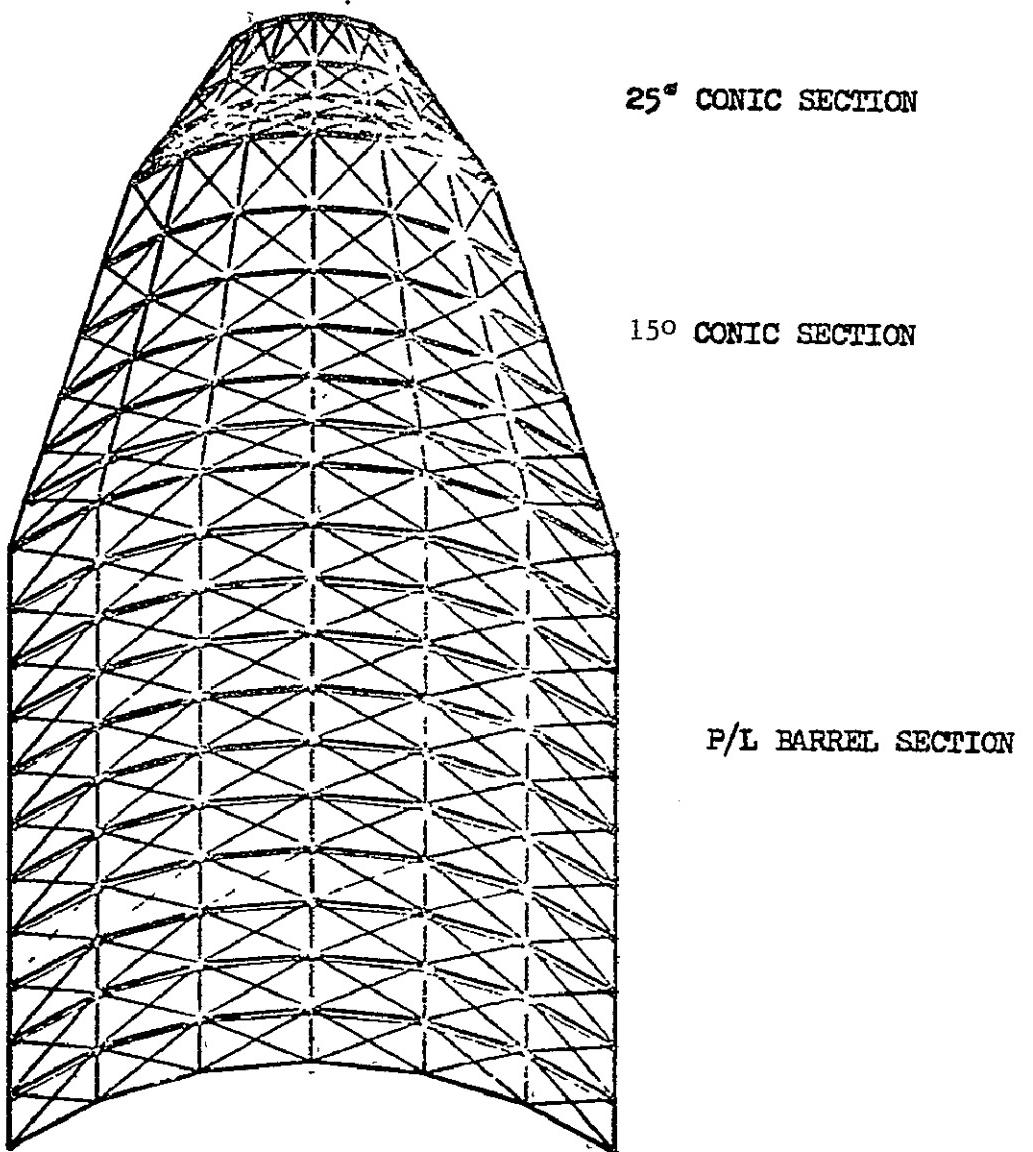
continued - -

NOTE: A-A is force antisymmetric about splitline, antisymmetric about backbone

Table A-4 (Cont.)

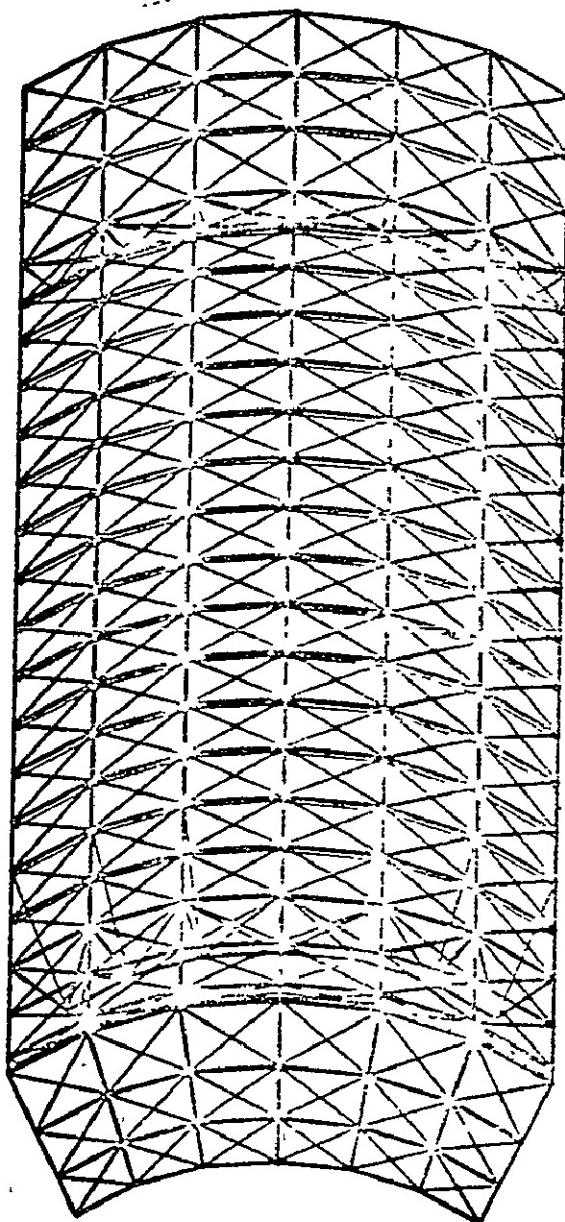
FORCING FUNCTION						NODE & DIR	COMMENTS
TIME	0.0	.510	.515				
FORCE	0.0	0.0	-4.2			620-Y	AFT SEAL
TIME	0.0	.285	.290	.305			
FORCE	0.0	0.0	-2.3	-2.3		614-Y	AFT SEAL
TIME	0.0	.305	.310	.345			
FORCE	0.0	0.0	-5.6	-5.6		615-Z	AFT SEAL
TIME	0.0	.345	.350	.395			
FORCE	0.0	0.0	-7.0	-7.0		616-Z	AFT SEAL
TIME	0.0	.395	.400	.445			
FORCE	0.0	0.0	-8.7	-8.7		617-Z	AFT SEAL
TIME	0.0	.445	.450	.490			
FORCE	0.0	0.0	-10.4	-10.4		618-Z	AFT SEAL
TIME	0.0	.490	.495	.510			
FORCE	0.0	0.0	-11.6	-11.6		619-Z	AFT SEAL
TIME	0.0	.510	.515				
FORCE	0.0	0.0	-6.0			620-Z	AFT SEAL
TIME	0.0	.005	.080	.085			
FORCE	0.0	+5.0	+5.0	0.0		162-Y	A/C DUCT
TIME	0.0	1.0					
FORCE	-83.5	-83.5				275-Z	UNBALANCE DUE TO MAIN THRUSTER TOLERANCES
TIME	0.0	1.0					
FORCE	83.5	83.5				678-Z	UNBALANCE DUE TO MAIN THRUSTER TOLERANCES (REACTION ON BOATTAIL)
TIME	0.0	.425	.430	.435	.455	.460	
	.465	.515	.520	.530	.535	.545	
	.550	.560	.565	.570	.575	.585	
FORCE	0.0	0.0	-60.0	0.0	0.0	-180.0	
	0.0	0.0	-150.0	-150.0	0.0	0.0	
	-150.0	-150.0	0.0	0.0	-150.0	-150.0	

ALL ELEMENTS STA 2867.25 TO 2514.00



CSS FINAL DESIGN
FIGURE A-1 (ref. 11)

ALL ELEMENTS STA 2514.00 TO 2180.48



FIR RING

CENTAUR SECTION

AFT BULKHEAD RING
SKIRT SECTION

BOAT TAIL SECTION

CSS FINAL DESIGN

FIGURE A -2 (ref. 11)

HJT 1 RADIAL EDGE DEFLECTION VS STATION
328° SKEW, POST SEPARATED
(MODEL PREDICTION)

CSS-NWTEMP EDGE DISP.CHECK

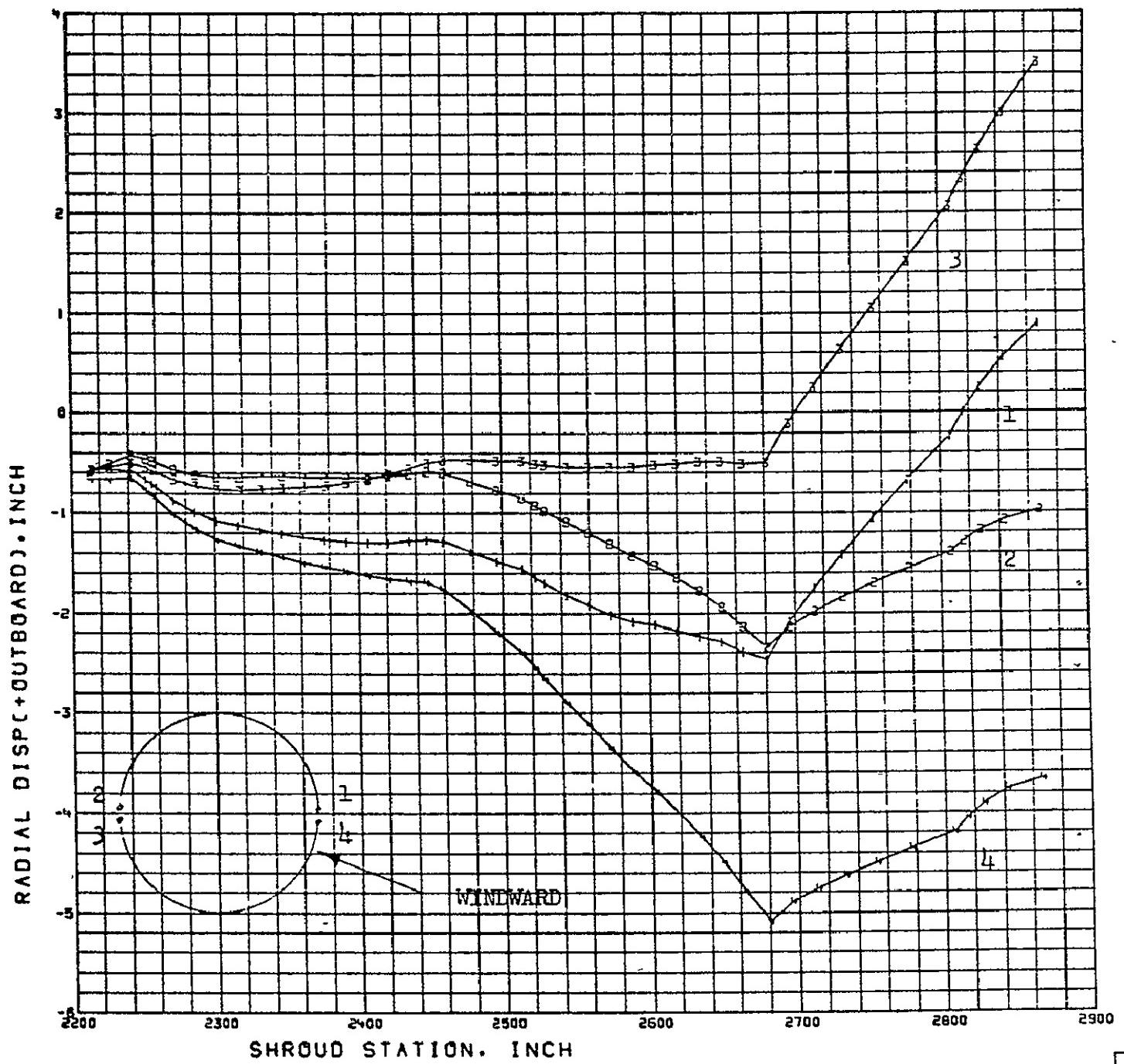


Figure A-3 (ref. 8)

HJT 2 RADIAL EDGE DEFLECTION VS STATION
0° SKEW, POST SEPARATED
(MODEL PREDICTION)

CSS*NWTEMP EDGE DISP.CHECK

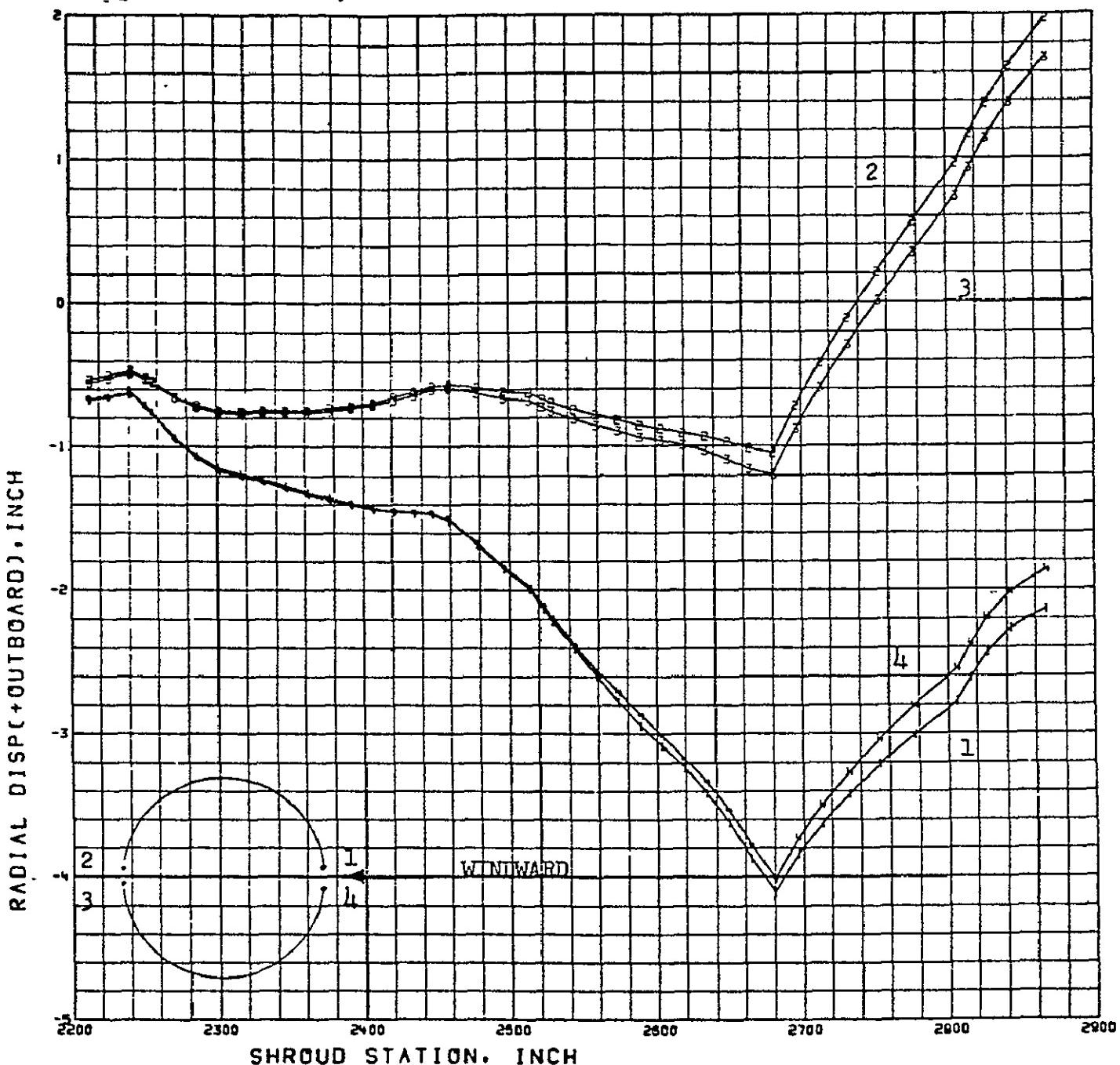


FIGURE A-4 (ref. 8)

FLOW CHART OF THERMAL/MECHANICAL
NON-LINEAR DYNAMIC RESPONSE ANALYSIS

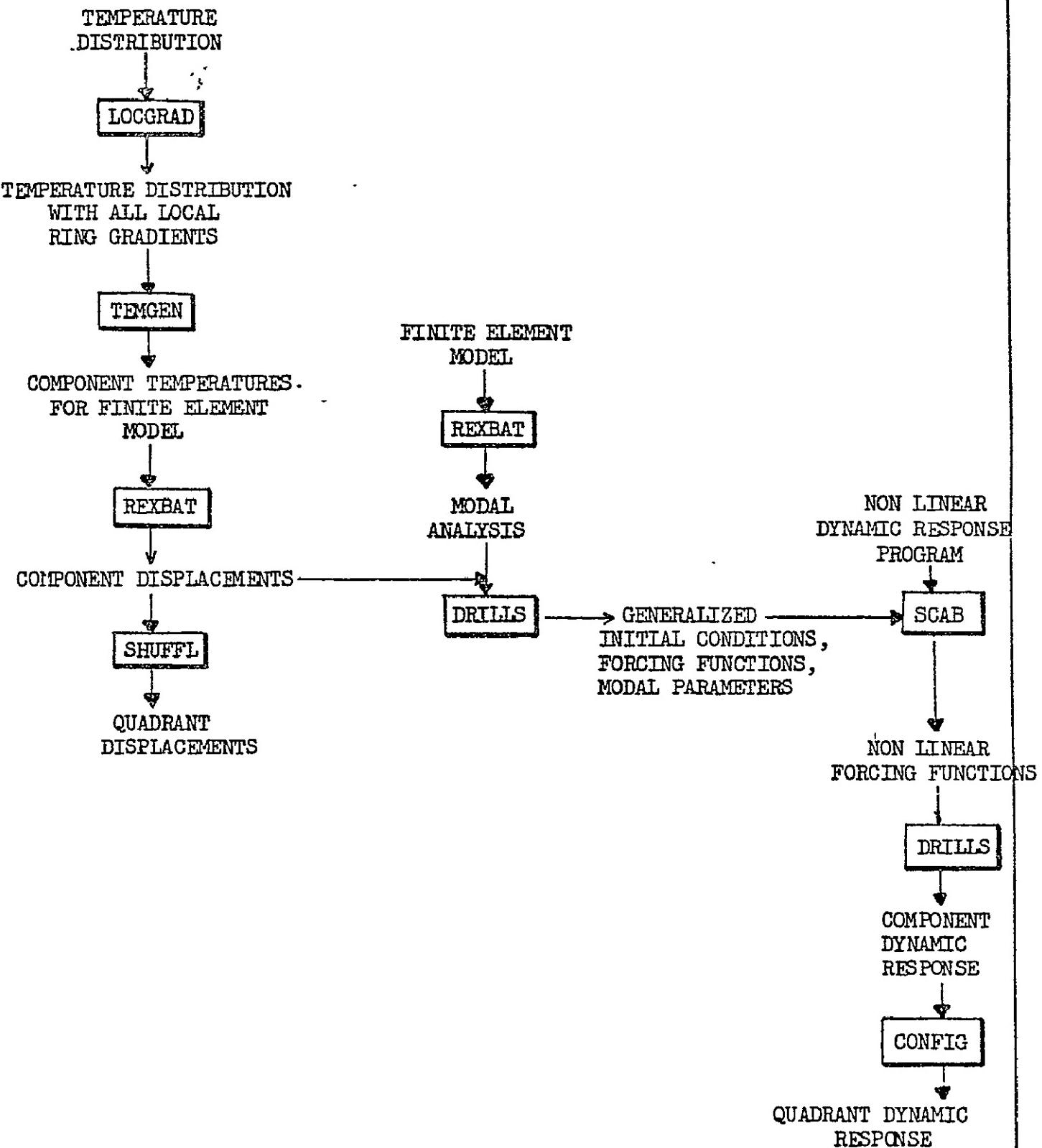


FIGURE A-5 (ref. 8)

CLEARANCE REDUCTION VS. TIME
STATION 2664 Q4
HJT-2 0° SKEW

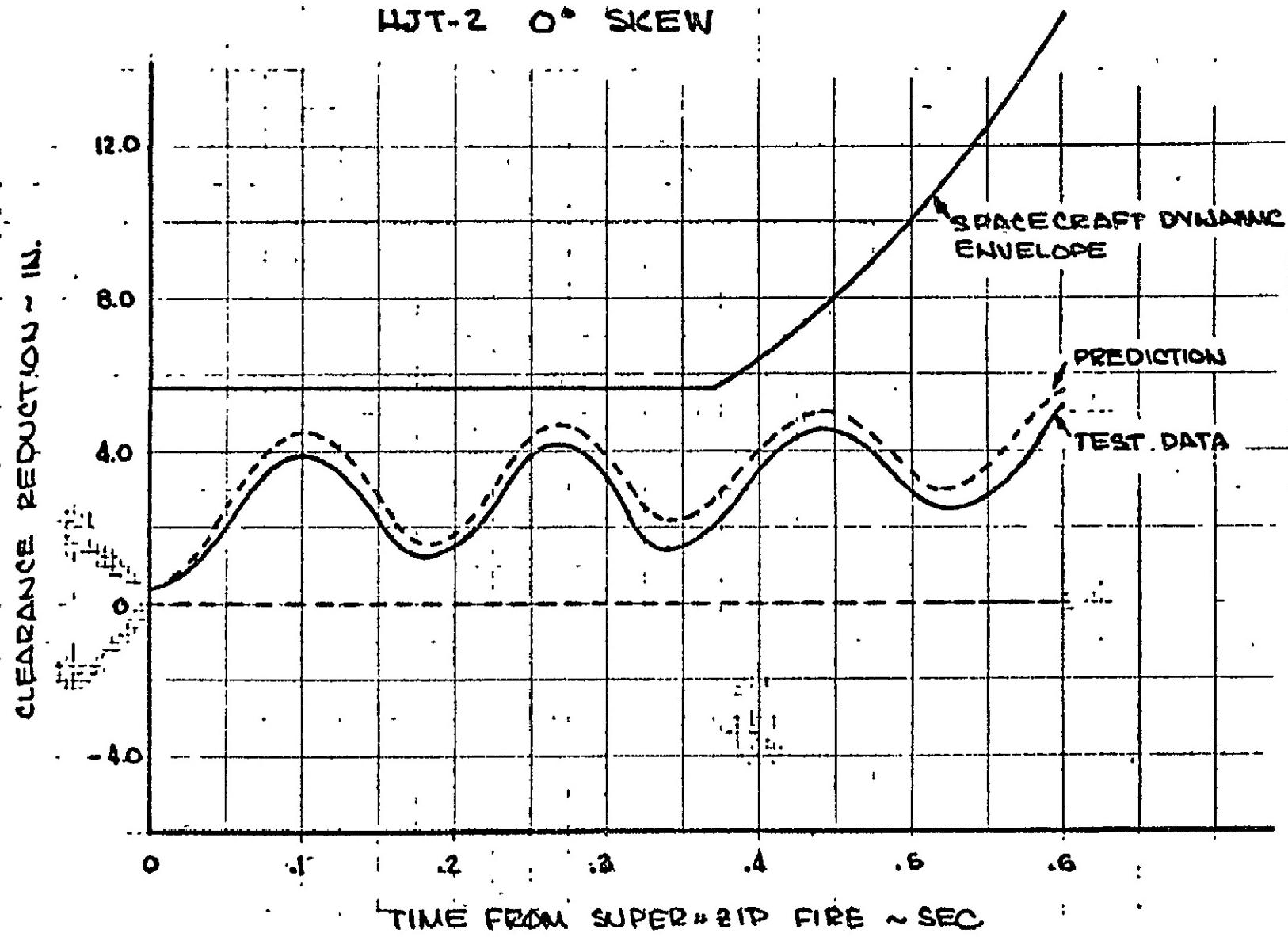


FIGURE A-6 (ref. 8)

APPENDIX B

Comparison of Test Results to Thermal Model Calculations

Anthony Fortini

Introduction

Temperature gradients can cause thermal deflections on large shrouds which may be severe enough to result in large reductions in shroud/payload clearances during shroud jettison. This potential problem requires accurate computations of gradients throughout a shroud structure in order to predict thermal deflections and jettison performance of a shroud. Therefore, thermal models were developed by LMSC to calculate temperatures throughout the CSS structure during ascent flight. The results of the model calculations are compared with data obtained in tests 1 and 2. Much of the material in this Appendix is taken from reference 7.

Thermal Models

The CSS thermal models were constructed using standard thermal modeling techniques. Each specific area of the CSS being analyzed is divided into isothermal units of mass, or nodes, and each is assigned a thermal capacitance based on the material and the volume of the node. The nodes are then connected by thermal resistances. Conduction resistors are a function of heat transfer path, length and area. Radiation resistors are a function of surface area, geometry, optical properties, and temperature. The completed model is analogous to an electrical circuit with nodes as capacitors, thermal resistance as resistors, temperature as voltage, and heat flow as current.

A complete modeling of the CSS required 14 separate models, one for each of the 14 major types of structure of the CSS. These separate models are listed in table B-1.

A typical node network is depicted in figure B-1. Although this figure is for a cylinder Zee-ring, the following discussion is applicable to all models.

Each thermal model is constructed to take advantage of thermal symmetry where possible. For example, the Zee-ring models extend to locations midspan between rings on each side of the ring being modeled. At these end points, the longitudinal temperature gradient and longitudinal conduction transfer are zero. The ring models are one corrugation wide in the circumferential direction and divided into valley, side, and peak nodes. The gradient within the corrugation and the corrugation fin effect are therefore accounted for, but the heat transfer from corrugation to corrugation circumferentially is assumed to be negligible for purposes of analysis. The skin is divided into nodes representing areas under the corrugation valley, sides, and hat. Rings are divided axially into nodes corresponding to those on the skin and vertically on the web.

CSS Intermediate Scale Tests. - In order to define the boundary conditions and thermal resistors required within the models for both flight and the Heated Altitude Jettison Tests, Intermediate Scale Tests (IST) of a corrugated section of the CSS shell were performed at two ambient pressure levels. A pressure of 10^{-5} torr simulated the flight condition, while a pressure of 20 torr was used to obtain data for the jettison test condition. An analysis of the IST data indicated that:

1. The effective surface emissivity of the lamp black painted CSS surface was 0.9 when the CSS was radiating to distant (black) surroundings, and the effective emissivity of the same surface radiating to the heater reflector with the heater in place was 0.5.
2. The heat flux (per unit area) ratio of the corrugation side to its valley was 0.4, and the ratio of peak to valley was 1.5.
3. The temperature-time history of the valley node at the midspan has the same slope as the skin thermocouple directly beneath it.
4. The conductance of the Weldbond interface between the skin and the corrugation (for the whole valley width) was computed to be $600 \text{ BTU/hr-ft}^{2-0}\text{F}$.
5. At 10^{-5} torr, a correlation of the data shows the interface resistance between the skin and ring flange under the corrugation valley is equal to 1700 times a mass averaged temperature difference, between the skin and the ring flange temperatures, raised to the $1/3$ power.
6. At 20 torr, the data correlation shows that there is a parallel resistance due to air trapped in the gap, across the skin-flange interface under the corrugation valley which is equal to 2.823 times the interface resistance between the skin and ring flange under the corrugation valley (item 5) at 10^{-5} torr.
7. At 20 torr, the data correlation shows that there is an additional resistance, due to air between the skin under the corrugation hat and the ring flange, which is equal to 1.5 times the resistance across the skin-flange interface under the corrugation valley at 20 torr (item 6).

The foregoing resistance correlations are applicable to an interface area of 0.353 in^2 under the corrugation valley (one-half the valley width). The correlations are also based on a Weldbond interface conductance of $600 \text{ BTU/hr-ft}^{2-0}\text{F}$ (item 4). For the air conduction resistance under the corrugation hat (item 7), the interface area is 0.963 in^2 .

Mass averaged skin and ring flange temperatures refer to the averaging of the three skin nodes above the ring flange, and the three outboard ring flange nodes. As shown in figure B-1, the skin nodes are 94, 128, and 111, and the ring flange nodes are 137, 138, and 139. The mass averaged temperatures are calculated as follows:

$$\text{Mass averaged skin temperature} = \frac{C_{94} T_{94} + C_{128} T_{128} + C_{111} T_{111}}{C_{94} + C_{128} + C_{111}}$$

and

$$\text{Mass averaged ring temperature} = \frac{C_{137} T_{137} + C_{138} T_{138} + C_{139} T_{139}}{C_{137} + C_{138} + C_{139}}$$

Where C is thermal capacity and T is temperature.

From the IST data, an electrical analog was evolved which could be used to calculate the temperature gradients in the Zee-rings, both for the 20-torr tests and for flight. For the 20-torr tests, all conductances and resistances, as described above, were used in the thermal model. For the flight case, items 6 and 7 are treated as infinite resistances.

Thermal Conductance. - Since IST data were limited to the Zee-ring model, the conductance values for the remaining models were back-calculated from the test data of the CSS Heated Jettison Tests. These conductance values are listed in table B-2.

Comparison of Test Data with Model Calculations

Sketches of the 14 thermal models, along with the thermocouple locations for tests 1 and 2, are shown in figure B-2. Actual temperature gradients are compared with gradients calculated by the thermal models in figures B-3 through B-10, and in figures VA-5 through VA-8. The data are represented by unconnected symbols and the calculations are shown by curves. These data are typical test results. All of the results obtained in tests 1 and 2 are summarized in table B-1 and are presented in detail in reference 7.

In making calculations, the radiant heat input to the model was assumed to be uniform around the model. The heat input was back-calculated from a nearby free-skin temperature. An example is shown in figure B-3. The midspan thermocouple (circular symbols) measures free-skin temperature. Comparison of the calculated and actual ring flange temperatures indicates successful modeling and the adequacy of various interface resistance values.

Calculations for the forward separation ring, figure B-9, do not agree with the data. It is believed that the discrepancy is due to large mass variations in this area which were not considered in the thermal modeling. Also, termination of the heater lamps just aft of this ring resulted in less average heating to this area during testing than was assumed in the model. By correcting the heat input into this area, LMSC improved the calculated temperatures to an acceptable accuracy (See ref. 7).

Table B-2 shows that the calculations sometimes yield higher and sometimes lower temperatures than were measured during tests 1 and 2. In general, the calculated temperatures were within 16°F of the measured temperatures at the time of CSS jettison. It is judged that the thermal models, calculating techniques, and interface resistance values are adequate for the CSS and for the type of heating trajectory simulated by the Heated Altitude Jettison Tests.

TABLE B-1

COMPARISON OF ACTUAL AND CALCULATED TEMPERATURE RISE FROM START OF TEST TO TIME OF JETTISON FOR
ALL 14 THERMAL MODELS, TEST 1 & 2

	Thermal Models (See Figure B-2)	Station/ Azimuth	TEST 1						TEST 2						
			Actual Temperature Rise ($^{\circ}$ F)			Calculated Temperature Rise ($^{\circ}$ F)			Actual Temperature Rise ($^{\circ}$ F)			Calculated Temperature Rise ($^{\circ}$ F)			
			A	B	C	A	B	C	A	B	C	A	B	C	
211	1. 25 $^{\circ}$ Cone Ring	2827/324	316		N.G.	300		264		313		281	308		265
	" " "	2827/338													
	2. 15 $^{\circ}$ Cone Ring	2778/350	244		187	244		184		257		175	241		179
	" " "	2778/338													
	3. Cone Cylinder Junction Ring	2680/15													
	4. Zee-Ring	2634/335	227		160	228		159		231		160	225		153
	& 5. "	2634/206	155		117	152		116		160		116	157		114
	"	2479/351	168		118	178		126		180		124	197		133
	"	2479/200	145		100	141		107		140		99	139		100
	"	2347/336	210		136	206		140							
	"	2347/155	151		107	157		115		144		102	146		106
	"	2227/318	158		112	168		120		150		105	158		110
	"	2227/209	95		74	111		87		103		82	118		89
	6. Aft Purge Seal Bulkhead	2242/332	85	18	0	84	21	0	84	18		82	19		
	" " " "	2242/195	56	13		56	16		62	12		61	16		
	7. Forward Separation Ring	2213/318	68	50	40	83	62	24	63	45	36	77	58		36
	" " "	2213/209	44	35	34	53	39	18	46	37	34	56	44		29
	8. FBR Ring	2459/347	98	34		103	34		96	24		109	36		
	" "	2459/203	80	30		79	29		75	23		80	29		
	9. Super*Zip Conic	2792/1	143			148			159				155		
	" " Cylinder	2612/1	120			139							150		
	10. Encapsulation Bulkhead	2523/351											76	139	78
	11. Manufacturing Joint	2589/15	170	151	N.G.	196	152	76							
	12. Skin Splice	2627/288	237	247		243	247								
	13. Ring Splice	2634/300	149	94	94	139	96	87							

TABLE B-2

CONDUCTANCE VALUES USED IN CSS THERMAL MODELS

Model and Conductance Location	Conductance, Btu/Hr-ft ² -°F
1. 25 degree cone ring, between ring and skin	150
2. 15 degree cone ring, between ring and skin	150
3. Cone-cylinder junction ring, between ring and skin	150
4. For all Zee-rings in cylinder	600
5. Aft purge seal, between diaphragm and inner and outer caps; also, between outer cap and field joint	600
6. Forward separation ring, between web and inner and outer caps; also, between ring and skin	600
7. Forward bearing reaction ring, for all interfaces	600
8. Encapsulation bulkhead, between ring and web	150
9. Manufacturing joint, for the doubler	150
10. Zee-ring splice, at the splice interface	150
11. Skin splice, at the splice joint	600

RESISTORS # 1-148 CONDUCTION IN CORRUG.

149-230 CONDUCTION IN SKIN

231-262 CONDUCTION IN RING

263-296 SKIN/CORR INTERFACES

297-299 SKIN/RING INTERFACES

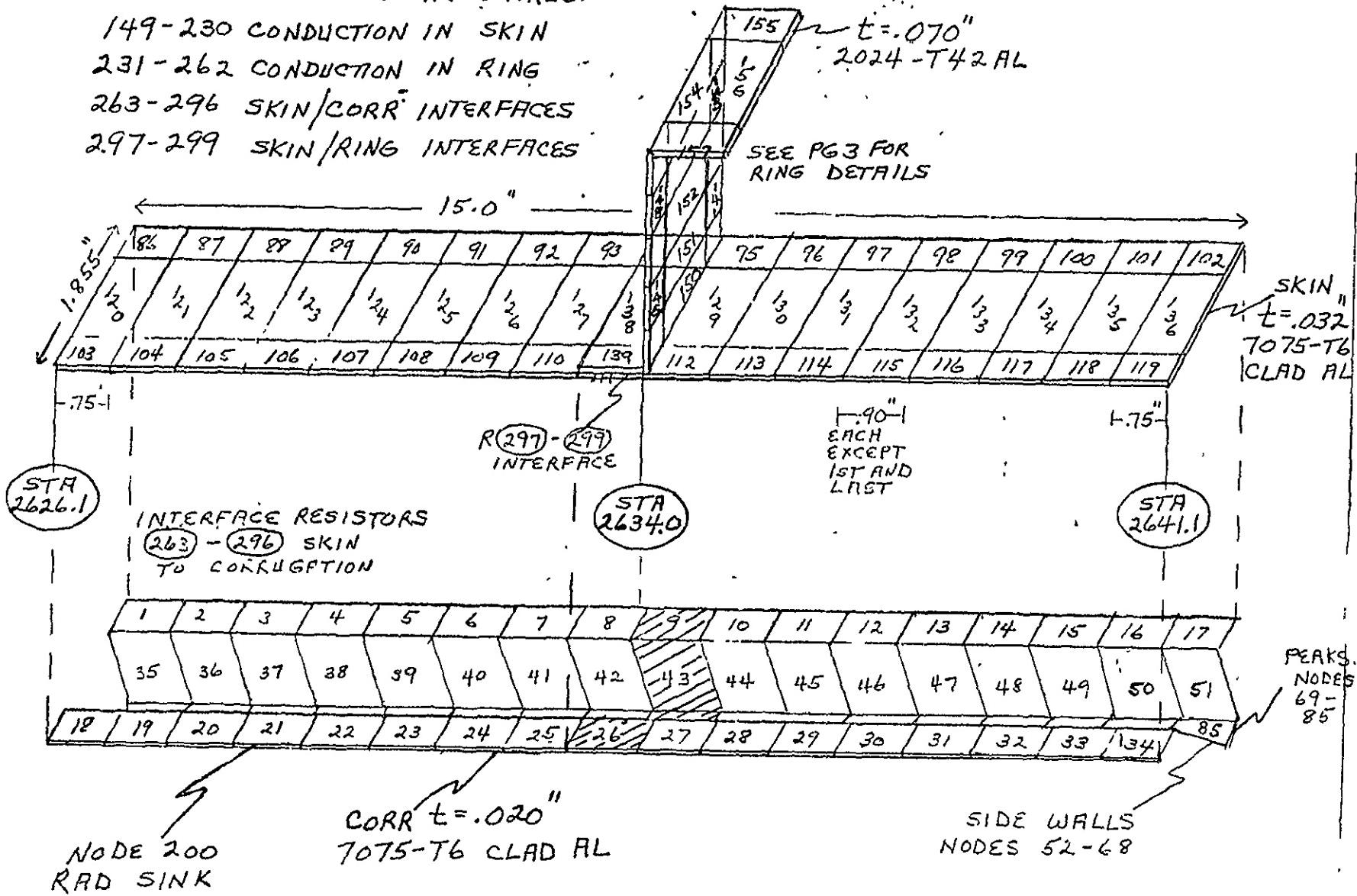
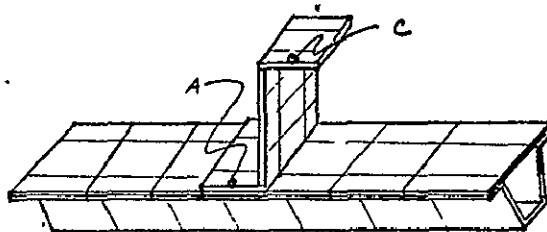
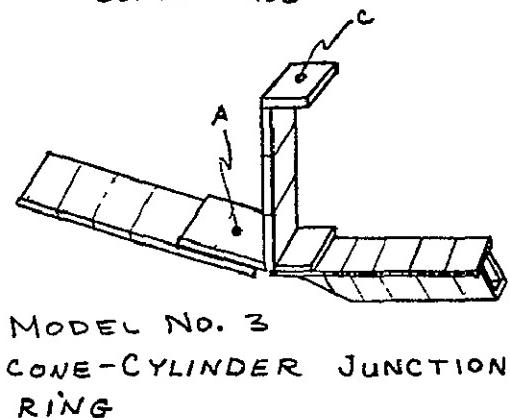
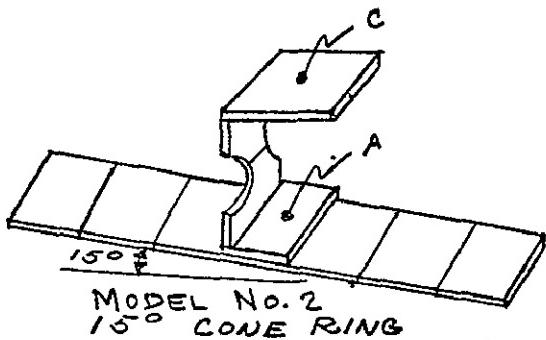
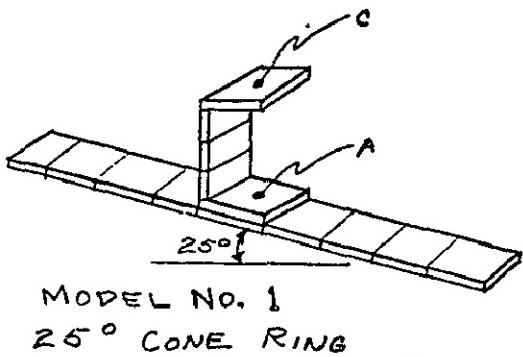


FIGURE B-1 THERMAL MODEL NO. 4 OF CYLINDER ZEE-RING, STATION 2634



MODEL NO. 5 - ZEE RING AND .040
SKIN, .025 CORRUGATED PANEL

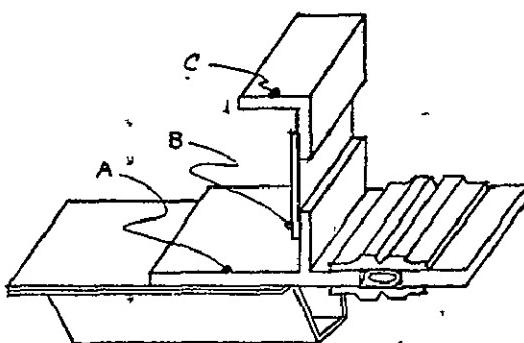
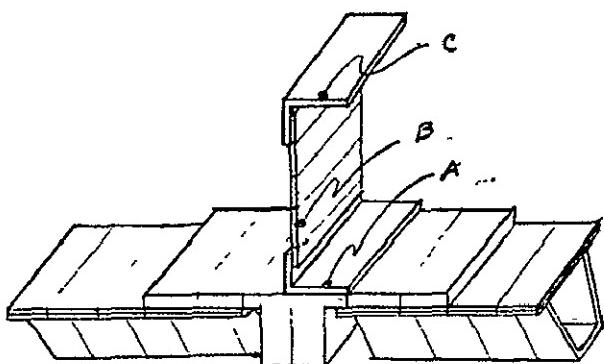
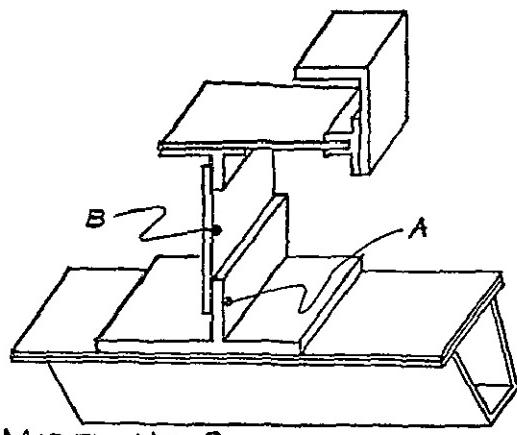
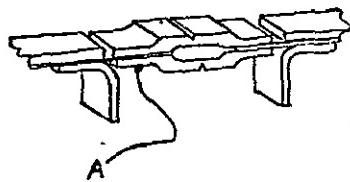


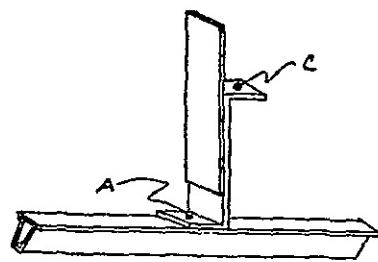
FIGURE B-2 SCHEMATICS OF THERMAL MODELS
SHOWING THERMOCOUPLE LOCATIONS FOR
TESTS 1 & 2, AND INDICATING SOME
TYPICAL THERMAL NODE LAYOUTS.



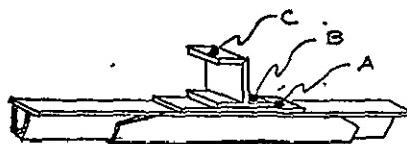
MODEL NO. 8
FORWARD BEARING
REACTION RING



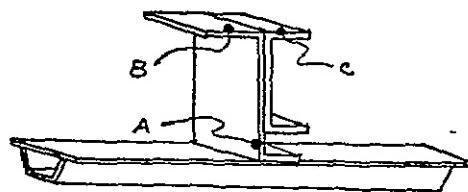
MODEL NO. 9 - SUPER-ZIP AXIAL
JOINT IN NOSE CONE



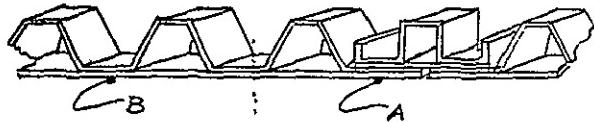
MODEL NO. 11
ENCAPSULATION BULKHEAD



MODEL NO. 12
MANUFACTURING JOINT



MODEL NO. 14
ZEE-RING SPLICE



MODEL NO. 13
SKIN SPLICE

FIGURE B-2 CONCLUDED

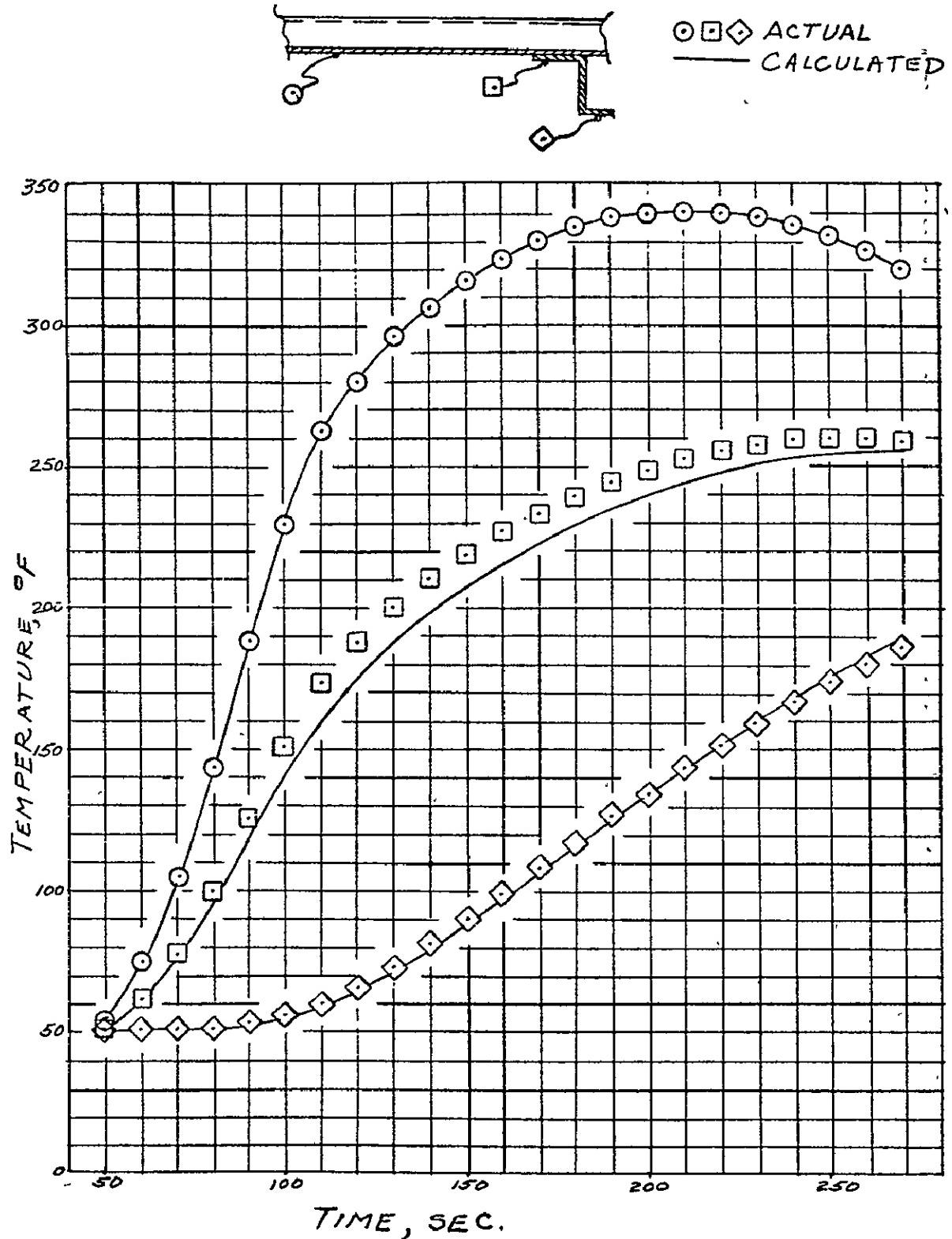


FIGURE B-3 CALCULATED AND ACTUAL TEMPERATURE HISTORIES FOR CYLINDER ZEE-RING, MODEL NO. 4, STATION 2347, AZIMUTH 335°, TEST 1

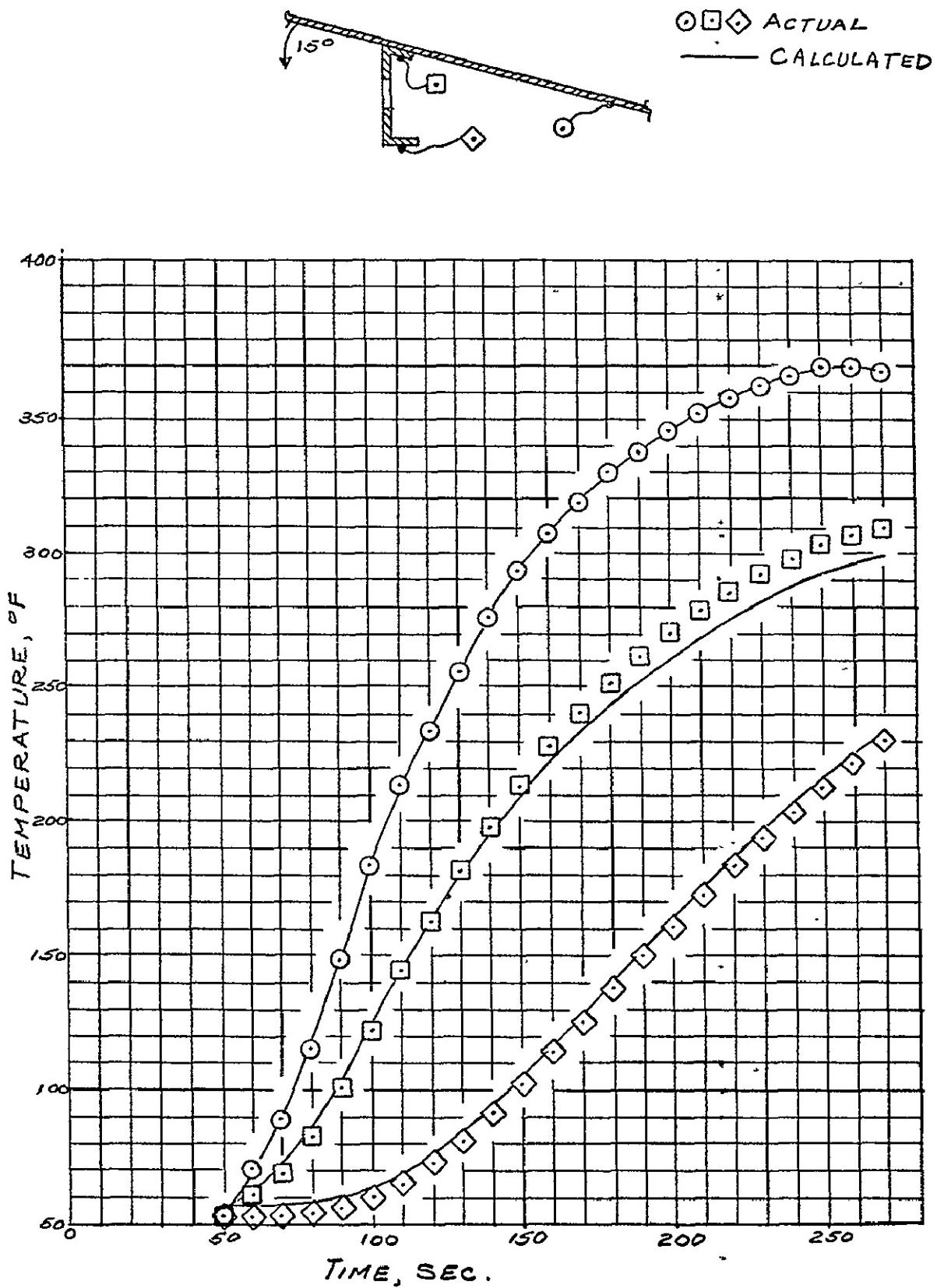


FIGURE B-4 CALCULATED & ACTUAL TEMPERATURE HISTORIES FOR
15° CONE RING (MODEL No. 2), STATION 2778, AZIMUTH 338°, TEST 2

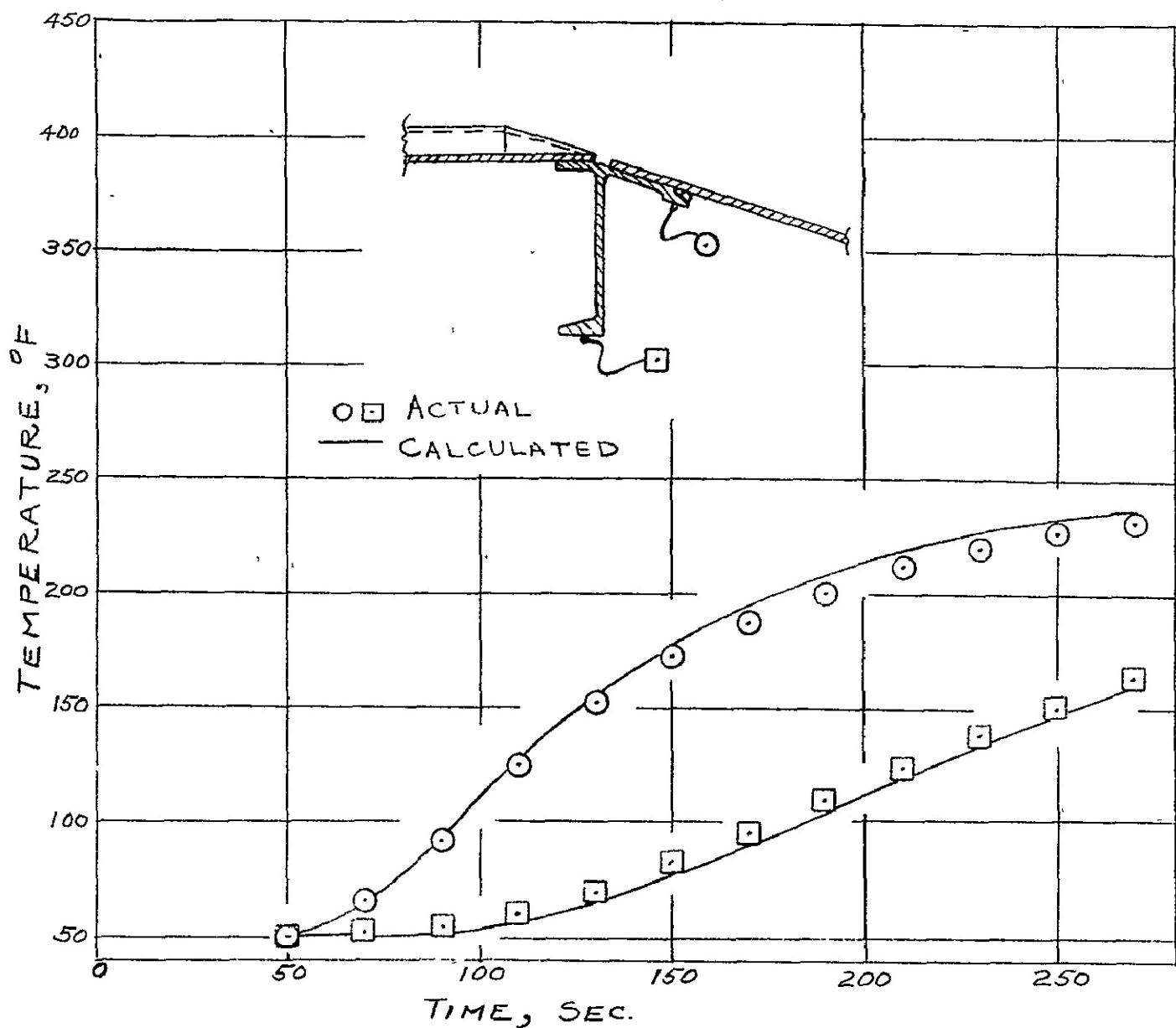


FIGURE B-5 CALCULATED AND ACTUAL TEMPERATURE HISTORIES FOR CONE-CYLINDER JUNCTION RING (MODEL NO 3), STATION 2680, AZIMUTH 15°, TEST 2

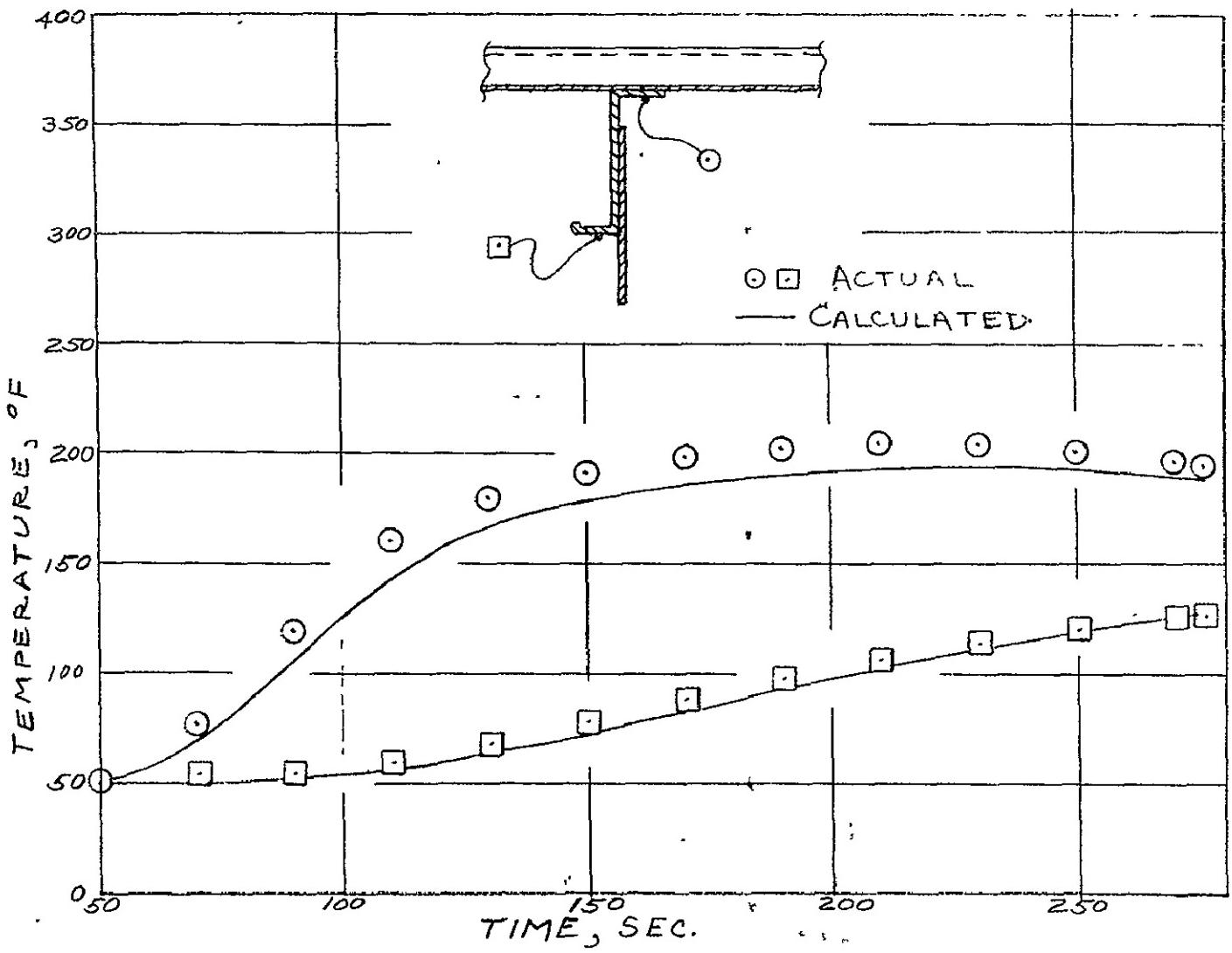


FIGURE B-6 CALCULATED AND ACTUAL TEMPERATURE HISTORIES FOR ENCAPSULATION BULKHEAD (MODEL NO. II), STATION 2523, AZIMUTH 351°, TEST 2

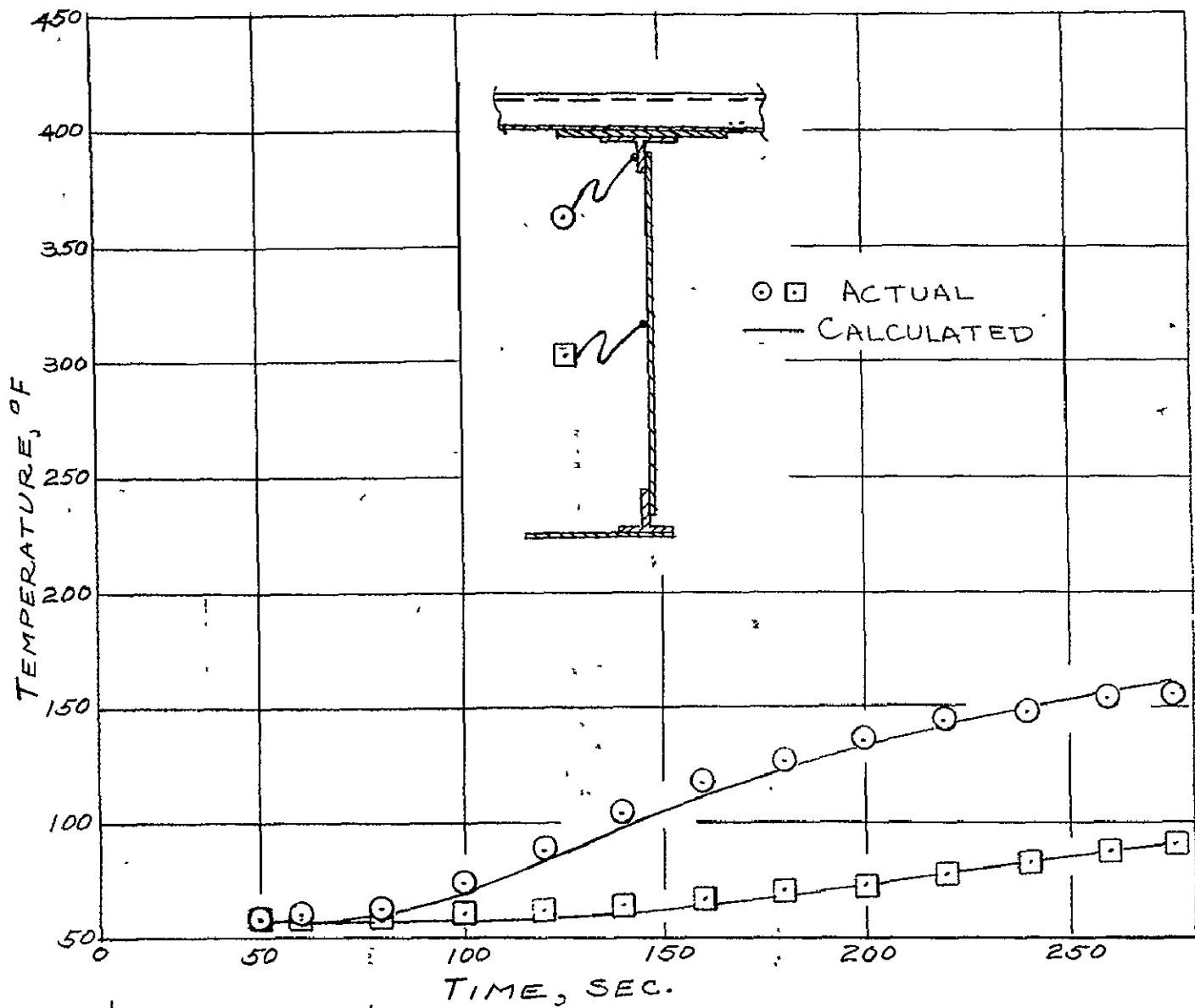


FIGURE B-7 CALCULATED AND ACTUAL TEMPERATURE HISTORIES FOR FBR RING (MODEL NO. B), STATION 2459, AZIMUTH 347°, TEST 1

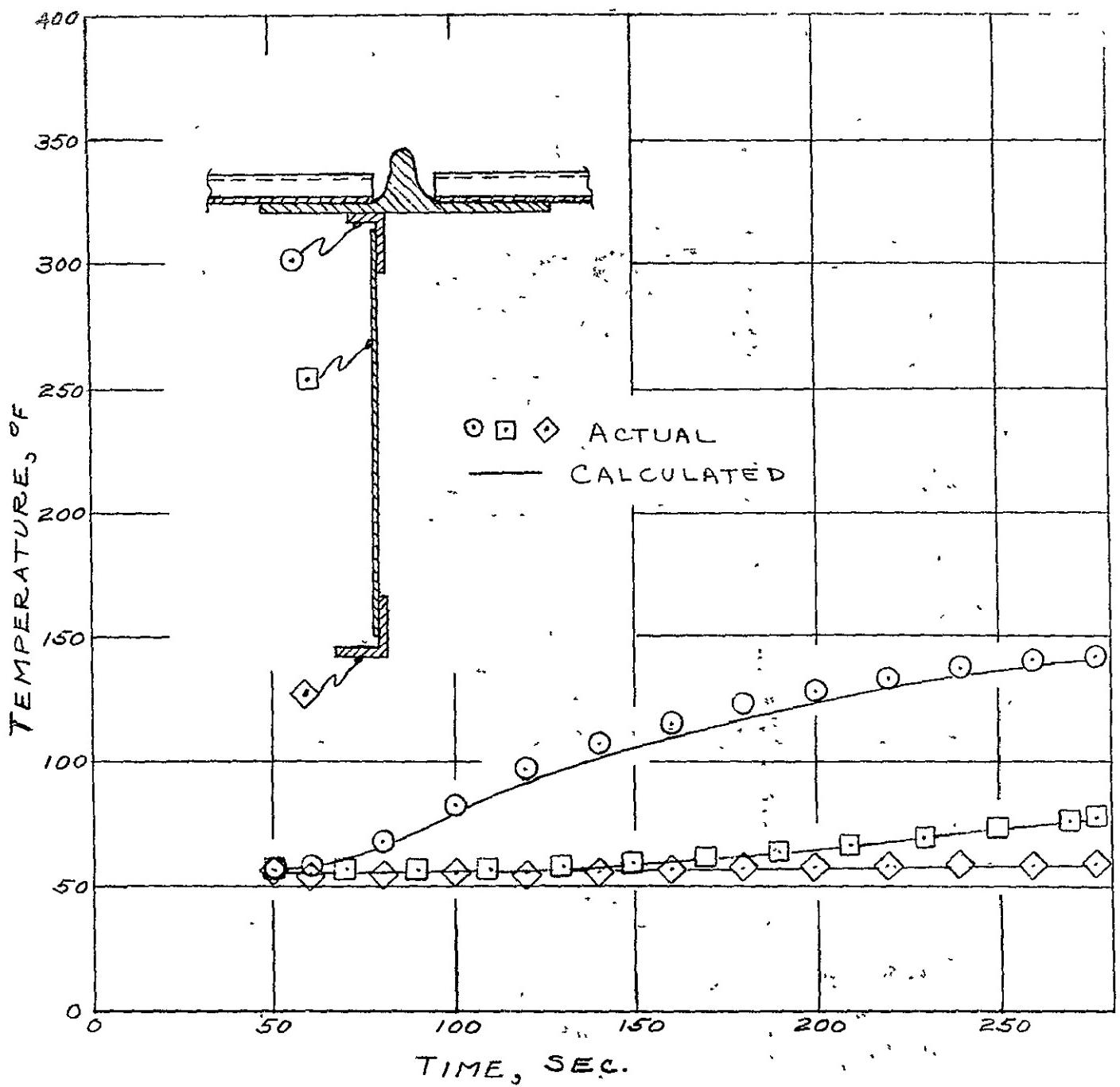


FIGURE B-8 CALCULATED AND ACTUAL TEMPERATURE HISTORIES FOR AFT PURGE SEAL BULKHEAD (MODEL No. 6), STATION 2242, AZIMUTH 332°, TEST 1

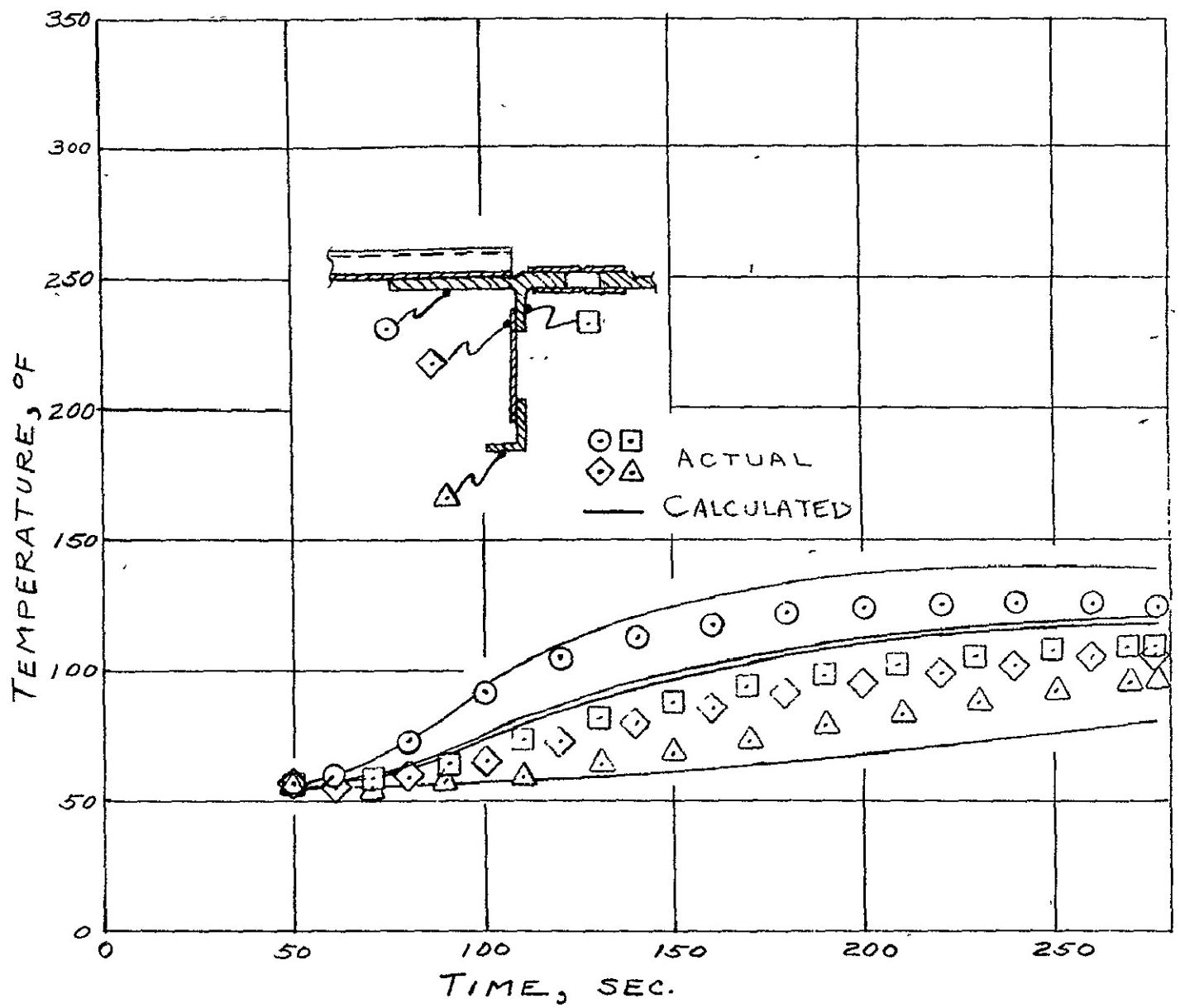


FIGURE B-9 CALCULATED AND ACTUAL TEMPERATURE HISTORIES FOR FORWARD SEPARATION RING (MODEL NO. 7), STATION 2213, AZIMUTH 318° , TEST 1

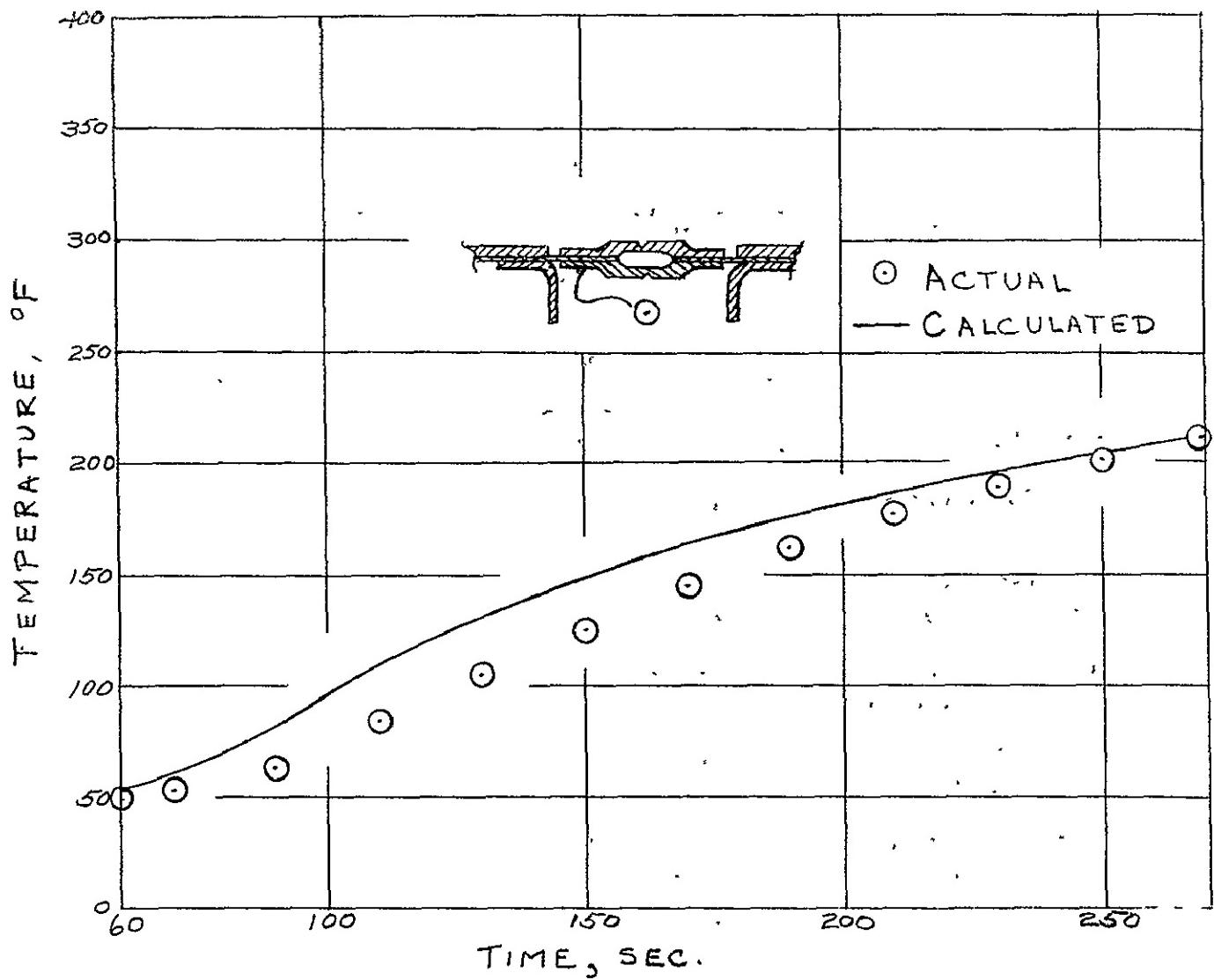


FIGURE B-10 CALCULATED AND ACTUAL TEMPERATURE HISTORY FOR SUPER*ZIP AXIAL JOINT (MODEL NO. 9)
STATION 2792, AZIMUTH 0°, TEST 2

APPENDIX C

Differences in Configuration between the Proof Flight and Test CSS

Herbert E. Ledyard

Proof Flight CSS Design Changes Not Retrofitted to Test CSS

1. Flight CSS has five Aft Purge Seal (APS) doors (test CSS has four doors).
2. Flight CSS incorporates lock bolts at the split lines (test CSS uses rivets).
3. Flight CSS has strengthened ring at station 2523, and an additional ring at station 2251 (test CSS has unmodified ring configuration).
4. Flight CSS boost pump door was redesigned to be solid with full-length stiffeners (test CSS has no door).
5. Flight CSS has Radioactive Thermoelectric Generator (RTG) cutout with a channel stiffener on the inboard surface (test CSS has no RTG cutout).
6. Flight CSS forward and aft thermal shields have strengthened tiedown tags (test CSS has unmodified thermal shield configuration).
7. Flight CSS FBR bearing block/fitting assembly made of steel (test CSS block/fitting of aluminum).
8. Flight CSS has lock bolts at Range Safety Command (RSC) splice (test CSS uses rivets).
9. Flight CSS uses production tank section batting containment kit (for tests 2 and 3, test CSS batting was taped for containment and Kapton strips were used at the split lines).
10. Flight CSS detonator block fairings were sealed with production seals (test CSS detonator block fairings used seals made at Plum Brook).
11. Flight CSS nose cone and payload blankets are 1/2-mil aluminized Kapton (test shroud has 3-mil aluminized Kapton).
12. Flight CSS has production aft split line seal flap installation (test CSS flap was made at Plum Brook).

Test Peculiar Features Not on Proof Flight CSS

1. LH₂ Vent Fin was not installed for tests. An aluminum cover plate was installed at the interface.
2. Only a partial LH₂ Balanced Vent System was installed; i.e., only those portions interfacing with the CSS.
3. The silicone paint was removed from the nose cone, and the CSS was painted black.
4. CSS bolt-ons were not sealed with aerospace sealant compound per print.

Other Test Configuration Differences or Changes

1. After tests 1 and 2, the forward seal, Forward Seal Releaser System/explosive bolts, and the forward seal/Releaser Assist System were not reinstalled.
2. The Titan Skirt Bellows (quad 3), which was damaged during test 1, was not reinstalled.
3. The Payload Vent Gas Retainer was installed starting with test 2.
4. Titan Skirt Bellows brackets were installed starting with test 2.
5. GDC FBR foam blocks replaced the LMSC blocks starting with test 2.

APPENDIX D

Calculations of CSS Edge Motions from Accelerometer Data

Theodore W. Porada

A double integration of six accelerometers was performed on an analog computer to determine edge motion deflections of the CSS. Four accelerometers were mounted at station 2664 (two per half) and two were mounted at station 2460 on the light half as shown in figure D-1. In the time interval between jettison command and approximately 1.2 seconds following, these six acceleration measurements were integrated to obtain deflections.

The method of obtaining deflections by integrating accelerometer data on an analog computer resulted in some problems which require qualifying the results. The high gains through the integrating amplifier result in unacceptable drifts due to DC biases on the data and drift associated with the amplifier itself. This problem was partially solved by filtering the data using a transfer function of the type shown in figures D-6 and D-7. Nothing could be done to solve the integrating amplifier drift. Consequently, the deflection data shows drift which may or may not be associated with fairing rocking. Absolute deflection data, therefore, should not be extracted from this data. It was also found that some accelerometers calibrated to ± 10 g's showed outputs significantly beyond 10 g's (in many cases over 15 g's) due to the shock at the time the pyrotechnics were fired. This resulted in exceeding not only the range of the instrument, but also the range of the recording equipment (an FM system calibrated at 1.0V. = 10 g's). Computed initial deflections in the first 150 milliseconds following the jettison command in these cases showed no correlation with camera data. A combination of exceeding the range of the measuring instrument and the recording equipment, due to the shock associated with the jettison event, is the most probable cause of this discrepancy. Data that is useful, however, are the peak-to-peak amplitudes after the initial shock of jettison has subsided. This data correlates with camera data.

For the first heated jettison test, figure D-2 shows the results of the double integration of accelerometers 962A, 963A, 960A and 961A. These four accelerometers were mounted on the -Y light half of the CSS. At station 2664 just following the jettison command, CSS edge deflection camera data show that approximately 2.2 inches of inboard motion resulted. Deflection calculations at station 2460, where the forward bearing reaction struts are located, showed significantly smaller deflections of 0.4 inches inboard. The predominant average frequency was calculated to be 6.0 Hz.

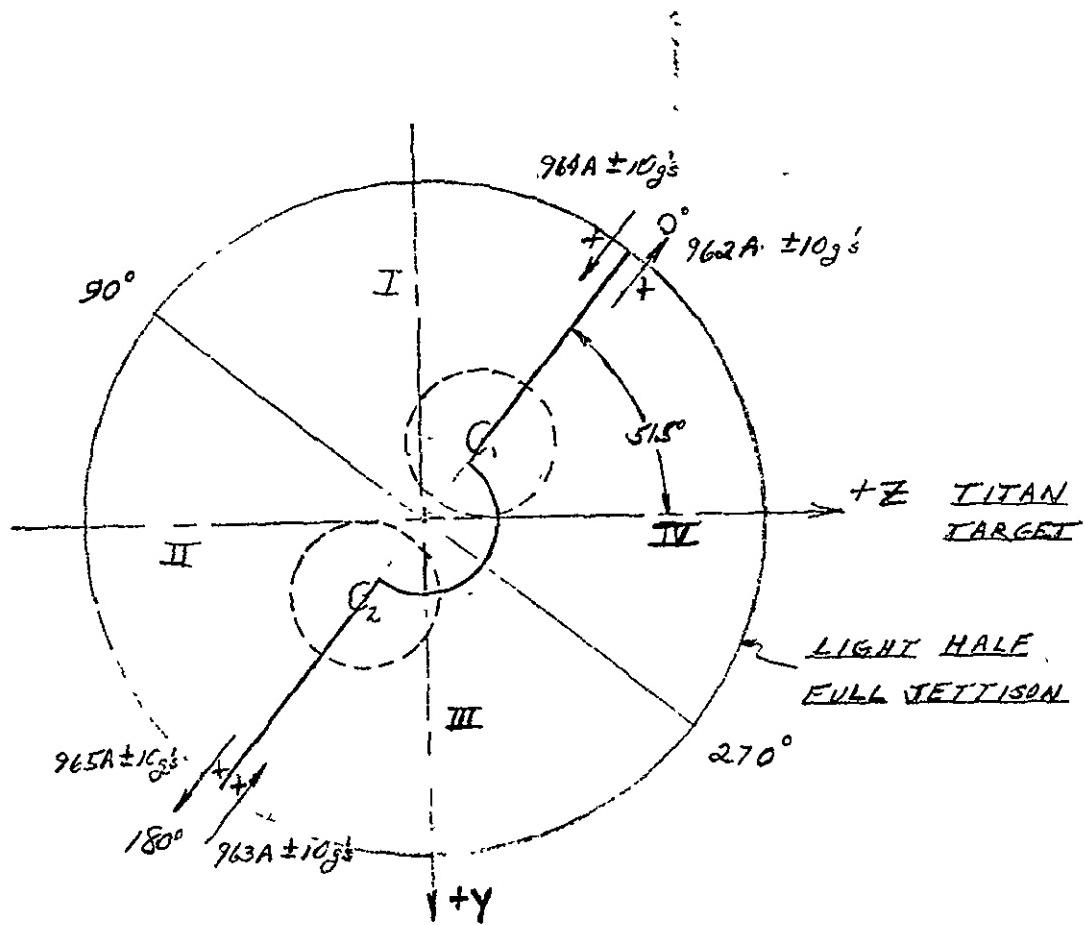
Accelerometers on the +Y heavy half were mounted only at station 2664, one of which (accelerometer 965A) failed. The double integration of the remaining accelerometer (964A) is shown in figure D-3. This calculation showed 0.1 inches of inboard motion following the jettison command. This data does not correlate with

camera data of the +Y heavy half or show any similarity in magnitude to those accelerometers which were mounted on the light half. The evidence indicates that accelerometer 964A did not perform or was improperly calibrated.

Figure D-4 shows the double integration of the four accelerometers located at station 2664 for the heated jettison test 2. These are 962A and 963A located on the -Y light half and 964A and 965A located on the +Y heavy half. No useable deflection data could be extracted from 962A for those reasons mentioned early in the test. The double integration of the remaining accelerometers showed a sustained oscillation with peak-to-peak deflections of approximately 2.5 inches at a frequency of 5.5 Hz. The initial shock at the jettison event exceeded the calibration range of the accelerometer and the recording equipment. The data for the first 150 milliseconds is not useful and does not represent the actual motion of the CSS.

Figure D-5 shows the double integration of the four accelerometers located at station 2664 for the unheated jettison test 3. The double integration of accelerometer 963A produced no useable data and accelerometer 962A showed excessively high drift. The remaining accelerometers, 964A and 965A, showed computed peak-to-peak amplitudes of 0.8 inches at a frequency of 5.3 Hz. The initial deflection following jettison command indicated inboard motion of approximately 1 inch. This data correlates with camera data.

STA 2664



STA 2460

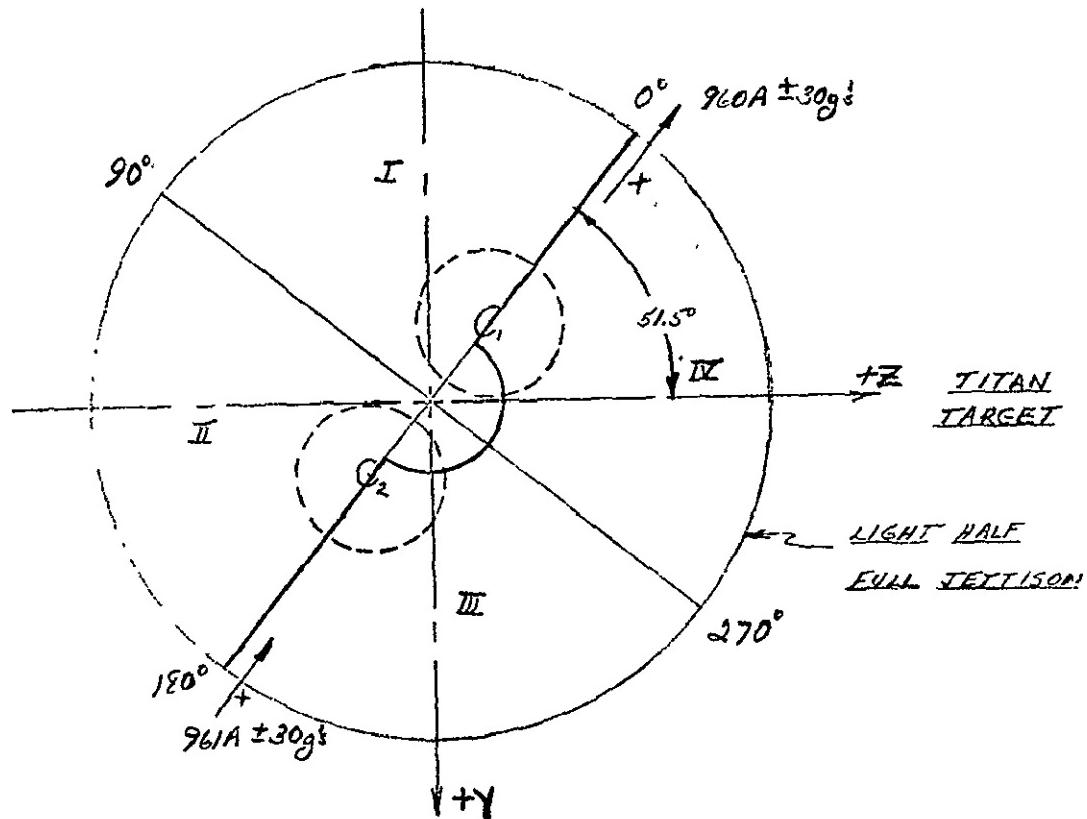


FIGURE D-1 ACCELEROMETER LOCATIONS, CALIBRATION RANGES,
AND POLARITY CONVENTIONS

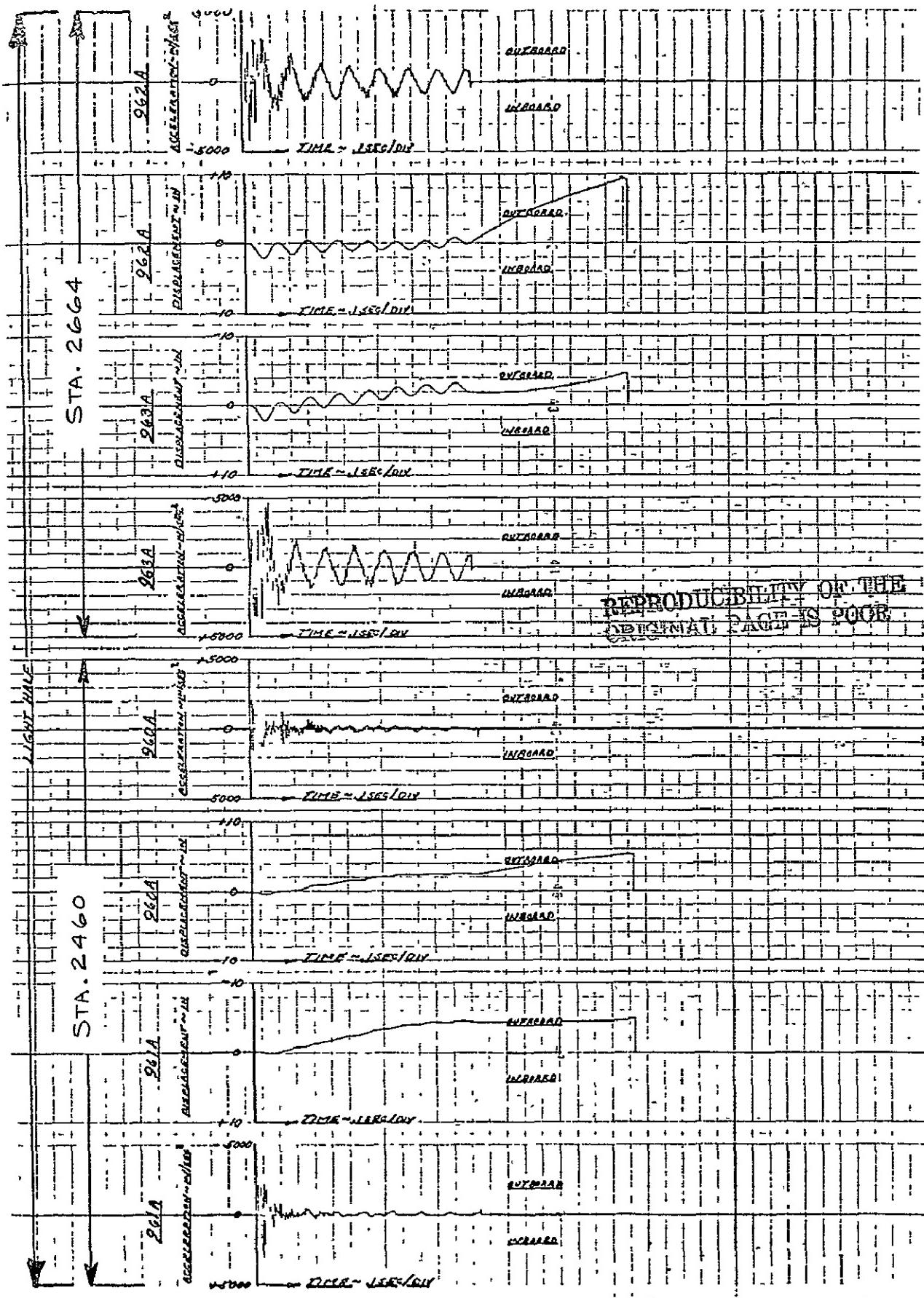


FIGURE D-2 CSS ACCELEROMETER ANALYSIS FOR HJT#1

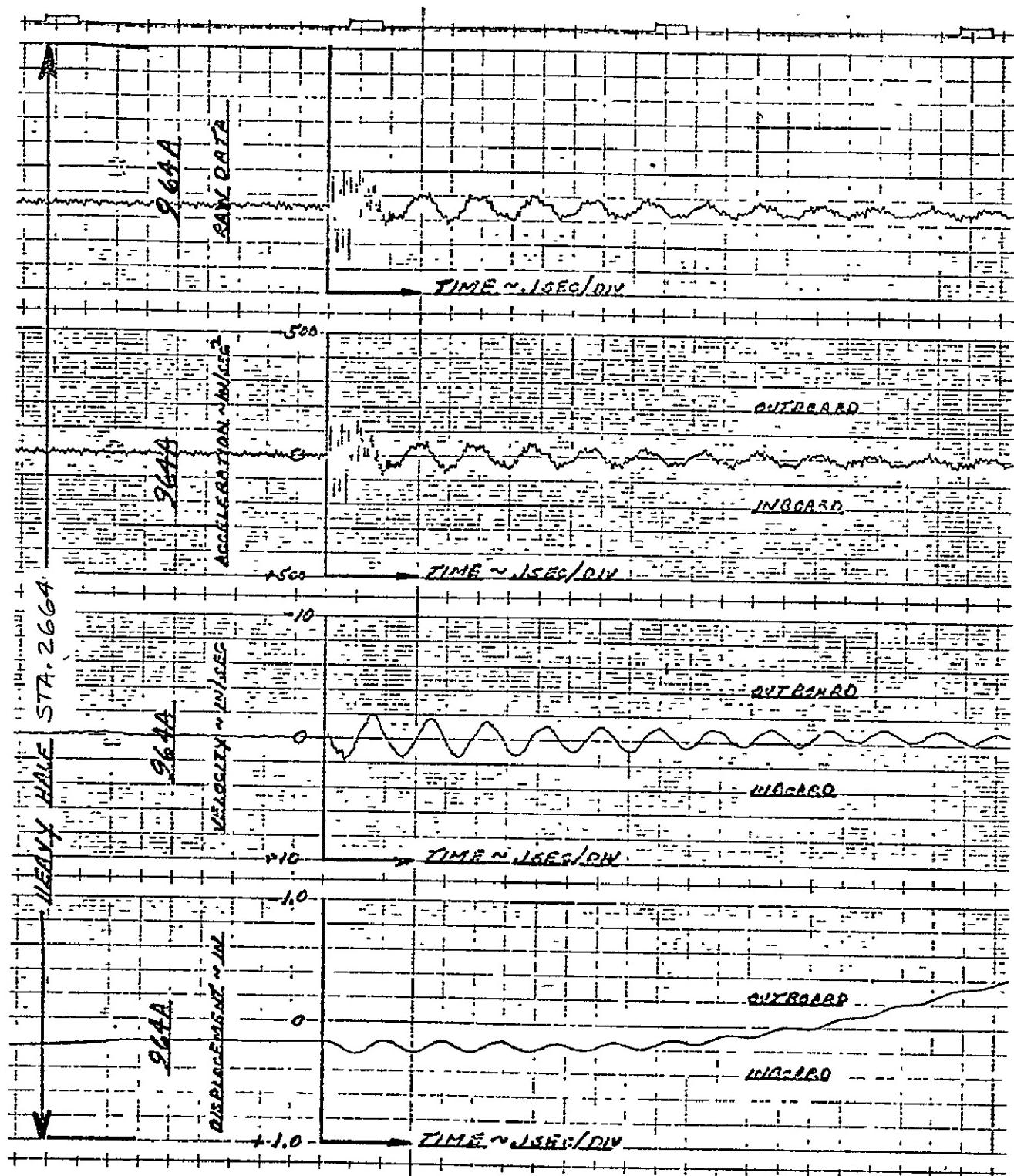


FIGURE D-3 CSS ACCELEROMETER ANALYSIS FOR HJT#1

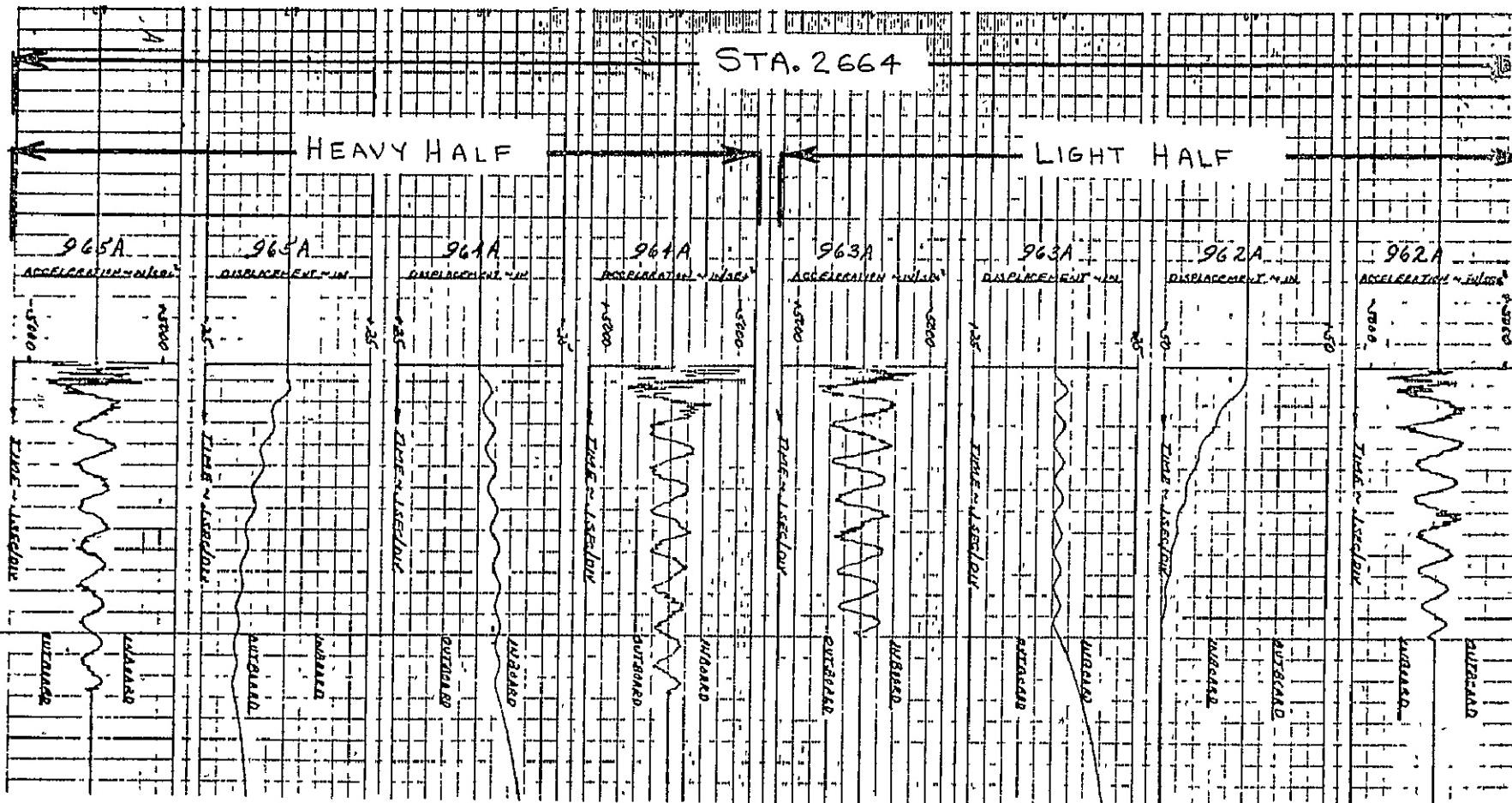
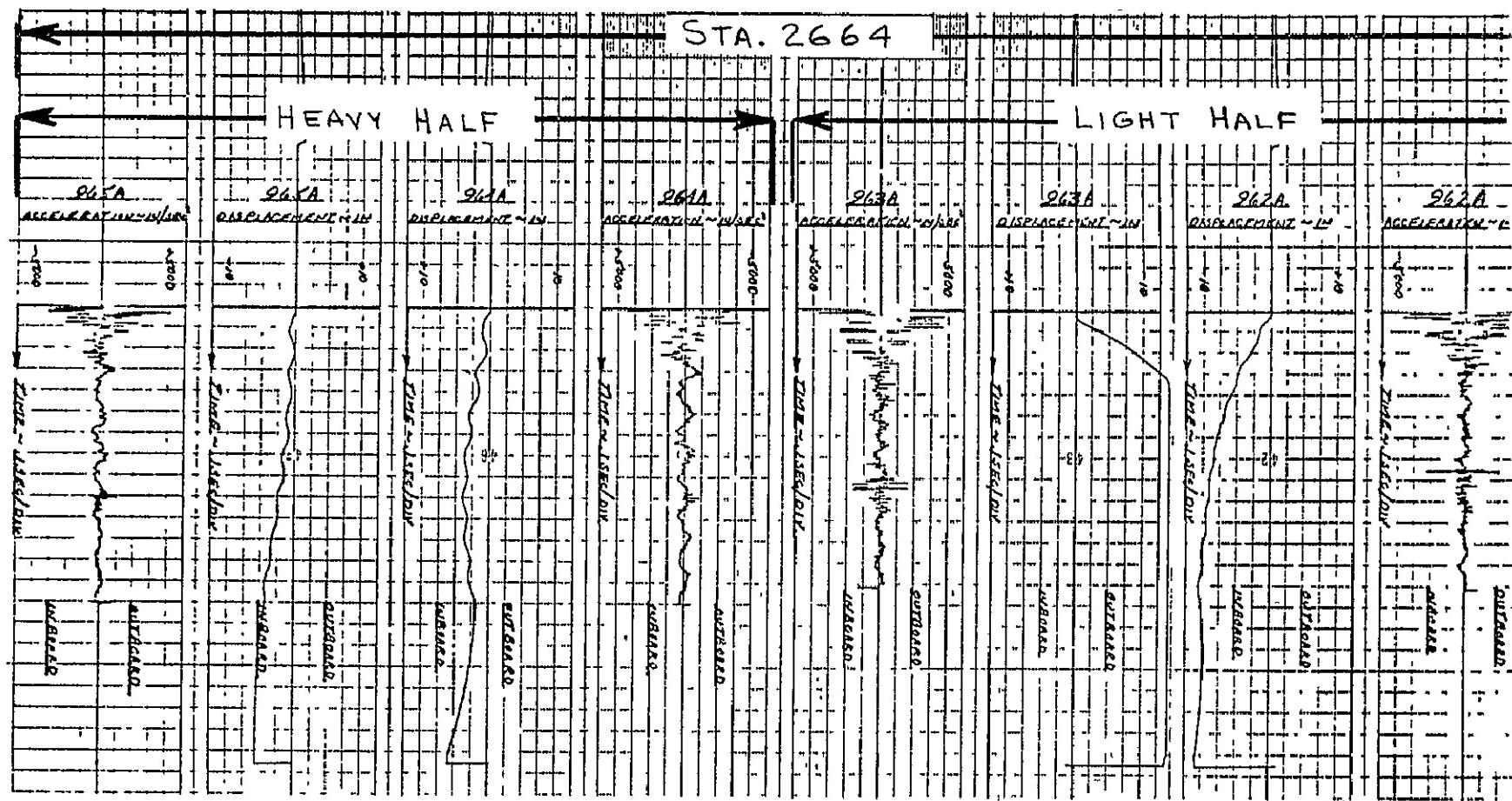
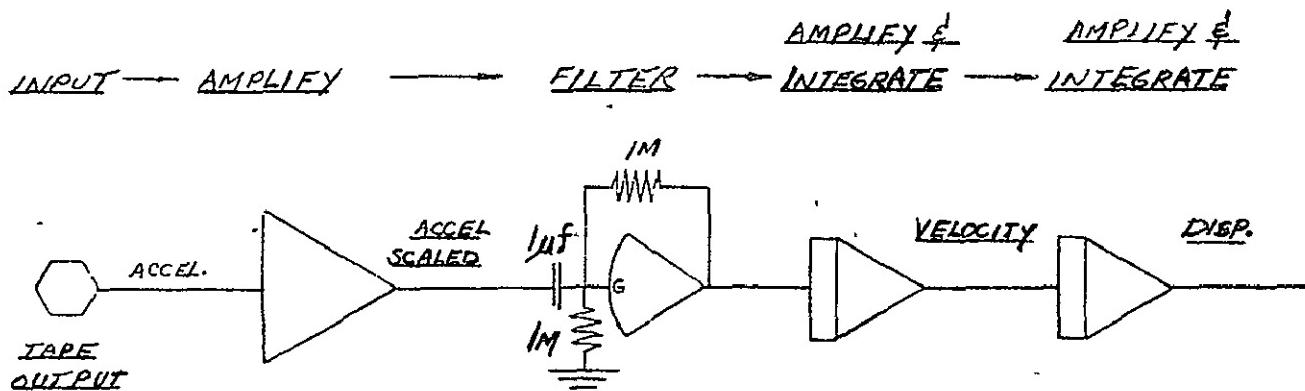


FIGURE D-5 CSS ACCELEROMETER ANALYSIS FOR UNHEATED TEST #3





FILTER TRANSFER FUNCTION

$$\frac{S}{S+1}$$

INPUT ————— $\frac{S}{S+1}$ ————— OUTPUT

S = RAD/SEC.

FIGURE D-6 TYPICAL INTEGRATION CIRCUIT

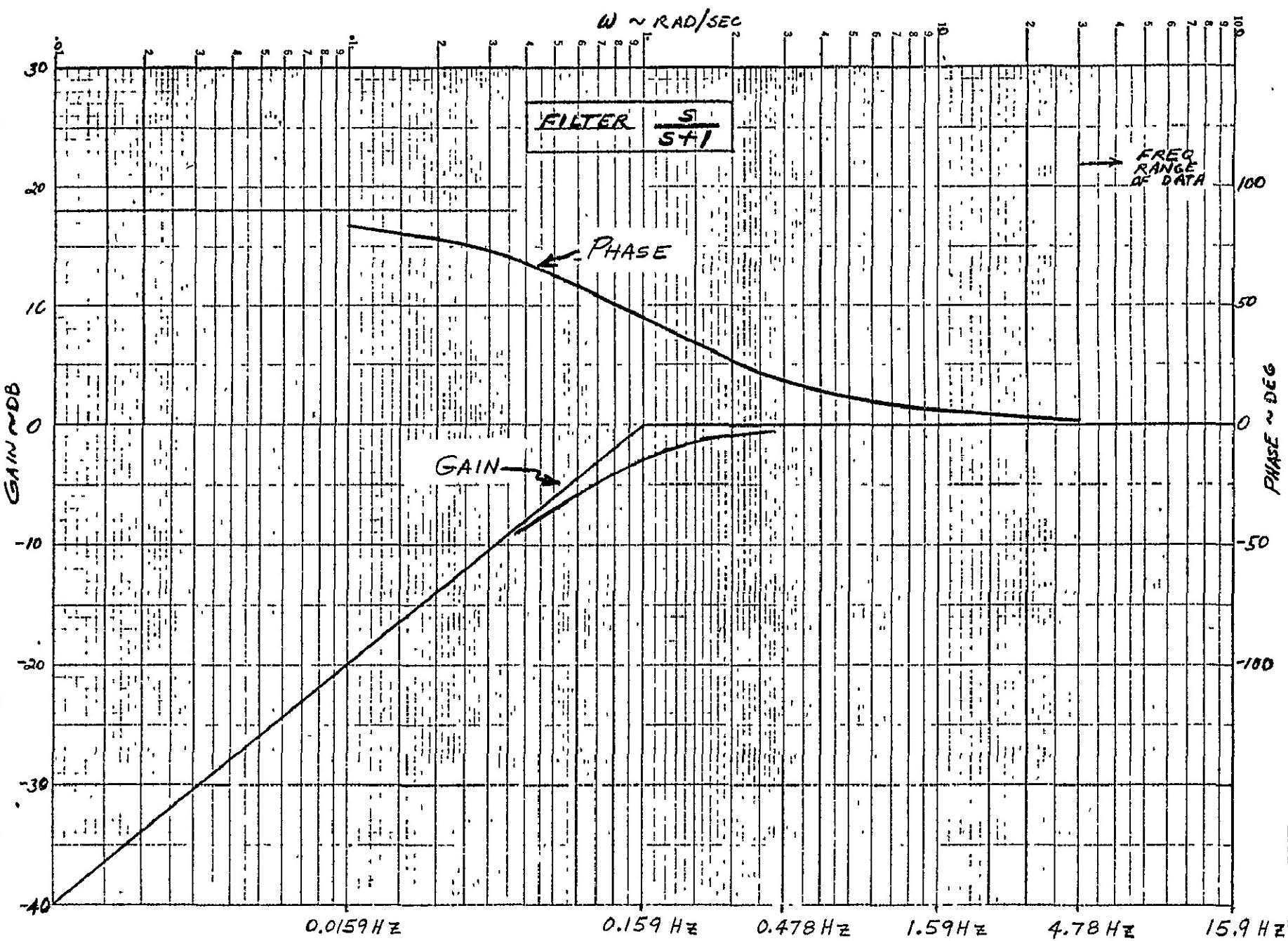


FIGURE D-7 ACCELEROMETER FILTER GAIN AND PHASE VS. FREQUENCY

REFERENCES

1. Stofan, A. J.: Titan/Centaur NASA's Newest Launch Vehicle. NASA TM X-68249, July 1973.
- 1a Eaton, R. B.: Design, Development and Testing of the Centaur Standard Shroud Separation System. LMSC/B159399, November 1972.
2. Bauman, R. E.: Static Structural Test Evaluation, CSS Aft Hinge Structure. LMSC/D159642, September 1972.
3. Staff of Lewis Research Center: Centaur Standard Shroud (CSS) Cryogenic Unlatch Tests. NASA TM X-71455, October 1973.
4. Anon.: Centaur Standard Shroud Cryo-Unlatch Test Final Report. LMSC/D337090, April 20, 1973.
5. Staff of Lewis Research Center: Centaur Standard Shroud (CSS) Static Limit Load Structural Tests. NASA TM X-71727, April 1975.
6. Hohenshelt, J. N.; and J. Jue: Ascent Heating of Corrugated Fairings. LMSC/D346083, June 14, 1973.
7. Moudy, W. D.: Input to the Centaur Standard Shroud Heated Altitude Jettison Tests Final Report. LMSC/EM 13503-56, March 20, 1974.
8. Wilson, J. F.; and McKinley, M. K.: Centaur Standard Shroud Heated Altitude Tests Separation Analysis Report. LMSC/D424241, July 1974.
9. Anon.: Centaur Standard Shroud Structural Analysis. LMSC/D152792, February 16, 1973.
10. Staff of Lewis Research Center: Test Requirements Document Centaur Standard Shroud, Heated Altitude Jettison Tests CSS Qualification Test Program. LeRC/TCPO-33, August 15, 1973.